

EXTENDING ATMOSPHERIC PRESSURE MASS SPECTROMETRY:  
DESORPTION AND IONIZATION CONSIDERATIONS

By

KEVIN TURNEY

A DISSERTATION PRESENTED TO THE GRADUATE SCHOOL  
OF THE UNIVERSITY OF FLORIDA IN PARTIAL FULFILLMENT  
OF THE REQUIREMENTS FOR THE DEGREE OF  
DOCTOR OF PHILOSOPHY

UNIVERSITY OF FLORIDA

2004

Copyright 2004

by

Kevin Turney

This dissertation is dedicated to my parents, Marsha and James, for their support; to my sister, Angela, for her friendship; and to my wife, Kimberly, for her patience.

Strange how much you've got to know before you know how little you know.  
—unknown

## ACKNOWLEDGMENTS

Any success that I have had is entirely because of the people who have mentored, guided, and literally pushed me in the right directions. I could never show my full gratitude, yet below is my brief and pathetic attempt.

I am indebted to my research advisor, Willard W. Harrison, for welcoming me into his laboratory and the Harrison Group family. Through the years I have had a chance to admire his scientific passion and managerial wit. The discussions in his office and at the *card table* will always be remembered.

The greatest benefit as a Harrison group member has been the connection shared with Dr. James D. Winefordner's Laboratory. As a research professor, Doc is supportive and compassionate of every graduate student. Also, I am grateful to Dr. Ben Smith for encouragement, and an occasional burger. It has been a delight to work alongside the Winefordner group members, enjoying the traditions and the history of the lab. The JDW laboratory is truly a special place.

Many members of the chemistry department have been both my colleagues and my friends. Dr. Eric Oxley has continued to support the Harrison group even after his departure. I am appreciative of his friendship and his strength in lifting motorcycles. There were times during graduate school that only a talk with Dr. Paige Oxley could brighten my day—I still miss the discussions. I thank Li Qian for teaching me science and game strategy.

Some people always wear a smile, walking through the lab making everyone feel just a little bit better. Over the last few years, for the Winefordner and Harrison groups, that person has been Dr. Tiffany Correll. Her sense of humor and good-natured spirit are truly unique. She always knew how to put me in my place—*Go Dumplings*.

Lock two people in a room for a few years and they may become friends or they may become enemies. I am happy to say the years I spent with my lab mate were filled with scientific discussion, data collection, and laughter. I consider Dr. Elizabeth Pierz Hastings a cherished and respected friend.

Many thanks also go to Dr. Wichong Tan's laboratory, the members provided me with scientific instrumentation and camaraderie. Special thanks go to a good friend, Tim Drake, for this help with science and university politics.

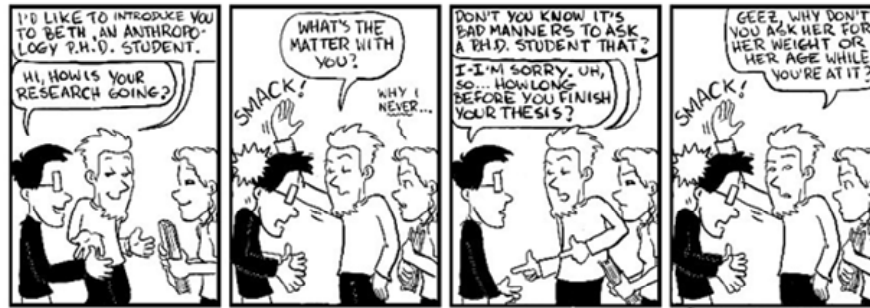
I may forget the science I learned along the way, but I will not forget the friends I made. My most prized memories of graduate school are the late nights and the coffee runs—both of which were not conducted alone.

My path to graduate school was long and not without ordeals. I would never have gotten here without the help of an influential Professor, Dr. Suzanne Bell. She provided an engaging scientific environment that made me want to be a part of science. I am deeply indebted to her for both scientific and personal growth.

On a more personal note, I thank my parents, James and Marsha DeMotta, for their never-ending support. I try my best everyday to simply make them proud. I thank my sister, Angela, for always being there—in good times and bad. Special thanks also go to my brother-in-law, Brian; and to my three wonderful nieces, Amanda, Alexis, and Abigail.

To one person I am most indebted: my wife Kimberly. She may be last on paper, but she is always first in my mind. I thank her for her support, patience, and love—*more*. Neither this dissertation nor my graduate work would have existed without her.

If I've failed to iterate my thanks, or I left a crucial individual or two out, please do not fault me—as you know, I need help from time to time.



"Piled Higher and Deeper" by Jorge Cham  
www.phdcomics.com

## TABLE OF CONTENTS

	<u>Page</u>
ACKNOWLEDGMENTS .....	iv
LIST OF TABLES .....	xi
LIST OF FIGURES .....	xii
LIST OF OBJECTS .....	xvi
ABSTRACT .....	xvii
CHAPTER	
1 MOLECULAR MASS SPECTROMETRY .....	1
Historical Background .....	1
Ionization Techniques .....	1
Electron Ionization .....	2
Chemical Ionization .....	5
Biomolecule Analysis .....	8
Energy-Sudden Approach .....	8
Plasma Desorption .....	9
Fast Atom Bombardment .....	11
Laser Desorption Ionization .....	13
Matrix-Assisted Laser Desorption/Ionization .....	14
Mechanisms .....	16
Matrix considerations .....	21
Time-of-Flight Mass Spectrometry .....	22
Historical Perspective .....	22
Time-of-flight Theory .....	23
Kinetic energy spreads .....	25
Spatial spreads .....	26
Desorption Ionization Techniques .....	27
Conclusions .....	28

2	DESIGN OF AN ATMOSPHERIC PRESSURE MATRIX-ASSISTED LASER DESORPTION/IONIZATION SOURCE FOR AN ORTHOGONAL- ACCELERATION TIME-OF-FLIGHT MASS SPECTROMETER.....	29
	Introduction.....	29
	Background.....	29
	Orthogonal-Acceleration Time-of-Flight.....	29
	Atmospheric Pressure Inlets.....	31
	Atmospheric Pressure MALDI.....	33
	Experimental Methods.....	35
	Mass Spectrometer.....	35
	Electrospray Configuration.....	37
	Atmospheric Pressure MALDI Configuration.....	39
	Sample Preparation.....	41
	Solid matrix.....	41
	Liquid matrix.....	42
	Results and Discussion.....	42
	Electrospray Evaluation.....	42
	APMALDI Source.....	43
	Prototype I.....	43
	Prototype II.....	54
	Adjusting Interface Parameters.....	55
	Conclusions.....	61
3	LIQUID SUPPORTS FOR ULTRAVIOLET ATMOSPHERIC PRESSURE MATRIX-ASSISTED LASER DESORPTION/IONIZATION.....	62
	Introduction.....	62
	Experimental Methods.....	65
	Atmospheric Pressure MALDI Source.....	65
	Solution Preparation.....	65
	Results and Discussion.....	66
	Liquid Matrices.....	66
	Chromophore Concentration.....	66
	Support Liquid Variations.....	72
	Solids versus Liquid Matrices.....	76
	Quantitation.....	82
	Mixture Analysis.....	84
	Conclusions.....	86
4	LASER DESORPTION CONSIDERATIONS USING LIQUID MATRICES AT ATMOSPHERIC PRESSURE.....	87
	Introduction.....	87
	Background.....	89

Experimental Methods.....	90
Atmospheric Pressure MALDI oa-TOFMS .....	90
Fluorescence Measurements.....	91
Matrix and Analytes .....	91
Results and Discussion .....	92
Liquid Matrix Homogeneity.....	92
Laser Frequency .....	94
Fluence Dependence.....	96
Particle Ejection.....	100
Plume Interactions.....	106
Conclusions.....	107
5 FUNCTIONALIZED NANOPARTICLES FOR LIQUID APMALDI PEPTIDE ANALYSIS.....	109
Introduction.....	109
Experimental Methods.....	113
Materials.....	113
Nanoparticle Synthesis .....	113
Silica C18 functionalized nanoparticles .....	113
Magnetic aptamer nanoparticles.....	114
Matrix and Analyte Preparation .....	115
Instrumentation.....	115
Extraction Procedures.....	116
Results and Discussion .....	119
Background.....	119
Nanoparticle Characterization .....	119
Peptide Analysis by Liquid APMALDI with C18 Nanoparticles .....	122
Peptide Analysis by Liquid APMALDI with Aptamer Nanoparticles.....	129
Conclusions.....	132
6 SECONDARY IONIZATION OF LASER DESORBED NEUTRALS FROM ATMOSPHERIC PRESSURE MATRIX-ASSISTED LASER DESORPTION/IONIZATION .....	134
Introduction.....	134
Experimental Method .....	136
Atmospheric Pressure MALDI oa-TOFMS .....	136
Corona Discharge.....	136
Matrix and Analytes .....	138
Results and Discussion .....	139
Secondary Ionization of Desorbed Neutrals.....	139
Corona Discharge.....	142
Discharge mode.....	142
Water clusters.....	143

Neutral Molecule Fluence Threshold .....	145
Ion Transmission .....	149
Conclusions.....	150
7 CONCLUDING REMARKS.....	151
APPENDIX MALDI MATRICES AND PREPARATION .....	157
LIST OF REFERENCES.....	160
BIOGRAPHICAL SKETCH .....	172

## LIST OF TABLES

<u>Table</u>	<u>Page</u>
1-1 Common reagent gases for chemical ionization techniques..	7
1-2 Typical laser wavelengths, photon energies, and pulse widths used for MALDI...	17
2-1 Mass spectrometer conditions used to acquire electrospray spectra.	38
2-2 Mass spectrometer conditions used to acquire APMALDI spectra.	40
4-1 Conditions used to acquire the emission spectrum of the CHCA liquid matrix. ...	103
A-1 Common MALDI matrices.	158

## LIST OF FIGURES

<u>Figure</u>	<u>Page</u>
1-1 Diagram of an electron ionization source.....	3
1-2 Plot of ion yields versus electron energy. ....	4
1-3 Diagram of a chemical ionization source.....	6
1-4 Plot of rate constants for decomposition and vaporization versus $1/T$ .....	10
1-5 Diagram of californium plasma desorption ionization source. ....	11
1-6 Diagram of a fast atom bombardment ionization source. ....	13
1-7 Diagram of a matrix-assisted laser desorption/ionization source.....	16
1-8 Diagram demonstrating the principle theory in time-of-flight mass analysis. ....	24
2-1 Diagram depicting the complementary nature of atmospheric pressure ionization sources.....	34
2-2 Diagram of the orthogonal-acceleration time-of-flight mass spectrometer used in the studies presented is shown. ....	35
2-3 A photograph of the electrospray tip used for mass spectrometer characterization.	38
2-4 A diagram of the components in a typical atmospheric pressure matrix-assisted laser desorption/ionization source.....	39
2-5 Plots showing the A) total ion count chromatogram and B) a mass spectrum for the analysis of reserpine.....	44
2-6 Plots showing the A) total ion count chromatogram and B) a mass spectrum for the analysis of verapamil.....	45
2-7 A photograph of the first constructed APMALDI source (Prototype I). ....	47
2-8 A mass spectrum of reserpine analyzed in a solid DHB matrix.....	48
2-9 Plot of the total ion count chromatograms for solid and liquid matrices. ....	49

2-10	A photograph of the altered target assembly for liquid matrix analysis. ....	50
2-11	Mass spectrum of reserpine in a DHB liquid matrix taken using the modified target assembly. ....	51
2-12	A photograph of the source and target assembly with the curtain gas cover removed. ....	52
2-13	Mass spectra obtained with the target placed at a distance of A) 1.5 mm from the orifice and B) 2 mm from the orifice. ....	53
2-14	A photograph of the second APMALDI source (Prototype II). ....	54
2-15	Three mass spectra taken using gas flow rates of A) 0 L·min <sup>-1</sup> , B) 1 L·min <sup>-1</sup> , and C) 5 L·min <sup>-1</sup> . ....	56
2-16	An illustration of the mass spectrometer interface. ....	57
2-17	A three dimensional plot showing the relationship of target and nozzle voltage to analyte ion yields. ....	58
2-18	A three dimensional plot showing the relationship of nozzle and skimmer voltages to analyte ion signal intensity. ....	59
3-1	The plot shows analyte ion and matrix background intensity as a function of CHCA concentration in the liquid matrix. ....	68
3-2	Mass spectrum of five picomoles of angiotensin II analyzed using an optimized CHCA liquid matrix. ....	70
3-3	An illustration of the UV-Vis absorption spectra collected for common MALDI matrices. ....	71
3-4	A plot of analyte ion intensity as a function of DHB concentration. ....	72
3-5	A chart of analyte intensity versus the percentage of DEA in the liquid matrix. ....	74
3-6	A chart of analyte intensity versus solvent liquid used in the liquid matrix. ....	75
3-7	Mass spectra of bradykinin fragment 1-7 comparing solid and liquid matrix preparations. ....	77
3-8	Mass spectra of angiotensin I comparing solid and liquid matrix preparations. ....	78
3-9	Mass spectra of ACTH fragment 18-39 comparing solid and liquid matrix preparations. ....	80
3-10	Mass spectra of P <sub>14</sub> R comparing solid and liquid matrix preparations. ....	81

3-11	A calibration curve for angiotensin II. ....	83
3-12	A calibration curve for bradykinin fragment 1-7. ....	84
3-13	A mass spectrum for a peptide mixture using the CHCA liquid matrix. ....	85
4-1	A plot showing individual ion packets resulting from liquid matrix analysis. ....	93
4-2	A plot of analyte ion signals and pulse energy as a function of laser frequency. ....	95
4-3	A plot of small molecule analyte ion yields as a function of pulse energy. ....	97
4-4	A plot of peptide analyte ion yields as a function of pulse energy. ....	98
4-5	The calibration of a UV neutral density filter wheel for pulse energy. ....	99
4-6	Mass spectra for reserpine illustrating fragmentation produced at higher pulse energies ( <i>i.e.</i> , 10, 90, and 180 $\mu$ J). ....	100
4-7	Mass spectra for bradykinin fragment 1-7 illustrating fragmentation produced at higher pulse energies ( <i>i.e.</i> , 10, 90, and 180 $\mu$ J). ....	101
4-8	Emission spectrum of the CHCA liquid matrix using 337 nm excitation. ....	102
4-9	Fluorescence image of the laser impinging on the liquid matrix surface. ....	104
4-10	Fluorescence image of particles ejected from the liquid matrix. ....	105
4-11	Mass spectra demonstrating analyte signal suppression. ....	107
5-1	An illustration of the centrifugation technique used for nanoparticle extractions. ....	116
5-2	A diagram illustrating the utility of the nanoparticles with the liquid matrix. ....	117
5-3	An illustration of the magnetic separation technique used for nanoparticle extractions. ....	118
5-4	Nanoparticle characterization using fluorescence analysis. ....	120
5-5	A chart of the protonated molecular ion mass spectrometry signals for three peptides. ....	123
5-6	Mass spectra collected from nanoparticle extractions. ....	124
5-7	A chart showing the effect multiple washing steps has on the sodium adduct signals during mass spectrometry analysis. ....	125
5-8	Mass spectra collected for a 1 $\mu$ M angiotensin II solution before and after nanoparticle extraction. ....	126

5-9	A chart of the protonated molecular ion mass spectrometry signals for three varied length peptides.....	128
5-10	Mass spectra for L and D vasopressin before and after nanoparticle extractions. .	131
6-1	A diagram of the laser desorption atmospheric pressure chemical ionization source is shown.....	137
6-2	A photograph of the LD-APCI source. ....	138
6-3	The total ion chromatogram for three modes of source operation. ....	140
6-4	Mass spectra for reserpine using a CHCA liquid matrix in A) APMALDI and B) LDAPCI source modes.....	141
6-5	A figure showing the transition from a corona discharge to glow discharge.....	143
6-6	A mass spectrum for water clusters produced from the corona discharge in air....	145
6-7	A plot of the analyte ion intensity and corona current as the needle voltage is adjusted (low fluence laser desorption).....	146
6-8	Mass spectra of bradykinin fragment 1-7 using low fluence APMALDI and LD-APCI modes. ....	147
6-9	Mass spectra for P <sub>14</sub> R using low fluence APMALDI and LD-APCI modes. ....	148
6-10	Mass spectra for ACTH fragment 18-39 using low fluence APMALDI and LD-APCI modes. ....	148
6-11	A plot of the analyte ion intensity and corona current as the needle voltage is adjusted (high fluence laser desorption).....	149

## LIST OF OBJECTS

<u>Object</u>	<u>Page</u>
2-1 A file showing the ion source configuration after the target alteration for liquid matrix analysis (1.8 mb, PrototypeI.exe, repeating play file). .....	48
2-2 A file showing the orientation of the prototype II source (1.8 mb, PrototypeII.exe, playable file).....	54
4-1 A video of the laser irradiating the liquid sample surface. (1.3 mb, Liquidregeneration.mpg, 50 seconds). .....	94
4-2 A video of the laser irradiating the liquid sample demonstrating particle ejection at 110 $\mu$ J pulse energy. (1 mb, 110pulseenergy.mpg, 10 seconds). .....	105
4-3 A video of the laser irradiating the liquid sample demonstrating particle ejection at 140 $\mu$ J pulse energy. (1 mb, 140pulseenergy.mpg, 10 seconds). .....	105
4-4 A video of the laser irradiating the liquid sample demonstrating particle ejection at 180 $\mu$ J pulse energy. (1 mb, 180pulseenergy.mpg, 10 seconds). .....	105
4-5 A video of the laser irradiating the liquid sample demonstrating particle ejection at 180 $\mu$ J pulse energy—magnified view. (1 mb, 110pulseenergyzoomed.mpg, 10 seconds). .....	105
4-6 A video of the laser irradiating the liquid sample demonstrating particle ejection at 180 $\mu$ J pulse energy—slow motion (non-false color) view. (5.5 mb, 180pulseenergyslowed.mpg, 50 seconds). .....	105
6-1 A file showing the orientation of the LD-APCI source (1.8mb, LDAPCI.exe, repeating play file). .....	137

Abstract of Dissertation Presented to the Graduate School  
of the University of Florida in Partial Fulfillment of the  
Requirements for the Degree of Doctor of Philosophy

EXTENDING ATMOSPHERIC PRESSURE MASS SPECTROMETRY:  
DESORPTION AND IONIZATION CONSIDERATIONS

By

Kevin Turney

December 2004

Chair: Willard W. Harrison  
Major Department: Chemistry

Biological mass spectrometry has received well-deserved attention for its role in biopolymer characterization. Matrix-assisted laser desorption/ionization (MALDI) is one method that allows the ionization of large intact biomolecules. For analysis, MALDI requires a suitable matrix for energy absorption and transfer to the analyte. The most widely accepted form of matrix is some form of solid that acts as an analyte host. While compatible with the low pressure environment of a typical ion source, the matrix presents a heterogeneous sample surface. Recent advances have allowed MALDI to be conducted at atmospheric pressure (AP), extending its flexibility in source design and applications. This research contributes in this area by expanding upon atmospheric pressure ionization techniques and their unique applications.

To further sample analysis opportunities at atmospheric pressure, a liquid matrix for UV APMALDI analysis was developed. Liquid matrices allow possible formulations focused on desorption and ionization versus vacuum stability and source contamination.

The liquid matrices we examined provide a self-renewing surface that eliminates sampling heterogeneity, increases sample lifetime, and provides shot-to-shot reproducibility. Ambient condition liquid sampling also allows measurements for laser penetration depth, fluence ranges, particle ejections, and chromophore concentration, which can add to the study of MALDI mechanistic pathways. The liquid matrix offers advantages that complement current MALDI methods.

Liquid sampling reduces sample preparation, compared to solid matrices; however, during biological analysis separations are often the rate determining step. We have explored further reductions in preparation time for biomolecules with the use of nanoparticles. Functionalized nanoparticles provided specific extraction, retention, and concentration of simple biopolymers.

During desorption process in MALDI, a large population of neutral molecules is created. A secondary ionization technique, such as atmospheric pressure chemical ionization, can provide reagent ions for interaction with laser desorbed neutrals. Results show that UV laser desorbed neutrals do interact with atmospheric pressure reagent ions; however, the individual optimization of each process is needed. Secondary ionization of the neutral molecules provides an avenue for probing ion-molecule chemistry.

The exploitation of AP interfaces with atmospheric pressure laser desorption techniques can provide needed advances in biological analysis.

## CHAPTER 1 MOLECULAR MASS SPECTROMETRY

“Molecules having the same mass numbers but differing in weight by an amount determined only by the difference in binding energies of the nuclear particles can be clearly resolved.... Extension of the use of the instrument to the resolution of heavy hydrocarbons should prove fruitful.”

—Alfred O. Nier 1955<sup>1</sup>

### **Historical Background**

The origins of mass spectrometry are deeply rooted in the field of atomic physics. Beginning with John Dalton, and his proposed new atomic theory, the idea that a unique measurable property (relative atomic weight) existed for each element, was born.<sup>2</sup> These masses make the basis of measurement in “mass” spectrometry. Years after the atomic theory was developed, J. J. Thompson was able to advance instrumentation and obtain the first charge-to-mass ratios,  $e/m$ , for hydrogen and oxygen.<sup>3</sup> The instrumentation directed discoveries in both experimental atomic physics and mass spectrometry. This type of paradigm, instrumentation progress leading to application-driven discoveries, has followed the mass spectrometry field throughout its existence. Even today resolution and precision advances have challenged ion formation mechanistic theories.<sup>4</sup>

### **Ionization Techniques**

All mass spectrometers comprise five major components: sample inlet, ionization source, mass analyzer, ion detector, and data acquisition system. At times, regions, such as the inlet and the ionization source, can be combined (*i.e.*, atmospheric pressure sources (*Vida infra*)). However, even when regions may seem indistinguishable, each is required

for mass analysis. With mass spectrometry's basis in physics, it is not surprising that the beginning dealt with ionization fundamentals. Using a combination of electrostatic and magnetic fields for spatial dispersion and photographic plates for detection, physicists focused on the ion source for further advancements.<sup>5</sup> For instance, Thompson's initial studies using mass spectrometry involved Goldstein's *Kanalstrahlen*, a glow discharge ionization technique.<sup>2</sup>

While early sources provided easy access to gases, they did not provide convenient analysis of solid samples. At least not until Arthur Dempster made use of a high-frequency spark discharge to determine the isotopic analysis of platinum, palladium, gold, and iridium.<sup>2</sup> Ions were created in the energetic discharge by using conducting samples as the counter electrode, but it was difficult to analyze semiconductors and insulators. Typical of ionization techniques, advances in the field provide new avenues for analysis (*i.e.*, solid samples); the advancements led to additional fundamental questions. The next step in ion source development eventually shifted the focus of mass spectrometry from the physicist's instrumentation to the chemist's analytical tool. While the pioneers of American mass spectrometry, Arthur Dempster, Walker Bleakney, Kenneth Bainbridge, Alfred Nier, and John Tate researched elemental composition and pure compounds, a need arose to analyze crude samples in the petroleum industry.<sup>6</sup> For this need to be met, new ionization techniques were required.

### **Electron Ionization**

Initially, electron ionization (EI) became the standard for hydrocarbon analysis in the petroleum industry, producing fragments for structural identification and molecular pattern recognition. Electron ionization is widely used in organic mass spectrometry, and is suitable for volatile and thermally stable molecules. EI is a technique that uses

energetic electrons to “hit” molecules and remove an outer electron, forming a radical ion. Devised by Dempster and improved by Bleakney and Neir, a diagram for a typical EI source is shown in Figure 1-1.<sup>7-8</sup>

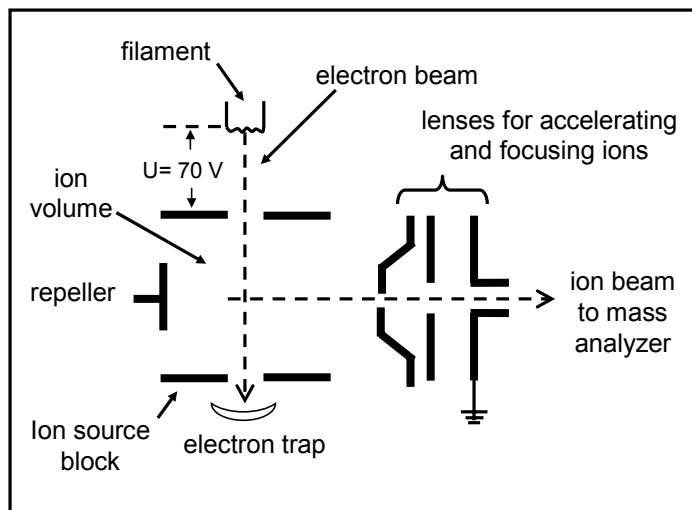
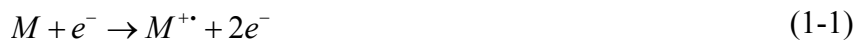


Figure 1-1. Diagram of an electron ionization source. Adapted from reference 9.

If an electron ( $e$ ) transfers enough energy to a neutral molecule ( $M$ ), exceeding its ionization energy, ejection of an electron generates a radical cation ( $M^{+\bullet}$ ):



Electrons are emitted from an electrically heated filament and accelerated to 70 eV by potential gradients. As sample molecules, typically vapor, enter the ionization region, the electron beam collides with the molecules, resulting in deposition of energy. Most organic molecules only require from 8 eV to 12 eV for ionization; therefore, the additional energy retained in the molecule causes fragmentation. Figure 1-2 shows how ion yields vary with electron energy. The decreased ionization efficiency at the lower potentials is due to inefficient collisions; the ionization efficiency also declines at higher potentials due to the collision efficiency. As the electron energy increases, the molecules start to become “transparent”, thereby lowering collision probabilities. Since each

electron has an associated wavelength (De Broglie wavelength), as the electron energy increases, the wavelength decreases, diminishing the possibility for energy transfer.<sup>10</sup>

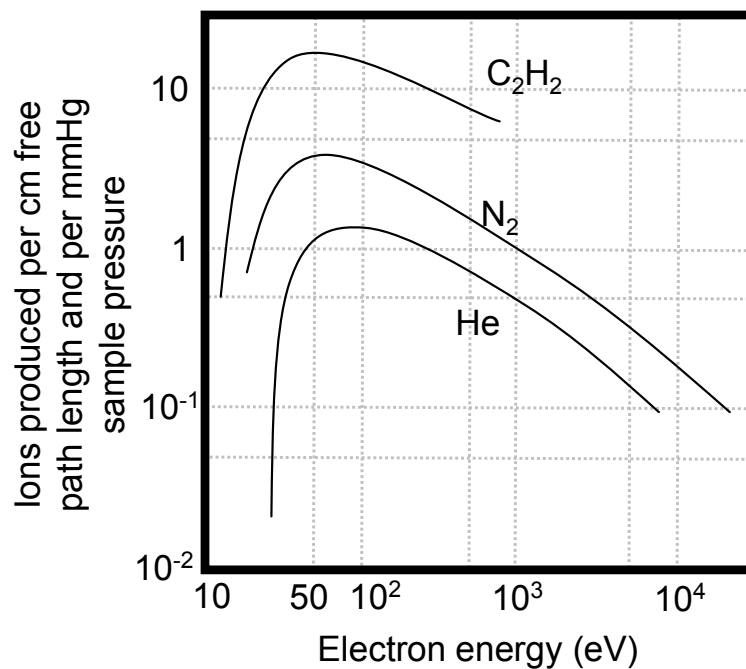


Figure 1-2. Plot of ion yields versus electron energy. A maximum ion yield occurs near 70 eV. Adapted from reference 10.

Ionization techniques must consider both the internal energy transferred and the physicochemical properties of the analyte. Some processes are energetic causing excessive fragmentation; others produce mainly molecular ions. In electron ionization, some classes of compounds have a critical energy for fragmentation that is extremely low, such that no molecular ions are produced. Lowering electron potentials only decreases overall ionization efficiency. It quickly became clear that a new methodology would be needed for molecular ion formation.

## Chemical Ionization

To understand electron ionization mass spectra, the factors affecting ion fragmentation must be considered. As advances in ion decomposition theory led chemists to recognize carbon-carbon cleavages and rearrangement mechanisms, energetics became the common theme for explaining ion formation, ion fragmentation, and gas-phase interactions.<sup>11</sup> Ion formation relates to the energy required to produce an ion from a neutral molecule. Ion fragmentation refers to the energy required to break a chemical bond. Ion interactions involve the energies associated with collisions of ions with neutrals, ions, or surfaces. The fundamental studies of ion-molecule interactions enabled an understanding of gas-phase chemistry, allowing the development of fragmentation limiting ionization techniques (*e.g.*, chemical ionization).

Chemical ionization (CI) produces ions with little excess energy using collisions of the analyte molecules with primary ions created in the source.<sup>12</sup> Ion-molecule collisions allow for a more controlled energy transfer process, reducing fragmentation and producing intact molecular ions. The reduction of fragmentation with the production of molecular ions is termed “soft” ionization. A typical CI source is shown in Figure 1-3.

The CI source, shown in Figure 1-3, uses an electron ionization filament to ionize the reagent gas, which is leaked into an evacuated chamber. The reagent ions formed interact with the neutral gas-phase analyte yielding positive and negative ions of the sample. The ion-molecule reactions in the CI technique (*i.e.*, proton transfer, charge exchange, and others) depend on the properties of both the reagent and analyte.<sup>12</sup> Consequently, the choice of both becomes important in the analysis process. Briefly, some aspects of the analyte and reagent population are described below.

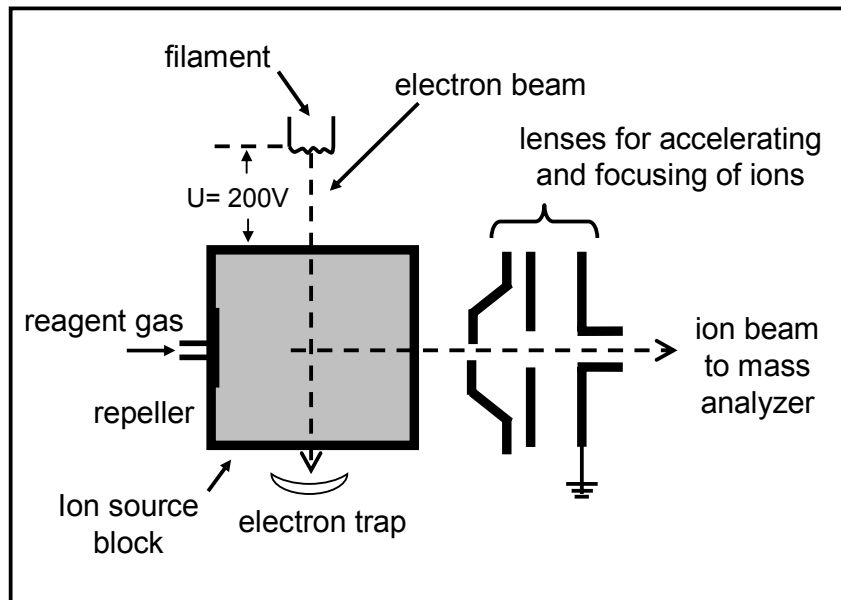


Figure 1-3. Diagram of a chemical ionization source. Adapted from reference 9.

A proton transfer reaction can occur in CI providing the proton affinity (PA) of the analyte (A) is greater than that of the reagent ion (B):



A caveat does exist. If the proton transfer reaction is highly exothermic,  $\Delta H^\circ = PA(B) - PA(A)$ , the excess internal energy will promote fragmentation, preventing maximum quasi-molecular ion formation  $[A+H]^+$ . Reagent ions have characteristic proton affinities listed in Table 1-1.<sup>12</sup>

An additional mode of ionization, in CI systems, is charge exchange. In this case, if the recombination energy (RE) of the reagent ion (B) is greater than the ionization energy (IE) of the analyte, an exothermic reaction proceeds:



The RE of the reactant ion is defined as the exothermicity of the gas phase reaction:



For a charge exchange reaction to occur, proton transfer reactions cannot be prominent. Proton affinities for larger organic molecules vary from approximately 160 to 240 kcal mol<sup>-1</sup>.

Table 1-1. Common reagent gases for chemical ionization techniques.

Reagent Gas	Reactant Ion (BH <sup>+</sup> )	Proton Affinity
CH <sub>4</sub>	CH <sub>5</sub> <sup>+</sup>	131.6 kcal mol <sup>-1</sup>
CH <sub>4</sub>	C <sub>2</sub> H <sub>5</sub> <sup>+</sup>	162.6 kcal mol <sup>-1</sup>
H <sub>2</sub> O	H <sup>+</sup> (H <sub>2</sub> O) <sub>n</sub>	166.5 kcal mol <sup>-1</sup>
CH <sub>3</sub> OH	H <sup>+</sup> (CH <sub>3</sub> OH) <sub>n</sub>	181.9 kcal mol <sup>-1</sup>
C <sub>3</sub> H <sub>6</sub>	C <sub>3</sub> H <sub>7</sub> <sup>+</sup>	179.5 kcal mol <sup>-1</sup>
NH <sub>3</sub>	H <sup>+</sup> (NH <sub>3</sub> ) <sub>n</sub>	204.0 kcal mol <sup>-1</sup>

\*Stable reactant ions and their proton affinities are listed. Degree of solvation depends on partial pressure of reagent gas. Thermochemical data for monosolvated proton.<sup>12</sup>

Electron ionization provides the information for structural elucidation that is necessary in the analysis of hydrocarbons and simple organic molecules. Chemical ionization yielded complementary information with molecular ion production for high proton affinity or low ionization energy molecules.

These two techniques, EI and CI, allowed chemists to accept mass spectrometry as a viable analytical technique; however, they do not provide an avenue to ionize more fragile, larger molecules.

## Biomolecule Analysis

As the biochemical and biological fields progressed, the need to measure molecular weights of biopolymers became increasingly important. Instead of a more direct measurement, molecular weight was determined by electrophoretic, chromatographic, and ultracentrifugation methods based upon the molecule's conformation, Stoke's radius, and hydrophobicity, respectively.<sup>10</sup> EI and CI require molecules to be in the gas-phase, so they are only amenable to volatile thermally stable compounds. In some cases, compounds suitable for derivatization can also meet those requirements.<sup>12</sup> The study of proteins, carbohydrates, cell membranes, and other large biological molecules necessitated ionization techniques capable of producing molecular ions of fragile thermolabile molecules. This need led to the eventual development of energy-sudden methods.

### Energy-Sudden Approach

Once again fundamental ion formation studies helped expand ionization techniques into new territory. In this case, the understanding of energy-sudden techniques was derived from the fundamentals of ion kinetics, with the basis lying in decomposition and desorption kinetics.

**Rapid heating.** If desorption and subsequent ionization take place before decomposition, a limited amount of fragmentation will occur.<sup>13</sup> This competitive notion for evaporation and decomposition yielded the idea of "rapid heating". The rate at which energy is deposited into a sample affects the production of neutral gaseous molecules over fragments. If a given compound AB is heated, it is assumed that AB will be released in the gas phase and will fragment into A and B. The two processes, vaporization and decomposition, can be written as shown in Equations 1-5 and 1-6.<sup>14</sup>



The Arrhenius equation allows the rate constants of the reaction to be viewed as logarithmic expressions as shown in Equations 1-7 through 1-9.

$$k = f \exp(-E/RT) \quad (1-7)$$

$$\ln K_v = \ln F_v - E_v/RT \quad (1-8)$$

$$\ln K_D = \ln F_D - E_D/RT \quad (1-9)$$

For thermally labile compounds that readily decompose, the rate constant for decomposition ( $K_D$ ) is larger than for vaporization ( $K_v$ ) at low temperatures. Because the activation energy for vaporization ( $E_v$ ) is higher than for decomposition ( $E_D$ ), the slope of the vaporization reaction is steeper than that of the decomposition reaction. Figure 1-4 is a plot of  $\ln k$  versus  $1/T$  for decomposition and vaporization reactions.

If the relationships based upon decomposition and vaporization hold true, then at high temperatures, where  $1/T$  is small, vaporization is favored over decomposition. In other words, reaching the maximum temperature as quickly as possible provides a high degree of desorption and limits fragmentation.

### Plasma Desorption

Desorption techniques were the energy-sudden ionization methods developed to produce molecular ions from compounds considered intractable (*i.e.*, nonvolatile and thermally unstable molecules). One of the first, demonstrated by MacFarlane and Torgerson, was plasma desorption mass spectrometry (PDMS).<sup>15-16</sup>

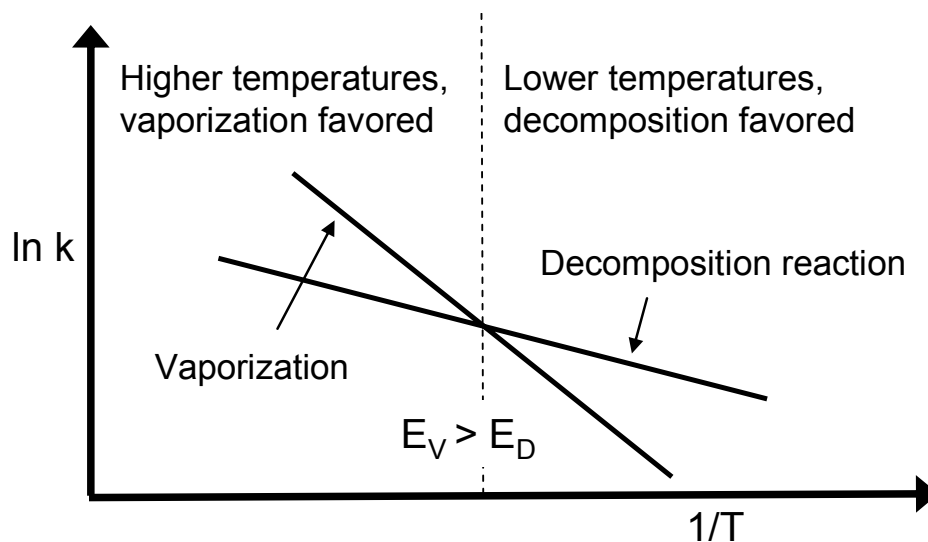


Figure 1-4. Plot of rate constants for decomposition and vaporization versus  $1/T$ . Adapted from reference 13.

Desorption and ionization occurred using energetic fission fragments from a radioactive californium source ( $^{252}\text{Cf}$ ). Californium-252 results in primarily (97%) emission of alpha particles, yet it also undergoes (3%) spontaneous fission, emitting two multiply charged fission fragments simultaneously and in nearly opposite directions. Typical decays involved  $^{106}\text{Tc}$  and  $^{142}\text{Ba}$  with energies of 104 and 79 MeV. The ionization technique works by using the pair of fission fragments to provide high energy collisions. One fragment penetrates a thin metal foil, releasing a burst of secondary electrons that begin the instrumentation timing sequence. The second fission fragment penetrates an aluminum foil holding the sample. Ions desorbed from the sample are accelerated to energies of 10 to 20 eV, pass through a drift tube, and are detected. Alpha particle emission is discriminated against by the production of lower kinetic energy ( $\sim 4$  MeV) secondary electrons. Commercialized by Bio-Ion Nordic (Uppsala, Sweden), PDMS

could analyze small proteins up to ~20 kDa.<sup>17</sup> A diagram of the source is shown in Figure 1-5.

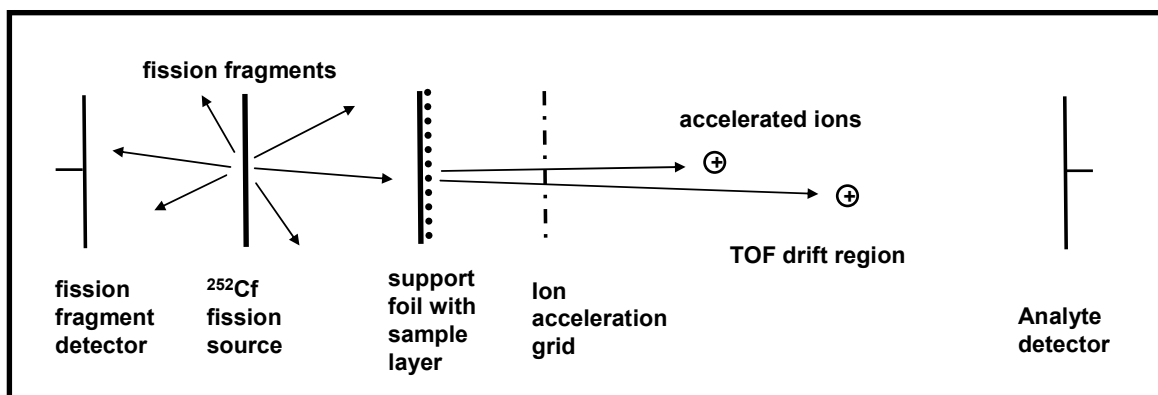


Figure 1-5. Diagram of californium plasma desorption ionization source. Adapted from reference 18.

### Fast Atom Bombardment

Next in the expansion of energy-sudden ionization techniques was fast atom bombardment (FAB). Developed by Barber, FAB uses high energy (5 keV) neutral atoms to impart energy onto a target, where a non-volatile liquid matrix (*e.g.*, glycerol, *m*-nitrobenzyl alcohol) contains analyte.<sup>19</sup> As the energetic atoms, typically argon, hit the sample surface a shockwave is induced that ejects ions and molecules.<sup>20</sup>

The development of FAB was partially to circumvent problems with electrostatic charging upon ion impact in secondary ion mass spectrometry (SIMS), which disturbed ion source potentials.<sup>21-22</sup> SIMS uses a focused ion beam to cause secondary ions to be emitted from a sample surface. Using the FAB technique, intact molecular or quasimolecular ions could be generated even in the case of highly polar compounds, which are known to be poor candidates for electron and chemical ionization.

Additionally, the use of a liquid matrix in FAB decreased the rapid decomposition

characteristic of the harsh conditions in desorption/ionization for certain samples.<sup>23-24</sup>

Using a FAB ion source, molecules nearing 10 kDa can be observed. A diagram of a FAB ionization source is shown in Figure 1-6.

Ion formation theories for FAB consist of the chemical ionization model and the precursor model.<sup>25-27</sup> The chemical ionization model assumes formation of the analyte ions in the region directly above the liquid matrix, referred to as the selvedge region. In this space, a plasma state similar to the reagent gas plasma in chemical ionization can exist due to the ions created from the supply of impacting primary atoms. Constituents in this region would undergo numerous reactions, including the protonation of analytes to yield quasimolecular ions (*i.e.*,  $[A+H]^+$ ). While matrix molecules are preferentially ionized for statistical reasons, they may act as the reagent ions in a system mimicking chemical ionization.

The precursor model of FAB mostly applies to ionic analytes or samples that are easily converted to ions in the liquid matrix. The model suggests that ions are preformed in the matrix and are merely transferred to the gas-phase. Support comes from observations that decreasing pH increases protonated analyte ion yields. Additionally, relative intensities for protonated ions seem independent of partial pressure of amines in the gas phase, and dependent on acidity of the matrix.<sup>28</sup> Chemical ionization reactions would suggest just the opposite. Furthermore, incomplete desolvation of preformed ions would explain observed matrix adducts  $[A+Matrix+H]^+$ .

Although the liquid matrix provides a fresh surface layer for ion production by convection and diffusion, it does have additional requirements.<sup>22,29</sup> The matrix must: (1) absorb the primary energy, (2) solvate the analyte, (3) have a low vapor pressure, and (4)

assist in analyte formation by yielding proton donating/accepting species upon bombardment. While a matrix can be adapted as analytes require, the wrong matrix may result in complete signal suppression.<sup>22</sup>

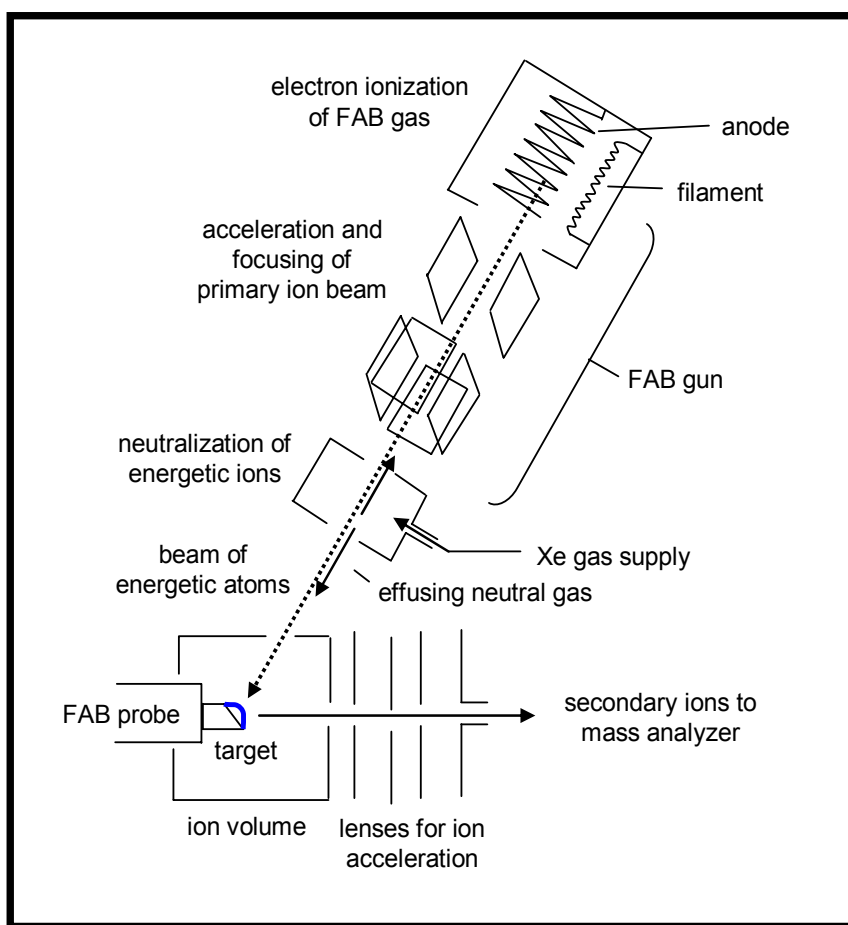


Figure 1-6. Diagram of a fast atom bombardment ionization source. Adapted from reference 9.

### Laser Desorption Ionization

Before the advent of plasma desorption and fast atom bombardment, laser desorption/ionization (LDI) sources were used to analyze low-mass organic salts and light-absorbing organic molecules.<sup>30</sup> While cases did exist for LDI to obtain mass spectra

of biomolecules, the analysis of fragile compounds over 1000 Daltons was not routine.<sup>9,31-32</sup> This allowed FAB and <sup>252</sup>Cf-PDMS to be far more effective in generating bimolecular mass spectra.

A number of laser systems were used for desorption techniques, yet infrared (IR) lasers (*e.g.*, CO<sub>2</sub> and Nd:YAG) saw extended use and provided mechanistic explanations of the process.<sup>33</sup> With instantaneous pulse energies of 100 mJ, and focused beams giving fluence values of 1 MW·cm<sup>-2</sup>, thermal mechanisms were predicted. As evidence, neutral and alkali species were observed to be desorbed from the sample beyond the actual laser pulse length.<sup>31</sup> This indicated that as the sample was heated, thermal desorption allowed ion emission. Additionally, at longer delay times, IR LD produced lower kinetic energy ions with less fragmentation.<sup>31</sup> Since there was also no apparent wavelength dependence, a thermal process fit the observations.<sup>33</sup>

Although time widths of the laser pulse ranged from nanoseconds to microseconds, and rapid heating seemed possible, the problem with laser desorption was that higher temperatures could not be reached quickly enough to obtain intact molecular ions. What was finally needed for the method to succeed was a medium that enabled the conversion of the irradiated photons to thermal energy without directly heating the analyte.

### **Matrix-Assisted Laser Desorption/Ionization**

A major change in mass spectrometry occurred with the addition of light-absorbing compounds to sample mixtures, allowing a controlled desorption/ionization event. Two matrix mixtures that allowed photon absorption were originally developed: (1) ultra-fine cobalt particles, glycerol, and analyte; and (2) a co-crystallization of analyte with organic matrix.<sup>13,34-37</sup> While both methods are capable of producing mass spectra of large fragile proteins ( $\geq 100$  kDa), the use of the cobalt particles is considered the first ionization

method that allowed the mass spectrometry community to think about analyzing thermally labile biomolecules. This is why Koichi Tanaka was awarded a portion of the Nobel Prize in 2002.<sup>13</sup> Using the absorbing particles allowed the collection of some of the first large biomolecule mass spectra.<sup>38</sup> However, the co-crystallization technique developed by Hillenkamp and Karas using light-absorbing organic matrices has been the more prolific method for biomolecule analysis.<sup>39</sup>

The co-crystallization method, referred to as matrix-assisted laser desorption/ionization (MALDI), uses a variety of light-absorbing matrix molecules to control uptake of laser irradiation and cause desorption and ionization of the analyte.<sup>40</sup> Unlike the wavelength independence seen in LDI, MALDI was developed from the wavelength dependence of tryptophan analysis.<sup>35</sup> In the simple system, the amino acid acted as the absorbing molecule. Hillenkamp later reported the matrix-assisted technique of molecular ion desorption with the use of a more traditional nicotinic acid matrix.<sup>41</sup> The components of a MALDI source are straightforward. Figure 1-7 shows the general configuration for the ion source.

The source comprises a laser, sample plate (with sample), and acceleration field for transfer into the mass analyzer. While the source is simple in construction, the underlying processes for desorption and ionization are less than trivial.<sup>42-46</sup> The critical parameters involve a minimum of laser wavelength, laser fluence, matrix formulation, and sample preparation. Additionally, the mass analyzer, ion transmission, and analyte parameters must be considered. The many variables to consider during the MALDI process have made mechanistic theories difficult to produce; therefore, the overall mechanism for ion formation is still a subject of continuing research.

An understanding of ionization pathways could help to maximize ion yields, control analyte charge states and fragmentation, and gain access to new classes of analytes. Knowledge of the ion formation process may also provide rational guidelines for matrix selection, something treated more as an empirical art than a scientific process.

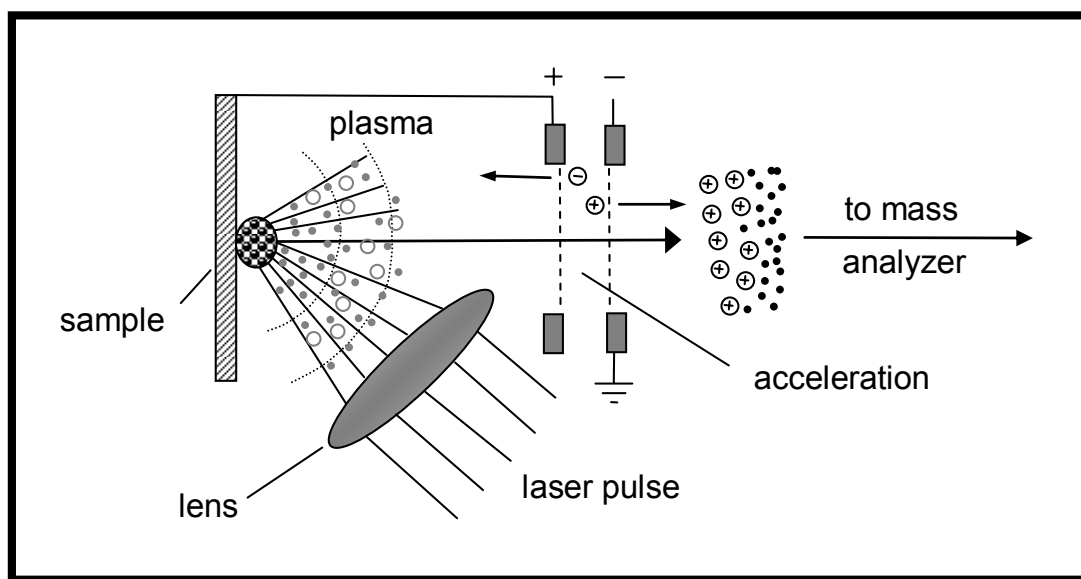


Figure 1-7 Diagram of a matrix-assisted laser desorption/ionization source. Adapted from reference 41.

### Mechanisms

Presently, no single chemical or physical pathway explains all positive and negative ions in the MALDI spectrum.<sup>43</sup> Since experimental variables drastically affect the mass spectra outcome, several mechanistic theories have been produced to describe each effect. The mechanisms can be divided into two categories: primary and secondary ionization.<sup>43,45-46</sup> Primary ionization refers to the generation of the first ions from neutral molecules—often matrix-derived species. Secondary mechanisms involve the ions not directly generated by primary processes—usually analyte ions.

Major primary mechanisms include: single molecule multi-photon ionization, energy pooling, excited-state proton transfer, disproportionation reactions, desorption of preformed ions, thermal ionization, and spallation. Major secondary ionization mechanisms include: gas-phase proton transfer and gas-phase cationization.

**Primary Ionization Reactions.** Since the wavelength dependence of MALDI assisted in its eventual discovery, laser wavelength plays an important role in many mechanistic theories. With the matrix requiring energy absorption, the laser wavelength must be matched with the matrix chromophore, the most common is 337 nm from a nitrogen laser; however, Nd:YAG harmonics, excimer lines, and infrared lasers have been employed. Table 1-2 shows typical photon energies and wavelengths for MALDI laser systems.<sup>43</sup>

Table 1-2. Typical laser wavelengths, photon energies, and pulse widths used for MALDI.<sup>43</sup>

Laser	Wavelength	Photon Energy (eV)	Pulse Width
Nitrogen	337 nm	3.68	4 ns
Nd:YAG x3	355 nm	3.49	5 ns
Nd:YAG x4	266 nm	4.66	5 ns
Excimer (XeCl)	302 nm	4.02	25 ns
Excimer (KrF)	248 nm	5.00	25 ns
Excimer (ArF)	193 nm	6.42	15 ns
Er:YAG	2940 nm	0.42	85 ns
CO <sub>2</sub>	10600 nm	0.12	~1 $\mu$ s

Even with the importance of the wavelength/matrix combination, MALDI spectra do not show significantly different ions with different laser wavelengths.<sup>47</sup> However, alterations in pulse energy and sample composition are necessary to obtain similar ion populations.<sup>48</sup>

**Multi-photon Ionization.** Multi-photon ionization explains the radical cations formed through the wavelength dependence of MALDI.<sup>35,49-50</sup> The reaction shown in equation 1-10 produces matrix (M) radicals, which could be key intermediates for analyte ions.



The criticism for the mechanism lies in the energetics needed to ionize the matrix molecules. Two photons from a nitrogen laser yield 7.36 eV; however, the ionization potentials (IP) for common matrix molecules are higher (*i.e.*, DHB at 8.05 eV).<sup>43</sup> The typical irradiances values,  $10^6$ - $10^7$  W·cm<sup>-2</sup>, make three photon ionization unlikely.<sup>51</sup> Recent experiments suggest that clustered matrix molecules may have lower IP, yet questions still remain about the accuracy of the solid matrix measurements.<sup>43</sup>

**Energy Pooling.** Direct multi-photon ionization may not seem plausible due to energetics, but the excited states of matrix molecules are considered a viable starting point.<sup>52-53</sup> A possibility is that two or more separately excited matrix molecules “pool” their energy to yield one matrix radical cation.<sup>54-55</sup> The reaction pathways for this “energy pooling” mechanism are shown in Equations 1-11 and 1-12.



Equations 1-11 and 1-12 could explain the fluence dependence associated with MALDI. A critical factor in the desorption/ionization process is the energy density supplied to the sample (fluence,  $\text{J}\cdot\text{cm}^{-2}$ ); however, alterations in the irradiance ( $\text{W}\cdot\text{cm}^{-2}$ ) seems to have less of an effect on the mass spectra.<sup>56-58</sup> Fluence versus irradiance dependence indicates that the number of photons delivered is important, not the rate at which they arrive.

**Excited-state proton transfer.** Furthering the excited-state theories is the excited-state proton transfer mechanism, which helps explain protonated species.<sup>36</sup> The pathway is shown in Equations 1-13 to 1-15.



Most matrices are not known to be good excited-state proton transfer agents.<sup>49,51</sup>

However, without a better knowledge regarding the local environment in a MALDI sample, refuting the mechanism is difficult.

**Disproportionation.** Each laser pulse in MALDI yields both positive and negative ions. To explain this observation, disproportionation reactions have been suggested.<sup>59</sup> The pathway is shown in equation 1-16.



The problem with the mechanism is that positive and negative ions are not correlated in mass spectra. The fluence thresholds for each ion polarity are also different, suggesting alternate pathways.

**Preformed ions.** Matrix solutions are typically made from organic acids; therefore, it is realistic to expect that preformed ions may exist in the sample. For ionic compounds, the idea that preformed ions are desorbed is reasonable, yet it is difficult to be certain whether the ions observed are truly preformed or the result of secondary gas-phase reactions discussed in the following section.<sup>60-62</sup>

**Physical mechanisms.** Chemical ionization mechanisms have dominated the MALDI literature, but physical mechanisms have also been considered. Both thermal ionization and spallation (structural fracture of the solid) have been suggested for IR MALDI.<sup>57,63</sup> Using infrared lasers, penetration depth is much greater, which may result in mechanical stress.<sup>64</sup> Additionally, since IR absorptions are weaker, the energy per volume deposited is typically too low to fully “melt” the material desorbed. Hillenkamp has proposed that spallation is an important mechanism in this case.<sup>63</sup> Thermally induced stress that builds faster than can be dissipated leads to a mechanical failure of the solid and ablation of material without direct vaporization.<sup>64</sup>

**Secondary ionization.** Molecular dynamics simulations have proposed that the MALDI plume after laser desorption is a dense cloud containing single molecules, ions, and clusters.<sup>66-67</sup> Thus, an impenetrable plume of material provides the opportunity for primary ions to undergo ion-molecule reactions, necessitating secondary ionization reactions.<sup>68</sup>

**Proton transfer.** If primary ions are radical cations then proton transfer matrix-matrix reactions can readily produce protonated matrix ions:<sup>49</sup>



This is similar to the proposed mechanism for protonated glycerol in FAB.<sup>69</sup> Likewise, matrix-analyte reactions can produce protonated analyte ions, important in MALDI spectra. Just as in chemical ionization mechanisms, the presence of protonated analyte requires a proton transfer reaction.



Again, as in CI the reaction proceeds when  $\Delta G < 0$ .<sup>12</sup> Since proton affinities of peptides and proteins are on the order of  $240 \text{ kcal}\cdot\text{mol}^{-1}$ , and most measurements of MALDI matrix proton affinities are between  $183\text{-}225 \text{ kcal}\cdot\text{mol}^{-1}$ , the reaction should be thermodynamically favorable.<sup>70-71</sup> It has also been noted that protonated analyte ion intensity increases for basic residue peptides indicating a chemical ionization approach to protonation.<sup>62</sup> Additionally, varying matrices with a standard analyte alters the internal excitation available (due to proton affinity differences) and affects the degree of fragmentation. This has been referred to as “hot” and “cold” matrices.<sup>71-72,76</sup>

**Cationization.** Gas-phase cationization as a secondary ionization mechanism describes abundant cationized adducts in MALDI spectra.<sup>73-74</sup> Ion-molecule reactions of this type have also been proposed to explain the pseudo-molecular ion formed by laser desorption mass spectrometry without a matrix.<sup>63</sup> Studies have shown that salts added to MALDI samples allow the cationization of synthetic polymers, adding evidence to the mechanism.<sup>75</sup> Similar to protonation reactions, cationization requires cation affinities of the analyte to exceed that of the matrix.

### **Matrix considerations**

Even with numerous mechanistic studies, matrix choice is not systematic. Difficulties in analysis stem from both ionization and co-crystallization issues.<sup>43</sup> The

appendix contains a list of some common MALDI matrices and their corresponding analyte classes. Most use pulsed UV lasers, and consequently are UV absorbers. The matrices are derivatives of benzoic acid, cinnamic acid, and related aromatic compounds.<sup>76</sup>

Even when the appropriate laser/matrix system is chosen, matrices need further development for specific analyte applications. In MALDI sample preparation, peptides and proteins are generally solubilized in 0.1% aqueous trifluoroacetic acid at a concentration of approximately  $10^{-5}$  M.<sup>42</sup> One microliter of solution is then mixed with a saturated aqueous matrix solution (around  $10^{-3}$  M), which is allowed to evaporate forming crystals. Additional crystallization techniques are described in the appendix.

## **Time-of-Flight Mass Spectrometry**

### **Historical Perspective**

With the development of plasma desorption, fast atom bombardment, laser desorption ionization, and matrix-assisted laser desorption/ionization, the challenge in mass spectrometry became not the production of ions but rather development of the mass analyzer. The first mass spectrographs devised by Thompson, Aston, and Dempster utilized magnetic and electrostatic fields for ion separation.<sup>2</sup> While these configurations are still used as today's high resolution double-focusing spectrometers, research focusing on the reduction of magnetic fields provided the most widely used MALDI coupled mass analyzer. As magnets became a limiting factor in mass analyzer construction, primarily due to size and cost, W. E. Stephens devised an analyzer that did not require magnetic fields. In 1946, Stephens stated:<sup>77</sup>

“Such a mass spectrometer should be well suited for composition control, rapid analysis, and portable use. Magnets and stabilization equipment would be eliminated.”

He described the mass analyzer, the time-of-flight (TOF) mass analyzer, in his patent as:<sup>78</sup>

“...apparatus for obtaining pulses of ions segregated according to mass-velocity relationships, collecting the ions to obtain pulses of current dispersed in time and recording the result. Separation of ions of different masses does not depend upon slit width as in the case for a conventional mass spectrometer, but depends upon only the path length, the accelerating voltage, pulse length and the detecting device.”

### **Time-of-flight Theory**

The basic principle of the time-of-flight mass spectrometer (TOFMS) is the measurement of time as an ion travels a fixed distance. The time is related to the ion's mass-to-charge ratio. The simplest time-of-flight consists of a source extraction region, a drift region, and a detector. A diagram for a TOF is given in Figure 1-8.

In the source region, a voltage is applied to a backing plate that accelerates ions to a final kinetic energy (eV):<sup>31</sup>

$$KE = \frac{1}{2}mv^2 \quad (1-19)$$

$$\frac{mv^2}{2} = eV \quad (1-20)$$

The mass ( $m$ ) and velocity ( $v$ ) of the ion are then related to the energy it obtains.

Dimensional analysis can be conducted by considering units of  $kg$  for mass,  $m \cdot s^{-1}$  for velocity, and using  $1.60 \times 10^{-19} \text{ J} \cdot eV^{-1}$ . The drift region is field free, so the ions cross the region with constant velocities that are inversely proportional to the square root of their masses.<sup>31</sup>

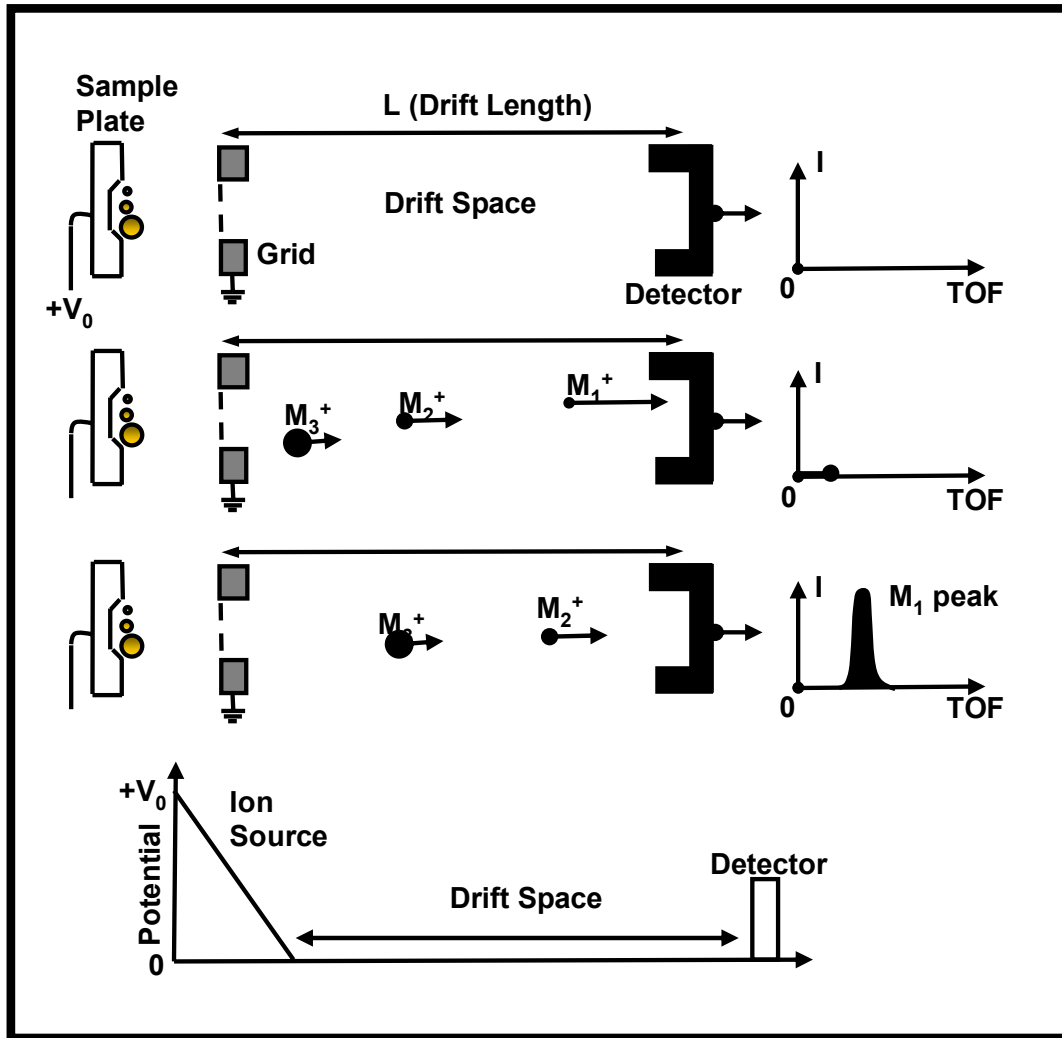


Figure 1-8. Diagram demonstrating the principle theory in time-of-flight mass analysis. Adapted from reference 31.

$$v = \left( \frac{2eV}{m} \right)^{1/2} \quad (1-21)$$

Thus, light ions travel faster and arrive at the detector sooner. Ion flight times fall in the range of 10 to 200  $\mu\text{s}$  depending on the spectrometer arrangement. Flight time ( $t$ ) is then related to velocity by the length of the drift tube ( $D$ ).<sup>31</sup> Typical units are  $s$  for time and  $m$  for tube length.

$$t = \left( \frac{m}{2eV} \right)^{1/2} D \quad (1-22)$$

A general derivation of the ion flight time should include the time the ions spend in the source region, yet if the region is short with respect to the drift tube the resulting equation is essentially the same as equation 1-22.

Relating flight time to molecule mass requires a mass scale that follows a square-root law. The linear equation:

$$t = am^{1/2} + b \quad (1-23)$$

allows masses to be determined with as little as two known masses. While constant  $a$  relates to flight tube length and acceleration voltages, constant  $b$  takes into account time offsets due to the laser or detector.

The mass resolving power for a mass spectrum is defined as  $m/\Delta m$ .<sup>79</sup> In a time-of-flight analyzer this equates to a temporal resolving power as follows:

$$\frac{m}{\Delta m} = \frac{t}{2\Delta t} \quad (1-24)$$

where  $\Delta t$  is commonly measured as the full width at half maximum (FWHM). The basic resolution equation is derived from rearrangement of equation 1-22:

$$m = \left( \frac{2eV}{D^2} \right) t^2 \quad (1-25)$$

### **Kinetic energy spreads**

Equation 1-25 is derived from TOF theory; however, deviations in kinetic energy and spatial formation exist.<sup>80</sup> Ions are generally formed with some initial kinetic energy, so  $KE = eV + U_0$ , where  $U_0$  corresponds to the initial kinetic energy. Kinetic energy

spreads can account for velocity differences in the ions, detrimental to spectral resolving power.<sup>83</sup> Resolving power enhancements can be seen by increasing accelerating voltages (*i.e.*, 3-30 kV), giving the ions a total energy much higher than the initial energy. Time-lag focusing is also used to reduce the initial kinetic energy spreads.<sup>85</sup> Developed by Wiley and McLaren, time-lag focusing provides a time delay between the ionization period and the ion-extraction pulse. This enables ions to drift within the field-free source before extraction, allowing them to distribute according to their initial kinetic energy.<sup>31,80</sup> The distributions are converted to spatial spreads. One drawback for time-lag focusing is its mass-dependent nature.<sup>31</sup> Only a narrow range can be focused for a particular value of time-delay.<sup>80,85</sup> Further minimization of the energy distributions, sometimes inherent in the ionization technique, can be done using a reflectron.<sup>31,84,88</sup> The simplest of reflectrons acts as an electrostatic ion mirror, enabling the ion kinetic energy to be converted into penetration depths. Longer times in the reflectron yield the same total time-of-flight for isobaric ions due to their increased kinetic energy and shorten drift region times.

### **Spatial spreads**

Spatial distributions occur when ions are formed in different regions of the source, and then are accelerated through varying distances in the extraction field, resulting in higher drift velocities.<sup>31,85</sup> Using a uniform accelerating field in the extraction region yields a plane, the spatial focus plane, located a distance twice that of the extraction region. This is where isobaric ions of differing velocities would be focused.<sup>85</sup> In this arrangement, the spatial focus plane is typically not located at the detector, which would minimize spatial spreads. To move the focus plane closer to the detector, a two-stage extraction region is used.<sup>31,80,81</sup> Additional flight time spreads can also be caused by

*turn-around time*. This is the time ions having initial velocities in the opposite direction of the flight path spend in the source.

Since some time spreads cannot be prevented, and because time distributions ( $\Delta t$ ) are maintained as the ions approach the detector, mass resolving power is limited. However, considering the resolving power equation for time-of-flight mass spectrometers,  $t/2\Delta t$ , an increase in total time, can increase resolving power with a constant time spread. This equates to using longer flight tubes for further enhancements.<sup>86</sup>

### **Desorption Ionization Techniques**

Using a gas-phase ionization technique, such as EI or CI, with a linear TOF-MS requires either pulsing of the ion source or accumulation of the continuously formed ions before the extraction pulse.<sup>31,80</sup> Yet, with a desorption/ionization technique (*i.e.*, MALDI) the system is simplified. Since the sample is placed on a surface, spatial distributions and ion turn-around time are less significant. The ions are formed on a plate parallel to the detector. Additionally, with plasma desorption occurring within  $10^{-9}$  s of impact, and MALDI generally using laser pulse widths of 3 to 100 ns, ionization times are shorter than the drawout pulse resulting in minimal initial temporal distributions.<sup>31</sup>

The first commercial time-of-flight mass spectrometer was produced by the Bendix Corporation (Detroit, MI).<sup>2</sup> The system had a mass range (at repetition rate of 10 kHz) of about 400 amu, and a mass resolving power of 200. The Bendix spectrometer was the platform that allowed the addition of multiple ionization techniques to be examined with TOF. At this early stage, success of the TOF was limited by both its mass range and mass resolving power. Combining the use of pulsed ionization techniques with boxcar recording methods together produced an extraordinary low duty cycle. It was not until

the further development of detectors, data acquisition systems, and the coupling of desorption ionization techniques did TOF mass analyzers become standard equipment.<sup>82</sup> Today, time-of-flight mass spectrometers can obtain resolving powers of over 10,000 with detection limits near attomole range.<sup>42,87</sup>

### **Conclusions**

Each developmental stage of an ionization technique or mass analyzer affords new analytical opportunities. While the recent advances in MALDI and TOF allow for the routine study of biomolecules, subtle alterations (atmospheric pressure and orthogonal geometry) also present additional advantages. The research in this document involves the fundamental and practical study of the processes in an atmospheric pressure MALDI source coupled to a TOF mass spectrometer. The focus is on liquid matrices, their interactions at atmospheric pressure, and the prospective analytical utility they provide.

CHAPTER 2  
DESIGN OF AN ATMOSPHERIC PRESSURE MATRIX-ASSISTED LASER  
DESORPTION/IONIZATION SOURCE FOR AN ORTHOGONAL-ACCELERATION  
TIME-OF-FLIGHT MASS SPECTROMETER

**Introduction**

“As a pulsed technique, MALDI is easily compatible with time-of-flight mass spectrometry and has been responsible (more than any other technique) for the renewed interest and active development of this mass analyzer.”

—Robert Cotter<sup>31</sup>

A passage from Robert Cotter’s 1997 book *Time-of-Flight Mass Spectrometry* reflects the general scientific community agreement on matrix-assisted laser desorption/ionization (MALDI) and mass spectrometry instrumentation. Therefore, it’s ironic that recent developments in time-of-flight (TOF) instrumentation have been directed towards the use of continuous ionization sources.

**Background**

**Orthogonal-Acceleration Time-of-Flight**

Orthogonal-acceleration time-of-flight mass spectrometry (oa-TOFMS) uses ion beam deflection techniques.<sup>88</sup> In an oa-TOFMS, mass analysis is done “orthogonal” to the ion source axis. Older instruments have used beam deflection techniques to narrow the ion packets pulsed into the flight tube. With orthogonal geometry, developed by O’Halloran, deflection is taken to the extreme (90°), yielding an ability to sample continuous ion sources.<sup>88-90</sup> For years there was minimal interest in orthogonal geometry instruments, until the configuration’s rediscovery by Dawson, Guilhaus, and Dodonov.<sup>91-</sup>

<sup>92</sup> Today the configuration provides numerous benefits to the TOF instrumentation community.

Orthogonal-acceleration TOFs offer improved mass resolving power, duty cycle, and compatibility with continuous high-energy spread ions (*e.g.*, electrospray ionization (ESI)). With orthogonal deflection a new component of velocity, which is independent of initial ion source velocity, is added to the sampled ions.<sup>88</sup> The decoupling of mass analysis from the ion source leads to reduced time distributions for the ions. Instead of the initial kinetic energy distributions (due to ionization processes) affecting mass resolving power, orthogonal sampling discriminates against energy spreads in the ion source axis. Axial spreads are then distributed perpendicular to the pulse-out electrode of the flight tube, and do not affect time resolution. Provided the detector is large enough, the ion spread in the axial direction will disperse over the detector plate of the oa-TOF.

While the oa-TOF provides a duty cycle advantage, the term has been misunderstood and at times referred to as “increased sensitivity.” Duty cycle in mass spectrometry is the ratio of the time ions are extracted for mass analysis over the total time ions are produced. In a properly arranged oa-TOF, as an ion packet is mass analyzed, a new packet is filling the pulser region of the flight tube.<sup>88</sup> In theory this allows for a 100% duty cycle, yet it says nothing about the analyzer transmission and detector efficiency, the parameters needed to determine instrument sensitivity.

With the ability to effectively sample continuous ion sources, electrospray ionization (ESI) was one of the first techniques adopted for the oa-TOFMS.<sup>93-94</sup> ESI, originally developed by John Fenn, is a process by which ions in solution are transferred to the gas-phase with limited ion fragmentation.<sup>95-96</sup> The coupling of ESI to oa-TOFMS

affords three main advantages: increased duty cycle, improved mass accuracy, and higher  $m/z$  capability.<sup>88,97-98</sup> While oa-TOF mass spectrometers were used for continuous ionization source mass analyzers, MALDI sources were coupled to oa-TOFs for different reasons. Unlike continuous sources, MALDI was compatible with the pulsed scheme of linear TOF analyzers. However, MALDI generates large initial kinetic energy spreads for ions, effectively reducing mass resolving power. While ion mirrors, reflectrons, and delayed extraction correct for some energy spread distributions, improvements were needed.<sup>99</sup> Delayed extraction, for instance, must be tuned for each desired  $m/z$  range.<sup>31</sup> Orthogonal-acceleration TOF spectrometers decouple the energy of the desorption/ionization processes from mass analysis, thereby increasing mass resolving power and mass accuracy.<sup>98</sup>

### **Atmospheric Pressure Inlets**

Coupling atmospheric pressure ionization (API) sources to a mass analyzer requires a  $10^7$  to  $10^8$  reduction in pressure, demanding precise inlet designs and efficient vacuum pumps. Since the sampling efficiency of an API source is dependent upon the number of ions and the amount of gas that can be introduced into the orifice, multi-stage pumping systems are routinely required. The gas expansion that occurs from atmospheric pressure to vacuum, termed a supersonic jet expansion, also complicates the design of an API source, creating two major consequences: (1) ions must be sampled with a skimmer cone, and (2) ion-solvent clusters must be prevented.<sup>33</sup>

Skimmer cones are required due to the nature of free jet expansions. The expansion of a gas from a high-pressure region into a low-pressure region through a small nozzle produces a supersonic jet of gas with a narrow velocity distribution and a high flux per unit area.<sup>100</sup> The sonic jet travels at the local speed of sound in the gas.<sup>101</sup> The

expansion generates a shock wave terminating at the Mach disk where gas slows and diffuses. Extracting the sample through an orifice (skimmer) placed within the region before the Mach disk, termed the zone of silence, allows for maximum ion collection.<sup>101</sup>

When a mixture of gas and ions is transferred from atmospheric pressure to low pressure within the MS instrument, adiabatic cooling occurs as the mixture rapidly expands in the vacuum.<sup>102</sup> If polar neutrals (*e.g.*, water or solvent) are present in the mixture at that time, condensation of these neutrals on the analyte ions occurs. The size of the formed clusters may then exceed the mass range of the analyzer and also lower the analyte signal by distributing it over several ion signals. In modern MS instruments designed for atmospheric pressure ionization (API), the problem with clustering is of high concern. The most common methods to prevent large ion-solvent clusters from entering the mass analyzer are the addition of: (1) an axial potential gradient, (2) a heated bath gas, or (3) a counter-current dry bath gas. A potential gradient between the nozzle and skimmer results in a field to accelerate the ions relative to the neutral carrier gas molecules, producing energetic collisions that fragment the clusters.<sup>101-102</sup> A heated bath gas allows the temperature to remain above the condensation value during free jet expansion. Finally, a counter-current dry bath gas provides cluster prevention by removing solvent molecules, averting resolution. A counter-current flow also limits non-ionized material from entering the system, making it more tolerant to “dirty” samples. While electrostatic and electromagnetic forces play a pivotal role in ion transmission, high-pressure sources also introduce aerodynamic forces that affect ion trajectories.

## Atmospheric Pressure MALDI

The advent of the oa-TOF using an AP inlet allowed MALDI sources to be operated at atmospheric pressure. Laiko and Burlingame were the first to examine APMALDI sources for analytical purposes.<sup>103-104</sup> Although the oa-TOF format provided a logical means for examining the APMALDI source, additional groups coupled the new source to commercial ion trap mass spectrometers.<sup>105-107</sup>

APMALDI sources offer reduced constraints on ion source pressure. This can be useful for high-throughput screening, where automation must be used for source construction. Atmospheric pressure conditions also provide an opportunity to examine volatile matrices or other vacuum incompatible samples. Furthermore, an APMALDI source could be interchangeable with other AP sources on an atmospheric pressure interface mass spectrometer. The last benefit, interchangeability, allowed the original APMALDI investigators to form a company, Mass Technologies, directed at producing commercial APMALDI sources for a variety of currently employed spectrometers.<sup>108</sup> With interchangeable ion sources a user can add utility to an already high cost instrument. Each ionization process allows for a range of chemical classes to be ionized, and in specific cases may provide complementary information. Figure 2-1 shows the complementary nature of atmospheric pressure ionization sources for mass analysis. ESI may dominate the liquid chromatography market due to eased liquid separations coupling, but MALDI remains the method of choice for peptide/protein identification.

By most accounts, APMALDI spectra are “similar” to vacuum MALDI spectra.<sup>105</sup> Therefore, our initial experimental goals were not focused on spectra evaluation, but the opportunities available for additional analytical utility using APMALDI. Furthermore,

with the limited history of APMALDI, the study of desorption and ionization phenomena at atmospheric pressure may assist in understanding MALDI.

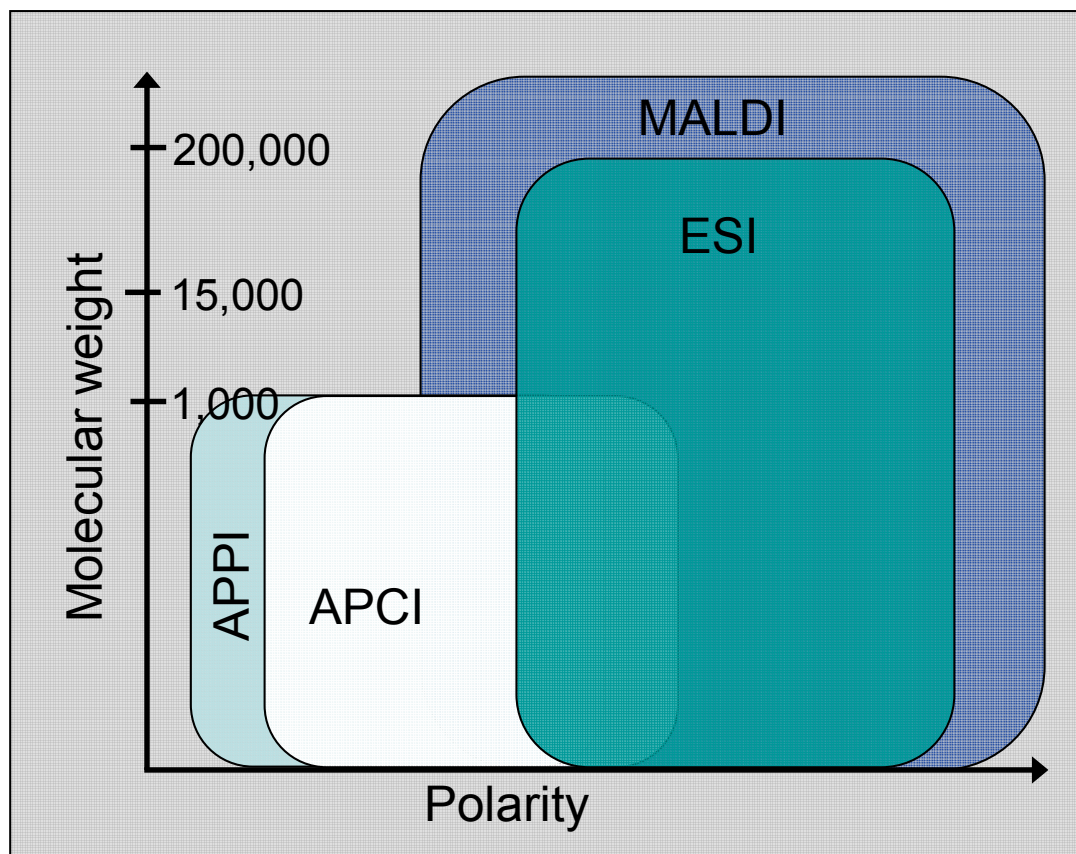


Figure 2-1. Diagram depicting the complementary nature of atmospheric pressure ionization sources is shown. Each technique, atmospheric pressure photo ionization (APPI), atmospheric pressure chemical ionization (APCI), electrospray ionization (ESI), and matrix-assisted laser desorption/ionization (MALDI), has a selective region of polarity and molecular weight in which it is most effective. Adapted from reference 109.

Fundamental research in MALDI has become more of a topic for scientific discussion, as one of the founders of MALDI, Franz Hillenkamp, recently wrote, "...it is time to go back and do some more basic research."<sup>110</sup> The beginning of these studies required the design, construction, and optimization of an APMALDI source. This chapter describes the efforts to couple an APMALDI source to an oa-TOFMS.

## Experimental Methods

### Mass Spectrometer

The mass spectrometer used is an orthogonal-acceleration time-of-flight (oa-TOF).

Figure 2-2 is a diagram of the oa-TOF.

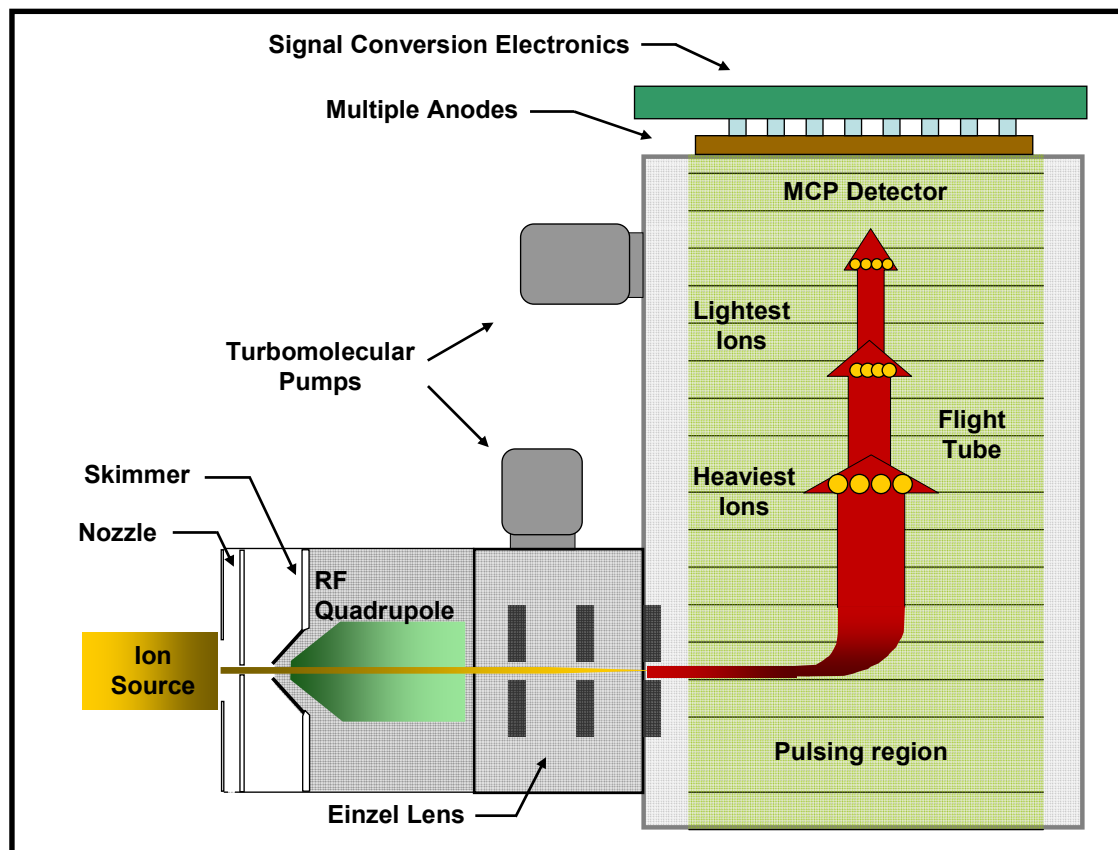


Figure 2-2. Diagram of the orthogonal-acceleration time-of-flight mass spectrometer used in the studies presented is shown.

The spectrometer is a prototype developed by LECO Corporation (St. Joseph, MI, USA). Originally designed for an ESI source, the spectrometer uses a heated curtain gas for ion cluster prevention. Once the ions enter the 254  $\mu\text{m}$  nozzle orifice, they are sampled through a skimmer cone (2 mm inner diameter) located  $\sim 6$  mm away. Voltages for the nozzle and the skimmer cone can be altered independently; the pressure in the region between the two components is  $\sim 3$  Torr. This region is pumped by a two stage

rotary vane roughing pump (E2M18,  $4.7 \text{ L}\cdot\text{s}^{-1}$ , BOC Edwards, Willmington, MA, USA), which also backs two turbomolecular pumps. Next, the ions travel into an RF-only quadrupole. The RF supply runs at a fixed 1 MHz frequency with the quadrupole also having an adjustable DC offset of 0-300 V. A DC gradient of 0-50 V can also be applied. The region within the quadrupole is maintained at a pressure of  $\sim 0.1$  Torr by the second stage of a hybrid turbomolecular drag pump (TMH261,  $210 \text{ L}\cdot\text{s}^{-1}$ , Pfeiffer, Germany). The primary stage of the hybrid pump is connected to the flight tube. Ions exit the quadrupole region through a 2 mm by 0.5 mm rectangular slit. An Einzel lens focuses and directs the ions into the flight tube pulser. A second turbomolecular pump is used to evacuate the Einzel region (TMH71,  $70 \text{ L}\cdot\text{s}^{-1}$ , Pfeiffer, Germany). The pulser then accelerates the ions up the flight tube (maintained at a pressure of  $1.5 \times 10^{-7}$  Torr). The flight tube is 50 cm long and constructed of printed circuit board.<sup>111</sup> The tube is segmented into 39 electrodes, from pulser to detector. Potentials are applied to the electrodes through a voltage divider to form a parabolic potential field for the ions, designed to improve mass resolution.

The detector used in the spectrometer is a chevron configuration dual microchannel plate (MCP) assembly. Electrons from the MCPs (4 cm by 8 cm, Hamamatsu, Japan) strike an array of 36 anodes. The detection system, termed a time-to-digital converter multi-anode detector (TDC-MAD), provides rapid temporal resolution (1 ns) and digitization rate (1 GHz) while allowing a large dynamic range from the multiple anodes.<sup>112</sup> The signals from the anodes are fed into comparators and then a combiner board. The data from the combiner board is sent to a host board where successive spectra are summed and sent to an array board for compression and transfer to a PC via SCSI

(Small Computer System Interface). The pulser is operated at a frequency of 5 kHz, while the array board can output summed spectra at a rate varying from 0.1 to 100 spectra·s<sup>-1</sup>. This allows the summation of 50 to 50,000 pulses for each output spectrum. Software, ChromoToF version 3.21 Beta (LECO Corp., St. Joseph, MI, USA), allows spectral viewing. The mass spectrometer provides both positive and negative ion detection modes at a rated mass range of ~1 to 6000 *m/z*. Resolving power is listed as ~2000 at *m/z* 600.

### **Electrospray Configuration**

The ESI setup consisted of an uncoated pulled fused silica fiber with 30 μm inner diameter and 360 μm outer diameter (FS360-100-30-N, New Objective, Woburn, MA, USA). Figure 2-3 is an optical image of the ESI tip taken using a Charge-Coupled Device (CCD) camera (5M, Pixera, Los Gatos, CA, USA) mounted on a microscope (Edmund Scientific, Barrington, NJ, USA).

The flow rate, 0.5 μL·min<sup>-1</sup>, was applied using a syringe pump (Pump 11, Harvard Apparatus, Holliston, MA, USA). A voltage of 3250 V was applied to a liquid junction contact by a power supply internal to the mass spectrometer. The needle was placed ~10 mm from the orifice of the spectrometer and a curtain gas cover directed heated nitrogen gas (80 °C at 800 mL·min<sup>-1</sup>) towards the ESI tip. The voltage on the curtain gas cover was set to 1550 V. Spectra were acquired at a rate of 4.17 spectra·s<sup>-1</sup> (1200 pulsed packets). Reserpine and verapamil solutions were 2 ng·μL<sup>-1</sup> in 50% aqueous methanol solutions with 1% acetic acid. All chemicals and solvents were purchased from Sigma Aldrich (St. Louis, MO, USA) and used without further purification.

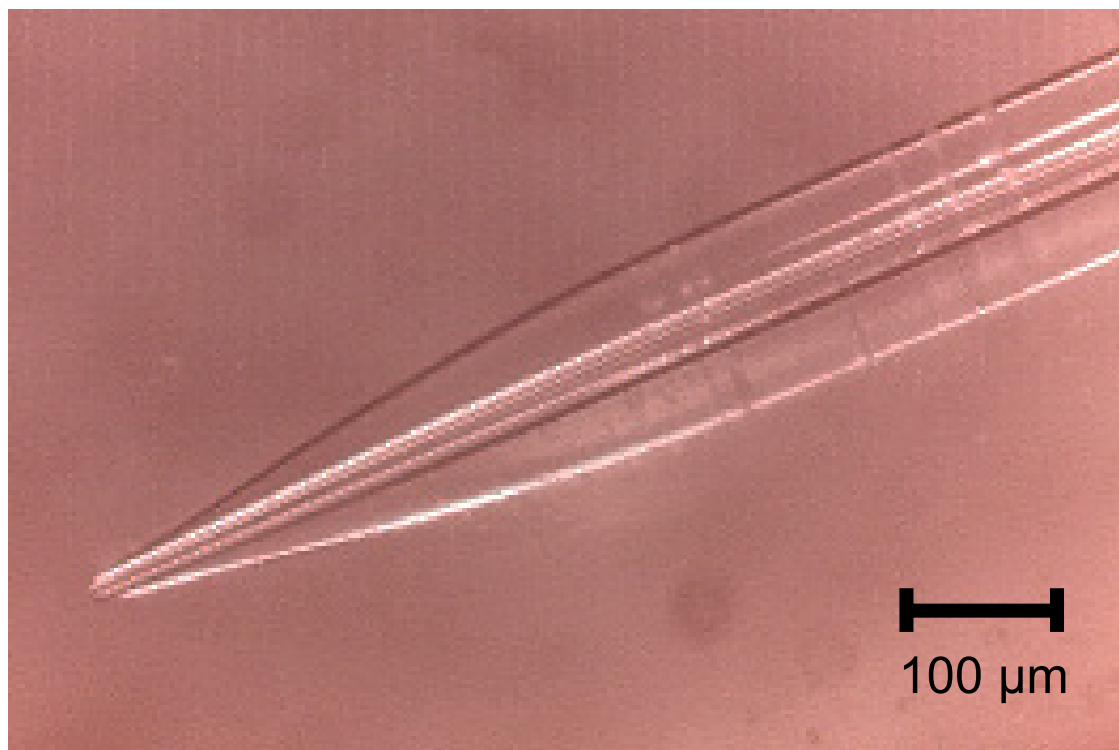


Figure 2-3. A photograph of the electro spray tip used for mass spectrometer characterization.

Table 2-1 lists the potentials of the ion transfer optics and the mass analyzer when using an electro spray ionization source.

Table 2-1. Mass spectrometer conditions used to acquire electro spray spectra.

Nozzle	150 V
Skimmer	65 V
Quadrupole RF	300 V
Quadrupole High	41 V
Quadrupole Low	44 V
Quadrupole Exit	22 V
Focus	-11 V
Horizontal Deflect	4 V
Vertical Deflect	1 V
Einzel Focus	-15 V
Einzel Horizontal Deflect	3 V
Einzel Vertical Deflect	1 V

Table 2-1. Continued.

Repeller	977 V
Pusher	791 V
Doorway	443 V
Long Field Flattener	41.7 V
Short Field Flattener 1	-80 V
Short Field Flattener 2	-80 V
Accelerator 1	228 V
Accelerator 2	-240 V
Accelerator 3	-423 V
Accelerator 4	-672 V
Accelerator 5	-883 V
Flight Tube	-4000 V
Detector	2650 V
Threshold	2020

### Atmospheric Pressure MALDI Configuration

A simplified diagram of an APMALDI source is shown in Figure 2-4.

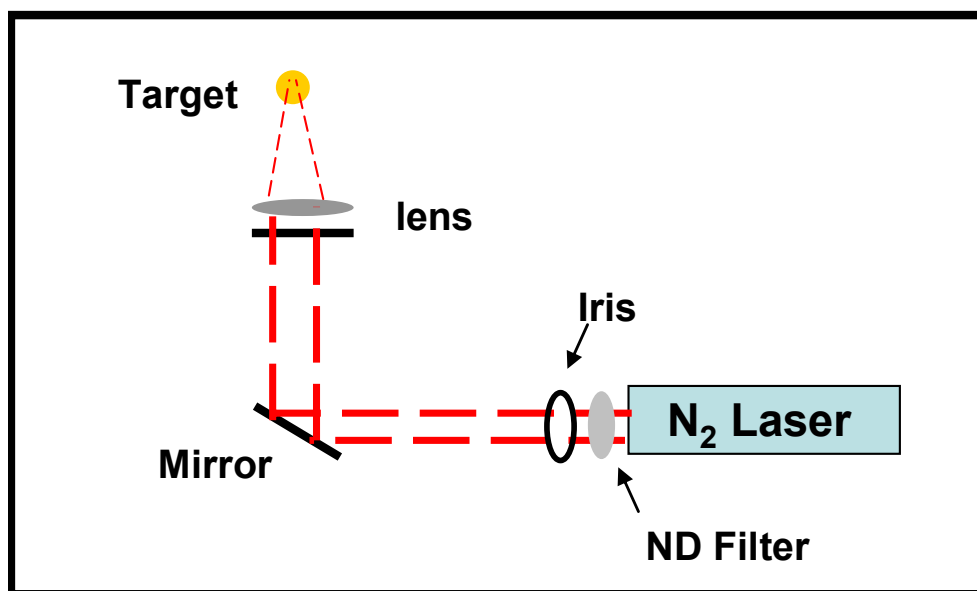


Figure 2-4. A diagram of the components in a typical atmospheric pressure matrix-assisted laser desorption/ionization source is shown.

While the arrangement of components varied throughout the design process, constant to the system were: (1) a 337 nm nitrogen laser (VSL-337-ND-S, Spectra-

Physics, Mountain View, CA, USA), (2) UV enhanced aluminum coated positioning mirrors (Edmund Industrial Optics, Barrington, NJ, USA), (3) a variable iris (Edmund Industrial Optics, Barrington, NJ, USA), (4) UV attenuating optics (*i.e.*, neutral density (ND) filters (Edmund Industrial Optics, Barrington, NJ, USA) or wheels (Reynard Corporation, San Clemente, CA, USA)), and (5) a fused silica focusing lens (Edmund Industrial Optics, Barrington, NJ, USA). Two sources were constructed, prototype I and II. In each case, repetition rate of the laser was monitored using an oscilloscope (TDS 210, Tektronics, Beaverton, OR, USA). Laser power was measured using a pyroelectric detector (J4-09-030, Molelectron Detector, Inc., Santa Clara, CA, USA). Prototype I's target was a 4 mm diameter stainless steel rod. The newer target, prototype II, is a 2 mm diameter gold coated post. Target positioning was accomplished in the first prototype by a stepper driven motorized *xyz* translational stage (CMA-12CCCL/ESP300; Newport, Irvine, CA, USA). The reduced size APMALDI source, prototype II, incorporated a piezoelectric transducer driven *xyz* stage (8302/IPico Driver, New Focus, San Jose, CA, USA). Targets were insulated from the positioning devices and held at a voltage ranging from 0 to 2500 V using an internal power supply from the mass spectrometer.

Table 2-2 lists the potentials of the ion transfer optics and the mass analyzer when using an APMALDI source.

Table 2-2. Mass spectrometer conditions used to acquire APMALDI spectra.

Nozzle	300 V
Skimmer	75 V
Quadrupole RF	300 V
Quadrupole High	42 V
Quadrupole Low	41.5 V

Table 2-2. Continued.

Quadrupole Exit	20 V
Focus	-30 V
Horizontal Deflect	4 V
Vertical Deflect	1 V
Einzel Focus	0 V
Einzel Horizontal Deflect	3 V
Einzel Vertical Deflect	1 V
Repeller	977 V
Pusher	791 V
Doorway	443 V
Long Field Flattener	41.7 V
Short Field Flattener 1	-80 V
Short Field Flattener 2	-80 V
Accelerator 1	228 V
Accelerator 2	-240 V
Accelerator 3	-423 V
Accelerator 4	-672 V
Accelerator 5	-883 V
Flight Tube	-4000 V
Detector	2650 V
Threshold	2020 V

## Sample Preparation

### Solid matrix

The dried-droplet method was used for co-crystallization of the matrix and analyte.<sup>113</sup> Saturated matrix solution was made by dissolving 10 mg of 2,5-dihydroxybenzoic acid (DHB) (Sigma Aldrich, St. Louis, MO, USA) in 1 mL of 50% aqueous acetonitrile with 0.05% trifluoroacetic acid (TFA). Reserpine (Sigma Aldrich, St. Louis, MO, USA) was prepared as a stock solution of 1 nmol· $\mu\text{l}^{-1}$  in 50% aqueous methanol with 0.1% TFA. Peptides were prepared at a concentration of 1 mg· $\text{mL}^{-1}$  in 0.1% aqueous TFA, and diluted as necessary. For crystallization, equal portions of matrix and analyte were mixed together and  $\sim 1.5 \mu\text{L}$  of resulting solution was placed on

target. The target was placed into position after the solution was dried at ambient conditions for 20 minutes.

### **Liquid matrix**

Two liquid matrix preparations were used during the ion source optimization stage. The first matrix used 2,5-dihydroxybenzoic acid (DHB) in a glycerol-solvent solution at a 1:3 mass ratio. The glycerol-solvent solution consisted of 75% glycerol, 15% water, and 10% methanol with 0.1% TFA. The second matrix also used a 1:3 ratio, but of  $\alpha$ -cyano-4-hydroxycinnamic acid (CHCA) (Sigma Aldrich, St. Louis, MO, USA) with diethanolamine (DEA) (Sigma Aldrich, St. Louis, MO, USA). Each liquid matrix was sonicated for 10-15 minutes to ensure dissolution. For analysis, 1  $\mu$ l of matrix and 0.5  $\mu$ l of analyte were mixed on target.

## **Results and Discussion**

### **Electrospray Evaluation**

Using a prototype mass spectrometer, it was important to evaluate instrument response independent of a new ionization source; therefore, the use of electrospray ionization (ESI) was incorporated into initial studies. ESI determined a reference point for ion transmission efficiency, mass resolving power, and ion signal stability.

Figures 2-5 and 2-6 show the total ion counts (TIC) and mass spectra for directly infused reserpine ( $m/z$  609) and verapamil ( $m/z$  456). For each electrospray spectrum the resolving power is near 2500, determined by the full width half maximum definition ( $\Delta m/m$ ). The percent relative standard deviation for ion counts is ~10%, and the mass accuracy, determined by external calibration and 10 consecutive analysis of each compound, is between 6 to 8 ppm.

By using a sample introduction rate of  $0.5 \mu\text{L}\cdot\text{min}^{-1}$ , an extraction frequency of 5 kHz, a total summed transients of 1200, and a sample concentration of  $2 \text{ ng}\cdot\mu\text{L}^{-1}$ , the overall efficiency of ion detection can be calculated. The Reserpine mass spectrum shown in Figure 2-5B provides 1000 counts for the molecular ion (an injection amount of 0.008 ng during the acquisition time), yielding an efficiency of  $\sim 1 \times 10^{-7}$  counts per molecule sampled. While the calculated efficiency is an important parameter, it is not solely a factor of the instrument; it also includes the electrospray process efficiency.

ESI sensitivity, defined as the slope of the working curve, is determined by both the efficiency that molecules are converted to gas-phase ions and the efficiency that the formed ions are transferred through the mass spectrometer and detected.<sup>116</sup> The fraction of ions analyzed then depends upon the transfer optics and the mass analyzer. Absolute efficiency of the ESI process is unknown; however, the literature generally agrees that the limiting factor in sensitivity is ion transmission, not formation.<sup>116</sup> Thus, as an instrumental parameter, the overall efficiency obtained with ESI can be considered a maximum. With optimized ion transmission into the inlet, and estimate for signal intensities can be based upon ion formation efficiencies.

## **APMALDI Source**

### **Prototype I**

The original configuration for the APMALDI source was designed to allow maximum adjustment for the optical components; therefore, standard optical elements and hardware were used for the assembly. Figure 2-7 is a photograph of the prototype I source. Inset in the figure is a magnified view of the target assembly.

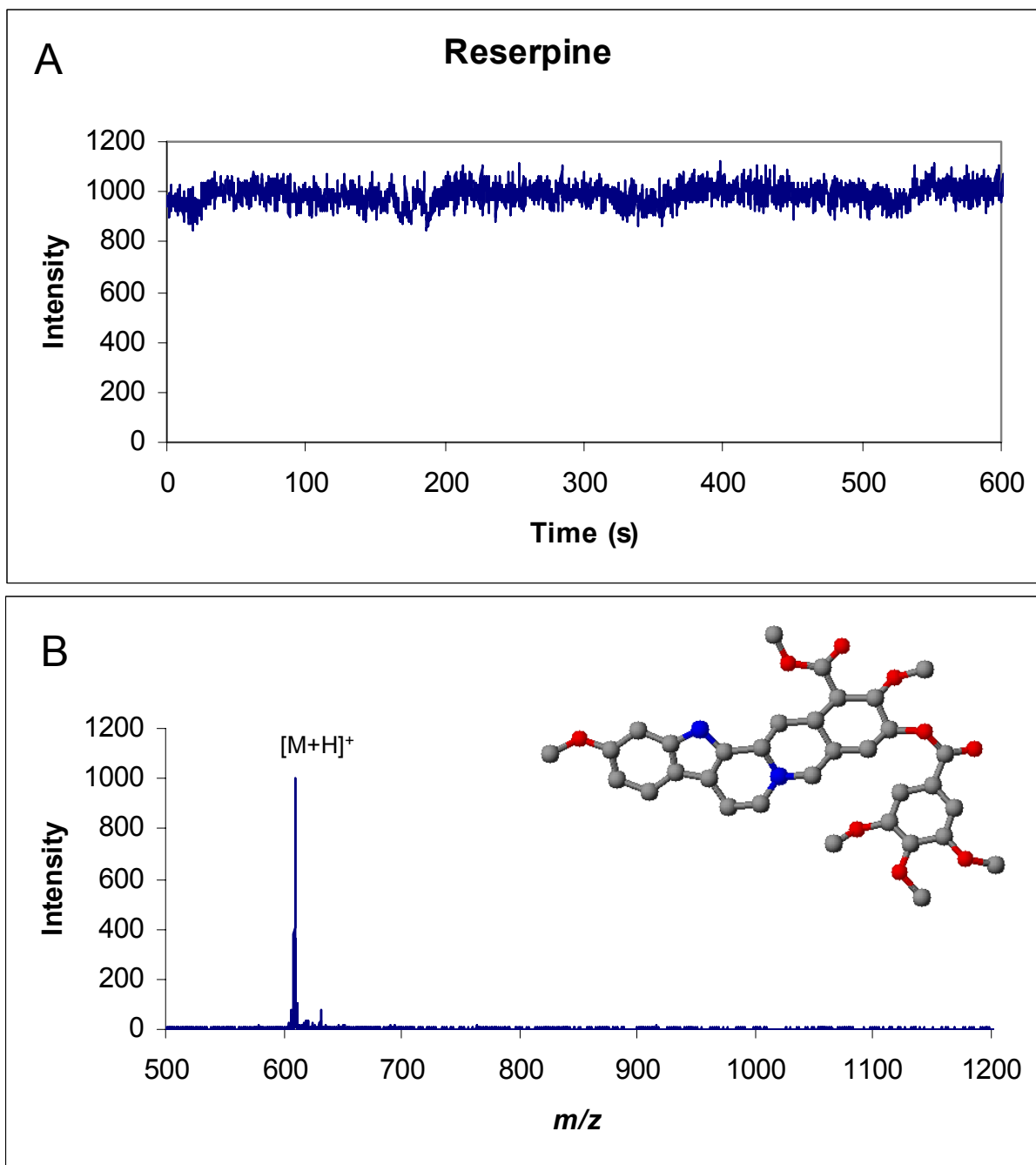


Figure 2-5. Plots showing the A) total ion count chromatogram and B) a mass spectrum for the analysis of reserpine. Inset in the figure is a ball and stick image of the molecule analyzed.



The 337 nm nitrogen laser outputs a rectangular beam area of approximately 5 mm by 7 mm with a pulse width of 4 ns. In this arrangement the laser beam is focused to a spot size on target of  $\sim 250\ \mu\text{m}$  by  $\sim 300\ \mu\text{m}$  in diameter (elliptical shaped). The target is held at  $\sim 45$  degrees from the normal of the laser beam. The original electro spray curtain gas cover was modified by reducing a 22 mm diameter section of the piece to 1 mm in thickness. In the electro spray mode, the original and modified covers produced identical results; however, the benefit for APMALDI was that the new cover allowed the target to move within 2.5 mm of the orifice.

**Solid matrix.** When ion production is not consistent, source optimization is difficult. Since the oa-TOF is run asynchronously with the laser pulse, single shot spectra (as done typically with vacuum MALDI on a linear TOF) produce drastically different ion intensities, negating any attempt at parametric studies.

At this point in ion source development, a continuous ion signal was needed. In a preliminary attempt, the laser repetition rate was increased to 10 Hz to produce a quasi-continuous ion beam, but increased laser frequency rapidly depleted the solid sample. Figure 2-8 is a mass spectrum of solid matrix (DHB) obtained using the prototype I. While the quasi-molecular ion  $[\text{M}+\text{H}]^+$  is visible, DHB clusters are seen throughout the  $m/z$  range.

With the laser operating at 10 Hz and the  $xyz$  motorized stage translated continuously (rate of 0.5 mm per minute), solid matrices still produced erratic ion production. Figure 2-9 shows total ion count (TIC) traces for the solid and liquid matrices. The lower trace demonstrates the ion signal reproducibility obtained with solid matrices. The drastic variations in the ion trace occur due to heterogeneity in the matrix

crystals. The idea of a liquid matrix was appealing during this stage of development; however, to accommodate solution droplets, the target angle needed to be altered.

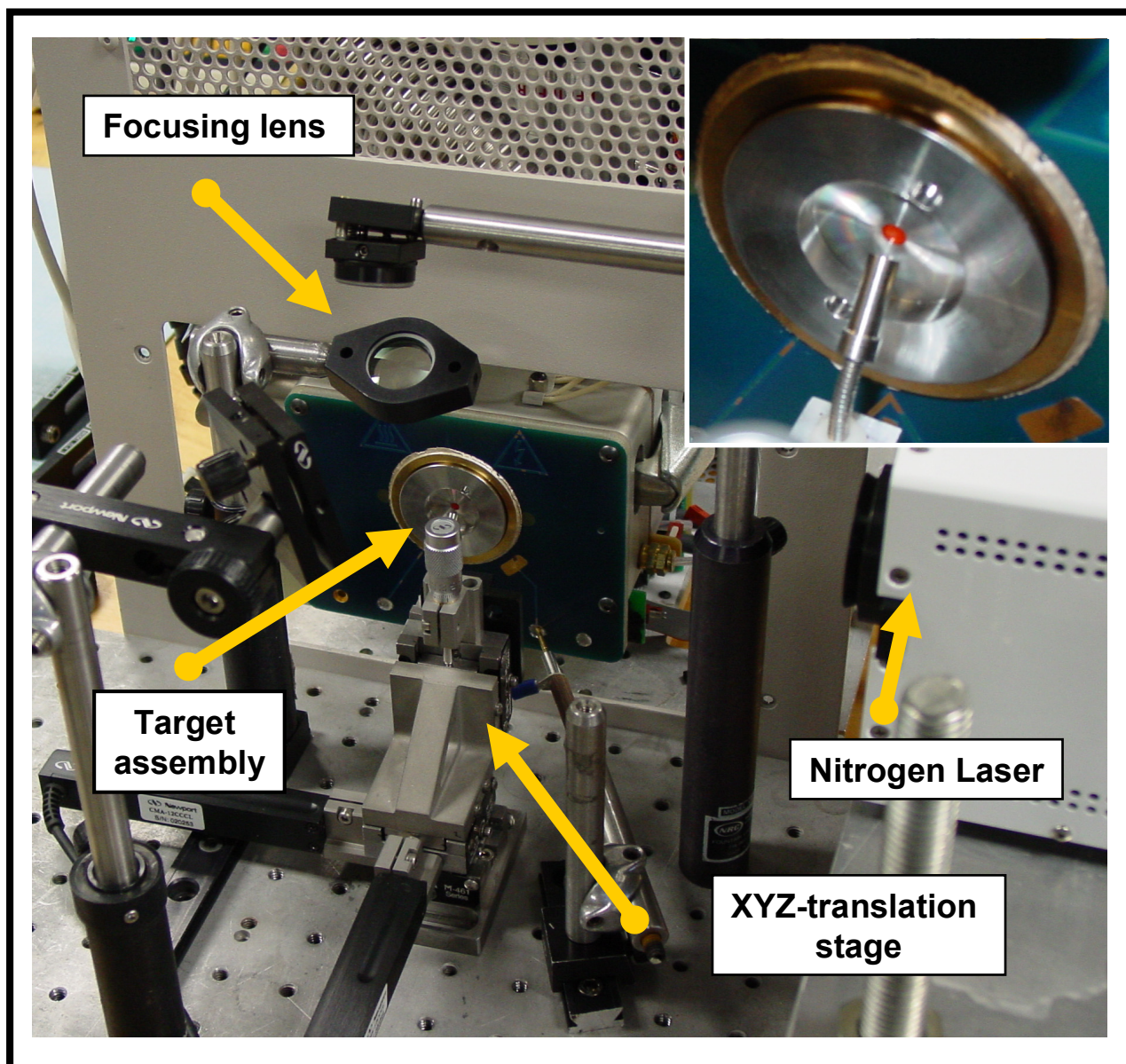


Figure 2-7. A photograph of the first constructed APMALDI source, prototype I. Inset in the figure is a magnified view of the target assembly.

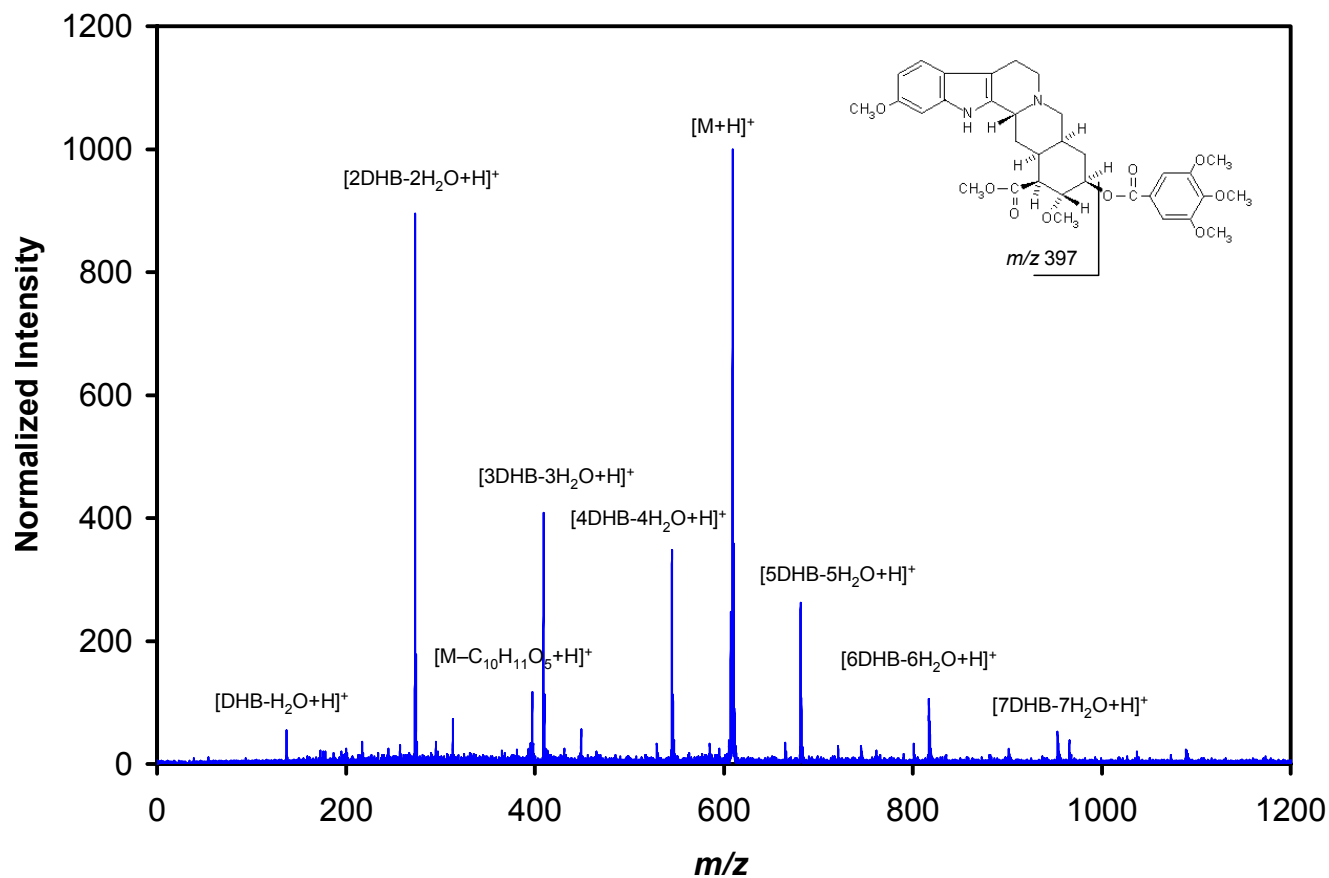


Figure 2-8. A mass spectrum of reserpine analyzed in a solid DHB matrix is shown. Analysis was done using the prototype I APMALDI source.

**Liquid matrix.** A photograph of the target assembly constructed for liquid matrices is shown in Figure 2-10. Inset in is a computer aided drawing (CAD) (Solidworks, Concord, MA, USA) of the target showing its relative position and the laser angle used for desorption. Additionally, a three dimensional depiction of the target assembly and its orientation to the orifice is shown using a executable output file from the CAD program.

Object 2-1. A file showing the target alteration for the liquid matrix (1.8 mb, PrototypeI.exe, repeating play file).

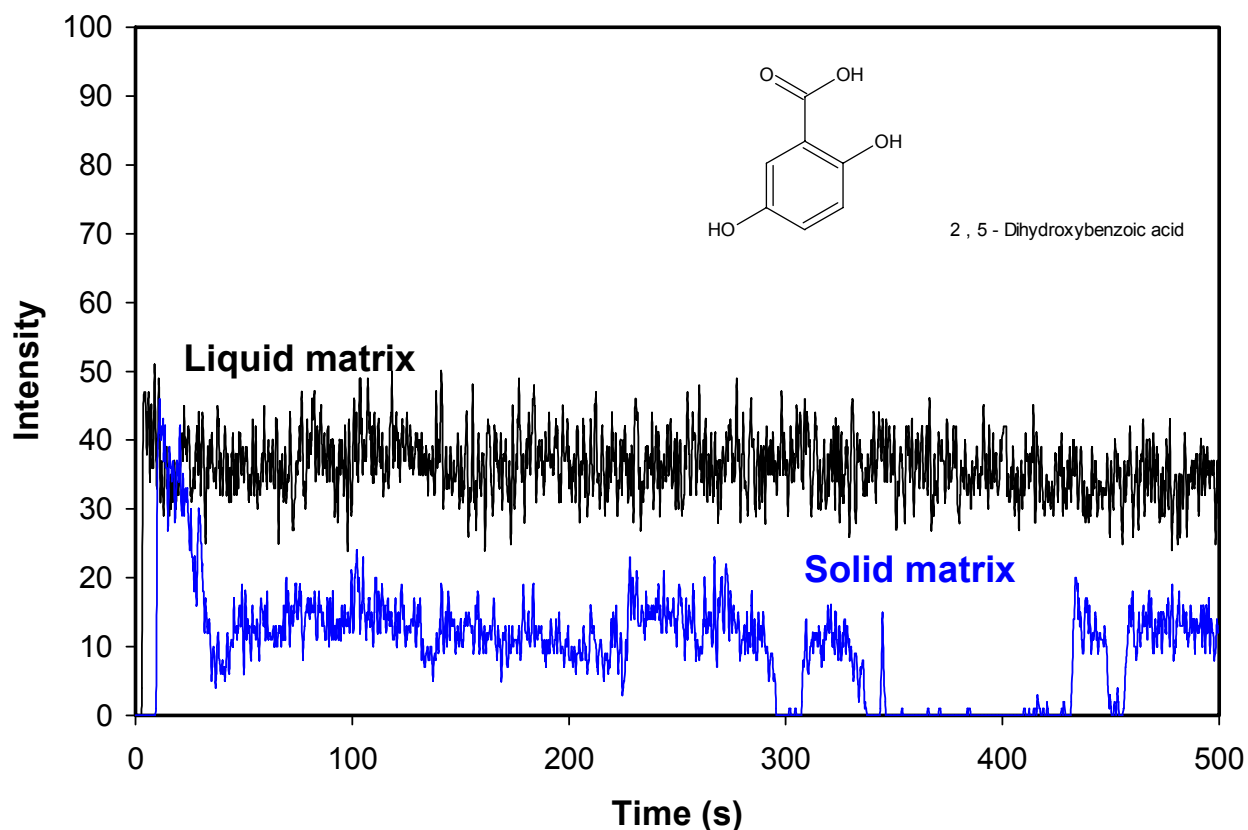


Figure 2-9. Plot of the total ion count chromatograms for solid and liquid matrices. DHB was used as the absorbing chromophore with reserpine as the analyte.

Figure 2-11 shows a liquid matrix mass spectrum collected using the new target holder. The spectrum is an improvement over the solid matrix analysis (*i.e.*, reduction of matrix clusters). While improvements in solid matrix preparations can also lower the background, the important feature of the liquid matrix is the continuous ion production, as seen in Figure 2-9. In the TIC trace, as the laser is operated at 10 Hz, the liquid matrix sample stage is kept in a fixed position. This provided extended ion production, enabling interface optimization.

**Atmospheric pressure sampling.** Critical in atmospheric pressure (AP) interfacing is cluster prevention; therefore, during source optimization the curtain gas cover, gas mass flow rates, and interface potentials were examined as they related to maximum ion signal

production. Additionally, moving ions at AP is difficult due to the number of collisions occurring. Unlike the reduced pressure flight tube, the mean free path of an ion at atmospheric pressure is on the order of nanometers.

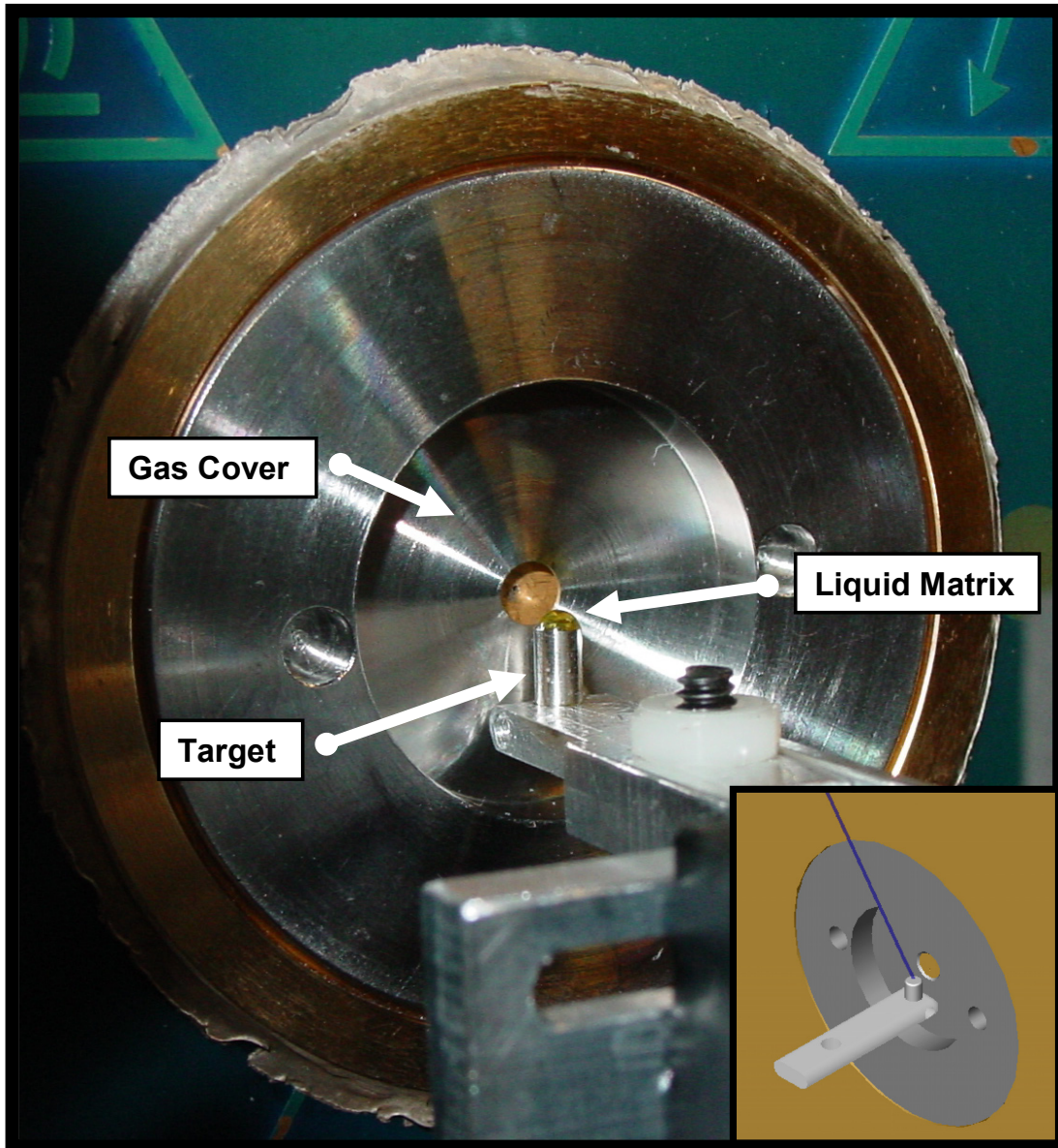


Figure 2-10. A photograph of the altered target assembly for liquid matrix analysis. Inset is a computer aided drawing of the target showing the laser angle.

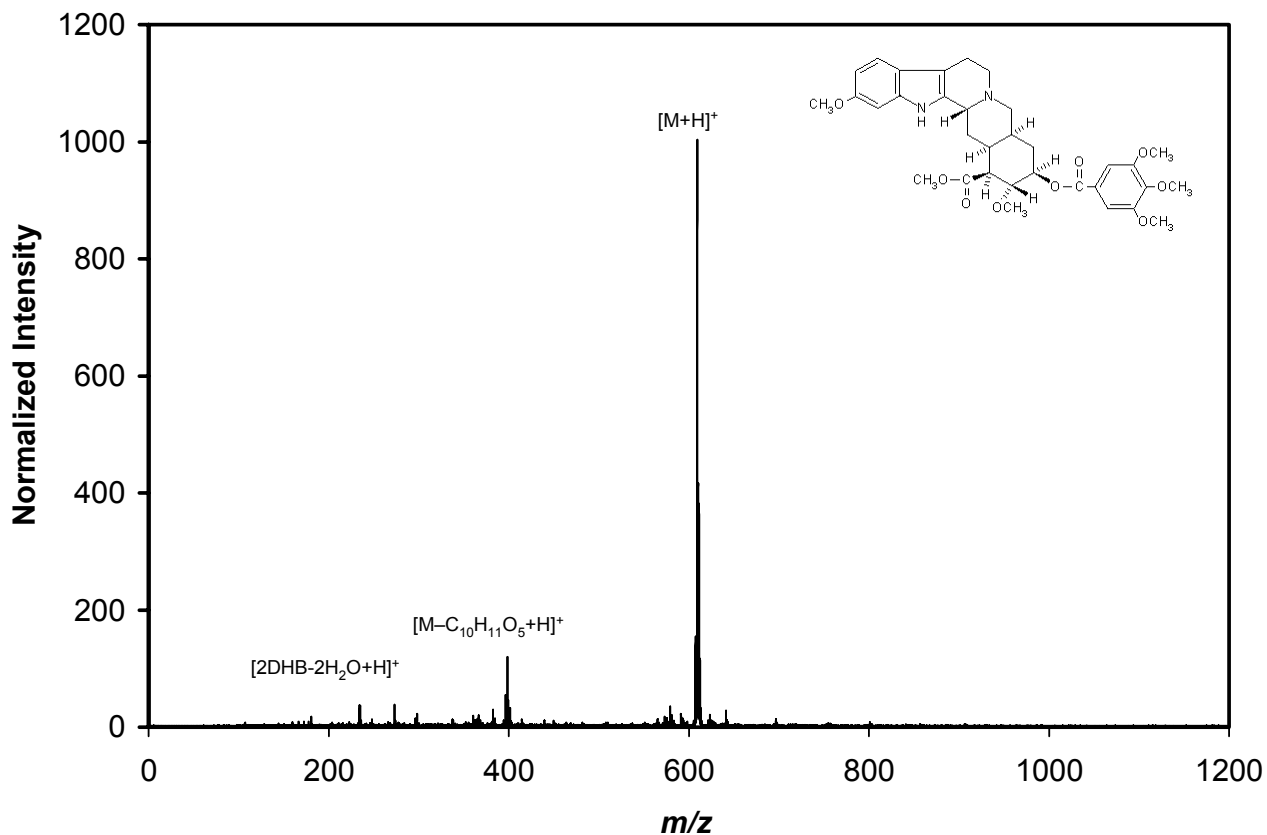


Figure 2-11. Mass spectrum of reserpine in a DHB liquid matrix taken using the modified target assembly is shown.

Mean free path can be expressed by the following equation:

$$\lambda = \frac{kT}{\sqrt{2}\sigma p} \quad (2-1)$$

where the mean free path ( $\lambda$ ) is related to the collisional cross section ( $\sigma$ ), pressure ( $p$ ), Boltzman constant ( $k$ ), and temperature ( $T$ ).<sup>117</sup> Since effective transmission is important in improving ion signals, the distance between the target and the orifice was reduced in an attempt to increase ion signals. To minimize the target-orifice distance, the curtain gas cover was removed. Figure 2-12 is a photograph of the source and target assembly with

the curtain gas cover removed. This image can be compared with Figure 2-10 where the curtain gas cover is in place.

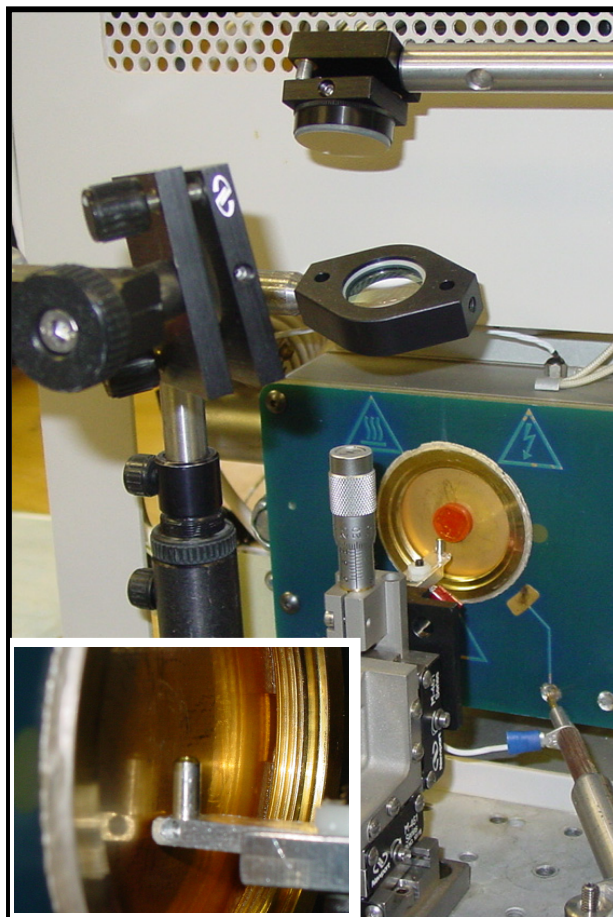


Figure 2-12. A photograph of the source and target assembly with the curtain gas cover removed.

No ion signal differences were visible with the removal of the curtain gas cover alone; however, when the target was positioned closer to the orifice the ion signal intensities increased  $\sim 30\%$ . Figures 2-13 A and B show mass spectra obtained at the different target-orifice distances of A) 1.5 mm and B) 2 mm.

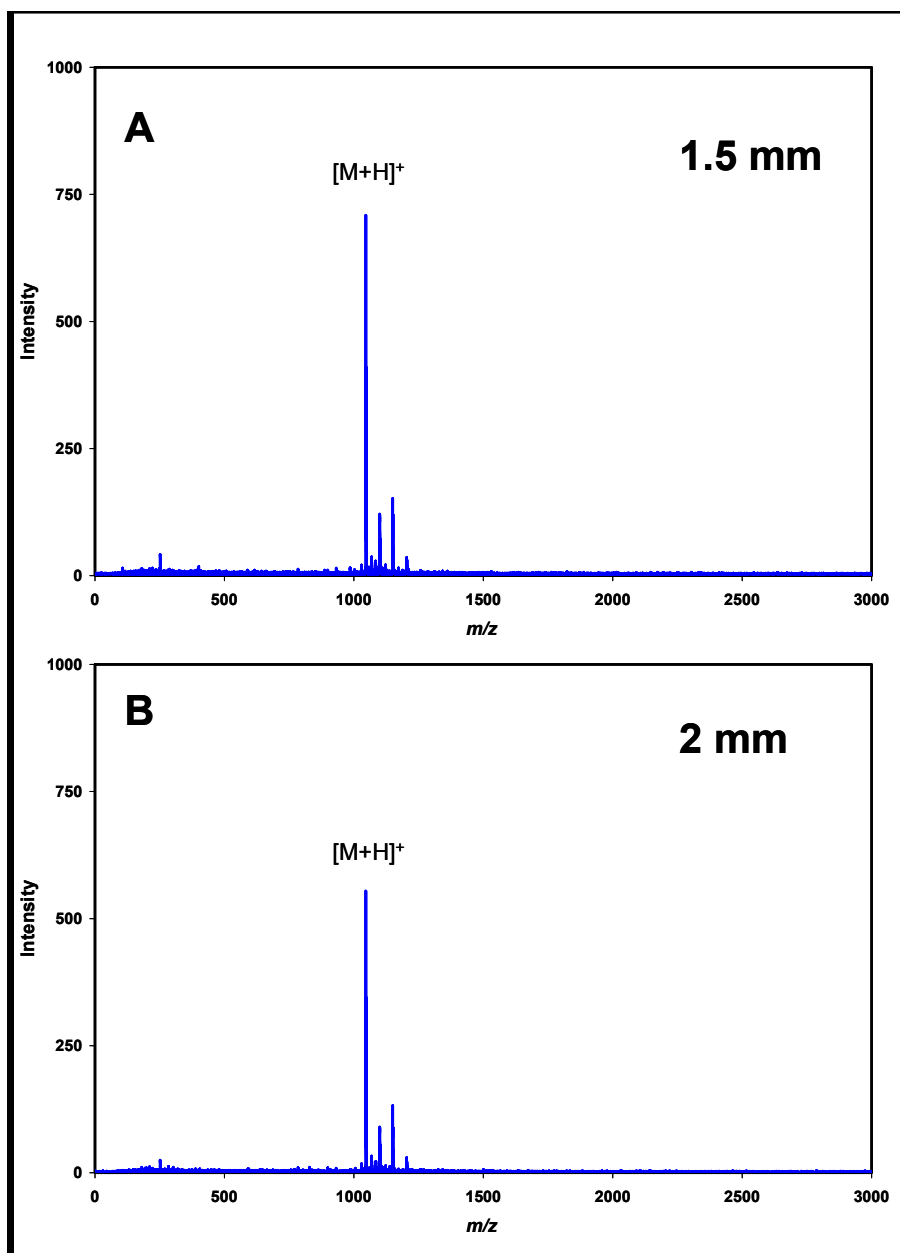


Figure 2-13. Mass spectra obtained with the target placed at a distance of A) 1.5 mm from the orifice and B) 2 mm from the orifice.

Moving the target closer than 1.5 mm from the nozzle resulted in high voltage arcs, and reductions in the voltages reduced ions signals to levels below that obtained at larger distances. Interestingly, a 25% decrease in target-orifice distance allowed a 30% increase in ion signals; however, this does not suggest a direct relationship.

## Prototype II

The second iteration of the APMALDI source minimized optical component positioning and reduced the overall size. Figure 2-14 is a photograph of the second APMALDI prototype. Inset in the figure is a new target assembly that positioned the translational stage away from the orifice axis. The impetus for moving the translational stage away from the orifice will be described in Chapter 6. Additionally, a three dimensional depiction of the prototype II source is shown in Object 2-2.

Object 2-2. A file showing the prototype II source (1.8 mb, [PrototypeII.exe](#), repeating play file).

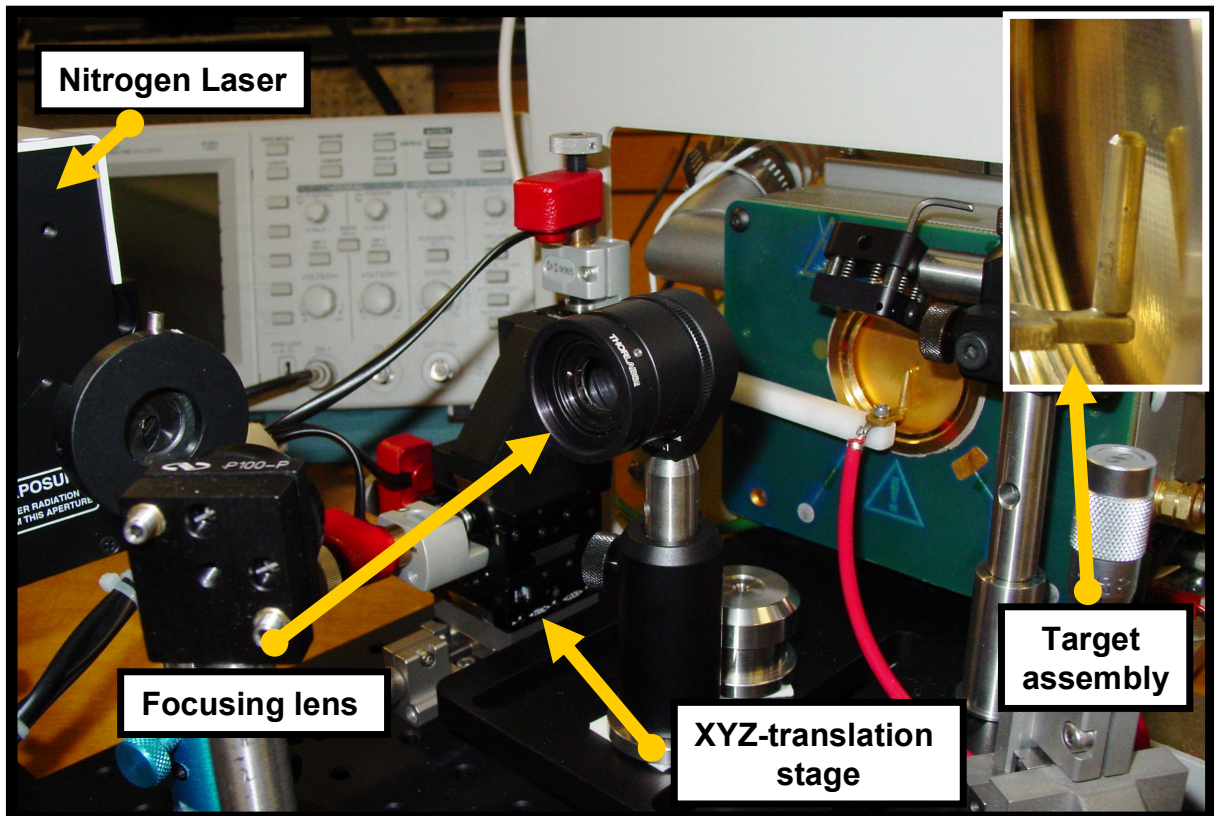


Figure 2-14. A photograph of the second APMALDI source, prototype II. Inset in the figure is a new target assembly that positioned the translational stage away from the orifice axis.

The prototype II APMALDI source uses a smaller diameter (2 mm) target with rounded edges. The edges reduced the possibility of arcing from the target to nozzle. The target is also coated with gold to minimize sample carryover. Target positioning is done using piezoelectric transducer driven motors. The smaller piezoelectric transducers not only diminished the source's overall size, but also minimized the controller, which fit inside the mass spectrometer housing. An additional advantage of the modified source was safety. The target assembly completed a closed loop circuit to initiate all interface voltages. Accidental shocks were reduced. With miniaturized optical components (New Focus, San Jose, CA, USA), the complete source (sans laser) could be constructed inside an enclosure attached to the mass spectrometer—a key benefit for commercial compatibility.

### **Adjusting Interface Parameters**

Initial measurements taken with the curtain gas flow indicated that higher flows yielded larger analyte ion intensities and reduced background. The original device used a limited  $1 \text{ L}\cdot\text{min}^{-1}$  mass flow controller. To increase the range, a  $5 \text{ L}\cdot\text{min}^{-1}$  mass flow controller was added to the system. Figure 2-15 shows mass spectra as the counter-current gas flow is set at 0, 1, and  $5 \text{ L}\cdot\text{min}^{-1}$ , respectively.

In each case the analyte signal, angiotensin I ( $m/z$  1296.68), increased while the background, DEA dimer ( $m/z$  211), was reduced. Additionally, the ratio of sodium adduct  $[\text{M}+\text{Na}]^+$  to protonated molecular ion  $[\text{M}+\text{H}]^+$  was minimized with a  $5 \text{ L}\cdot\text{min}^{-1}$  gas flow. Considering the fundamentals of the cluster prevention mechanism using a counter-current gas flow, it seems reasonable that increased gas flows (counter-current) should provide analyte signal increases through a reduction in clusters.

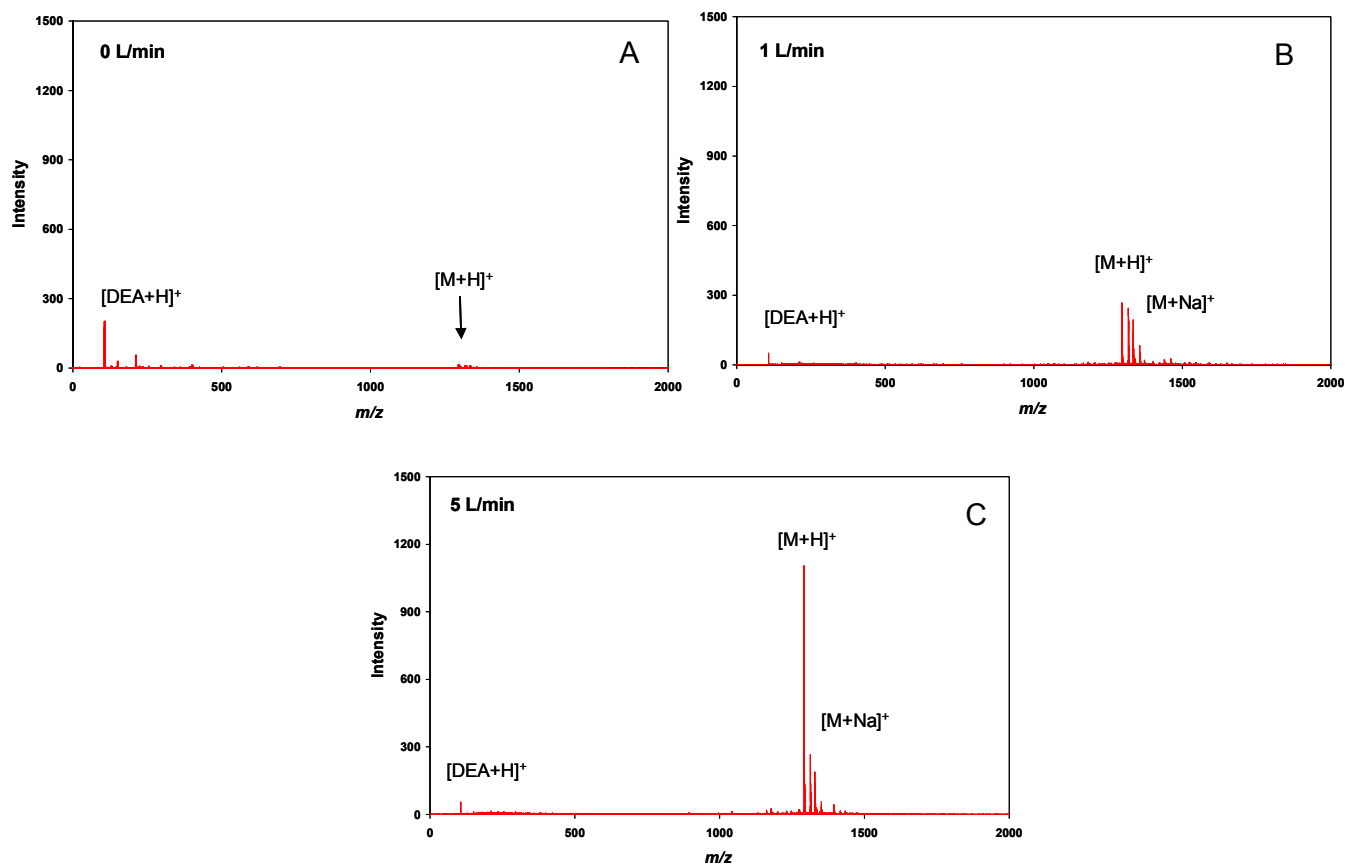


Figure 2-15. Three mass spectra taken using gas flow rates of A) 0 L·min<sup>-1</sup>, B) 1 L·min<sup>-1</sup>, and C) 5 L·min<sup>-1</sup>. Angiotensin II was used as the analyte in a CHCA liquid matrix.

The original literature for APMALDI saw a different effect for gas flow, indicating concurrent flows provided ion signal increases.<sup>104,106,114</sup> In original APMALDI orientations an angled probe tip was used for the sample and a stream of nitrogen gas directed at the nozzle entrained the ions. Only recently has literature pointed to counter-current gas flows increasing ion signals.<sup>115</sup>

The effect of temperature on the prevention of water clusters for supersonic jet expansion is known; thus, temperature was empirically examined.<sup>102</sup> A constant 100° C provided maximum ion signals without arcing. Higher temperatures provided no signal

increases or background decreases, yet more frequent arcs between the target and the nozzle occurred.

With an optimized target-orifice distance, target voltage was examined as it related to analyte ion yield. Although target voltage can be varied independently, it does not function independently for ion transmission. Instead, it is related to nozzle voltage, the voltage applied to the orifice. Figure 2-16 shows two diagrams of the mass spectrometer interface.

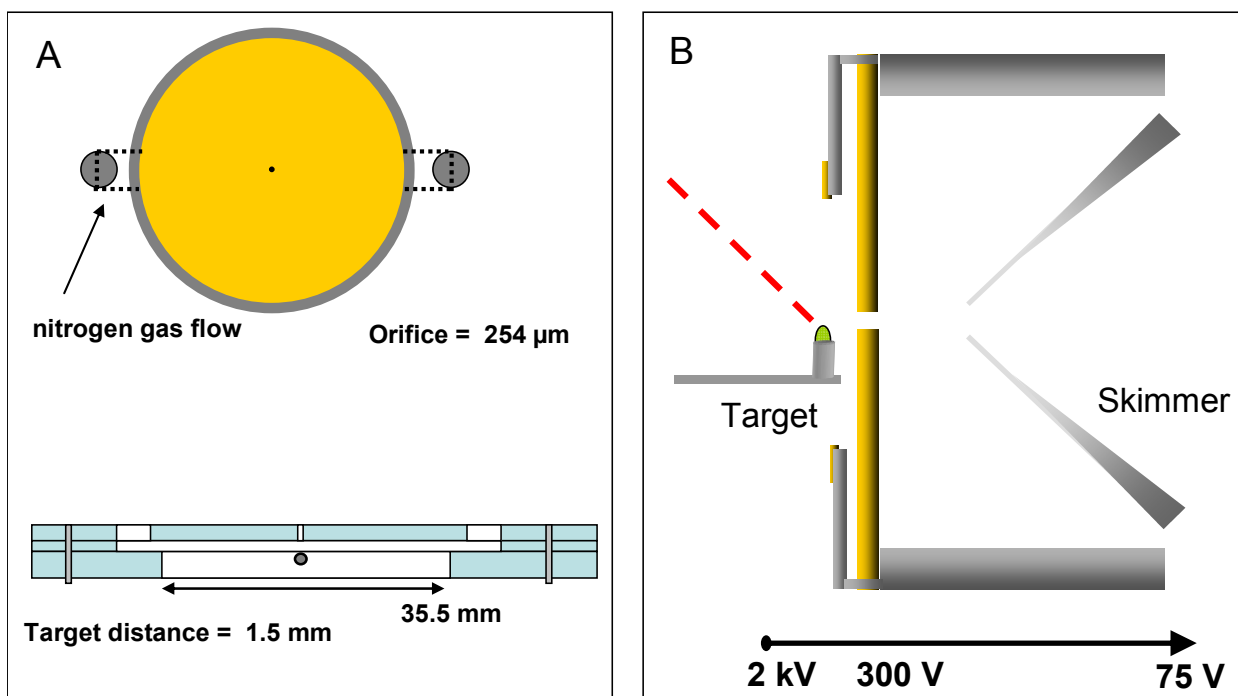


Figure 2-16. An illustration of the mass spectrometer interface. The two images show A) the gas orifices and mass spectrometer inlet, and B) the arrangement of the target, nozzle, and skimmer.

Together the target and nozzle form the electric field that transports ions from atmospheric pressure into the spectrometer. Figure 2-17 shows the interrelated functions of target voltage, nozzle voltage, and analyte (bradykinin fragment 1-7  $m/z$  756.4) ion yield.

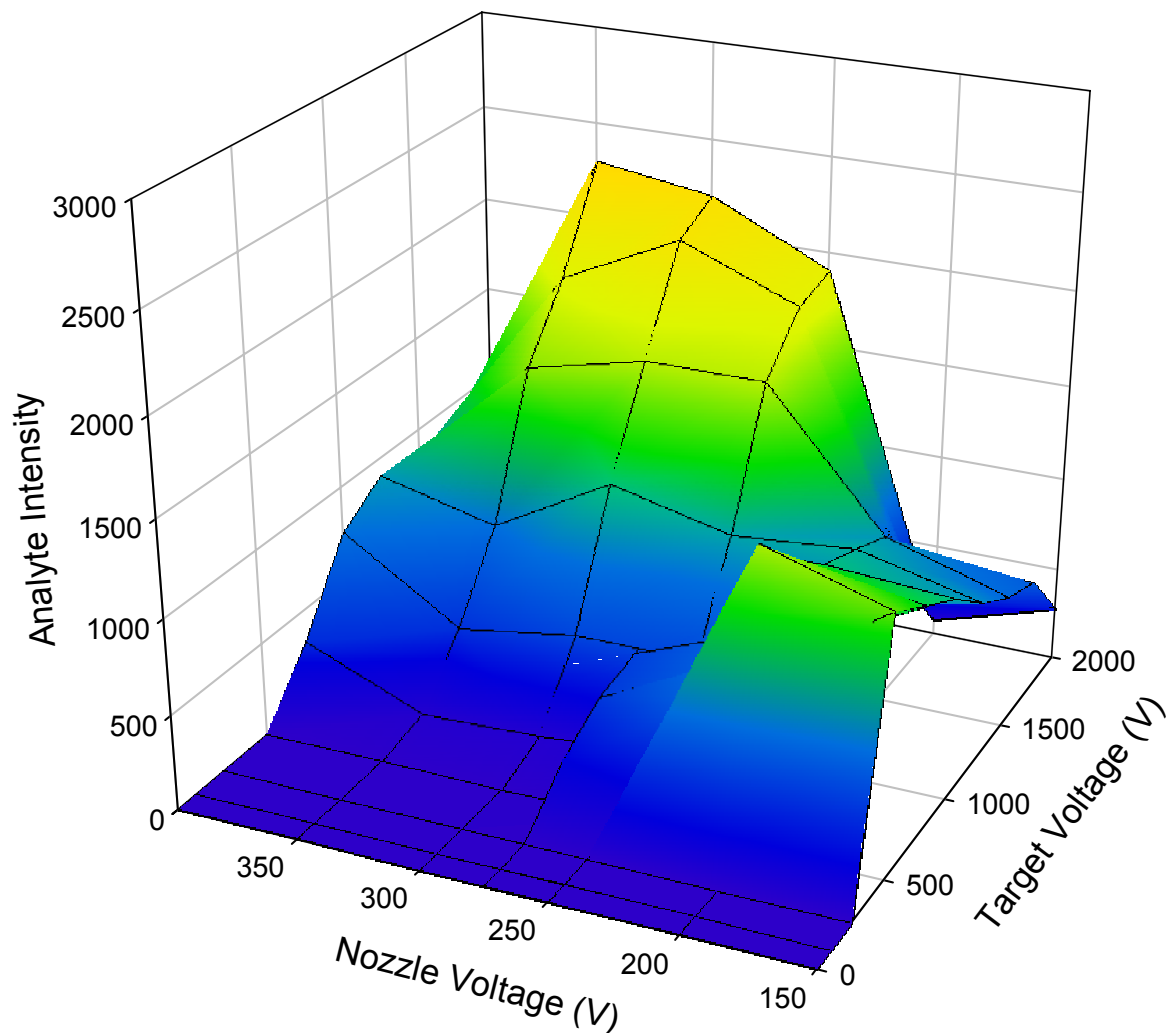


Figure 2-17. A three dimensional plot showing the relationship of target and nozzle voltage to analyte ion yields. The skimmer was maintained at 75 V. Bradykinin fragment 1-7 ( $m/z$  756.4) was the analyte in a CHCA liquid matrix.

Two events are demonstrated in Figure 2-17. First, increased ion yields occur at increased electrostatic fields. The maximum signals occur near  $1100 \text{ V}\cdot\text{mm}^{-1}$  (1700 V at a distance of 1.5 mm); however, the signals are not maintained as the target and nozzle voltages are lowered. Second, the potential for the skimmer is 75 V; therefore, a reduction in the nozzle voltage reduces the field between the nozzle and skimmer.

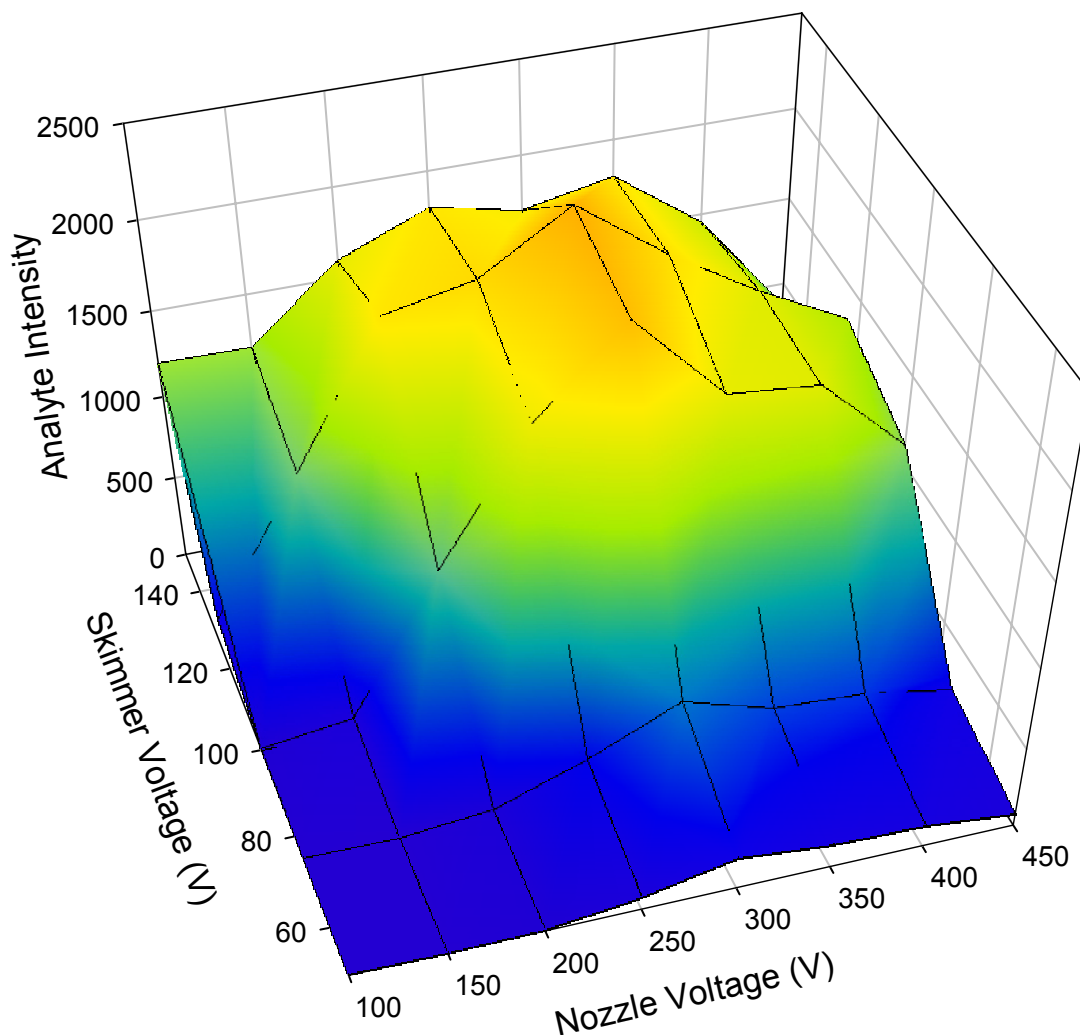


Figure 2-18. A three dimensional plot showing the relationship of nozzle and skimmer voltages to analyte ion signal intensity. The target was maintained at 2 kV. Bradykinin fragment 1-7 ( $m/z$  756.4) is used as the analyte ion in a CHCA liquid matrix.

Figure 2-18 was produced to investigate the ion intensity relationship between the nozzle and skimmer. For Figure 2-18, a broader range of electric fields, versus Figure 2-17, could be applied without significantly reducing the ion signals. In part, this may be due to reduced pressures between the nozzle and skimmer.

**Mass spectrometer conditions.** In a supersonic beam the energy of the ions is mass dependent due the ions being at constant velocity. When using an oa-TOFMS, a

mass dependent drift occurs in ion trajectories for the flight tube axis. Ions do not traverse the flight tube completely perpendicular to the pulser; some flight tubes are offset to account for the trajectory angle. However, since each mass requires a slight change in trajectory, methods must be incorporated to allow for a large range of different masses to reach the detector. The methods include using a large detector area to cover the trajectory range, providing deflection plates for specific masses, and adding energy to the supersonic beam to minimize the initial energy spreads (a larger total energy relative to the initial kinetic energies). An alternative approach is to use a collisional focusing RF-only multipole device containing an inert gas at elevated pressures (0.01 – 1 Torr).<sup>9-10</sup> The collisions with the gas reduce the average ion energy. Also, the multi-pole device focuses the ions to a beam as they approach the thermal energy of the gas.<sup>119-120</sup> Thus, the beam leaving the ion guide has a smaller spatial spread in the axis of the flight tube, and these properties are almost independent of the original parameters of the ion beam delivered by the source (*i.e.*, no memory of spatial or kinetic distributions from the ion formation processes).<sup>89</sup>

Further optimization of the mass spectrometer conditions (pulser voltages, Einzel lens voltages, etc.) was undertaken, but showed little effect. The optimization of the parameters for ESI and APMALDI (besides the interface and initial ion transmission parameters) yielded similar results. The mass spectrometer voltages remain constant primarily due the sampling method of the jet expansion.<sup>117</sup> While the conditions are not directly related to the jet expansion, they are indirectly related due to the use of the collisional focusing in an RF-only quadrupole.

## Conclusions

This chapter demonstrates the initial instrument characterization, using an ESI source, and the construction of an APMALDI source. Using an oa-TOFMS, the optimization of interface parameters (*i.e.*, target distance, gas flow, target voltage, nozzle voltage, and skimmer voltage) must be accomplished to maximize APMALDI ion collection and transmission. An added benefit to the use of an RF-only quadrupole, besides collisional focusing, is the reduction in ion source memory, easing spectrometer parameter adjustments. The APMALDI source designed and implemented presents an ion source that would be easily interchangeable with a common ESI source configured mass spectrometer. The adjusted parameters and their relationship to ion yields demonstrates the necessity of optimizing atmospheric pressure transmission. Additionally, liquid matrices were introduced as the first analytical advantage for APMALDI. Further evidence for this is demonstrated in upcoming chapters.

CHAPTER 3  
LIQUID SUPPORTS FOR ULTRAVIOLET ATMOSPHERIC PRESSURE MATRIX-  
ASSISTED LASER DESORPTION/IONIZATION

**Introduction**

Matrix-assisted laser desorption/ionization (MALDI) has seen widespread use in bioanalytical analysis.<sup>111</sup> For analysis of large intact biomolecules, MALDI requires a suitable matrix to absorb energy and transfer it to the analyte. Many types of matrices exist, yet the most widely accepted today is some form of solid, crystalline structure that acts as an analyte host. This solid, low volatility matrix allows convenient application in the low pressure environment of a mass spectrometer ion source; however, the rigid lattice matrix presents a heterogeneous sample surface for successive laser pulses. As the crystal surface is ablated, analyte ion signals fluctuate due to the non-uniform sample surface.<sup>121</sup> Enhanced homogeneity of the surface through sample preparation assists in providing more reproducible MALDI analyses.<sup>122-124</sup> Despite the numerous sample preparation methods reported, sample heterogeneity remains an issue.<sup>121,125-127</sup>

A liquid matrix, with its self-renewing surface, eliminates the sample heterogeneity problem associated with solid matrices. Liquid sampling systems have found prior use in mass spectrometry to combat signal irregularities and to provide increased signal lifetime. Fast atom bombardment (FAB) and liquid secondary ion mass spectrometry (LSIMS) demonstrated the use of viscous liquids as an effective sample surface.<sup>128-129</sup> The process of energy transfer differs in these two methods, but the surface replenishment principle is

similar. Drawing on that success, laser desorption methods have also incorporated the use of liquid supports.<sup>34</sup>

A number of MALDI liquid supports have been studied, including neat liquids, particle suspensions, and chemical doping. Neat liquids provide direct absorption of the laser and limit matrix preparation time. Unfortunately, relatively few vacuum stable liquids provide adequate UV absorption.<sup>130-133</sup> The addition of absorbing particles to a vacuum stable liquid, a particle suspension matrix, provides a low volatility medium that absorbs UV wavelengths.<sup>134-137</sup> These particle suspension matrices allow desorption and ionization, although the mechanism for desorption is not typical of a solid MALDI matrix.<sup>45</sup> The particle suspension matrix has been regarded to induce a thermal event, whereby rapid heating at the particle surface allows thermal desorption of analytes.<sup>134,136-137</sup> Chemically doped liquid matrices may be more analogous to solid MALDI systems with their use of energy absorbing molecules.<sup>138-139</sup> A variety of absorbing molecules have been used in binary mixtures with some success.<sup>132,138,140</sup> Wang et al. developed vacuum stable chemically doped liquid matrices by using typical solid MALDI chromophores, 2,5-dihydroxybenzoic acid (DHB) and  $\alpha$ -cyano-4-hydroxycinnamic acid (CHCA), in viscous liquids such as glycerol and diethanolamine (DEA).<sup>139</sup> In some cases, a solubilizing agent was added to the mixture to ensure chromophore dissolution.

Liquid matrices have provided excellent shot-to-shot reproducibility and long-term analyte signal stability; however, the liquid systems have been evaluated in a vacuum ion source—necessitating a low volatility medium.<sup>132,138</sup> Liquid matrices placed in a vacuum environment have encountered problems with source contamination and high backing pressures ( $5 \times 10^{-6}$  Torr), limiting their incorporation for routine analysis.<sup>132,137</sup> The

development of atmospheric pressure (AP) MALDI provides new opportunities for liquid matrices under conditions where sample volatility need not be as restricting.<sup>104-105,109</sup> An APMALDI source provides good limits of detection and has been suggested as a softer ionization method due to increased collisional cooling.<sup>114</sup> With the MALDI ion source operating in an open ambient environment, vacuum stable matrices are not necessary.

To expand sample analysis opportunities, while providing the benefits of traditional MALDI chromophores, we have explored suitable liquid matrices for UV APMALDI.<sup>141</sup> Glycerol-based liquid matrices, which absorb in the IR, have become common for use with IR lasers at 2.94  $\mu\text{m}$  and 10.6  $\mu\text{m}$ .<sup>48,114,142-143</sup> However, due to cost and availability issues, IR laser systems are less commonly used for MALDI applications. The UV nitrogen laser (337 nm)—simple to use, relatively inexpensive, and readily available in many laboratories—has become the most widely used MALDI laser source.<sup>48,142</sup>

Our experimental goals focused on developing a UV-compatible liquid matrix by doping a typical MALDI chromophore,  $\alpha$ -cyano-4-hydroxycinnamic acid (CHCA), into a liquid medium. The liquid support comprises a solvent liquid for analyte solubility and a viscous component for signal lifetime. Formulation of a UV absorbing liquid matrix for use at AP presents unique problems and advantages. As noted above, Wang et. al demonstrated similar studies for the formulation of chemically doped matrices optimized for a vacuum ion source.<sup>139</sup> Out of the vacuum, matrices are not limited by vapor pressure or source contamination; however, desorption and ionization at AP must be characterized through alterations in the liquid systems. We show an example of an AP liquid matrix that provides an effective avenue for UV APMALDI analysis. In this chapter, we report on the use of suitable liquid matrices for UV APMALDI, showing ease

of use, representative spectra, and promising quantitation. The parameters studied include chromophore concentration, liquid support variations, and quantitation capability. We believe this approach offers advantages that complement current MALDI methods.

## **Experimental Methods**

### **Atmospheric Pressure MALDI Source**

The mass spectrometer is an orthogonal-acceleration TOFMS (LECO Corporation, St. Joseph, MI, USA), which is described in detail in Chapter 2. The APMALDI ion source used a 337 nm nitrogen laser (VSL-337-ND-S, Spectra-Physics, Mountain View, CA, USA), focused by a fused silica lens, to irradiate the sample on a gold coated target, 2 mm in diameter. The laser spot was  $\sim 250$   $\mu\text{m}$  by  $\sim 300$   $\mu\text{m}$  in elliptical diameter and yielded  $\sim 60$  to  $80$   $\mu\text{J}$  per pulse. The target, onto which the sample and matrix were deposited, was positioned relative to the MS orifice using a motorized *xyz* translational stage (8302/IPico Driver, New Focus, San Jose, CA, USA). Held at 2 kV, the target was on-axis  $\sim 1.5$  mm from and  $\sim 1$  mm below the  $254$   $\mu\text{m}$  orifice, which was maintained at 300 V. Ions from the matrix/sample solution were transferred into the spectrometer using a counter-current gas flow interface. The nitrogen flow was set to  $5$   $\text{L}\cdot\text{min}^{-1}$  and heated to  $100^\circ\text{C}$ .

### **Solution Preparation**

The matrix was prepared by mixing CHCA (Sigma-Aldrich Corp., St. Louis, MO, USA) with the liquid support made from a solvent liquid and a viscous component. The solvent liquids used were ethanol, acetonitrile, acetone, and water (Fisher Scientific, Fair Lawn, NJ, USA). Aqueous solutions of trifluoroacetic acid (TFA) (Sigma-Aldrich Corp., St. Louis, MO, USA) were also used as test solvents for the liquid matrix. The viscous

component was diethanolamine (DEA) (Sigma-Aldrich Corp., St. Louis, MO, USA). Each matrix preparation was sonicated and vortexed to ensure dissolution. Peptides were prepared in aqueous acetonitrile with 0.1% TFA, unless otherwise stated. Sample analysis was conducted by spotting 0.5  $\mu\text{L}$  of matrix onto 0.5  $\mu\text{L}$  of analyte solution.

## Results and Discussion

### Liquid Matrices

Current mass spectrometers dedicated to electrospray ionization (*e.g.*, oa-TOF) are directly amenable to APMALDI, yet the advantages of using non-vacuum compatible matrices have not been broadly investigated.<sup>109,143-144</sup> The liquid matrix used in these studies comprises a chromophore, a support liquid, and a solvent liquid. The chromophore, CHCA, absorbs and transfers energy to the analyte in a controlled manner.<sup>37</sup> The support liquid, DEA, is used as a viscous component for sample longevity; however, it also acts as a solubilizing agent for CHCA.<sup>136,139</sup> The solvent liquid is used for reducing viscosity, allowing for enhanced signal intensity and an increase in analyte solubility.

### Chromophore Concentration

In solid sample MALDI, CHCA crystals are embedded with analyte, leaving the crystalline matrix to serve directly as the chromophore.<sup>37</sup> In this mode various matrix-to-analyte molar ratios are possible, providing different degrees of analyte isolation and energy transfer.<sup>145</sup> Matrix-to-analyte ratios are believed to play a role in effective analyte isolation.<sup>45</sup> As the analyte molecules become more isolated from one another, efficient soft desorption and ionization occurs.

In the liquid system, the matrix-to-analyte ratio is not based only on CHCA amounts. The liquid matrix differs in that it contains water, ethanol, and diethanolamine in large quantities to isolate the analyte without the addition of the chromophore. Thus, analyte isolation within the support liquid can be maintained while chromophore concentration is studied. To evaluate chromophore concentration dependence, CHCA amounts doped into the liquid support were altered while monitoring analyte ion intensity. The liquid support consisted of a solvent liquid, 50% aqueous ethanol, and a viscous component, diethanolamine. Figure 3-1 shows the analyte and matrix background mass spectrometry ion counts as the chromophore concentration is increased.

The protonated analyte, angiotensin II ( $m/z$  1046.5), and the matrix background, total ion count (TIC) below  $m/z$  300, are plotted against CHCA concentrations. At concentrations below 100 mM, insufficient laser energy is absorbed to effect desorption and measurable ionization of the analyte. As the concentration increases, both the analyte and matrix signals rapidly increase. Up to approximately 800 mM of CHCA, there is a direct relationship between analyte ion intensity and the amount of added chromophore; however, further additions of absorber actually lower the analyte signal.

As the chromophore concentration is altered the absorption characteristics of the matrix are changed. The CHCA allows the coupling of the laser energy to the solution, so with increasing chromophore concentration, the amount of laser energy absorbed in a finite volume on the surface of the solution also increases.

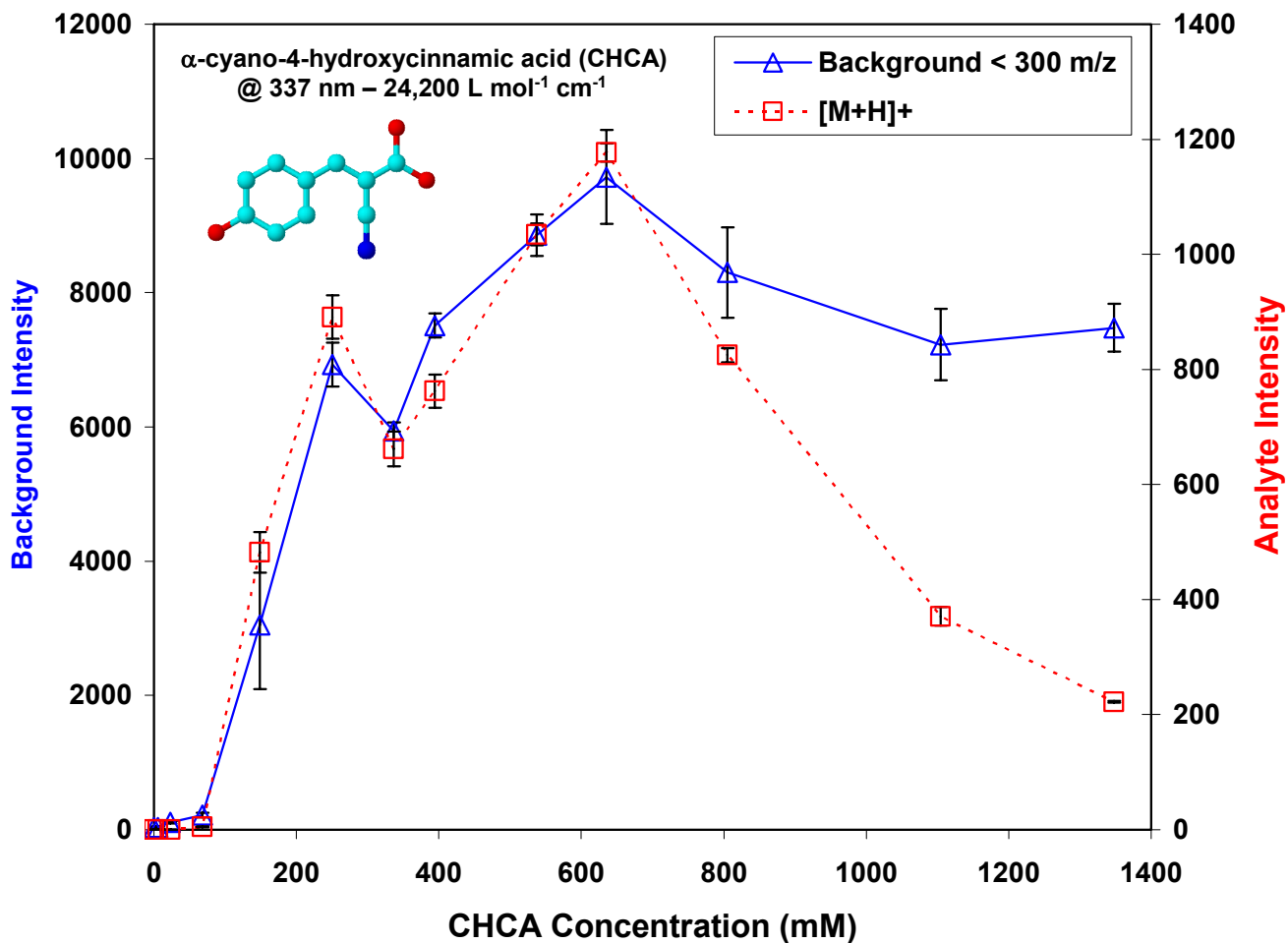


Figure 3-1. The plot shows analyte ion and matrix background intensity as a function of CHCA concentration in the liquid matrix. The matrix background is the total ion count for all species below  $m/z$  300. Fifty picomoles of angiotensin II was spotted on target to monitor analyte signal intensities. Chromophore concentration changes were done using one liquid matrix support, 50% aqueous ethanol mixed with an equal part DEA.

The Beer-Lambert law indicates that the laser intensity transmitted decays exponentially with distance and a constant related to absorber concentration.<sup>145</sup>

$$\frac{\Phi}{\Phi_0} = e^{-kb} \quad (3-1)$$

Where  $\Phi$  is incident laser flux,  $\Phi_0$  is transmitted laser flux,  $b$  is the distance from the solution surface to the measurement of the transmitted power, and  $k$  is dependent upon concentration and molar absorptivity ( $\epsilon$ ).

$$k = \frac{\epsilon c}{0.434} \quad (3-2)$$

Given a value of  $\epsilon = 24,200 \text{ L mol}^{-1} \text{ cm}^{-1}$  for CHCA, we can estimate the penetration of the laser into the optically thick solution.<sup>139</sup> Using the  $1/e$  definition of laser penetration depth, we obtain a distance of  $\sim 300 \text{ nm}$  for the  $630 \text{ mM}$  concentration. This concentration provided maximum analyte ion signal and was used in the studies presented below. The concentration range studied would suggest laser penetration depths from  $100 \text{ nm}$  to  $30 \text{ }\mu\text{m}$ .

The penetration depth may provide some rationale for the trend observed in Figure 3-1. As the chromophore concentration rises, the effective penetration volume of the laser is lowered, thus reducing the number of analyte molecules affected by each laser pulse. For a laser spot size of  $\sim 300 \text{ }\mu\text{m}$ , an estimate for the effective sample volume can be determined (saturation effects for the absorbers were not considered due to the low laser powers used). Using the  $630 \text{ mM}$  CHCA concentration, the laser penetration volume element is estimated at  $\sim 1.5 \times 10^4 \text{ }\mu\text{m}^3$ , within which there would be  $3 \times 10^{14}$  water molecules,  $2 \times 10^{13}$  ethanol molecules,  $2 \times 10^{13}$  DEA molecules, and  $3 \times 10^{12}$  CHCA molecules. Considering  $5 \text{ picomoles}$  of angiotensin II loaded on target, the volume element of the laser would contain  $\sim 75 \text{ attomoles}$  of analyte,  $4.5 \times 10^7$  angiotensin II molecules.

Figure 3-2 shows a mass spectrum collected using the  $630 \text{ mM}$  CHCA matrix with  $5 \text{ picomoles}$  of angiotensin II loaded on target. The major analyte peak is the  $[\text{M}+\text{H}]^+$ ,

with some sodium and potassium adducts also present in the spectrum. The insert, Figure 3-2A, is an expanded view of the protonated analyte peak showing a resolution of  $\sim 2500$ .

The analyte also forms an adduct with DEA,  $[M+DEA+H]^+$ , at  $m/z$  1152.5. The matrix background shows peaks for protonated DEA ( $m/z$  106) and the protonated DEA dimer ( $m/z$  211). Other unidentified peaks also reside below  $m/z$  300 at low intensity levels.

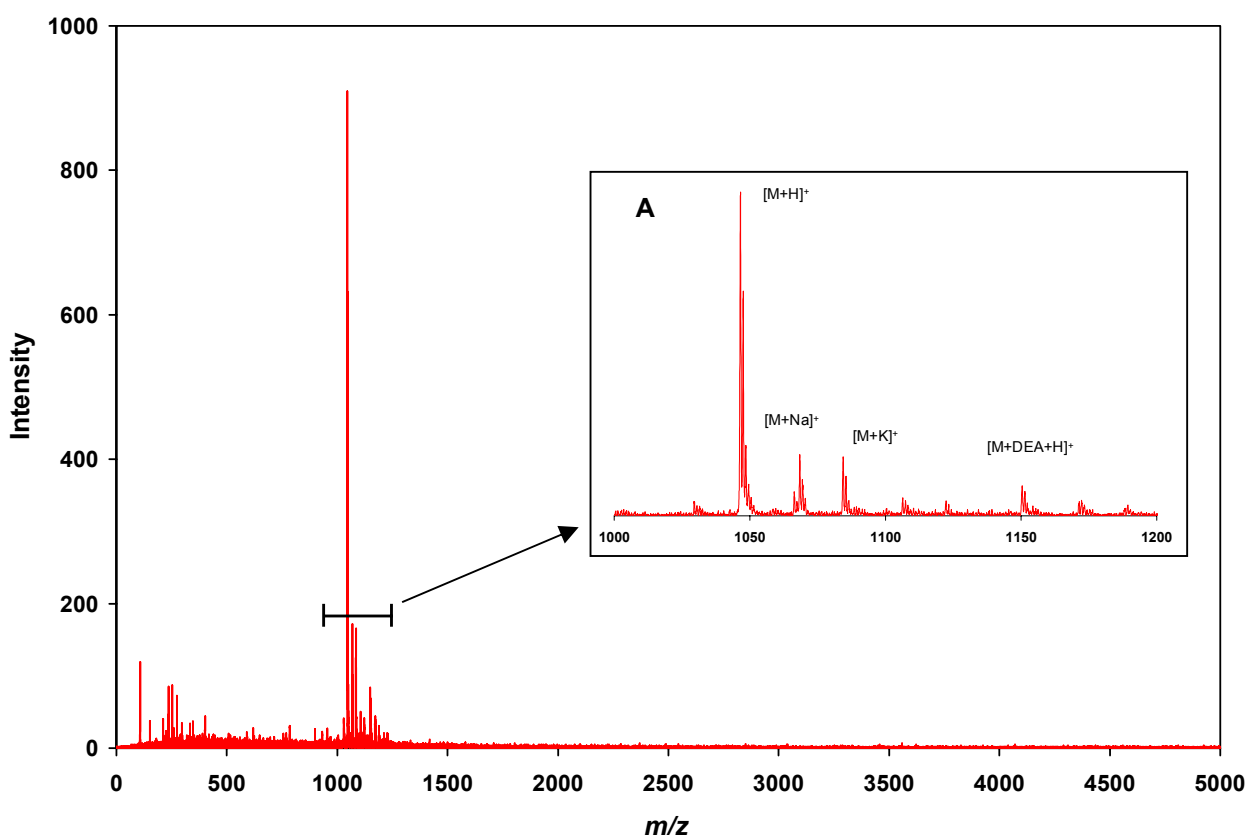


Figure 3-2. Mass spectrum of 5 picomoles of angiotensin II analyzed using an optimized CHCA liquid matrix. The spectrum is a 5 minute summation with the laser operating at 20 Hz. The liquid matrix contained 630 mM CHCA and a 50% aqueous ethanol solution mixed with an equal part DEA. Figure 3A is a scaled view of the analyte peak and adducts.

To further examine chromophore concentration adjustments, a different chromophore was incorporated into the matrix. Studying a second chromophore may

determine if the absorption required for desorption and ionization is independent of the absorber. Each MALDI chromophore has a unique absorption distribution as shown in Figure 3-3; however, all provide useful results when used with the proper analyte type and with the correct matrix-to-analyte ratio.

### UV absorption of Matrices

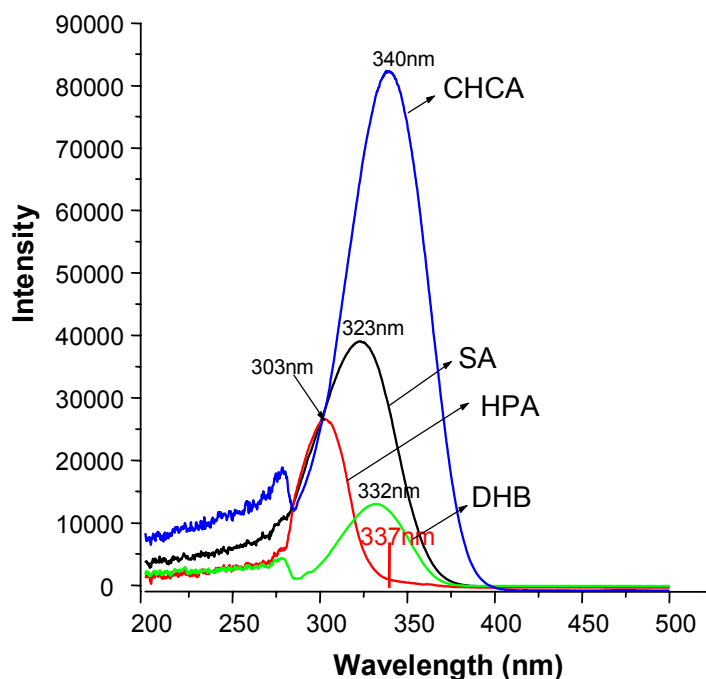


Figure 3-3. An illustration of the UV-Vis absorption spectra collected for common MALDI matrices is shown. Adapted from reference 147.

The MALDI chromophore 2,5-dihydroxybenzoic acid (DHB) is considered a general UV matrix useful for a variety of analyses. As a comparison to CHCA results, DHB concentration studies were conducted. Figure 3-4 shows the analyte ion signals (substance P  $m/z$  1347) versus DHB concentration.

With a lower molar absorptivity at 337 nm ( $3800 \text{ L mol}^{-1} \text{ cm}^{-1}$ ), higher concentrations of chromophore (DHB) were required for maximum analyte signals. Further increases in the DHB concentration could not be studied due to solubility

difficulties. A comparison of DHB to CHCA concentration at maximum analyte signals shows a ratio of ~6.8:1 (4300 mM/630 mM).

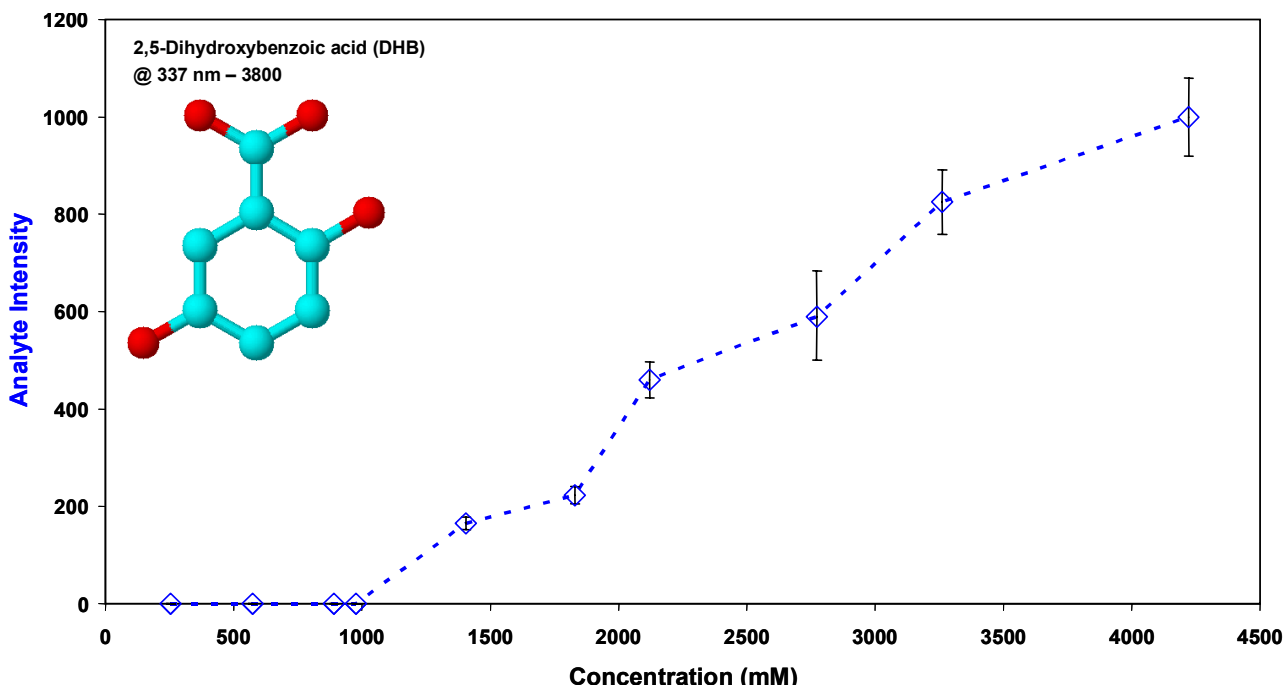


Figure 3-4. A plot of analyte ion intensity as a function of DHB concentration is shown. Fifty picomoles of substance P (Arg-Pro-Lys-Pro-Gln-Gln-Phe-Phe-Gly-Leu-Met) was deposited on target. Chromophore concentration changes were done using one liquid matrix support, 50% aqueous acetonitrile with an equal part glycerol.

This ratio is equivalent to the ratio of molar absorptivities 24,200/3,800 ~6.4:1. These results may point to an optimal value for absorption required to yield analytical results; however, studies including other matrices must be compared.

### Support Liquid Variations

The non-absorbing components in the liquid matrix are the solvent liquid and the viscous component.<sup>139</sup> DEA has been used as a viscous component to enable liquid analysis in vacuum MALDI; however, APMALDI allows liquid matrix volatility constraints to be reduced.<sup>139</sup> While the addition of DEA to a volatile solvent limits evaporation, enabling increased sample lifetimes, the ratio of viscous component to

solvent liquid requires investigation. Using the CHCA concentration that provided the largest analyte ion signal (~630mM), different ratios of solvent liquid to DEA were examined. The solvent liquid used was a 50% aqueous ethanol solution. As the viscous fraction, DEA, was decreased, the solvent liquid was increased to maintain a 1  $\mu$ L volume, with a fixed chromophore concentration.

Reducing the DEA fraction limits the liquid sample lifetime, and thereby the available time for sample analysis; however, the total viscosity of the liquid matrix also plays a role in analyte desorption. Increased viscosity represents strengthened intermolecular forces. In this case, more DEA in the mixture allows additional hydrogen bonding, thereby requiring more energy for desorption to occur. Desorbed molecules require additional energy to overcome the increased intermolecular forces, making desorption from the liquid phase more difficult. Figure 3-5 shows the analyte signal intensity as the percentage of DEA is increased in the liquid matrix.

Above 50% DEA, analyte signal intensities decrease as viscosity increases, but the signal lifetime is prolonged. The typical analytical lifetime for a 50% DEA liquid matrix during laser desorption is 30 minutes. While analysis can be completed in 1-5 minutes, increased lifetimes allow both source optimization and larger summation times for signal-to-noise enhancements. The 25% and 75% solutions provided signals for ~10 and ~60 minutes respectively. The 0% DEA mixture has a limited lifetime, < 1 minute, and provided low analyte signals with large variations. Also, without diethanolamine added to the matrix, the water and ethanol were not effective in solubilizing the CHCA, so the mixture was not homogeneous. The 100% DEA mixture was also a heterogeneous mixture due to the difficulty in mixing such a viscous solution.

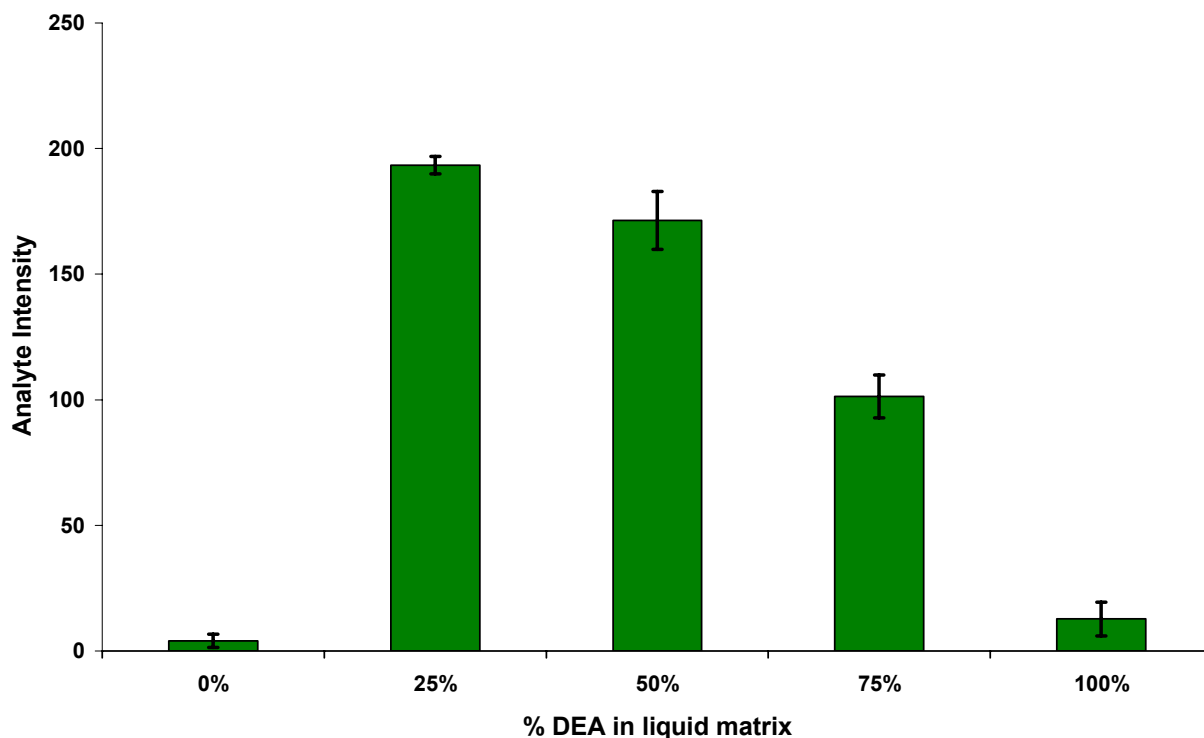


Figure 3-5. A chart of analyte intensity versus the percentage of DEA in the liquid matrix is shown. The signals represent 1 minute summed mass spectrometry signals. Five picomoles of angiotensin II was placed on target for analysis.

From measured sample lifetimes, liquid removal rates can be estimated. For the 50% DEA mixture, ~14 picoliters per laser pulse is estimated based on the amount of liquid spotted (1  $\mu\text{L}$ ) and the amount remaining after analysis (~0.5  $\mu\text{L}$ ). Analyte removal rates can be determined using the analyte signal lifetime and the amount loaded. A 5 picomole sample lasts ~36,000 laser shots, yielding a single pulse analyte removal rate in the attomole range. While removal rates are influenced by liquid matrix composition, the summation of analyte signals for longer periods allows enhancements of signal-to-noise.<sup>148</sup>

Composition of the solvent liquid is also important for the liquid matrix. To determine the effect that solvents have on analyte signal intensities, we examined

common solvents. Figure 3-6 demonstrates the effect solvent variations have on analyte ion signal using a 50% DEA liquid matrix.

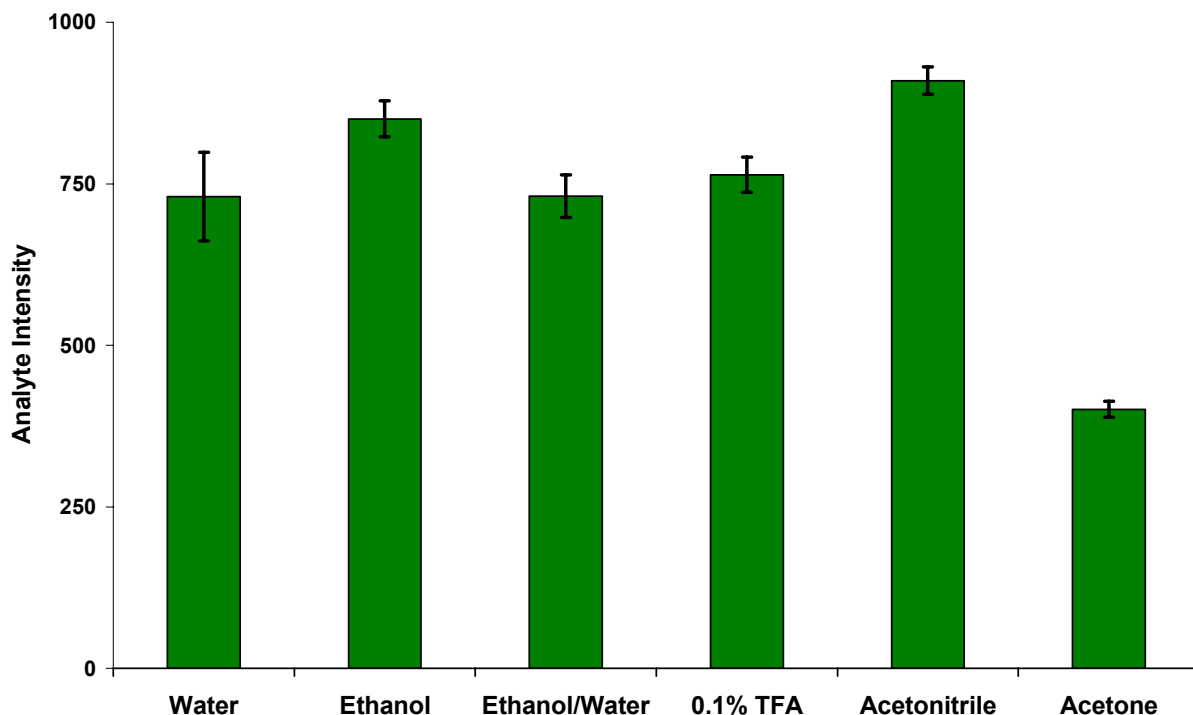


Figure 3-6. A chart of analyte intensity versus solvent liquid used in the liquid matrix. Each column is the solvent added to a 50% DEA mixture. The signals represent 1 minute summed mass spectrometry signals. Fifty picomoles of angiotensin II was placed on target for analysis.

The CHCA concentration was kept constant at ~630 mM. The analyte signals for the solvent studied provided consistency in intensity and reproducibility. Spectral backgrounds for the solvents were also comparable.

While a limited variety of solvents was tested with the liquid matrix, the results demonstrate a flexible range over which the matrix can provide useful results. A select solvent may be necessary for specific analyte solubility. Also, considering typical reverse phase liquid chromatography (LC) solvents, alternative matrix solvents could prove useful for online LC/APMALDI.

### Solids versus Liquid Matrices

For liquid matrices to be useful in analytical analysis they must provide analyte signals comparable to solid matrices. To examine the comparison, a study was conducted using the dried-droplet solid matrix preparation and the optimized liquid matrix preparation.<sup>37</sup> For the solid matrix analysis 1 mL of 50% ACN in 0.05% TFA solution was mixed with 10 mg of CHCA matrix. Next, 10  $\mu$ L of analyte sample was mixed with an equal volume of matrix solution. One microliter of the mixture was spotted onto the target and allowed to dry for 20 minutes. Bradykinin fragment 1-7 ( $m/z$  757.4), human angiotensin II ( $m/z$  1046.5), human Adrenocorticotropin (ACTH) fragment 18-39 ( $m/z$  2465.2), and synthetic peptide P<sub>14</sub>R ( $m/z$  1533.8) were dissolved in aqueous 0.1% TFA (Sigma-Aldrich Corp., St. Louis, MO, USA). The same peptide solutions were used for liquid matrix analysis. The liquid matrix consisted of 630 mM concentration of CHCA with a support liquid of 50% DEA and 50% aqueous ethanol. The deposited liquid matrix consisted of 0.5  $\mu$ L of matrix solution placed on top of 0.5  $\mu$ L of analyte solution to ensure mixing. For both solid and liquid analysis, total peptide placed on target was 25 picomoles.

Figures 3-7 to 3-10 show MALDI mass spectra for peptide analytes using either solid and liquid matrix preparations. All mass spectrometer and source conditions were kept constant. Figures 3-7 and 3-8 show bradykinin fragment 1-7 and angiotensin II analyzed with both solid and liquid matrices.

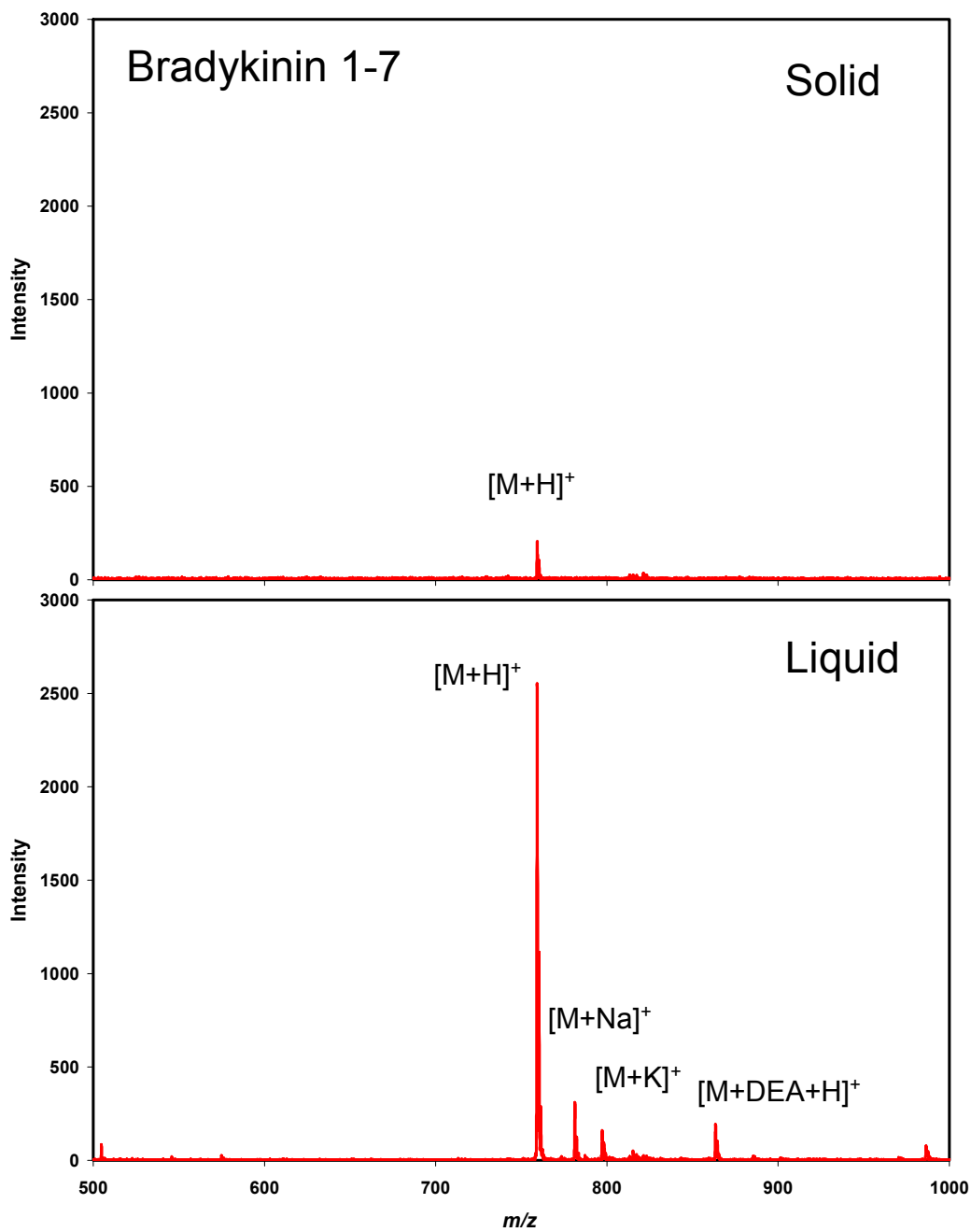


Figure 3-7. Mass spectra of bradykinin fragment 1-7 comparing solid and liquid matrix preparations. Twenty-five picomoles of analyte was deposited on target, and each spectrum was the summation of 100 individual spectra.

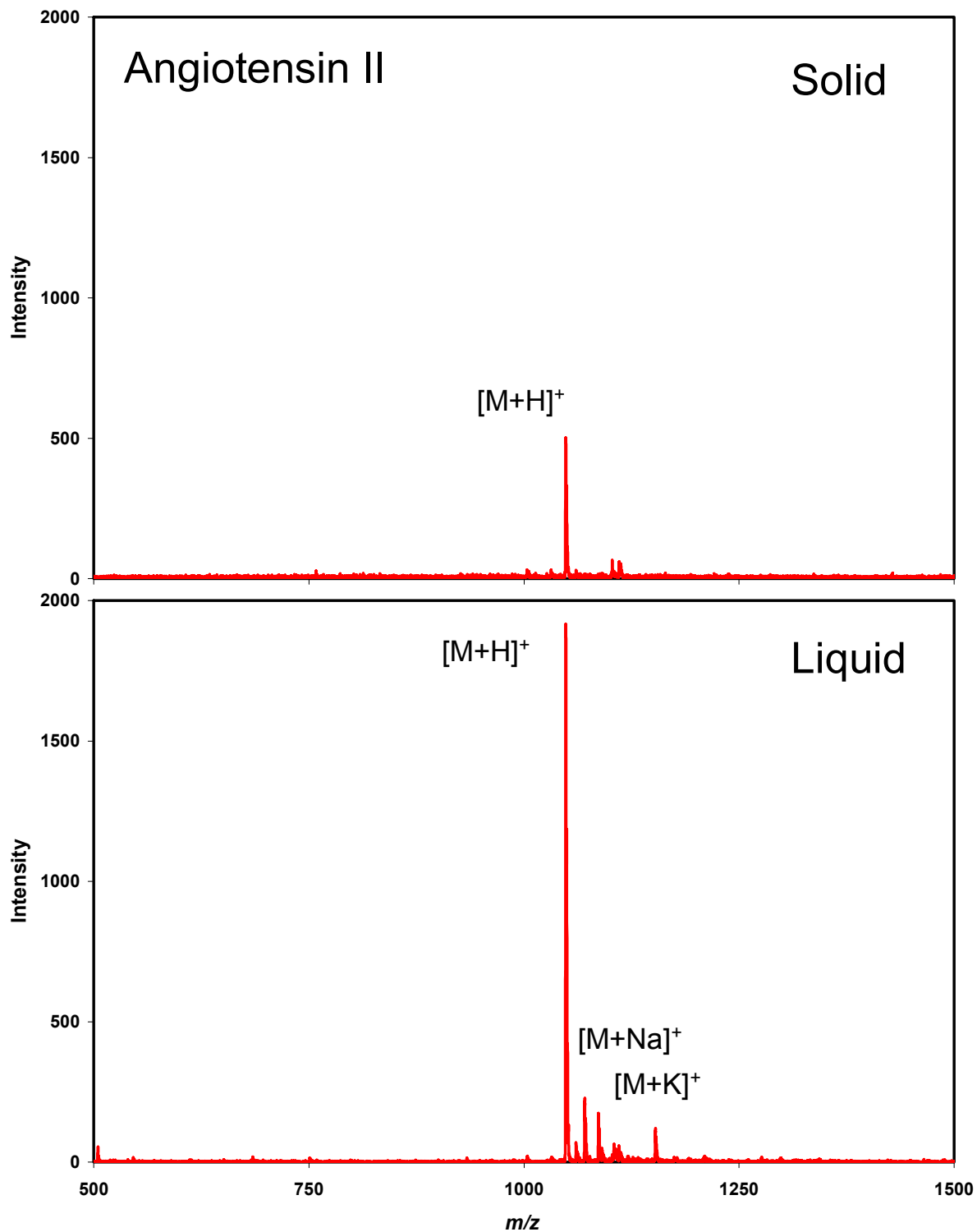


Figure 3-8. Mass spectra of angiotensin I comparing solid and liquid matrix preparations. Twenty-five picomoles of analyte was deposited on target, and each spectrum was the summation of 100 individual spectra.

In both Figures 3-7 and 3-8, the protonated molecule signals can be seen in the solid and liquid matrix formulations. The liquid matrix differs in signal intensity and adduct formation. Though the liquid matrix presents larger  $[M+H]^+$  signals, no fluence adjustments were made to optimize solid matrix analysis; therefore, conclusions cannot be drawn on the limits of detection of liquid versus solid matrices. However, what can be considered in Figures 3-7 and 3-8 is the appearance of alkali metal and DEA adducts. While DEA is not available in the solid matrix formulation, sodium and potassium are present. The formation of adducts is a known phenomenon for APMALDI.<sup>114</sup> Adducts in the liquid matrix suggest a softer desorption/ionization event. Collisional cooling at AP is thought to provide the stabilization for adducts to remain intact. Softer ionization modes can provide benefits when examining non-covalent interactions or analyzing fragile compounds (*e.g.*, deoxyribonucleic acids). Additionally, instrumental and sample preparation methods are available to reduce analyte adducts (*e.g.*, ultra-clean targets, high-grade reagents, larger declustering voltages between nozzle and skimmer).

Figure 3-9 shows ACTH fragment 18-39 analyzed with both solid and liquid matrices. In Figure 3-9 no analyte signal differences were present between the solid and liquid matrix preparations. Also, CHCA cluster formation is seen with both the solid and liquid matrices.

Figure 3-10 shows P<sub>14</sub>R analyzed with both solid and liquid matrices.

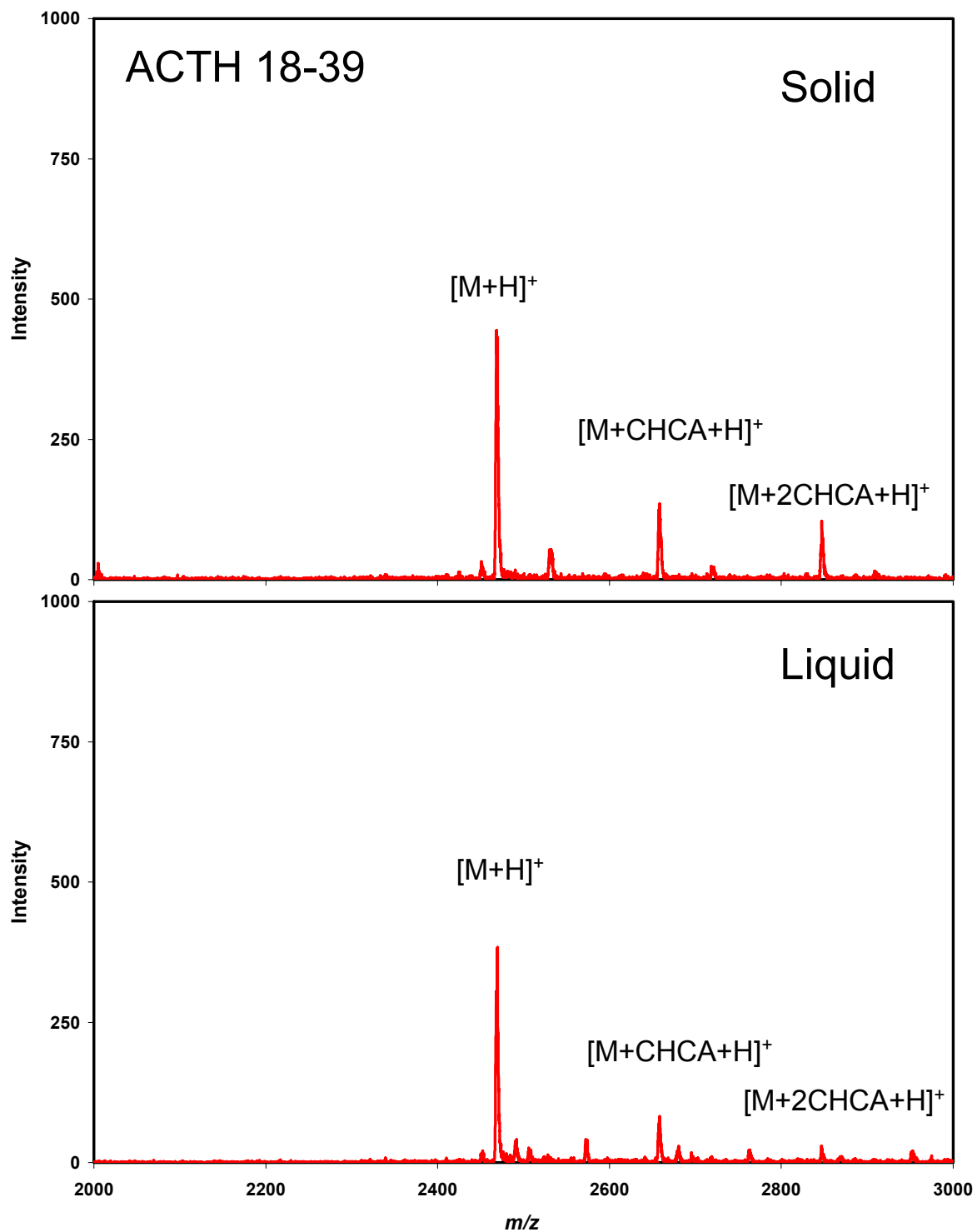


Figure 3-9. Mass spectra of ACTH fragment 18-39 comparing solid and liquid matrix preparations. Twenty-five picomoles of analyte was deposited on target, and each spectrum was the summation of 100 individual spectra.

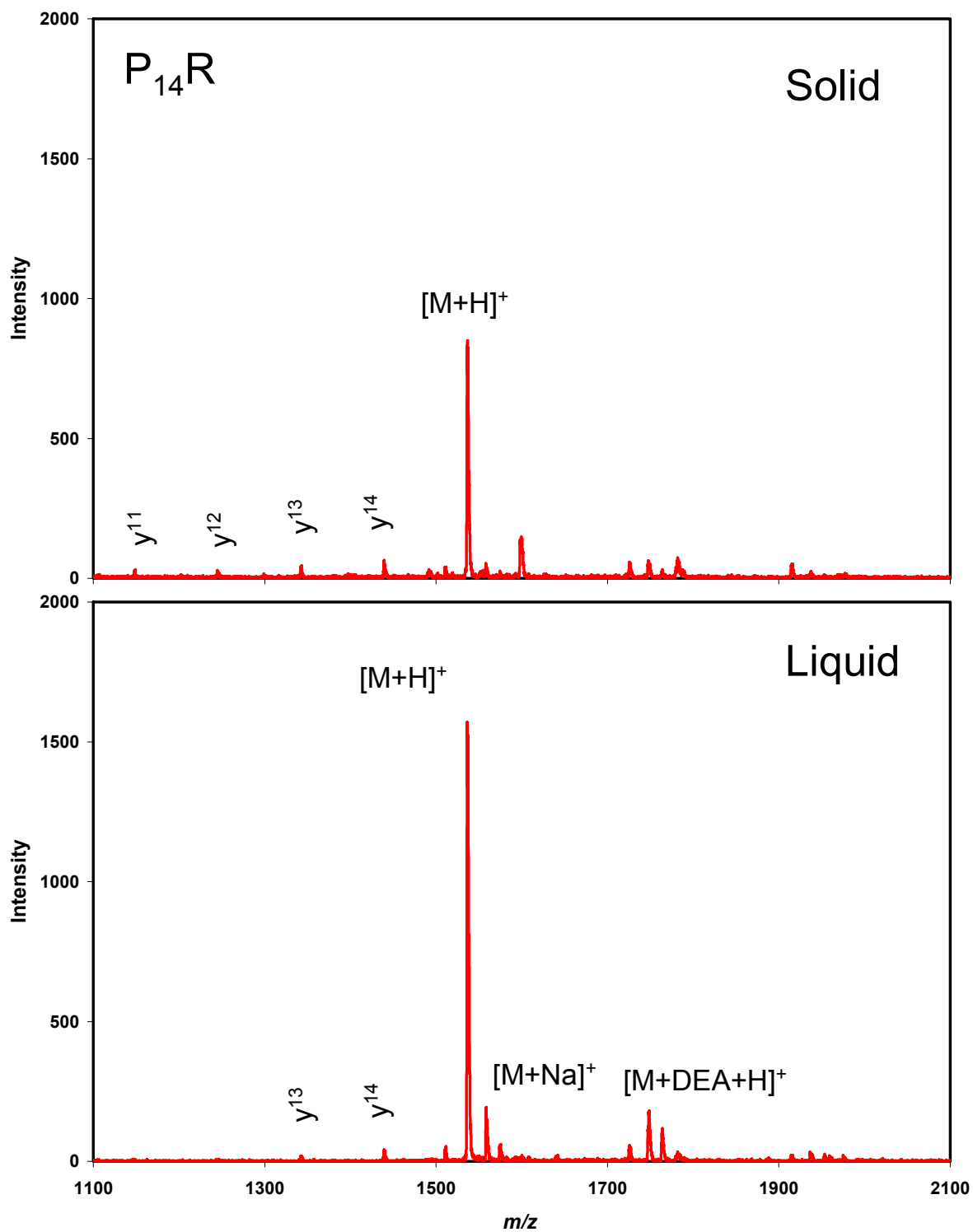


Figure 3-10. Mass spectra of  $P_{14}R$  comparing solid and liquid matrix preparations. Twenty-five picomoles of analyte was deposited on target, and each spectrum was the summation of 100 individual spectra.

For the synthetic peptide, fragmentation is known to occur under mild conditions.<sup>149</sup> Both matrix formulations show y series ions. This ion series is the c-terminal ion series formed during fragmentation of the peptide, so it contains the c-terminal and extensions from this residue (*i.e.*, y14 represents PPPPPPPPPPPPPR). While different matrix chromophores have shown more or less fragmentation, it appears that the liquid formulation has fewer fragments present, again indicating a softer mechanism for desorption and ionization.<sup>150</sup>

### **Quantitation**

The liquid matrix acts as a homogeneous sampling environment for desorption and ionization, thus offering opportunity for quantitative analysis. To evaluate the reproducibility of liquid sampling, intra and inter-sampling precision was determined. With a liquid matrix sample lasting tens of minutes, ten 1 minute summed spectra could be compared. Inter-sampling precision was calculated to be ~10-13% RSD, with intra-sampling precision at ~5-7% RSD.

Quantitation capabilities, without an internal standard, were examined by producing calibration curves for angiotensin II and bradykinin fragment 1-7. Figure 3-11 shows the calibration curve obtained for angiotensin II using a liquid matrix. The curve was obtained by analyzing serial dilutions of a standard peptide mixture, with the volume of analyte placed on target maintained at 0.5  $\mu$ L. For Figure 3-11, each point represents a one minute sum with standard deviations obtained from five analyses. The inset shows a scaled section of the curve for the femtomole to low picomole range. While the  $R^2$  values demonstrate the ability for direct quantitation, the dynamic range for MALDI becomes apparent when viewing both ranges in Figure 3-11. For this reason, two analytical functions are presented, one for each range.

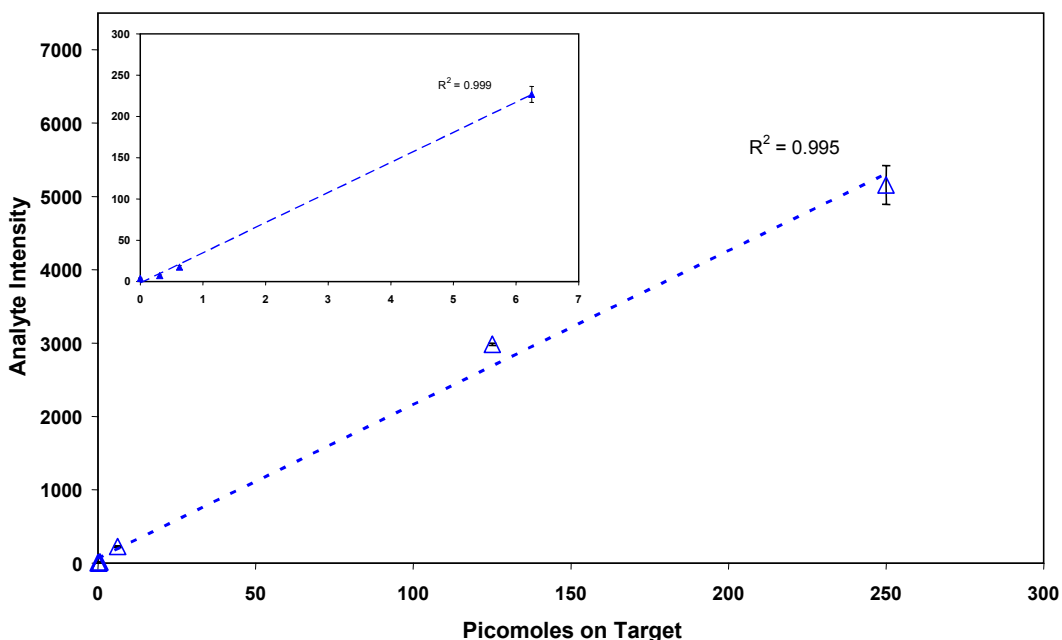


Figure 3-11. A calibration curve for angiotensin II. The calibration curves obtained include calculated  $R^2$  values for each analyte range. The inset shows a scaled view of the full range.

Figure 3-12 shows a similar calibration curve for bradykinin fragment 1-7. For the bradykinin fragment 1-7 calibration curve, a smaller range was examined using reduced amounts of peptide placed on target.

The current open design of the ion source may prevent further reductions in the limit of detection (LOD) values. An enclosed source minimizes water vapor contributions, assists cluster prevention, and increases analyte signals. Our source uses a nitrogen counter-current gas for cluster prevention. Typically used with ESI, the use of a nitrogen current gas with APMALDI has been more limited. Recently, Miller and Perkins described a counter-current gas ( $5 \text{ L} \cdot \text{min}^{-1}$  of nitrogen gas at a temperature of  $300^\circ\text{C}$ ) for an enclosed APMALDI ion source coupled to an ion trap mass spectrometer that yielded detection limits of  $\sim 125$  attomoles.<sup>115</sup>

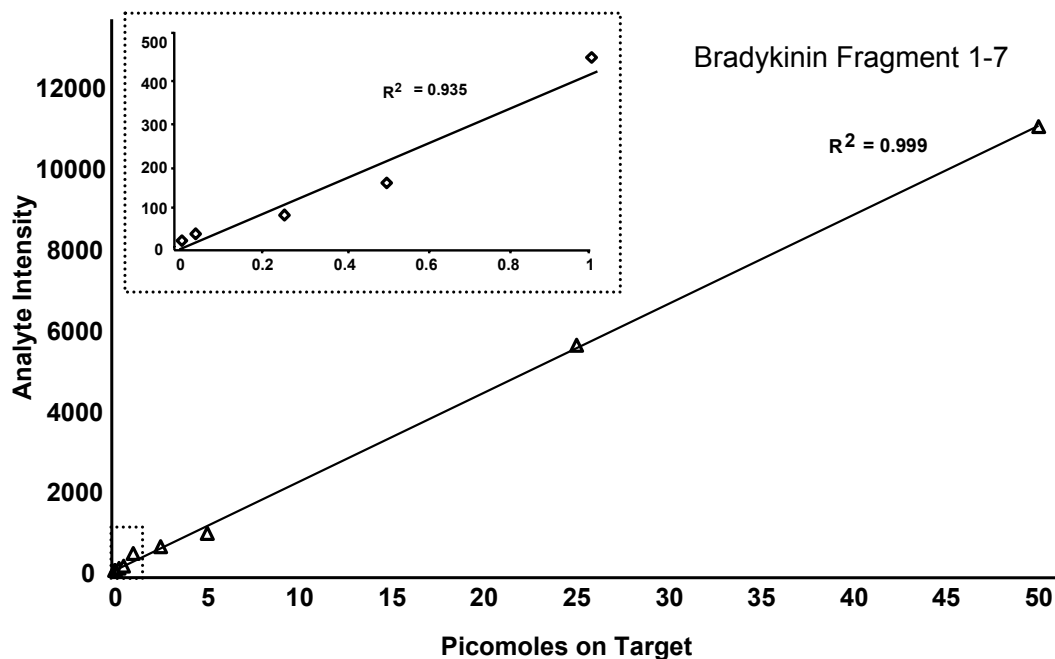


Figure 3-12. A calibration curve for bradykinin fragment 1-7. The calibration curves obtained include calculated  $R^2$  values for each analyte range. The inset shows a scaled view of the full range.

Declustering was determined to be the largest contributor for detection limit enhancements. Thus, by enclosing the source in a nitrogen purged environment, additional declustering could increase analyte signals.

The detection limits shown for both calibration curves are not to the levels possible using vacuum MALDI. Ion collection and transmission is most likely the limiting factor, not the liquid matrices. All values were obtained on a laboratory built ion source. Decreased LODs may be possible with increased summation times, further source optimization, and an appropriate enclosure (to control the ion transfer environment).

### Mixture Analysis

To demonstrate the liquid matrix's utility for peptide analysis, a mixture of standard peptides was examined as a test sample. Figure 3-13 depicts a one minute

summed mass spectrum for a mixture of bradykinin fragment 1-7, angiotensin II, ACTH fragment 18-39, and insulin oxidized B chain (2 picomoles each).

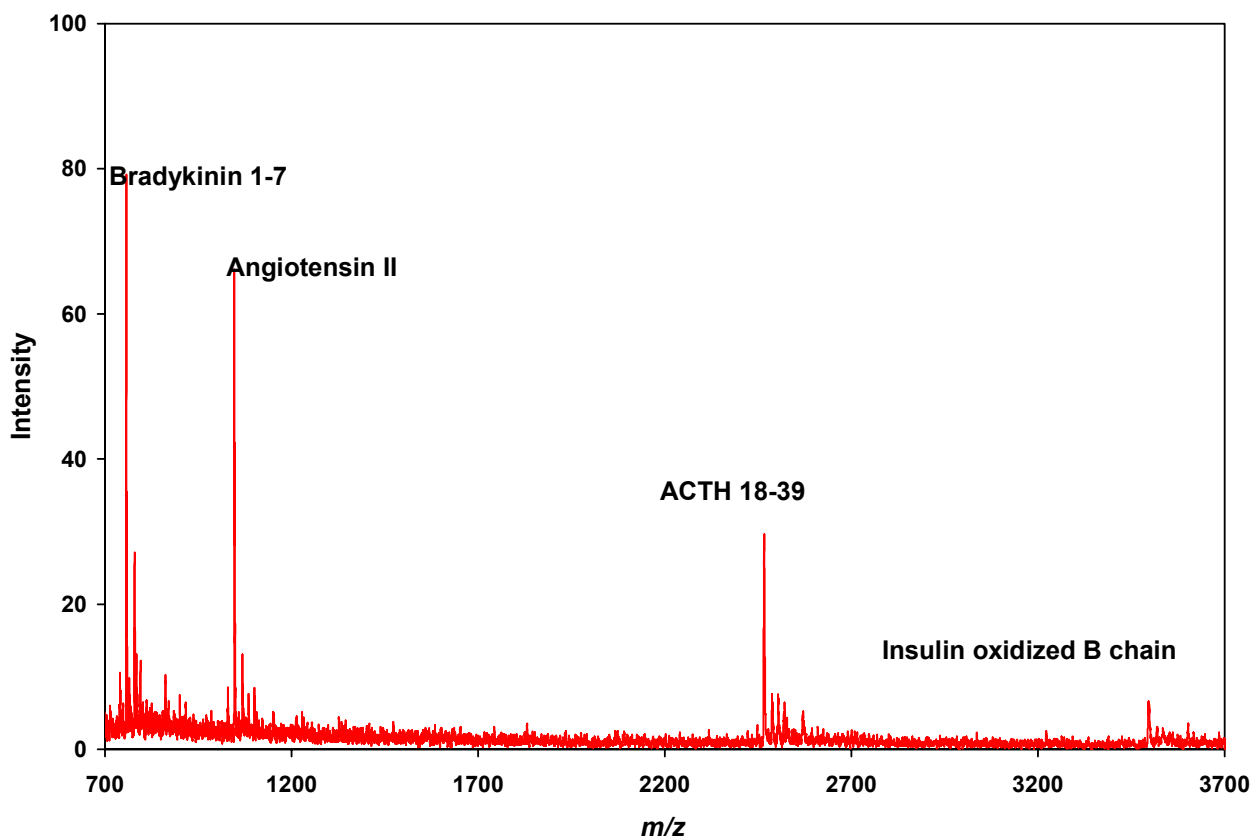


Figure 3-13. A mass spectrum for a peptide mixture using the CHCA liquid matrix. The mixture contained angiotensin II, bradykinin fragment 1-7, ACTH fragment 19-39, and insulin oxidized B chain. Two picomoles of each peptide were mixed and placed on target.

The decay of signal intensity with increasing mass shown in Figure 3-13 is reproducible, but somewhat puzzling. There is some indication that the input quadrupole may be one of the factors affecting this response. The mass range examined was based on the available instrumentation and is not believed to be a liquid matrix limitation. An alternate RF power supply as well as pressure variations in the quadrupole region may assist in increasing the mass range.

## Conclusions

The liquid matrix provides a homogenous sample allowing easy sample preparation, increased sample lifetime, and added utility for an atmospheric pressure matrix-assisted laser desorption/ionization source. With the use of a typical MALDI chromophore,  $\alpha$ -cyano-4-hydroxycinnaminic acid, the matrix provides the known properties of an organic absorbing matrix with the added benefits of a liquid sampling system. Chromophore concentration adjustments provided insight into the necessary absorbance for UV APMALDI and demonstrated the importance of laser penetration depth in MALDI liquid sampling. Liquid support variations allowed adjustments of sample lifetime and analyte solvents. The sample lifetime is beneficial for instrument tuning and source optimization; however, too high a liquid viscosity lowers signal intensity. Quantitation without the use of internal standards may be possible with a liquid matrix. Reproducibility suggests that the liquid matrix can alleviate some inconsistencies seen with solid sample MALDI. The liquid system also provides a convenient avenue for fundamental studies of desorption. The measurements for laser penetration depth, solution viscosity, and solvent additives could add to the information on MALDI mechanisms. While the liquid matrix provides immediate benefits for APMALDI analysis with its ease of use, additional possibilities include an on-line liquid UV APMALDI ion source for chromatography or reaction monitoring.

## CHAPTER 4 LASER DESORPTION CONSIDERATIONS USING LIQUID MATRICES AT ATMOSPHERIC PRESSURE

### **Introduction**

The production of analyte ion signals using matrix-assisted laser desorption/ionization (MALDI) can be affected by both sample preparation and matrix formulation.<sup>151</sup> Detection of the ions is determined by interface and mass spectrometer settings—allowing for increased ion transmission. While instrument and sample/matrix parameters provide some insight into MALDI processes, the underlying mechanisms are still elusive.<sup>43</sup> Parametric studies present the standard method for adding mechanistic information. For example, investigating the laser-sample interactions provides detailed information on photon absorption characteristics and yields an experimental basis for future applications. Most studies are concerned with the relationships between ion yield and laser fluence.<sup>152-153</sup> Ejected particles have also been a focus in deciphering how the desorption process affects ion formation.<sup>154</sup>

Traditional laser modifications have included alterations in absorption wavelength, pulse duration, and input fluence. Studies on wavelength dependence have shown that the matrix absorption directly relates to the wavelength used.<sup>45</sup> While cases exist for using laser wavelengths outside of the matrices' major absorption bands, most studies reveal absorption-excitation dependence.<sup>155</sup>

Short pulse width lasers (*e.g.*, UV ~4 ns and IR ~6-200 ns) provide ion generation without thermal degradation of the analyte. Longer irradiation causes heating of the bulk material and extensive fragmentation.<sup>156</sup> However, IR systems have shown that decreased pulse widths can reduce photon flux thresholds for ion detection.<sup>157</sup>

Fluence is defined as energy input per unit area; in MALDI typical fluences are in the range of 100-1000 J·m<sup>-2</sup>.<sup>45</sup> Irradiance is fluence divided by the laser pulse duration; MALDI irradiances are in the range of 10<sup>6</sup>-10<sup>7</sup> W·cm<sup>-2</sup>.<sup>45</sup> While MALDI shows some irradiance dependence, it is the fluence values that have direct relationships to analyte ion yields. When fluence is below a threshold level no ion production is observed. These threshold values are a key factor for understanding underlying mechanisms.<sup>44</sup> Fluence values can be used to estimate the number of excited matrix molecules, which are necessary for further ion-molecule reactions. Fluence values depend on the matrix and analyte in the sample. However, the values can also vary with source pressure. Higher pressures have been noted to require higher fluence values.<sup>43,157</sup> A recent study using APMALDI provided fluence values through the focusing and defocusing of the laser beam onto the target. In this mode, spot size adjustments were made versus pulse energy.<sup>157</sup>

Under vacuum conditions, spot size variations (with the corresponding pulse energy changes, keeping fluence constant) have drastically altered the measured fluence ranges.<sup>57</sup> The variations are considered to be due to the inconsistencies in reporting laser spot sizes.<sup>45</sup>

Large-scale molecular dynamics (MD) simulation studies have provided valuable data to close the gap between the experimental results and theoretical considerations.<sup>45</sup>

The MD simulations show how laser ablation from organic solids can be characterized into two mechanisms for molecular ejection defined by fluence threshold values. Below the threshold, mainly singly charged molecules are desorbed from the surface. Above the threshold, the ablation processes become important and larger molecular clusters are introduced into the MALDI.<sup>57,152,158</sup> The measurements of fluence dependent ion yields may focus on the interactions of the two theoretically proposed pathways.

The studies presented in this chapter focus on the laser-sample interactions at atmospheric pressure using a volatile liquid matrix. By using a UV laser, variations in frequency and pulse energy can be related to ion yields. The homogeneity of the sample was also examined through single laser shot measurements. Pulse energy variations allowed a detailed examination of fluence dependence on analyte ion yields. Additionally, the examination of particle ejections from the matrix at higher fluences helped explain ion signal reductions. These measurements may prove useful for determining mechanistic pathways.

## **Background**

While the ionization processes involved in MALDI are complex and still largely undetermined, much more is understood about the desorption phase. In MALDI desorption, a plume is formed comparable to a pulsed jet expansion. Theoretical simulations describe the UV MALDI plume as an explosive solid-to-gas phase transition. Ion emission is observed within nanoseconds of the laser pulse, while neutral desorption can occur microseconds after.<sup>158</sup> Matrix ion velocities in the plume of a solid matrix MALDI analysis can reach up to  $1000 \text{ m}\cdot\text{s}^{-1}$ , depending upon matrix preparation and composition. Analyte ions are generally  $100\text{-}200 \text{ m}\cdot\text{s}^{-1}$  slower.<sup>159</sup>

The mechanistic view of the MALDI plume is that primary ions are created in a hot, dense bath of neutral matrix molecules and clusters, and undergo collisions before being extracted into the mass spectrometer. Thus, secondary ion-molecule reactions are expected.<sup>46</sup> The final ions observed in MALDI mass spectra can be a result of the primary ions formed; therefore, a major goal of matrix design must be to improve the number of primary ions created while limiting the fraction of large clusters and chunks.<sup>46</sup>

During desorption, single molecules, clusters, and aggregates of matrix are ejected. The fraction of free molecules and small clusters is considered greatest at low fluence, yet the absolute ion yield is greatest at higher fluence.<sup>43,45</sup> Optimizing laser fluence may minimize the amount of large clusters produced and maximize the ion production.

## **Experimental Methods**

### **Atmospheric Pressure MALDI oa-TOFMS**

The orthogonal-acceleration time-of-flight mass spectrometer (oa-TOF) used in this research was previously described in Chapter 2. Briefly, the APMALDI source used a 337 nm nitrogen laser (VSL-337-ND-S, Spectra-Physics, Mountain View, CA, USA) for desorption - pulse width ~4 ns. The laser was operated asynchronous with the TOF acquisition pulse at 5 kHz. Pulse energies ranged from ~5-180  $\mu$ J, measured directly using a pyroelectric detector (J4-09-030, Molectron Detector, Inc., Santa Clara, CA, USA). Variations in the energy transmitted to the sample came from a gradient UV attenuating wheel (Reynard Corporation, San Clemente, CA, USA). Laser repetition rates were monitored using an oscilloscope (TDS 210, Tektronics, Beaverton, OR, USA).

Target positioning was accomplished using a piezoelectric transducer driven *xyz* stage (8302/IPico Driver, New Focus, San Jose, CA, USA). The atmospheric pressure

interface used a heated counter-current nitrogen gas ( $100^{\circ}\text{C}$ ,  $5\text{ L}\cdot\text{min}^{-1}$ ) for cluster prevention. The ion transport field between the target and nozzle was  $1100\text{ V}\cdot\text{mm}^{-1}$ . Gas pressures in the skimmer and RF-only quadrupole were 3 Torr and  $10^{-1}$  Torr respectively.

Video monitoring of the matrix deposited on the target was done using a charged-coupled device (CCD) (Sensicam, IPentamax III, Roper Scientific, Trenton, NJ, USA) fitted with an adjustable lens. Images were acquired using the manufacturer's software (Tillvision, Roper Scientific, Trenton, NJ, USA). The spectra shown are an accumulation of summed spectra for 1-5 minutes.

### **Fluorescence Measurements**

The emission profile for CHCA in solution was taken using a plate reader (TECAN Safire, Research Triangle Park, NC, USA) in fluorescence mode. Excitation was 337 nm with 5 nm scan increments from 400 to 700 nm to produce the spectrum. An integration time of  $40\mu\text{s}$  was used for each increment.

Imaging of the ejected CHCA particles was conducted on an inverted microscope, 100X magnification (Olympus, Melville, NY, USA), using an intensified CCD (Sensicam, IPentamax III, Roper Scientific, Trenton, NJ, USA). A 460 nm bandpass filter was used to select matrix emission. Integration time was set at 50 ms.

### **Matrix and Analytes**

Liquid matrices were prepared by mixing  $\alpha$ -cyano-4-hydroxycinnamic acid (CHCA) with a liquid support. The liquid support was equal parts of 50% aqueous ethanol and diethanolamine (DEA). Chromophore concentration, CHCA, was 600 mM. To ensure homogeneity and dissolution, the matrix solution was sonicated for 10-15 minutes. Immediately before analysis the matrix was vortexed for 10 seconds. For each

analysis, 0.5  $\mu\text{L}$  analyte solution and 0.5  $\mu\text{L}$  matrix solution were deposited on target, and in the order presented.

For direct analysis, analytes were prepared in aqueous 0.1% TFA. Stock solutions of analyte were prepared at 50  $\text{pmol}\cdot\mu\text{L}^{-1}$ , and diluted as noted. All analytes (angiotensin II, bradykinin fragment 1-7, bradykinin, reserpine, and spiperone), matrix, and solvents were used unpurified (Sigma Aldrich, St. Louis, MO, USA).

## Results and Discussion

### Liquid Matrix Homogeneity

Ion yield inconsistencies in solid matrix MALDI analysis are due to irreproducible sample deposition and laser shot-to-shot variations.<sup>152</sup> A liquid sample is homogeneous and provides a reproducible deposition onto the target. While shot-to-shot variations exist with all laser systems, the nitrogen UV laser has only a  $\sim 3.5\%$  standard deviation in pulse energy (VSL-337-ND-S, Spectra-Physics, Mountain View, CA, USA). The inherent laser variations do not account for the large deviations in analyte ion signals seen with solid matrix MALDI. Instead, the signal fluctuations can be explained by considering the irregularities in crystal formation. Some crystals exhibit the optimal ratio of analyte and matrix, thus forming a “sweet spot” for the laser to desorb and ionize analytes. Other crystals may not incorporate analyte—preventing any ion signals.

Adding to the irreproducibility of the analyte ion signals, MALDI spectra, in terms of maximum resolution and minimum ion fragmentation, are best obtained slightly above the ion threshold fluence.<sup>152</sup> Unfortunately, the maximum ion yields are not obtained until higher fluence is used. Thus, single shot spectra taken at low fluence show low signal intensities and poor reproducibility.

To evaluate the liquid matrix shot-to-shot reproducibility, sequential laser pulses were analyzed for ion signal variations. Figure 4-1 shows five individual laser shots and the corresponding ion signals (using a liquid matrix). Important in the figure is that each shot produces analyte ions and that successive laser shots are reproducible.

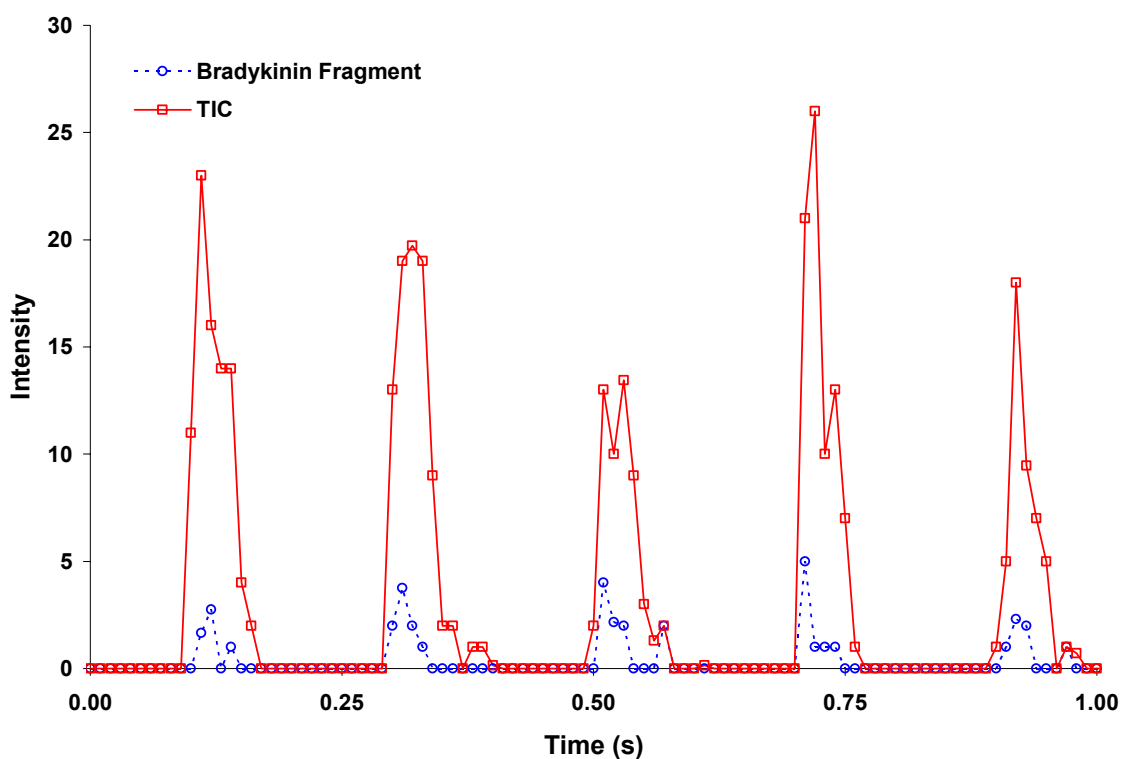


Figure 4-1. A plot showing individual ion packets resulting from liquid matrix analysis. The laser was operated at 5 Hz with the mass spectrometer data system collecting spectra at a rate of 100 Hz. The asynchronous timings of the laser and the pulser allow for temporal profiles of each ion packet to be obtained.

To allow for the detection of individual laser pulses, the TOF data system was set at a rate of 100 spectra per second. With the laser pulsing at 5 Hz, time profiles for the ion packets were sampled. Ion-molecule collisions at increased pressure spread the initial ion plume to a larger time width, resulting in an ion packet width  $\sim 100$  ms.<sup>102</sup> Figure 4-1

also shows a slight temporal discrimination of the background (total ion counts) from the analyte ions (bradykinin). The background ions were present after the analyte ion signal diminished. The ion profile data suggests that signal-to-noise ratios could be increased by temporally gating the detection system, allowing for less background collection between laser pulses. Alteration of the data system, for this purpose, could not be accomplished without software modifications, which were unavailable from the instrument manufacturer.

By using the liquid matrix, each laser pulse is able to interact with a “fresh” surface. A video of the liquid on the target, Object 4-1, shows surface regeneration with each pulse.

[Object 4-1. A video file of the laser irradiating the liquid sample is provided. \(1.3 mb, Liquidregeneration.mpg, 50 seconds\).](#)

### **Laser Frequency**

Laser frequency may alter the interactions the laser has with the liquid surface. While higher repetition rates introduce more ion packets, it may hinder the surface regeneration process. Instead, as the laser frequency was increased, signal variations were reduced as analyte ion signals were enhanced. As laser pulses occur closer together, ion packets began to overlap. The high pressure collisions spread each of the packets to approximately the same width, so the ion signals were combined in a dense ion beam. A quasi-continuous beam was created allowing for increased analyte ion signals using a fixed sampling rate. Figure 4-2 shows analyte ion intensity as a function of laser frequency.

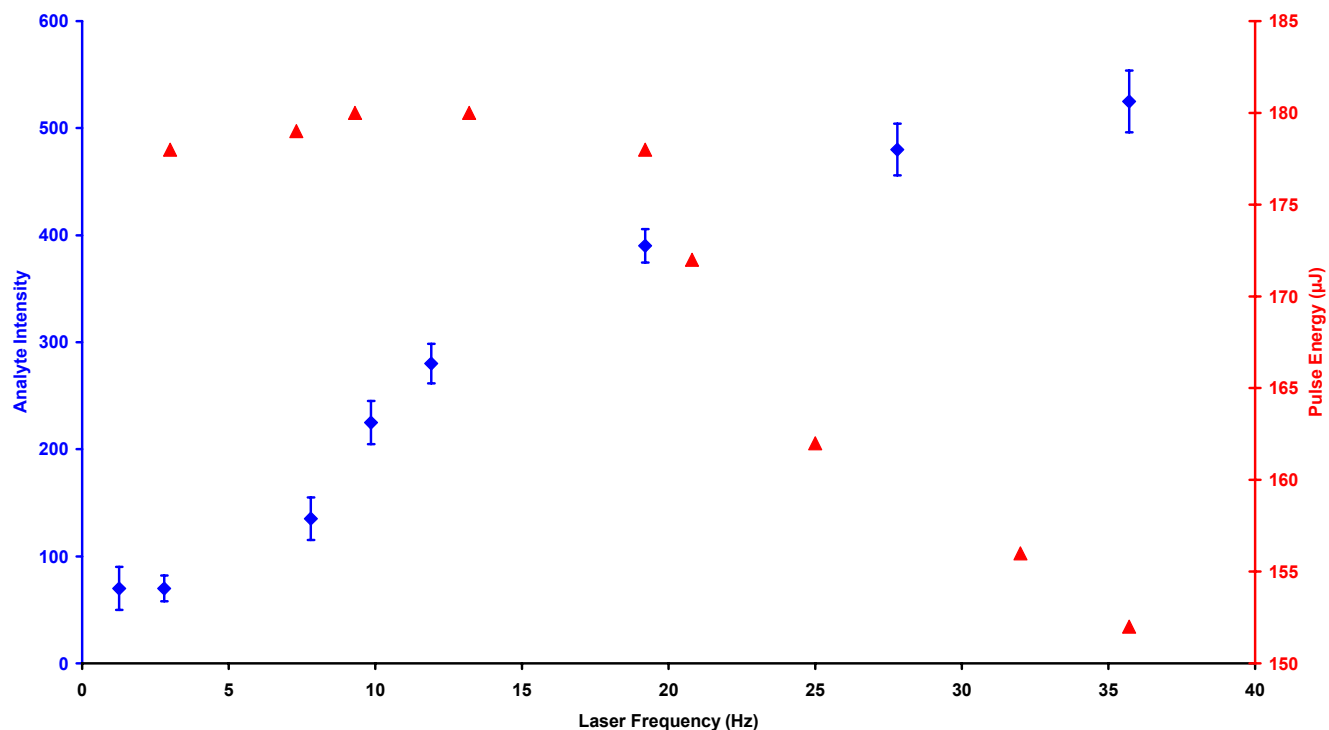


Figure 4-2. A plot of analyte ion signals and pulse energy as a function of laser frequency. The pulser and the laser were operated asynchronously. Deviations from linearity for the ion signals occurred as pulse energies decreased at higher laser frequencies. Pulse energies were direct measurements taken before the attenuating optics.

Increased frequency allows more ion packets to be overlapped, yielding a more intense ion beam. In Figure 4-2, the analyte ion signal begins to increase at  $\sim 8$  Hz. This frequency provides one pulse every 125 ms, coinciding with the beginning of ion packet overlap. A comparison of signal intensities at laser frequencies of 10 Hz and 20 Hz shows a nearly doubled analyte ion signal. At 20 Hz, or every 50 ms, two laser pulses are incorporated into the ion packet temporal profile of  $\sim 100$  ms. The 30 Hz frequency does not show this same increase, perhaps explained by the reduction in pulse energy at higher frequencies. Figure 4-2 also contains a secondary  $y$ -axis for pulse energy measured as a function of laser frequency. While the laser specifications rated the system for continuous use at 0-20 Hz, higher repetition rates (up to  $\sim 35$  Hz) were possible for

limited time periods. There was no mention in the laser manufacturer's specifications of variations in pulse energy with increased laser frequency. The pulse energy measurements shown in Figure 4-2 explain the non-linear increase in analyte signal intensities with laser frequency—pulse energies are not maintained.

Advances in solid-state UV lasers enable the production of compact laser systems capable of yielding high repetition rates (>1 kHz) with consistent pulse energies. A recent study has shown that incorporating a high repetition rate laser into a MALDI TOF instrument provides benefits for high-throughput analysis.<sup>160</sup> The oa-TOF used in the current study along with the liquid matrix would also benefit greatly from increased laser frequencies. Besides increasing analyte ion intensities, the liquid matrix allows a large number of laser shots (>30,000) before the sample needs to be replenished or the laser translated. A solid matrix, providing ~100 shots per spot and using a 1 kHz laser frequency, would require translation every 10 ms. This may become difficult when considering that each new area in the solid matrix MALDI may or may not provide analyte signals due to poor crystal formation.

### **Fluence Dependence**

The fluence ranges reported in the literature are inconsistent due to measurement inconsistencies for laser spot size.<sup>153</sup> Since spot sizes show strong dependence on fluence values, micrometer deviations can yield drastically different results. An order of magnitude difference in ion fluence thresholds can be seen for measurements made from larger spot sizes ~400  $\mu\text{m}$  to smaller spot sizes ~50  $\mu\text{m}$  (identical calculated fluence).<sup>45</sup>

Figures 4-3 and 4-4 show the analyte ion yield dependence of laser fluence for liquid matrices at atmospheric pressure. Fluence ranges are not considered to be mass dependent; instead, the ranges may be chemical class dependent.<sup>152</sup> Figure 4-3 illustrates

the analyte yields for reserpine and spiperone, and Figure 4-4 shows the analyte yields for bradykinin fragment 1-7 and angiotensin II.

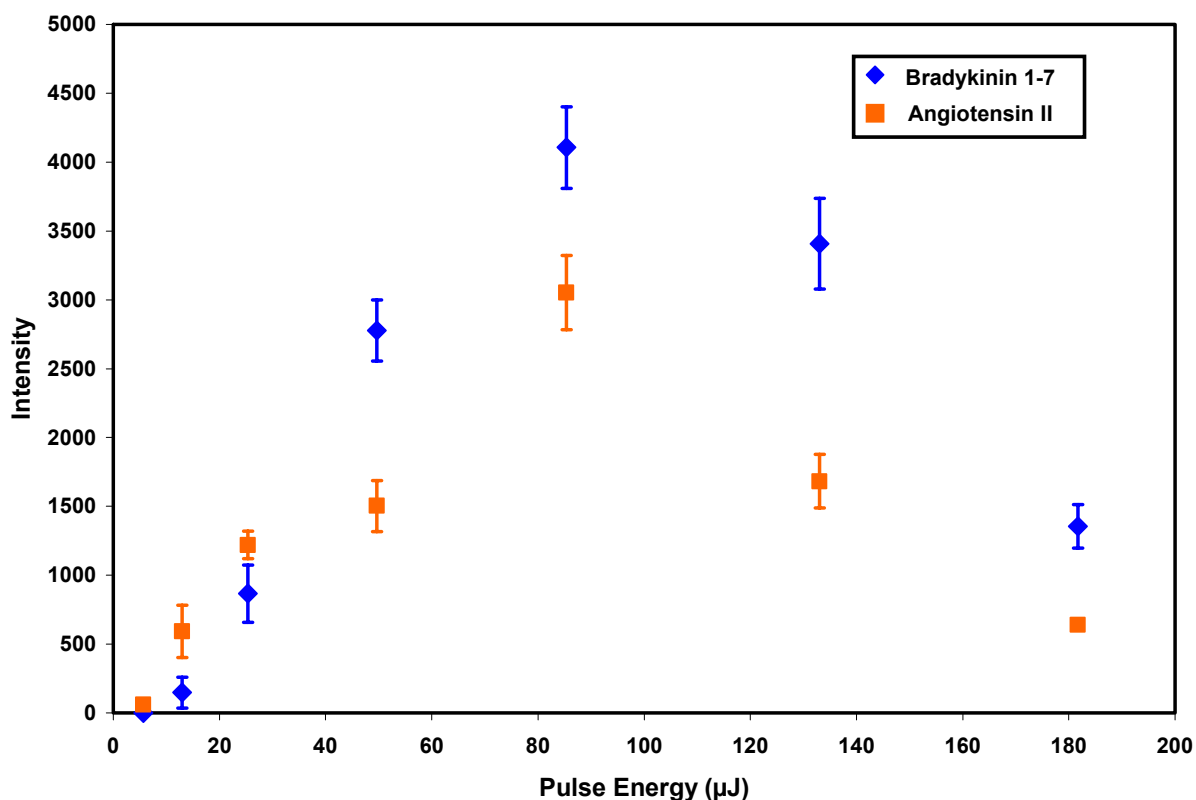


Figure 4-3. A plot of analyte ion yields as a function of pulse energy. The analytes, reserpine and spiperone, were examined at atmospheric pressure using a CHCA chromophore liquid matrix. The laser spot size was approximately elliptical with diameters of 250 μm by 300 μm. The pulse energies were measured after the attenuating optics.

The reporting of pulse energies versus calculated fluence may provide a broader insight into the data due to the drastic variations in the literature. The calculated fluence ranges for APMALDI with a liquid matrix are 200-2000 J·m<sup>-2</sup>. In both Figures 4-3 and 4-4, the spot size was elliptical with diameters of 250 μm and 300 μm. Typical ranges for vacuum solid matrix MALDI are 100-1000 J·m<sup>-2</sup>, with variations reported in the ranges of 30-10,000 J·m<sup>-2</sup>.<sup>45,152</sup>

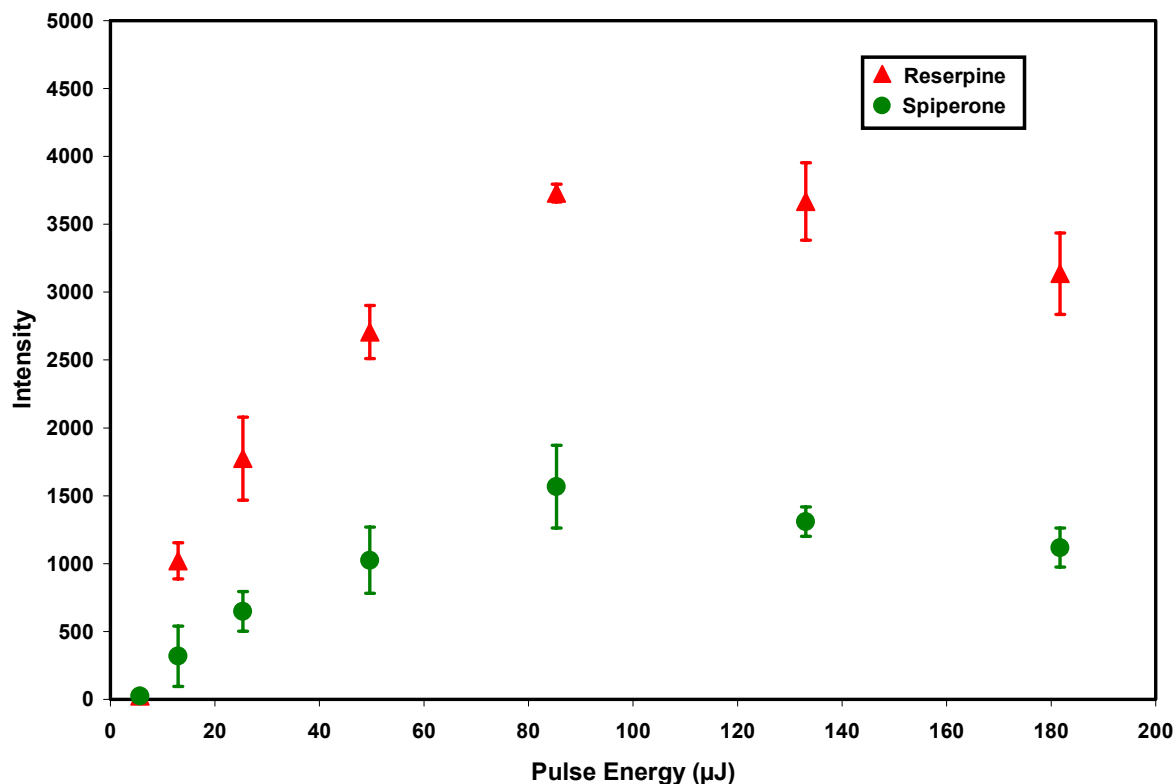


Figure 4-4. A plot of analyte ion yields as a function of pulse energy. The analytes, bradykinin fragment 1-7 and angiotensin II, were examined at atmospheric pressure using a CHCA chromophore liquid matrix. The laser spot size was approximately elliptical with diameters of 250  $\mu\text{m}$  by 300  $\mu\text{m}$ . The pulse energies were measured after the attenuating optics.

APMALDI tolerates a larger fluence range while still producing minimal fragmentation of molecular ions.<sup>157</sup> This trend holds true for the liquid matrix; however, unlike traditional fluence measurements with vacuum MALDI, lower pulse energy values could not be incorporated. Calibration of the UV neutral density filter wheel (with a variable gradient) showed that slight variations in pulse energy were not possible with the optical setup used. Figure 4-5 shows the UV wheel calibration with direct pulse energy measurements.

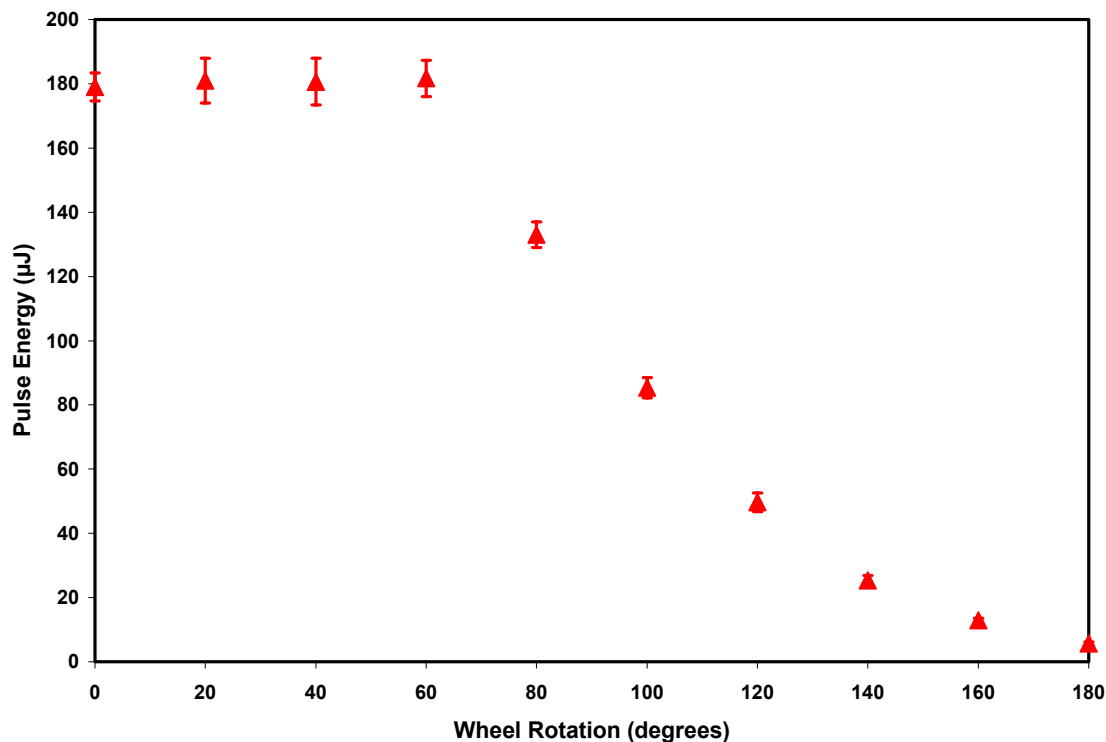


Figure 4-5. The calibration of a UV neutral density filter wheel for pulse energy.

At higher pulse energy ranges, ion yields leveled off or were reduced. This can be attributed partly to increased fragmentation of the protonated molecular ions. Figure 4-6 shows reserpine mass spectra obtained at different pulse energies (10, 90, and 180  $\mu\text{J}$ ). As the pulse energy, or fluence, is increased, fragment ions are produced.

Figure 4-7 shows bradykinin fragment 1-7 mass spectra obtained at different pulse energies (10, 90, and 180  $\mu\text{J}$ ). The peptide shows less structural fragmentation than the small molecule, reserpine, (Figure 4-6), yet both the diethanolamine adduct and protonated molecular ion show increased neutral water loss. The loss of neutral water from peptides is considered a low energy fragmentation pathway; therefore, even with the highest fluences used only limited fragmentation occurred with the liquid matrix.<sup>161</sup>

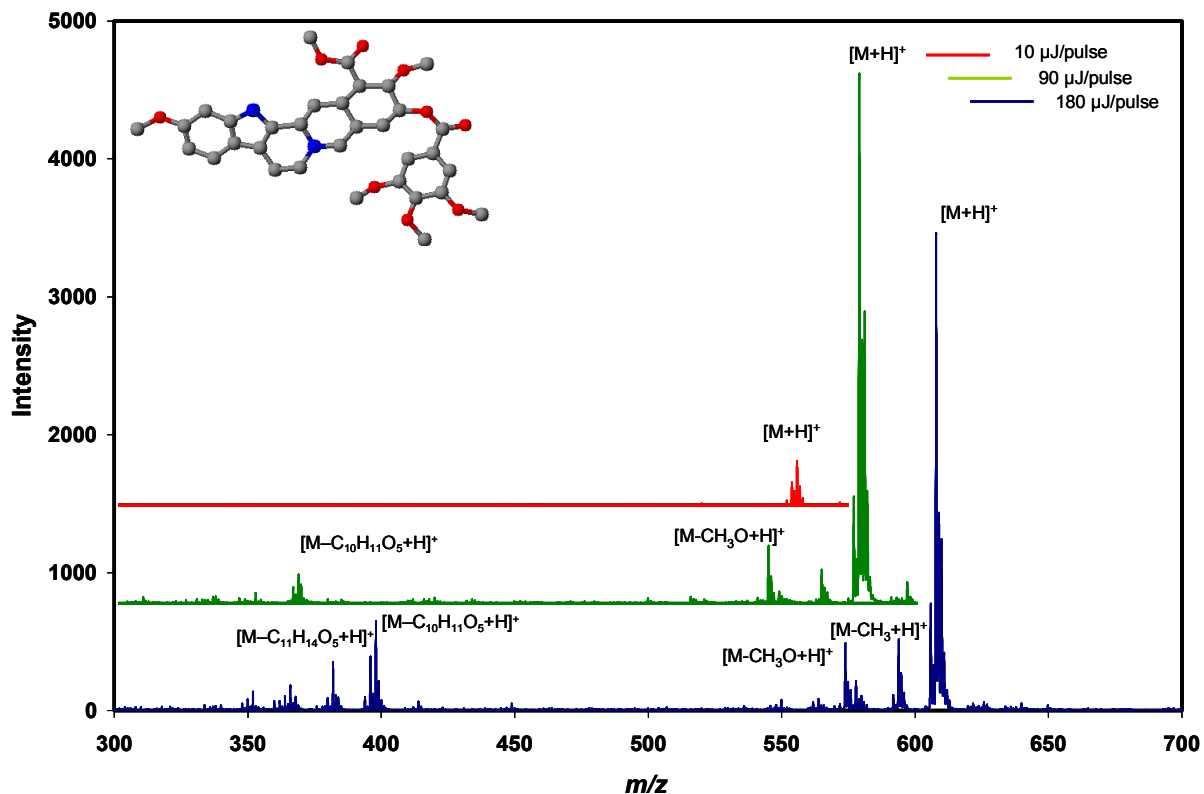


Figure 4-6. Mass spectra illustrating fragmentation produced at higher pulse energies (*i.e.*, 10, 90, and 180 μJ). The analyte was 25 pmol of reserpine.

### Particle Ejection

Decreased analyte ion yields shown in Figures 4-3 and 4-4 can not be fully accounted for by increased fragmentation alone. Suggestions have been made that higher fluences produce particle ejections during the MALDI desorption process. Using laser desorption, total particle yields have been collected onto a quartz microbalance as a function of laser fluence.<sup>162</sup>

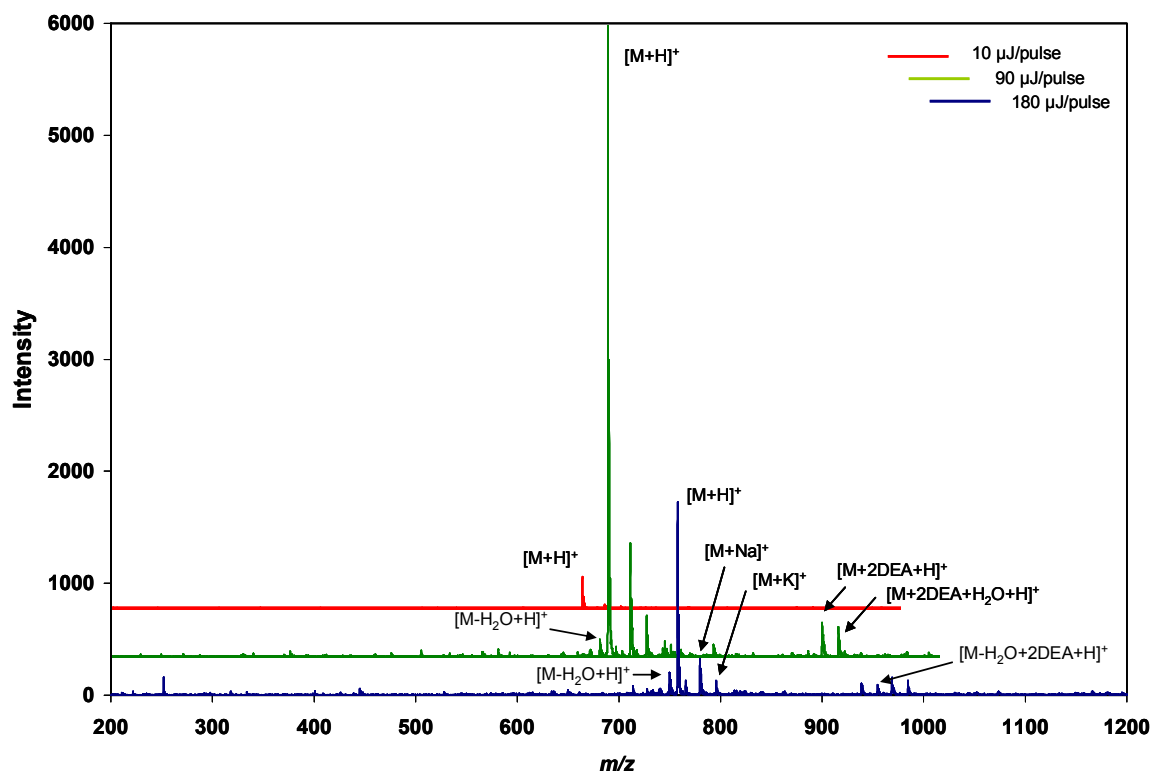


Figure 4-7. Mass spectra illustrating fragmentation produced at higher pulse energies (*i.e.*, 10, 90, and 180 μJ). The analyte was 25 pmol of bradykinin fragment 1-7

The study, done in vacuum, reports neutral molecules begin desorbing at  $11 \text{ mJ}\cdot\text{cm}^{-2}$ .

Alves, Kalberer and Zenobi examined charged particle ejections from MALDI matrices at atmospheric pressure.<sup>154</sup> They reported that the particles ejected were, on average, larger than those for vacuum MALDI. Estimates for the particles ranged from ~110 to 240 nm, depending on the matrix preparation and laser fluence. The APMALDI study also determined that as fluence increased, mean particle size also increased. Still it was deemed difficult to determine the contribution of particles produced by the laser ablation process versus the gas-phase processes occurring in the MALDI plume. Examination of liquid matrices under vacuum has also shown that increases in fluence can produce larger particle sizes.<sup>162</sup>

To provide an explanation for decreasing ion yields at higher fluence and obtain values for liquid matrices at AP, particle ejections were examined. By collecting fluorescence images of the liquid matrix during laser desorption, particles that were ejected could be imaged. Since the MALDI matrix requires a UV chromophore for the desorption and ionization processes to occur, an imaging method is inherent in the liquid matrix. Figure 4-8 shows the emission spectrum for the CHCA liquid matrix. Excitation occurred using 337 nm, the wavelength used for desorption/ionization. Table 4-1 lists the conditions used for the emission spectrum collection.

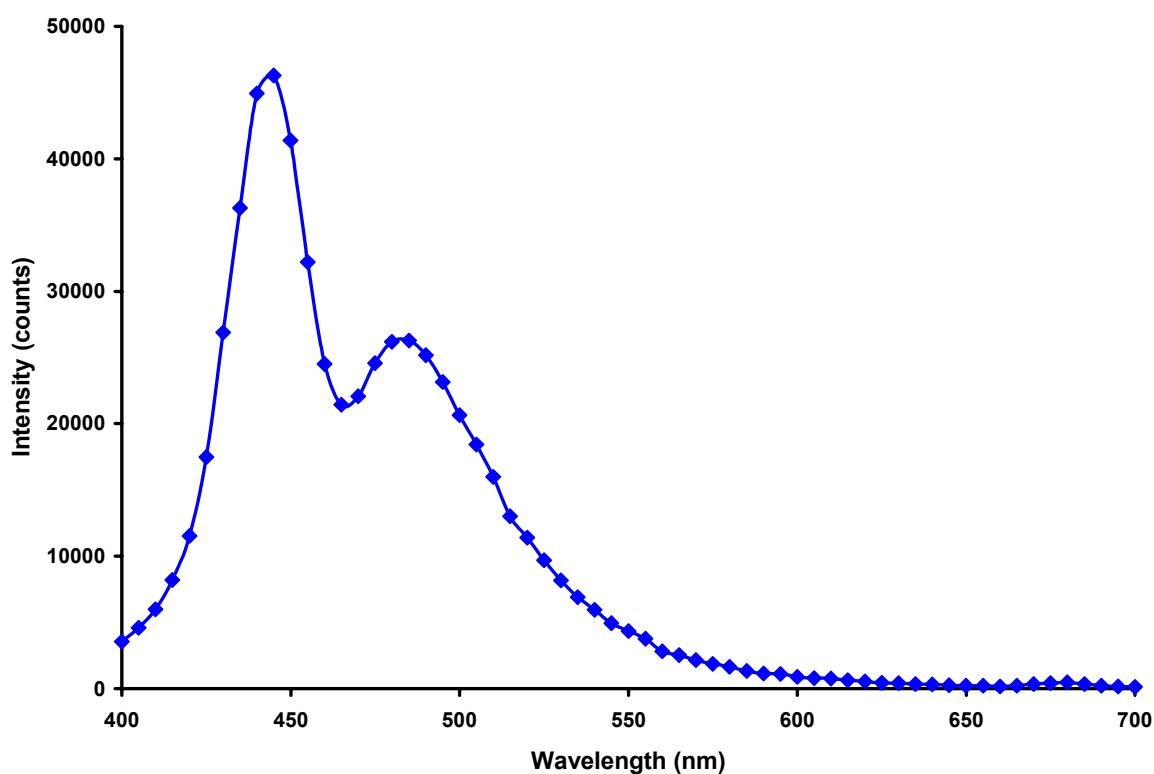


Figure 4-8. Emission spectrum collected for the CHCA liquid matrix using a 337 nm excitation wavelength.

Table 4-1. Conditions used to acquire the emission spectrum of the CHCA liquid matrix.

Measurement Mode	Fluorescence Top
Excitation wavelength	337 nm
Emission wavelength start	400 nm
Emission wavelength end	700 nm
Emission scan number	61
Emission wavelength step size	5 nm
Excitation bandwidth	12 nm
Number of flashes	10
Integration time	40 $\mu$ s

A 460 nm bandpass filter, a gated intensified CCD, and an inverted microscope (100X objective) were used to collect fluorescence images of the liquid matrix. The excitation source was the same 337 nm nitrogen laser used in the APMALDI configuration. Figure 4-9 shows the laser spot on the liquid matrix.

Collecting 50 ms images at varied fluences allowed videos of the particle ejection process to be constructed. Figure 4-10 shows a still image of the particles ejected at higher fluences (pulse energy 180  $\mu$ J) using the liquid matrix.

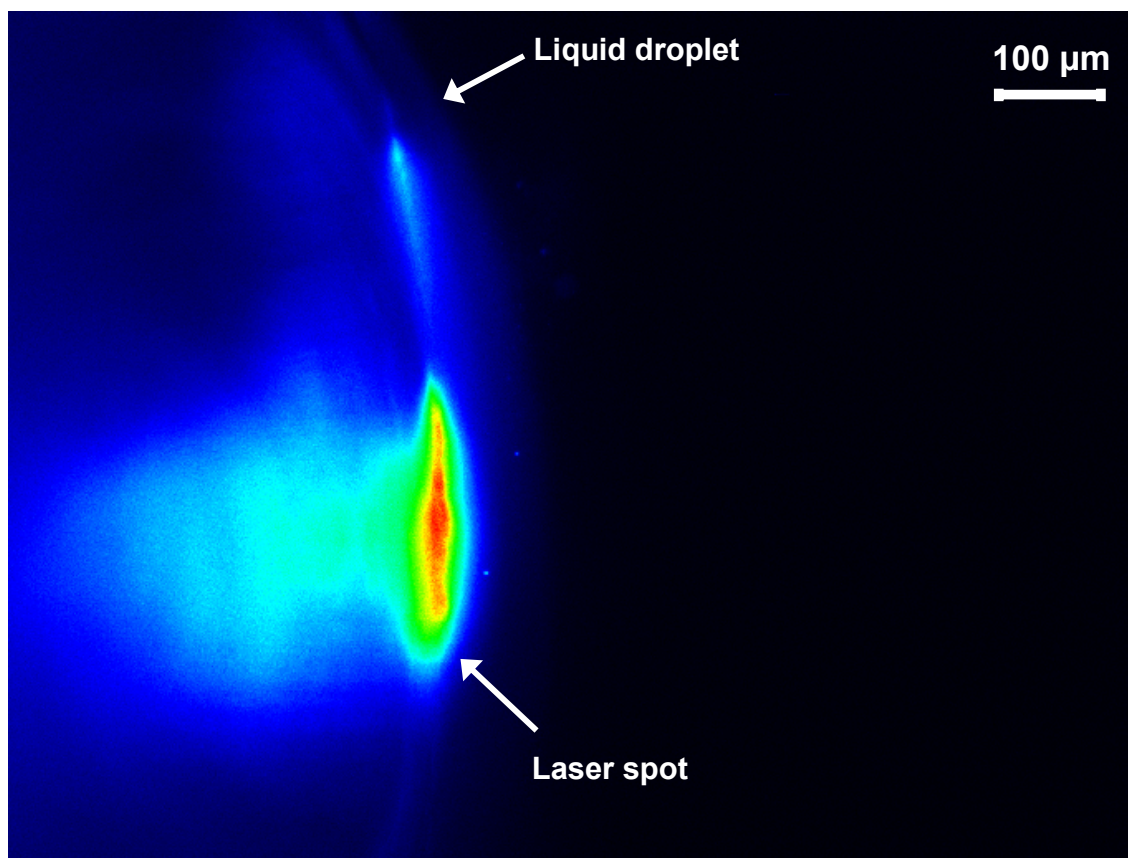


Figure 4-9. Fluorescence image of the laser impinging on the liquid matrix surface. The spot size can be estimated at  $\sim 300 \mu\text{m}$  in diameter.

Only approximate values for the number of particles ejected and the particles sizes are available. The images are obtained in a depth of focus field; therefore, only a slice of the particles ejected could be viewed. Also, the isotropic emission of the CHCA particles provides only a rough estimate of particle size, hundreds of nanometers. Important in the study is the dependence of particle ejection on pulse energy (and correspondingly fluence). Below  $90 \mu\text{J}$  pulse energy, particle ejection was erratic. Increasing pulse energies yielded more frequent ejection of particles. Fluorescence images collected at higher fluences showed particles ejected from the liquid matrix. Videos showed that the particle ejections occurred at pulse energies of 110, 140, and  $180 \mu\text{J}$ .

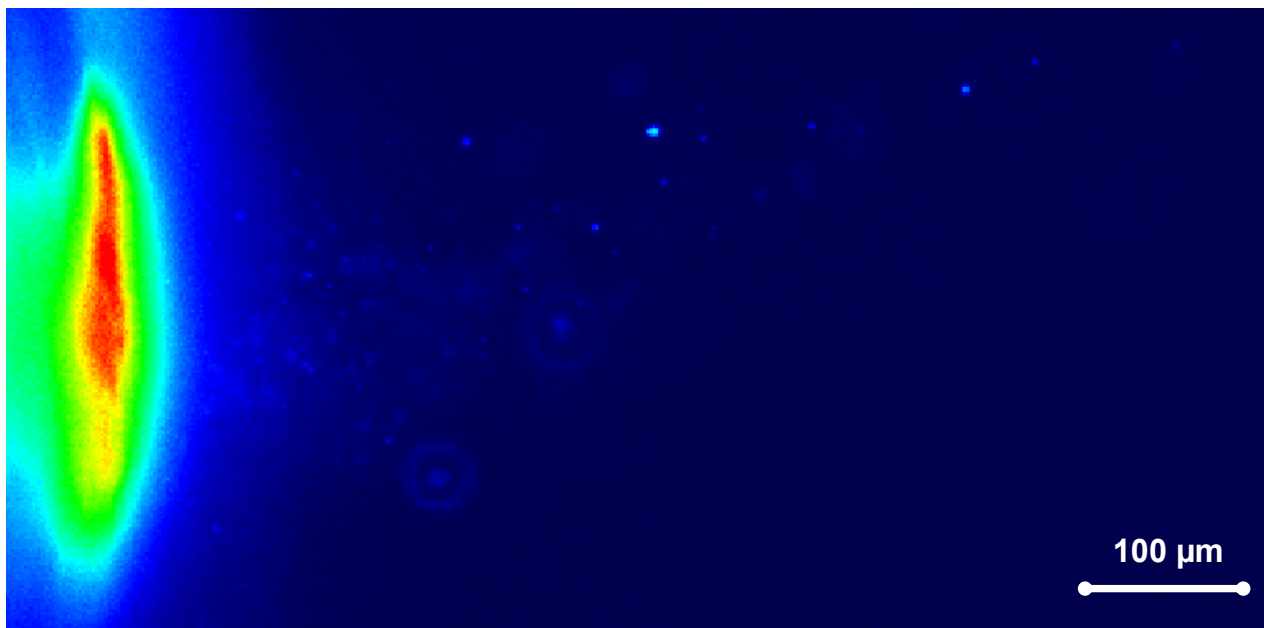


Figure 4-10. Fluorescence image of particles ejected from the liquid matrix. The pulse energy was  $\sim 180 \mu\text{J}$ .

Object 4-2. A video of the laser irradiating the liquid sample demonstrating particle ejection at  $110 \mu\text{J}$  pulse energy. (1 mb, 110pulseenergy.mpg, 10 seconds).

Object 4-3. A video of the laser irradiating the liquid sample demonstrating particle ejection at  $140 \mu\text{J}$  pulse energy. (1 mb, 140pulseenergy.mpg, 10 seconds).

Object 4-4. A video of the laser irradiating the liquid sample demonstrating particle ejection at  $180 \mu\text{J}$  pulse energy. (1 mb, 180pulseenergy.mpg, 10 seconds).

Object 4-5. A video of the laser irradiating the liquid sample demonstrating particle ejection at  $180 \mu\text{J}$  pulse energy—magnified view. (1 mb, 110pulseenergyzoomed.mpg, 10 seconds).

Object 4-6. A video of the laser irradiating the liquid sample demonstrating particle ejection at  $180 \mu\text{J}$  pulse energy—slow motion (non-false color) view. (5.5 mb, 180pulseenergyslowed.mpg, 50 seconds).

## Plume Interactions

Fluence ranges play a major role in the desorption processes for MALDI, yet interactions in the ejected plume also have important mechanistic consequences. Signal suppression illustrates possible process pathways. Two suppression effects are known to occur: the matrix suppression effect and the analyte suppression effect.<sup>163-164</sup>

The matrix suppression effect occurs when a sufficiently high analyte concentration suppresses matrix ion signals in MALDI spectra. When excited matrix molecules are in close proximity to the analyte, reactions can transfer energy and charge. Analyte signal suppression effects are also related to plume interactions. Specific analyte ion signals are reduced or increased due to their chemical properties and the ion-molecule interactions that occur in the MALDI plume. Since the liquid matrix provides a homogeneous environment, varying analyte molar ratios with peptide mixtures can demonstrate the analyte suppression effect (*i.e.*, plume interactions). Preliminary experiments demonstrating this phenomenon in the liquid matrix were conducted by analyzing equimolar peptide mixtures. Figure 4-11 shows the ion signals obtained for bradykinin fragment 1-7 and angiotensin II.

A comparison of Figure 4-11C with Figures 4-11A and 4-11B shows that ion signal intensities are not maintained. While the individual ion signals are not equivalent in most mixtures, due to ionization differences, the total peptide signal is also reduced dramatically. At a specific fluence (90  $\mu\text{J}$ ) a limited number of excited matrix molecules are emitted during desorption. These molecules undergo ion-molecule reactions in the plume. A limited number of excited molecules can only produce a specific amount of analyte ions—in this case only a fraction of each analyte in the mixture.

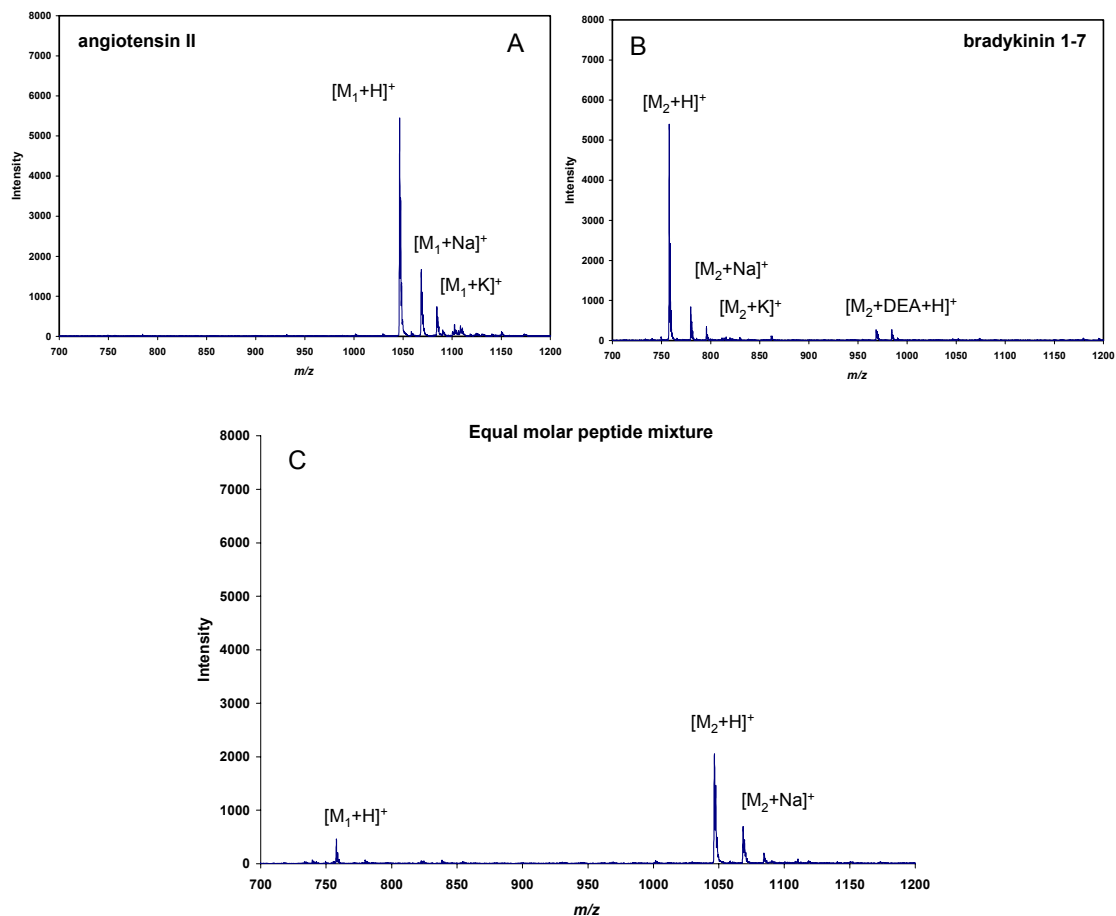


Figure 4-11. Mass spectra demonstrating analyte signal suppression are shown. The three spectra represent A) angiotensin II, B) bradykinin fragment 1-7, and C) the combined analysis of both peptides. For the single peptide analyses 25 picomoles of each was placed on target. For the combined analysis 25 picomoles of each peptide was placed on target.

## Conclusions

Atmospheric pressure liquid matrices can add analytical utility to mass spectrometry. With the initial studies for formulating liquid matrices completed, the focus shifted to characterizing desorption and ionization in liquid systems. Though viscous liquids have been examined in the vacuum chamber, relatively few studies have evaluated volatile matrices at AP.

This chapter evaluated UV liquid matrices at atmospheric pressure with respect to laser parameters. Using liquid matrices, ion yields and particle ejection were examined versus laser fluence adjustments. Fluence dependence is both matrix preparation and pressure dependent, so the optimal laser fluence needed to be determined for the liquid matrix preparation and sampling pressure used. Additionally, sampling rate becomes important when evaluating high-throughput techniques. Since liquid matrices provide regenerating surfaces and longer sampling times, the common nitrogen laser repetition rates, <20 Hz, have become a limitation.

While the details of ion formation in MALDI are still undetermined, parametric studies relating laser variables to analyte signals must be conducted for application development. The atmospheric pressure liquid matrix can be sampled at higher fluences before fragmentation and particle ejection decrease analyte ion yields. While ion yields can be related directly to laser parameters, MALDI plume interactions also affect ion intensities. Although the liquid matrix is homogeneous, the sample composition and sampling parameters dictates matrix and analyte ion populations.

CHAPTER 5  
FUNCTIONALIZED NANOPARTICLES FOR LIQUID APMALDI PEPTIDE  
ANALYSIS

**Introduction**

Koichi Tanaka during his 2002 Nobel lecture summarized the thoughts of numerous MALDI researchers, demonstrating what is known, not known, and what most of the scientific community does with the information.<sup>165</sup>

“Herein I have suggested the principles by which laser-light irradiation is able to generate huge molecular ions. However, these principles are not necessarily correct because they have not yet been fully proven scientifically...even if the principles are unverified, their application takes priority if they are useful and practical.”

—Koichi Tanaka 2002

With its ability to ionize and measure large biopolymers, biological mass spectrometry is a routine analysis tool. However, as samples become more complex and the analytes less abundant, methods for selective extraction and preconcentration must be developed. The recent instrumental development of atmospheric pressure matrix-assisted laser desorption/ionization (APMALDI) offers an advantage for biological analysis.<sup>103,108,114,143,166</sup> Atmospheric pressure (AP) sampling encourages alternative sampling approaches, such as simple UV absorptive liquid matrices that allow rapid and reproducible peptide analysis.<sup>168</sup> This chapter describes a new AP liquid matrix method that incorporates functionalized silica nanoparticles as scavenging agents for peptides.

For complex biological samples, analysis time is limited less by the mass analysis steps than by the precursor separation processes. In an effort to decrease separation

procedures prior to mass spectrometry analysis, various techniques are employed. In offline systems, solid phase extraction tools, such as Ziptips® (Millipore, Billerica, MA, USA), are often used for the removal of interferences from biopolymer samples.<sup>169</sup> This solid phase extraction (SPE) procedure includes a multiple step process for analyte adsorption and extraction. While the procedure does allow sample cleanup and preconcentration, it does not provide a means for selective analyte removal. Another approach, loosely adapted from SPE, is surface enhanced laser/desorption ionization (SELDI).<sup>170</sup> In SELDI, a MALDI target plate is functionalized for the selective retention of analytes. The surface functionalization allows analyte retention while removing mass spectrometry interferences through on-target washing. SELDI offers increased throughput for applications in biological system profiling; however, the technique currently requires the use of a vacuum chamber, necessitating a delay between analyses.<sup>171</sup>

As an alternative, discrete particles can be used for the removal of analytes prior to MALDI analysis. The range of material properties available provides choice in functionalization chemistry and extraction procedure. Previously, commercially available micrometer-sized particles have been used in conjunction with vacuum MALDI.<sup>172-173</sup> In this approach, nonselective interactions were used to concentrate analytes for conventional MALDI analysis. Recently, the affinity capture of analytes using magnetic micrometer-sized particles has been presented by Tempst et. al. These experiments also were conducted using traditional vacuum MALDI analysis.<sup>174-175</sup>

While silica based nanoparticles have been used as analyte recognition elements, their application to mass spectrometry analysis has not been extensively explored.<sup>176-177</sup>

We propose using them as a simple and rapid means for sample preparation for liquid APMADLI. Liquid matrices, which serve well for atmospheric pressure analysis, can also act as a medium for the functionalized nanoparticles. Liquid matrices alleviate the need for sample vacuum chambers and avoid the well known inhomogeneities associated with crystalline matrices. C18 nanoparticles (silica nanoparticles functionalized with 18 carbon hydrophobic chains) are shown to extract various standard peptides from solutions and allow a rapid analysis by directly analyzing the particles with liquid APMALDI. While the C18 nanoparticles utilize hydrophobic interactions to facilitate analyte extraction, we have also investigated aptamer based nanoparticles and their ability to selectively isolate specific peptides. These take advantage of the affinity of single-stranded nucleic acids for peptide molecules. Aptamers are typically between 15 and 70 nucleotides in length and form elaborate three-dimensional structures and shapes, allowing the aptamers to have high selectivity and affinity for a wide range of molecules. Aptamers have been well documented in areas such as investigating cellular protein functions and protein/ligand interactions.<sup>178-180</sup> Selective analyte removal is often done using antibody-antigen interactions in bioanalysis procedures; however, while antibodies provide selectivity through conformational binding sites and a low dissociation constant ( $K_d$ ), yielding low detection limits, extensive characterization and *in vivo* production are required.<sup>181-182</sup> As an alternative to antibodies, aptamers have several inherent advantages. Since they consist of a short, single strand of DNA or RNA, they are less costly to synthesize and have a longer shelf life. The aptamer selection process mimics natural selection, so in theory it is possible to develop a highly specific aptamer for any target molecule. In comparison to engineering antibodies for particular applications, the

incorporation of site-specific labels or coupling sites into an aptamer is a less complex process. In addition, aptamers are synthesized completely *in vitro*, allowing for the development of high throughput selection methods.<sup>183-186</sup> The aptamer used in this study was previously selected for D-vasopressin (Cys<sup>1</sup>-Tyr-Phe-Gln-Asn-Cys<sup>6</sup>-Pro-Arg-Gly-NH<sub>2</sub>) and has a binding efficiency of ~1000 fold over L-vasopressin, as seen in studies conducted using the aptamer as a chiral separation group for affinity chromatography.<sup>187-</sup>

188

Nanoparticles for the extraction of peptides and subsequent analysis using atmospheric pressure matrix-assisted laser desorption/ionization (APMALDI) have been evaluated. The atmospheric pressure source allows particles to be directly introduced in the liquid matrix, minimizing sample loss and analysis time. Described in this chapter are two sample preparation procedures for liquid APMALDI analysis: a C18 functionalized silica nanoparticle for hydrophobic extractions, and an aptamer functionalized magnetite core nanoparticle for rapid, affinity extractions. The C18 particles provide a non-selective support for rapid profiling applications, while the aptamer particles are directed towards reducing the complexity in biological samples. The aptamer functionalized particles provide a more selective analyte-nanoparticle interaction whereby the tertiary structure of the analyte becomes more critical to the extraction. In both cases, the liquid APMALDI matrix provides a support for ionization, and acts as the releasing agent for the analyte-particle interaction. Additionally, analyte enrichment was possible due to the large surface to volume ratio of the particles. The experiments conducted with functionalized nanoparticles, in an atmospheric pressure

liquid matrix, present a basis for further methodologies and utilities of silica nanoparticles to be developed.

## **Experimental Methods**

### **Materials**

Peptide standards (Sigma-Aldrich Corp., St. Louis, MO, USA), angiotensin I, angiotensin II, bradykinin, bradykinin fragment 1-7, and L-vasopressin were prepared as stock solutions of  $500 \text{ pmoles} \cdot \mu\text{L}^{-1}$  using either acetonitrile (ACN), for C18 nanoparticle extractions, or water, for aptamer nanoparticle extractions. D-vasopressin (Genomechamix, Gainesville, FL, USA) was synthesized using conventional fluorenylmethoxycarbonyl chemistry, and dissolved in water for analysis. Biotynalated DNA was also purchased from Genomechamix (Gainesville, FL USA). Non-extraction analysis was conducted by spotting  $0.5 \mu\text{L}$  of matrix onto  $0.5 \mu\text{L}$  of analyte stock solutions.

### **Nanoparticle Synthesis**

#### **Silica C18 functionalized nanoparticles**

The silica C18 functionalized nanoparticles were prepared using a previously reported synthesis procedure.<sup>189-190</sup> Briefly, the nanoparticles were prepared using a water-in-oil (W/O) microemulsion with a water-to-surfactant molar ratio of 10:1. The synthesis produced uniform silica nanoparticles ( $60 \pm 5 \text{ nm}$  in diameter). Twenty hours into the synthesis,  $40 \mu\text{L}$  of octadecyltrimethoxysilane (Sigma-Aldrich Corp., St. Louis, MO, USA) and  $10 \mu\text{L}$  of  $\sim 30\%$  ammonium hydroxide (Fisher Scientific, Fair Lawn, NJ, USA) were added to the microemulsion. The mixture was stirred for an additional 4 hours to yield a C18 outer coating of the silica core nanoparticles. Prior to peptide extraction, the nanoparticles were washed with ethanol, acetone, and water three times

each, and redispersed in acetonitrile. The final concentration of the nanoparticle suspension was approximated at  $\sim 6 \text{ mg}\cdot\text{mL}^{-1}$ .

### **Magnetic aptamer nanoparticles**

The iron oxide core magnetic nanoparticles were prepared using the Stöber method.<sup>191</sup> The magnetite core was formed by precipitating iron oxide through mixing ammonia hydroxide (2.5%) and iron chloride at 350 RPM using a mechanical stirrer (10 minutes). The iron chloride solution contained ferric chloride hexahydrate (0.5 M), ferrous chloride tetrahydrate (0.25 M), and HCl (0.33 M).<sup>192</sup> After three washes with water and once with ethanol, an ethanol solution containing  $\sim 1.2\%$  ammonium hydroxide was added to the iron oxide nanoparticles, yielding a final concentration of  $\sim 7.5 \text{ mg}\cdot\text{mL}^{-1}$ .

Tetraethoxyorthosilicate (200  $\mu\text{L}$ ) was added to create the silica coating for the magnetite core particles. The mixture was sonicated for 90 minutes to complete the hydrolysis process, and the nanoparticles were washed three times with ethanol to remove excess reactants.

Aptamers were immobilized onto the particle surface through avidin-biotin linkage (5' – biotin-TCACGTGCAT GATAGACGGC GAAGCCGTCG AGTTGCTGTG TGCCGATGCA CGTA).<sup>193</sup> For avidin coating, a  $0.1 \text{ mg}\cdot\text{mL}^{-1}$   $\text{Fe}_3\text{O}_4\text{-si}$  (silica coated magnetic nanoparticles) solution and a  $5 \text{ mg}\cdot\text{mL}^{-1}$  avidin solution were sonicated in the presence of the particles for 5 minutes and incubated at  $4^\circ \text{C}$  for 14 hours. The particles were magnetically separated and washed three times with 10 mM phosphate buffered saline (PBS) pH 7.4. The particles were redispersed at  $1.2 \text{ mg}\cdot\text{mL}^{-1}$  in 10 mM PBS and stabilized by cross-linking the coated nanoparticles with 1% glutaraldehyde (1 hour at  $25^\circ \text{C}$ ). After another separation, the particles were washed three times with 1M Tris-HCl buffer and spun for 10-15 minutes at 14,000 RPM. For aptamer attachment, the particles

were dispersed at  $0.3 \text{ mg}\cdot\text{mL}^{-1}$  in 20 mM Tris-HCl, 5 mM MgCl<sub>2</sub>, pH 8.0. Biotin labeled DNA was added to the solution at a concentration of  $0.2 \times 10^{-6} \text{ M}$ . The reaction was incubated at 4° C for 12 hours. Three final washings of the particles were done using 20 mM Tris-HCl, 5 mM MgCl<sub>2</sub> at pH 8.0. The nanoparticles were made to a final concentration of  $\sim 0.3 \text{ mg}\cdot\text{mL}^{-1}$  and stored at 4° C before use in the same buffer.

### **Matrix and Analyte Preparation**

The liquid matrix was a UV absorbing formulation developed for use with APMALDI. The matrix was prepared by mixing  $\alpha$ -cyano-4-hydroxycinnamic acid (CHCA) (Sigma-Aldrich Corp., St. Louis, MO, USA) with a liquid support containing a solvent liquid, equal parts ethanol and water (Fisher Scientific, Fair Lawn, NJ, USA), and a viscous component, diethanolamine (DEA) (Sigma-Aldrich Corp., St. Louis, MO, USA). The matrix was sonicated and vortexed to ensure dissolution.

### **Instrumentation**

The mass spectrometer used was an orthogonal-acceleration time-of-flight mass spectrometer (oa-TOFMS) (LECO Corporation, St. Joseph, MI, USA). Details of the mass spectrometer and source are described in Chapter 2. During analysis, the laser was pulsed (20 Hz) asynchronously with the MS repeller pulse (5 kHz). Spectra were exported and stored in an external computer at a rate of  $\sim 4$  spectra per second. The spectra shown are an accumulation of summed spectra for 1-5 minutes.

Fluorescence measurements for the extracted fluorescein labeled angiotensin II (Sigma-Aldrich Corp., St. Louis, MO, USA) were made using a microplate reader (TECAN Safire, Research Triangle Park, NC, USA) in an epi-illumination mode with excitation at 485 nm (5 nm bandwidth) and collection at 520 nm (5 nm bandwidth). Imaging of the C18 nanoparticles was conducted on an inverted microscope, 100X

magnification, (Olympus, Melville, NY, USA) using an intensified CCD (IPentamax III, Roper Scientific, Trenton, NJ, USA). Transmission electron micrographs (TEM) of nanoparticles were taken using a 7200 Hitachi transmission electron microscope.

### Extraction Procedures

Two procedures were used for peptide extractions: a centrifugation technique was applied for the silica C18 particles, while the magnetic particles required only a magnetic separation. The process of extraction for the C18 particles is demonstrated in Figure 5-1.

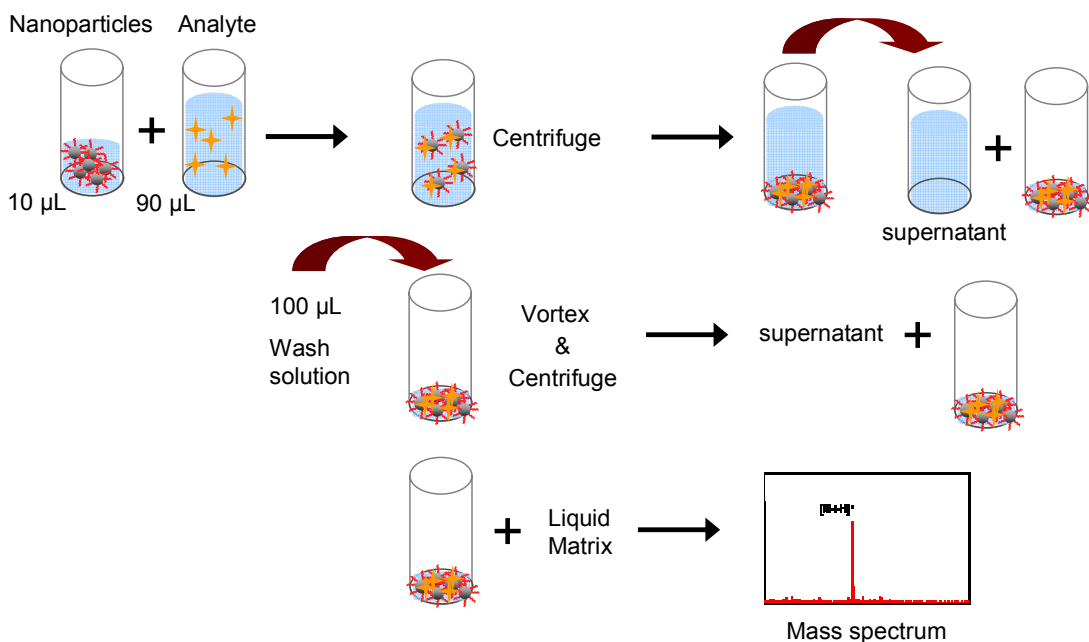


Figure 5-1. An illustration of the centrifugation technique used for nanoparticle extractions is shown.

For the C18 functionalized particles, 90 µL of nanoparticle solution ( $\sim 4 \times 10^{-8}$  M) was incubated with 10 µL of stock analyte solution ( $\sim 1:1000$  particle-to-analyte ratio) for 10 minutes. The mixture was centrifuged for 5 minutes at 14,000 RPM (Eppendorf 5180R, Fisher Scientific, Fair Lawn, NJ, USA). After centrifugation, the supernatant was

removed leaving  $\sim 1$   $\mu\text{L}$  of silica particles. The particles were washed to remove interferences and unabsorbed analyte. The wash solutions, 99  $\mu\text{L}$  of acetonitrile or water, were added and the mixture was vortexed  $\sim 5$  seconds. The wash solution used was dependent upon the desired result, analyte removal or retention. The procedure was repeated when additional washing steps were necessary. For nanoparticle extraction analysis, the silica particles remaining in the centrifuge tube after supernatant removal were pipetted directly to the MALDI target surface as shown in Figure 5-2.

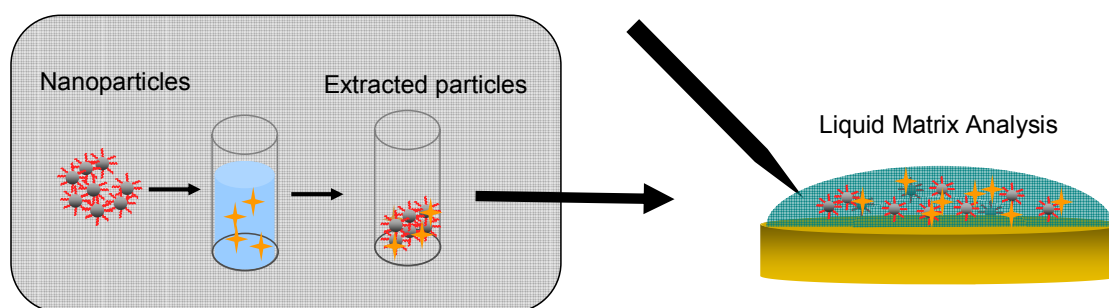


Figure 5-2. A diagram illustrating the utility of the nanoparticles with the liquid matrix is shown.

The aptamer functionalized magnetic nanoparticles allowed rapid separation using a simple magnetic extraction method rather than centrifugation. The simplified extraction procedure for the magnetic nanoparticles is shown in Figure 5-3A. Additionally, a depiction of the functionalized particles is shown as Figure 5-3B.

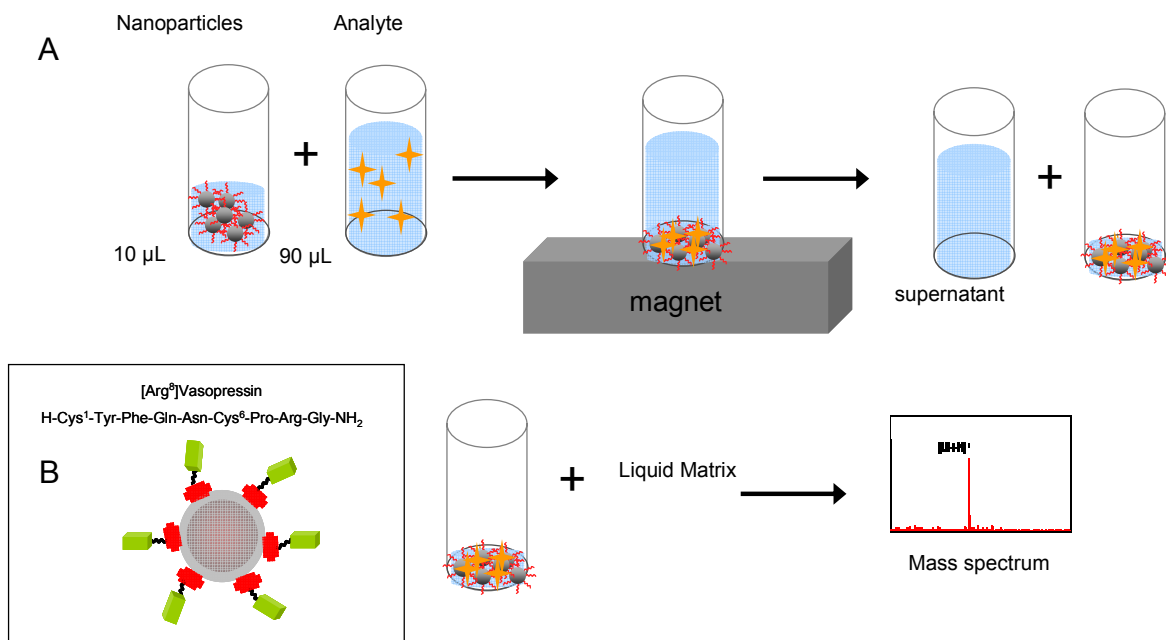


Figure 5-3. An illustration of the magnetic separation technique used for nanoparticle extractions is shown. Inset in the figure is representation of the aptamer functionalized magnetic nanoparticles.

First, a buffer exchange was conducted using 50 µL of aptamer conjugated nanoparticles ( $\sim 1 \times 10^{-8}$  M). The particles are removed from solution using a neodymium iron boron magnet (12,200 gauss, Edmund Optics, Barrington, NJ, USA) and washed with 5 mM phosphate buffer and then 3 mM MgCl<sub>2</sub>, pH 6.0. The buffer used was based upon the reported protocol for aptamer chiral separation of L and D vasopressin.<sup>187-188</sup> The resulting nanoparticle suspension was used in analyte extractions. For extraction, 10 µL of 50 pmol·µL<sup>-1</sup> analyte solution was incubated with 50 µL of the nanoparticle suspension for 10 minutes ( $\sim 1:100$  particle-to-analyte ratio). A magnet directed the particles to the bottom of the vial for removal of the supernatant. The remaining particles,  $\sim 1$  µL, were mixed with 5 µL of water and 5 µL of liquid matrix. Analysis was

conducted by pipetting 0.5  $\mu\text{L}$  of the aptamer particle/matrix mixture on the MALDI target.

## **Results and Discussion**

### **Background**

Atmospheric pressure matrix-assisted laser desorption/ionization offers the advantage of analyzing samples at ambient conditions. Limiting the vacuum constraint of a MALDI source allows analysis procedures to be developed using non-vacuum-compatible matrices. As the complexity of biological samples increases, simple methods that limit the necessary separation procedures will be valuable for biological mass spectrometry analysis.

### **Nanoparticle Characterization**

Two particle types were examined for use with liquid APMALDI: a C18 functionalized nanoparticle for hydrophobic extraction, and an aptamer functionalized magnetic nanoparticle for affinity extractions. These silica based nanoparticles were developed to aid and simplify sample preparations for liquid APMALDI applications. The C18 coated nanoparticles provide a support for rapid profiling applications while the aptamer nanoparticles are directed towards reducing the complexity in biological samples. In separation applications using silica coated nanoparticles, particle dispersion is a major concern.<sup>179</sup> One method to combat particle aggregation, and allow efficient analyte binding, is surface modifications.<sup>192</sup> The use of C18 provides hydrophobic binding for extractions while dispersing the particles in acetonitrile.

To explore extraction possibilities for the C18 silica particles, both size distribution and peptide attachment were examined prior to conducting mass spectrometric analysis.

Nanoparticle characterization is shown in Figure 5-4.

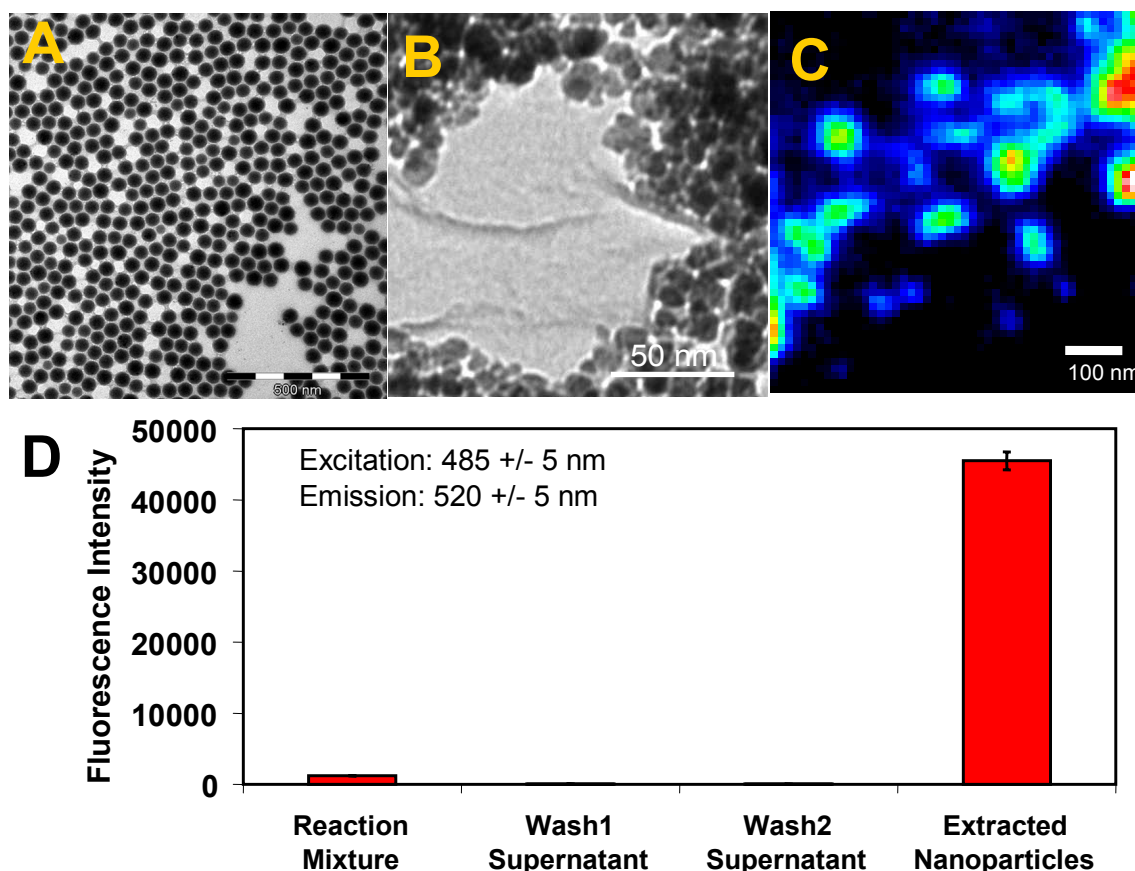


Figure 5-4. Nanoparticle characterization using fluorescence analysis is shown. Figure 5-4A is a TEM of the C18 functionalized silica nanoparticles. Figure 5-4B is a TEM of the D-vasopressin aptamer functionalized magnetic nanoparticles. Figure 5-4C is a fluorescence image of the silica nanoparticles with FITC labeled angiotensin II. Figure 5-4D shows the fluorescence intensity measured for the extraction and washing steps for FITC labeled angiotensin II with the C18 functionalized nanoparticles.

Figure 5-4A is a transmission electron micrograph (TEM) of the C18 functionalized silica nanoparticles. Figure 5-4B shows a TEM of the magnetic nanoparticles (~30 nm) with silica coating and aptamer attachment. The particles are well dispersed and have

an average size of ~60 nm. The D-vasopressin aptamer functionalized magnetic nanoparticles are ~30 nm in diameter as can be seen from Figure 5-4B. They are less dispersed due to aggregation. Before liquid APMALDI was performed, the ability of the C18 nanoparticles to extract peptides from a solution was investigated with fluorescence microscopy and spectroscopy. Figure 5-4C shows a fluorescence image for an isothiocyanate fluorescein (FITC) labeled angiotensin II peptide bound to a C18 functionalized silica nanoparticle. The labeled peptide was mixed, via the extraction procedure described previously (see Experimental), with the nanoparticles to determine if peptide adsorption occurred on the particle surface. The image demonstrates peptides can bind to the particle surface of the particle. Figure 5-4D shows the fluorescence intensity measured by a plate reader for each solution of the peptide extraction procedure. The initial reaction solution has minimal fluorescence after the extraction has taken place. Subsequently, the two washing steps also have minimal fluorescence after removing the particles. The minimal fluorescence signal for the reaction mixture, after the removal of the particles, shows an efficient extraction has occurred. The retention of the peptide on the nanoparticle after two washing steps is apparent from the prominent signal in the final nanoparticle extraction and no signal present in the washing solutions. Only ~3% of the total fluorescence signal remained in the mixture supernatant. The C18 functionalized nanoparticles offer nonspecific binding through *van der Waals* interactions; therefore, analytes bind through an adsorption method. The fluorescence results suggest that the C18 silica nanoparticles can extract peptide molecules from solutions using simple hydrophobic interactions.

The binding characteristics of the magnetic silica nanoparticles have been previously characterized.<sup>179,192</sup> For the avidin coated nanoparticles fluorescence DNA hybridization studies show approximately 30 aptamer molecules per magnetic nanoparticle. The aptamer molecules attached were estimated through fluorescence measurements based on the amount of complimentary DNA hybridized to the immobilized DNA on the particle surface.

### **Peptide Analysis by Liquid APMALDI with C18 Nanoparticles**

The C18 functionalized nanoparticles allowed the extraction of a fluorescently labeled peptide. To demonstrate mass spectrometric analysis, three peptides – angiotensin I, angiotensin II, and bradykinin fragment 1-7 – were extracted from solution and analyzed using liquid APMALDI. Crystallization of the matrix was not necessary. Instead, the particles were introduced directly into the liquid for analysis, yielding a rapid extraction and analysis procedure. Figure 5-5 shows a chart of normalized ion signals for each peptide's  $m/z$  during each successive step in the extraction process.

Five extractions for each peptide were conducted. Limited analyte signal is seen for all acetonitrile washes, demonstrating the nanoparticles' ability to extract biopolymers and then release them for MS analysis. The mixture supernatant ion signal can be attributed to overloading of peptide for each particle (1:1000 particle-to-analyte ratio); therefore, it is assumed the maximum number of analyte molecules was bound to the particle surface. In comparison to the fluorescence extraction data of the FITC labeled angiotensin II, the label may alter the nanoparticle binding characteristics. The increased hydrophobicity of the FITC label versus the non-labeled peptide is suggested by the decreased peptide extraction for mass spectrometry analysis in Figure 5-5. The extraction procedure was not optimal; however, the relationship between the mixture

supernatant signal and the nanoparticle suspension signal hints to the nanoparticle capacity.

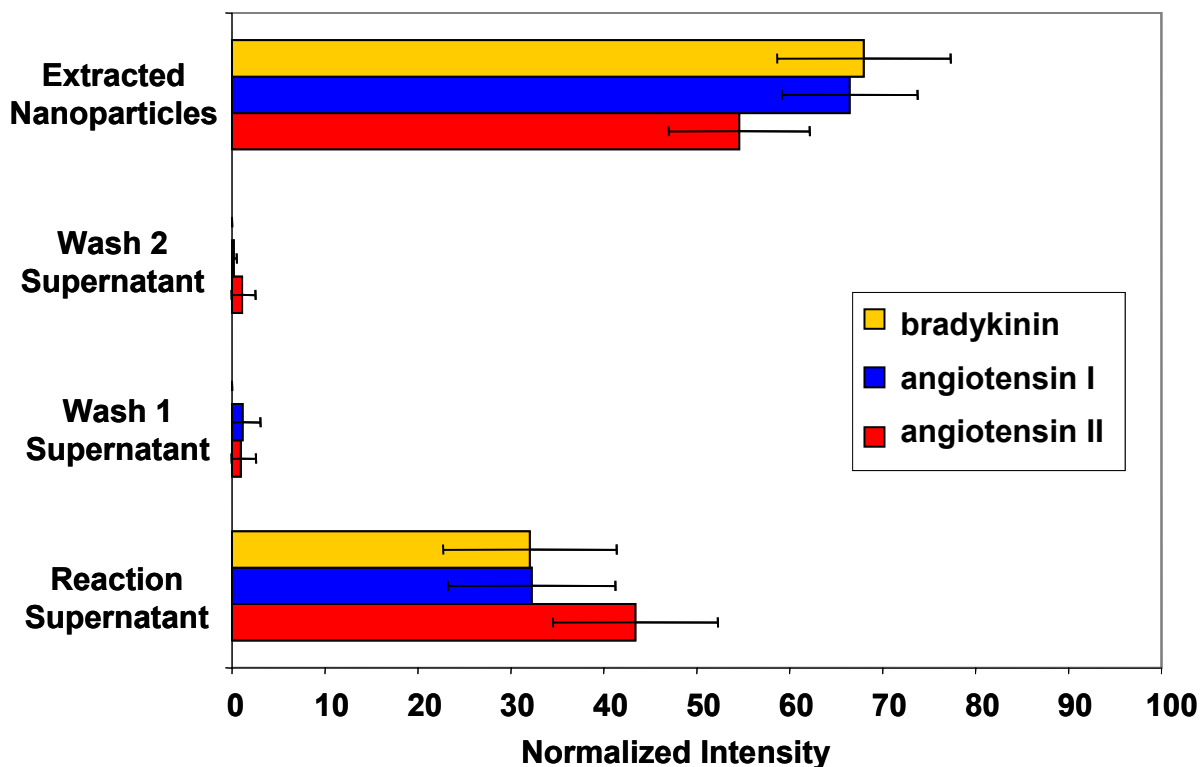


Figure 5-5. A chart of the protonated molecular ion mass spectrometry signals for three peptides is shown. Five extractions for each peptide were conducted using C18 functionalized silica nanoparticles. Extraction analysis included mass spectra for the reaction mixture after the particles were removed, the supernatants after each wash step and the nanoparticles after the final extraction. Washes were conducted using acetonitrile.

The peptide binding capacity for the nanoparticles is currently being evaluated using quantitative techniques. Analysis of the extracted and supernatant ion signals in Figure 5-5 may give some insight to the capacity, but additional quantitative studies will provide more definitive basis. This figure also demonstrates the ability of C18

functionalized nanoparticles to be used directly in a liquid APMALDI matrix, where the matrix acts as the releasing agent and allows for ionization to occur.

Figures 5-6A, 5-6B, and 5-6C, show spectra collected from the nanoparticle suspensions for angiotensin I, angiotensin II, and bradykinin of Figure 5-5 (extracted nanoparticles).

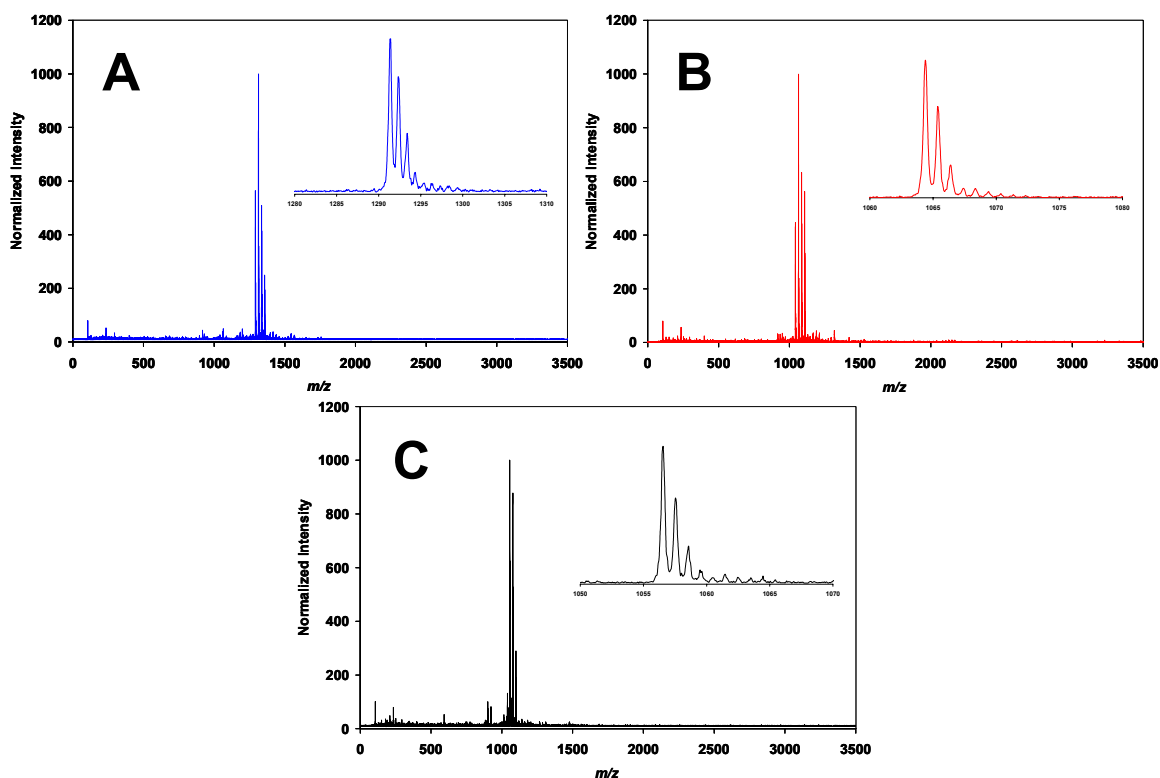


Figure 5-6. Mass spectra collected from nanoparticle extractions. Figures 5-6A, 5-6B, and 5-6C show spectra collected for the nanoparticle extraction of angiotensin I, angiotensin II, and bradykinin, respectively.

Protonated molecular ions, as well as sodium adducts, are present indicating the nanoparticles do not interfere with the APMALDI process. Minimal background in the low  $m/z$  range is generated with the nanoparticles in the liquid suspension. This fact becomes important when analyses of lower molecular weight components are analyzed

(*e.g.*, peptide fragments). On the other hand, the increase in adduct formation is most likely attributed to the nanoparticles. The porous silica nanoparticles allow entrapment of sodium during the synthesis procedure. Washing the nanoparticles with ethanol, acetone, and water before redispersing them in acetonitrile significantly reduced adduct formation, but does not eliminate it. Using peptide spiked nanoparticle suspensions, reductions in molecular ion suppression and adduct formation with subsequent water washings were monitored, as shown in Figure 5-7.

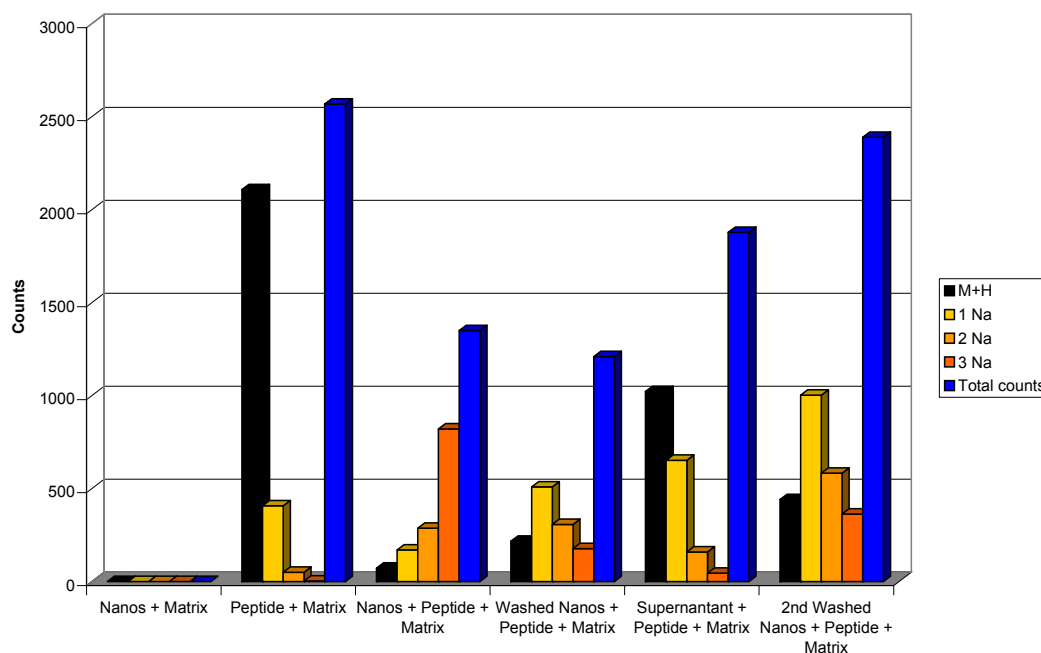


Figure 5-7. A chart showing the effect multiple washing steps has on the sodium adduct signals during mass spectrometry analysis.

Both the total and the molecular ion signal doubled from the first water wash to the second. The additional removal of salts can be done with cation-exchange resin beads, volatile ammonium salts such as ammonium citrate or ammonium acetate, and on-probe purification using nitrocellulose or modified Nafion film substrates.<sup>108</sup> While adducts were present for each analysis, the mass spectra of the peptides were not otherwise

adversely affected, as can be seen from the isotope ratios in Figure 5-6. Direct analysis of the nanoparticles in the liquid matrix limits analyte loss and provides the opportunity to concentrate the analyte. The nanoparticles have a unique advantage when they are used as a solid phase extraction support. The larger surface area to volume ratio can allow maximum peptide attachment in a minimum volume. A preconcentration of the analyte can occur by drawing peptide into a limited analysis volume. Because APMALDI is a mass sensitive technique, pulling all the analyte into a small sample volume allows the entire sample to be analyzed on target. To demonstrate, Figure 5-8 shows the analysis of a 1  $\mu\text{M}$  angiotensin II solution before and after nanoparticle extraction. Analysis was conducted by placing 0.5  $\mu\text{L}$  of sample on target and then adding 0.5  $\mu\text{L}$  of liquid matrix,  $\sim 500$  femtomoles on target. Figure 5-8A has the molecular ion peak for angiotensin II before preconcentration and figure 5-8B shows the mass spectrum of the analyzed nanoparticles.

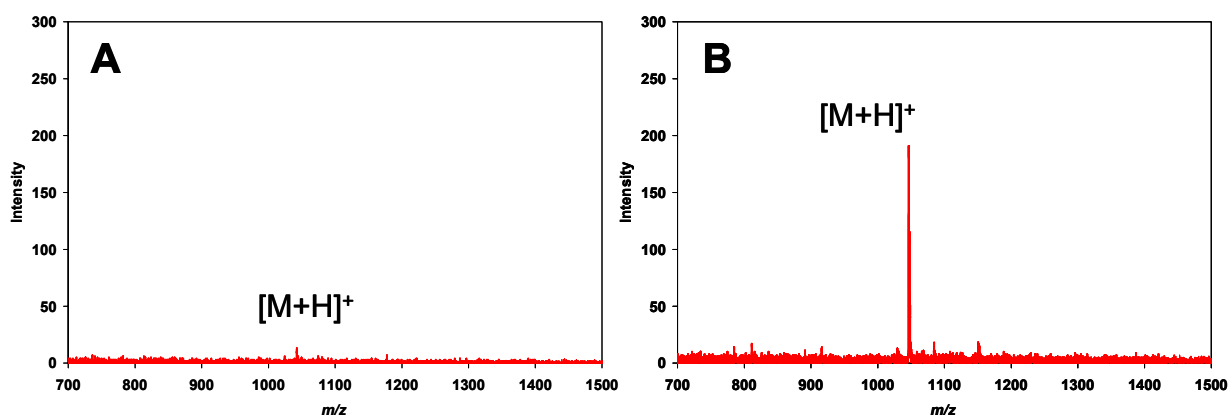


Figure 5-8. Mass spectra collected for a 1  $\mu\text{M}$  angiotensin II solution before and after nanoparticle extraction are shown. Figure 5-8A shows the spectrum for the analysis of 0.5  $\mu\text{L}$  of the solution,  $\sim 500$  femtomoles on target. Figure 5-8B shows the spectrum for the analysis of 0.5  $\mu\text{L}$  of the nanoparticle extract.

For extraction, a 1 mL solution of 1  $\mu$ M angiotensin II was combined with 30  $\mu$ L of C18 functionalized nanoparticles. After one acetonitrile wash, the extracted nanoparticles were redispersed in 5  $\mu$ L of acetonitrile, of which 0.5  $\mu$ L was used for analysis. A comparison of the two spectra shows  $\sim$ 15 fold concentration enhancement of the analyte. More selective analyte-nanoparticle interactions may permit wider applications. Concentrating the analyte may improve analysis when low amounts of analyte are present.

Previous biopolymer extractions coupled to MALDI remove the analyte from the support before analysis; however, our method incorporates the particle directly into the liquid matrix solution to alleviate sample transfer losses and reduce preparation time.<sup>194</sup> The matrix acts as the releasing agent to allow for analyte detection. Additionally, the increased surface area to volume ratio of the particles in comparison to micrometer-sized particles can increase extraction efficiency, yielding more analyte per sampling volume.

Using C18 functionalized supports, adsorption and removal of analyte is conducted through mobile phase flow. The molecules with limited retention enter the mobile phase and are eluted more rapidly. Applying this principle to nanoparticle applications, multiple washings were conducted with an extracted peptide mixture. Retaining and removing analytes using separation techniques allows for detection at each stage of a multiple step washing procedure. To demonstrate, a mixture of three peptides, GLY-TYR, VAL-TYR-VAL, and angiotensin II, was incubated with nanoparticles to examine retention and release. Figure 5-9 shows the peptides ion signals for each step in the washing procedure.

Di- and tripeptides are not retained on typical C18 solid supports in reverse-phase chromatography due to their limited hydrophobicity; therefore, these along with a large peptide were used to examine retention order.<sup>195-196</sup>

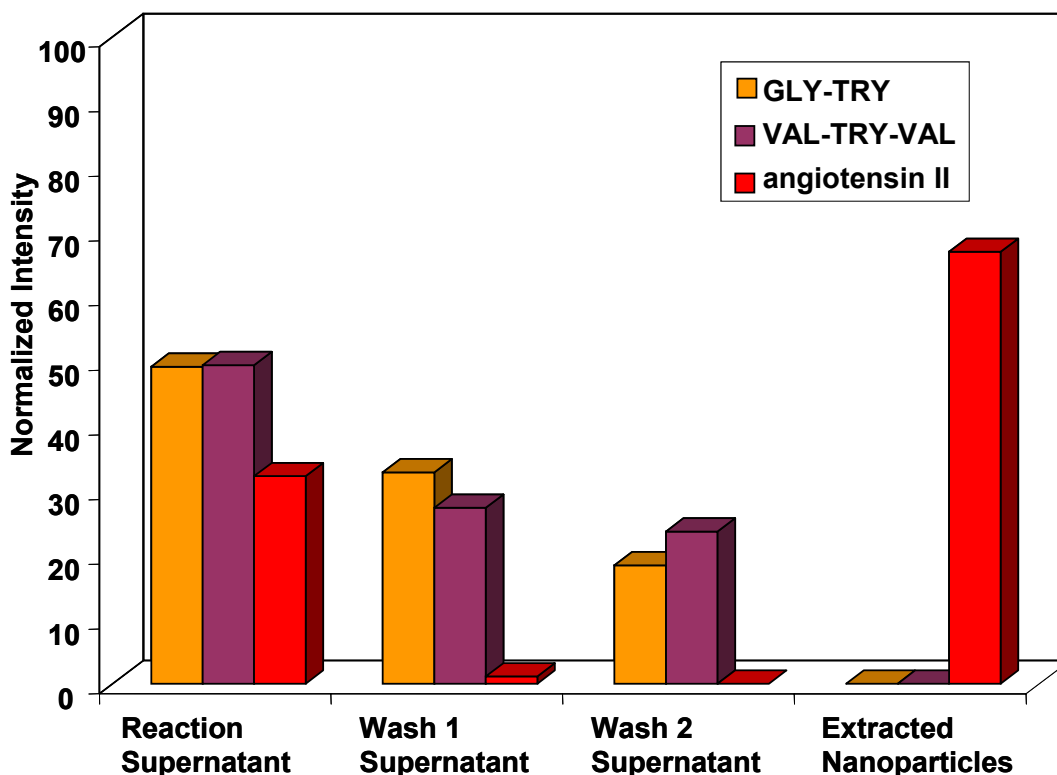


Figure 5-9. A chart of the protonated molecular ion mass spectrometry signals for three varied length peptides is shown. The smallest peptide is retained the least, while the largest peptide remains on the particle. The hydrophobic interactions are minimized with small peptides, so retention of the analyte on the particles is limited. Washes were conducted using acetonitrile.

Each peptide differs in its ability to bind to the C18. Using only acetonitrile washes, the smallest peptide was removed first (lowest retention time). The largest peptide, angiotensin II, is more hydrophobic and is retained after both washes. Also evident is the order the two smaller peptides are removed, GLY-TYR then VAL-TYR-VAL. While this process remains a low resolution separation mechanism, the elution order of the peptides correlates with hydrophobicity. The capability of controlled release adds to the

utility of these particles in biological mass spectrometry analysis in situations where hydrophobic properties as well as qualitative identification are important.<sup>197</sup>

### **Peptide Analysis by Liquid APMALDI with Aptamer Nanoparticles**

C18 nanoparticles allow simple separations utilizing hydrophobic interactions; however, aptamer nanoparticles offer the possibility of selective extractions in complex samples through affinity interactions of the analyte with immobilized aptamers. To demonstrate, magnetic nanoparticles were functionalized with DNA aptamers. With typical dissociation constants in the range of submicromolar to picomolar values, a growing number of aptamers are being described as scientific and biotechnological tools. The aptamer chosen here was selected for D-vasopressin and immobilized on the surface of the nanoparticles. While the aptamer offers selective analyte removal, nanoparticles function as the solid support for extraction. The magnetic property of the nanoparticles minimizes separation procedures, requiring only one step for extraction. Placing the particles directly into the liquid matrix allows a rapid analysis procedure that limits analyte loss. As a result, lower abundance samples can be analyzed.

The D-vasopressin aptamer offers high selectivity, yet has a large dissociation constant ( $K_d = \sim 1 \mu\text{M}$ ) allowing analyte removal from the particles.<sup>188</sup> Aptamer functionality has been previously examined when attached to a solid support through avidin-biotin interactions.<sup>187</sup> In this case, the aptamer showed little to no deterioration of its binding abilities. To examine the selectivity of the aptamer once attached to the particle, two controls were conducted. First, the D-vasopressin functionalized magnetic particles were incubated with two dissimilar peptides; angiotensin II (ASP-ARG-VAL-TYR-ILE-HIS-PRO-PHE) and bradykinin fragment 1-7 (ARG-PRO-PRO-GLY-PHE-SER-PRO). The aptamer did not have sufficient nonspecific binding for either peptide to

yield a mass spectrometry signal after extraction. The second control for selectivity focused on whether the analyte would nonspecifically bind to an aptamer functionalized particle. Individual aliquots of L and D-vasopressin were incubated with adenosine aptamer functionalized magnetic nanoparticles. The particles failed to remove either analyte as shown by the lack of mass spectrometry ion signals. This control demonstrates a lack of nonspecific binding of vasopressin analyte for a nonselective aptamer functionalized nanoparticle.

The  $K_d$  values for the D-vasopressin aptamer with L and D-vasopressin are in a ratio of 1000:1.<sup>187</sup> This ratio allows an interesting control to exist for the aptamer functionalized particles. Extraction of the L-vasopressin should present a limited mass spectrometry signal, demonstrating minimal extraction efficiency. The D-vasopressin ion signal should be larger due to a more efficient extraction. Figure 5-10 shows the mass spectra for L and D-vasopressin before and after the aptamer functionalized nanoparticle extractions. Figure 5-10A shows the L-vasopressin molecular ion and sodium adduct. The bottom spectrum in Figure 5-10A shows the nanoparticle extraction for L-vasopressin.

Limited signal intensity was obtained due to the D-vasopressin aptamer's limited affinity for L-vasopressin. Figure 5-10B shows the molecular ion and sodium adduct for D-vasopressin. The bottom spectrum in Figure 5-10B shows the nanoparticle extraction for D-vasopressin. The ion signal counts for the two extractions are estimated at a ratio of ~1000:1 (D to L-vasopressin), consistent with the  $K_d$  values for the aptamer of the two isomers. The D-vasopressin aptamer functionalized nanoparticles extract the D-vasopressin at binding values predicted. Additionally, in Figure 5-10B the before (top)

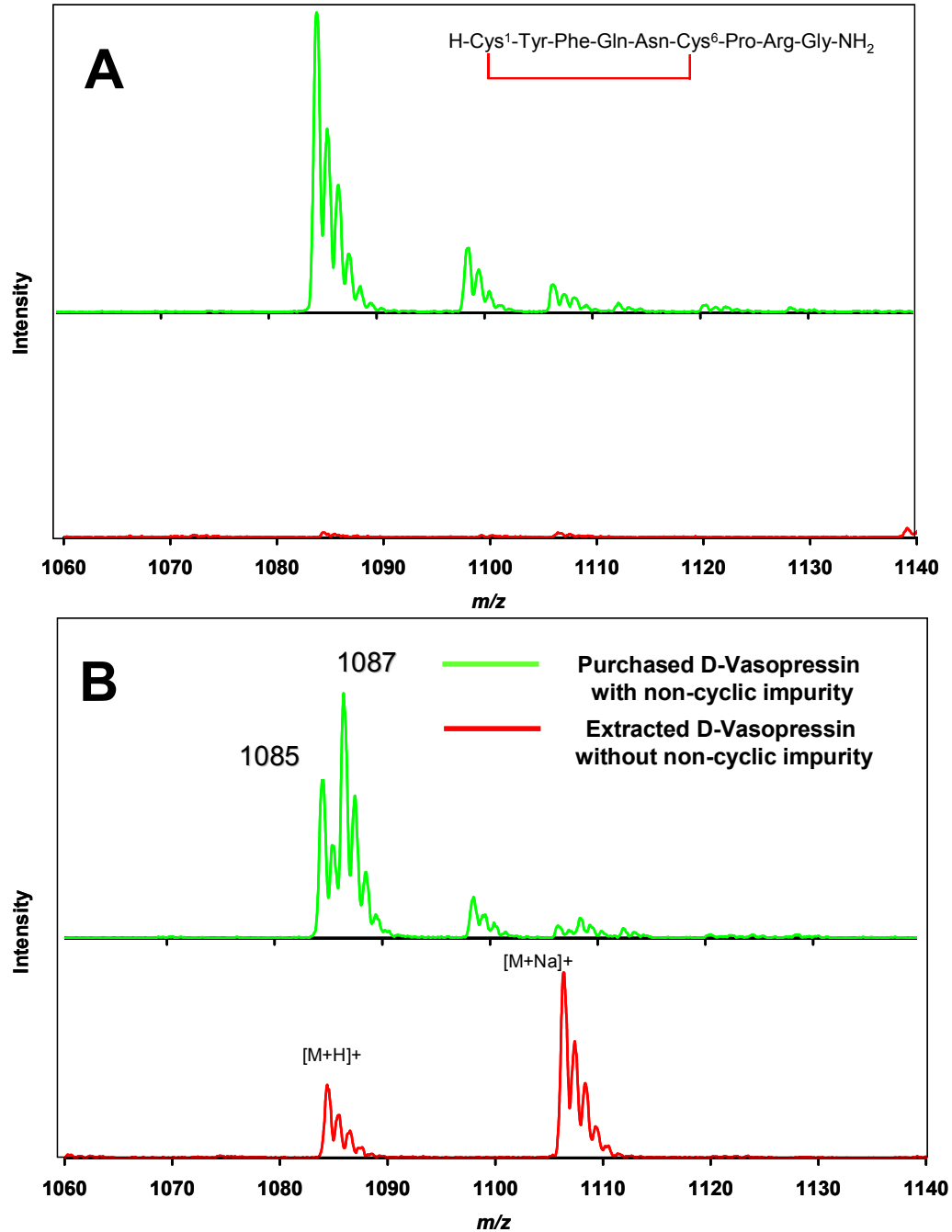


Figure 5-10. Mass spectra for L and D vasopressin before and after nanoparticle extractions are shown. Figure 5-10A shows the L-vasopressin before extraction (top) and after extraction (bottom). The L-vasopressin was not extracted well using the D-vasopressin aptamer. Figure 5-10B shows the D-vasopressin before extraction (top) and after extraction (bottom). The D-vasopressin was extracted more efficiently than the L-vasopressin. Also noticeable in the D-vasopressin is the lack of a mixture of disulfide and non-disulfide bond vasopressin. Only the disulfide bond containing D-vasopressin was extracted.

and after (bottom) extraction spectra show the aptamer's ability to extract only the disulfide bridge containing peptide. The original aptamer solution contained both the oxidized and reduced form of D-vasopressin; however, after extraction only the oxidized form was extracted by the aptamer nanoparticles. This hints to the aptamers ability to bind tertiary structure versus primary structure. Also, for this particular aptamer, the disulfide formation is critical to the formation of an aptamer—D-vasopressin complex. The coupling of aptamer functionalized magnetic nanoparticle with AP liquid MALDI analysis offers a rapid analysis using highly selective extraction agents and provides added sample clean-up.

### **Conclusions**

The use of a liquid APMALDI matrix has allowed the development of a rapid analyte extraction technique. Using known material types and functionalization chemistry, C18 and aptamer functionalized nanoparticles can act as scavenging agents for peptide molecules. Placing the particles directly into the liquid matrix allows a rapid analysis procedure that limits analyte loss and provides an improved preconcentration of the analyte. The C18 functionalized silica particles allow extraction of a variety of peptides simultaneously while MS analysis can be done directly in the liquid matrix.

The magnetic nanoparticles provided a simplified separation procedure through the use of magnetic extraction. The particles also contained selective functionalization for a more selective analyte-nanoparticle interaction; permitting wider applications and the possibility of analyzing lower abundance samples. The aptamer nanoparticles allowed the selective extraction of reduced D-vasopressin even in the presence of a structural analog. In addition, the extraction of L-vasopressin was possible, yet the extraction

efficiency matched the 1000:1 dissociation constant ratio for D versus L-vasopressin using the D-vasopressin aptamer.

These methods provide an avenue for advancement in liquid APMALDI sample preparation procedures. Optimizing the nanoparticle synthesis and washing procedures will be useful for further experimentation. An evaluation of the particle capacity and extraction efficiency will also prove helpful for the possibility of quantitative studies. More importantly, with an increasing number of available aptamers and the growing interest in their applications, an array of particles for specific mass spectrometry analyses could result. While the mechanistic aspects of the MALDI process are still unknown, applications involving the technique are thriving.

CHAPTER 6  
SECONDARY IONIZATION OF LASER DESORBED NEUTRALS FROM  
ATMOSPHERIC PRESSURE MATRIX-ASSISTED LASER  
DESORPTION/IONIZATION

**Introduction**

Matrix-assisted laser desorption/ionization (MALDI) produces ions from two convoluted steps—desorption and ionization. Determining the mechanisms of the individual steps is difficult because ion detection is affected by both processes as well as numerous instrumental parameters. Supplementary analysis methods, such as the fluorescence imaging of desorbed matrix particles, adds valuable information by characterizing one process at a time. By incorporating other supplementary methods we may further assist in understanding MALDI mechanistic events.

Secondary ionization techniques used in conjunction with laser desorption can provide a basis for examining the desorption process. By decoupling the ionization step, neutral populations can be independently studied. A variety of secondary ionization techniques (*e.g.*, electron and chemical ionization) have been used to determine neutral populations for vacuum laser desorption.<sup>198-199</sup> The studies revealed that neutral molecules were desorbed over longer times and in larger quantities than the ion populations. Vacuum MALDI has similar neutral molecule desorption properties. MALDI analysis yields  $\sim 10^4$  neutral molecules for every one ion produced.<sup>200-201</sup> Only a fraction of the total species present is then sampled by the mass spectrometer.

Previously, the Harrison research group introduced a secondary ionization technique for IR laser desorption.<sup>202-203</sup> In the technique, a corona discharge provided

reagent ions for the interaction with laser desorbed neutrals. This source has been referred as laser desorption atmospheric pressure chemical ionization (LD-APCI) for its combination of the two previously demonstrated techniques. Reagent ions from the corona discharge participate in chemical ionization reactions with neutral molecules produced during IR laser desorption.

This chapter focuses on applying the technique of atmospheric pressure chemical ionization with a corona discharge to a UV APMALDI source. The laser desorption process can be studied independently, allowing the corona discharge to probe neutral molecule formation at fluence thresholds. The key differences between the UV LD-APCI and the IR LD-APCI arrangements are the laser wavelength, mass analyzer, and AP inlet. Each of the above variations has played a significant role in how the more common UV MALDI laser, nitrogen 337 nm, has been applied to LD-APCI. IR lasers provide a larger population of neutrals and clusters, thus forming fewer ions.<sup>204</sup> The UV laser yields a reduced neutral/cluster population compared to the increased ion fractions from IR laser desorption. In previous IR LD-APCI experiments, an ion trap was utilized, which provided ion accumulation and temporal sampling. On the contrary, an oa-TOFMS, which operates asynchronously with the laser pulse, prevented ion accumulation from multiple laser pulses. Atmospheric pressure inlets dictate both arrangement of source potential fields and type of declustering method applied. Previously, declustering was done using a heated capillary inlet. The inlet extended out from the spectrometer. However, with the oa-TOFMS, cluster prevention is controlled by a nitrogen current gas, which directs large gas flows towards the sample. While each method provides benefits,

the source potential fields in the counter-current design are more space restricted, which is problematic for ion collection and transmission.

## **Experimental Method**

### **Atmospheric Pressure MALDI oa-TOFMS**

The atmospheric pressure MALDI source and the oa-TOFMS have been described in Chapters 2 and 3. The atmospheric pressure interface uses a heated counter-current nitrogen gas (100°C, 5 L·min<sup>-1</sup>) for cluster prevention. The ion transport field between the target and nozzle was 1100 V·mm<sup>-1</sup>. Gas pressures in the skimmer and RF-only quadrupole were 3 Torr and 10<sup>-1</sup> Torr respectively. As noted in Chapter 2, the laser source was a 337 nm nitrogen laser (VSL-337-ND-S, Spectra-Physics, Mountain View, CA, USA). Pulse energies ranged from ~5-180 μJ, measured directly using a pyroelectric detector (J4-09-030, Molectron Detector, Inc., Santa Clara, CA, USA). Variations in the energy transmitted to the sample originated from a gradient UV attenuating wheel (Reynard Corporation, San Clemente, CA, USA) and an adjustable iris (Edmund Optics Inc., Barrington, NJ, USA). Target positioning was accomplished using a piezoelectric transducer driven *xyz* stage (8302/IPico Driver, New Focus, San Jose, CA, USA). Mass spectra shown in this chapter are an accumulation of summed spectra for 1-5 minutes.

### **Corona Discharge**

The corona discharge was positioned using a flexible mount (flex lock 9940, New Focus, San Jose, CA, USA) and was attached to the mount with insulating connectors (Thorlabs, Newton, NJ, USA). High voltage, 0-12 kV, was applied using an external power supply (225-20, Bertan, Hicksville, NY, USA). Current was monitored directly on the power supply module. The needle distance was adjusted using a motorized *xyz* stage

(CMA-12CCCL/ESP300; Newport, Irvine, CA, USA). The optimal position for the needle was on-axis with orifice and 10 mm away. Relative to the target, the needle was ~8 mm back and 2 mm above. A sample executable file, Object 6-1, of the LD-APCI arrangement demonstrates the configuration. The executable file was produced using a computer aided drawing program (Solid Works, Concord, MA, USA) and shows a scaled view of the target, corona needle, and AP interface.

Object 6-1. A file showing the orientation of the LD-APCI source (1.8mb, LDAPCI.exe, repeating play file).

Figure 6-1 is a diagram of the laser desorption atmospheric pressure chemical ionization source. Figure 6-2 displays a photograph of the LD-APCI source.

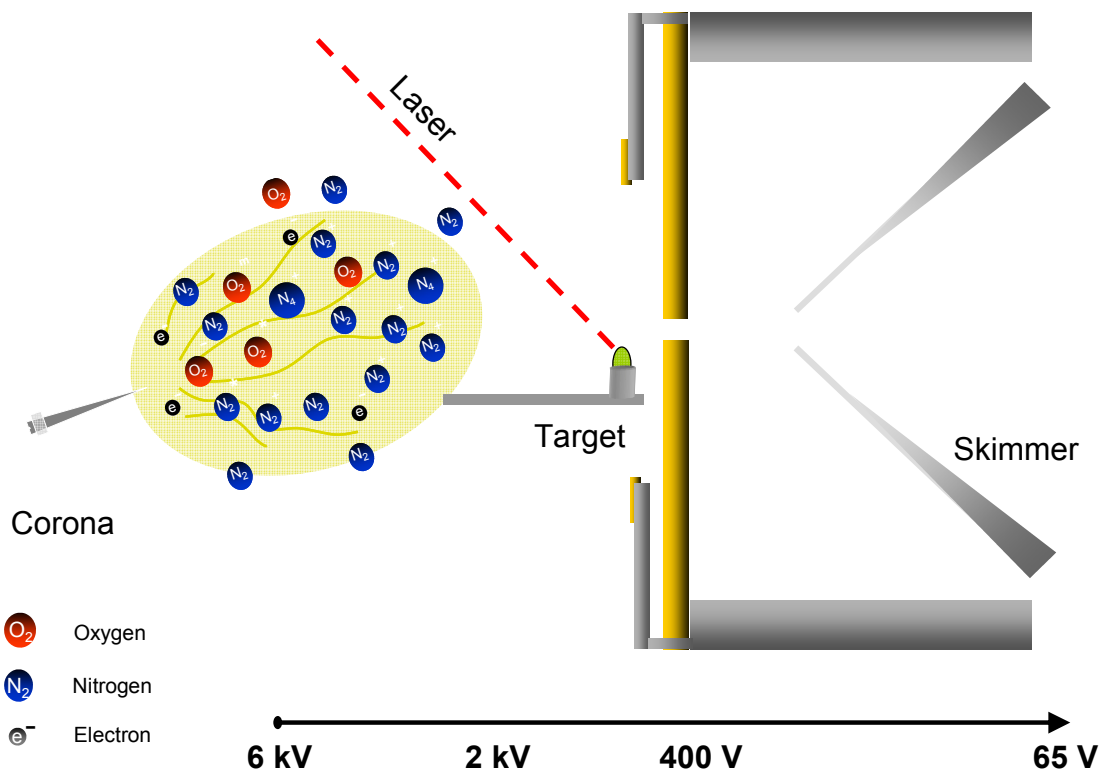


Figure 6-1. A diagram of the laser desorption atmospheric pressure chemical ionization source is shown. The orientation of the corona needle, target, laser, and interface can be seen.

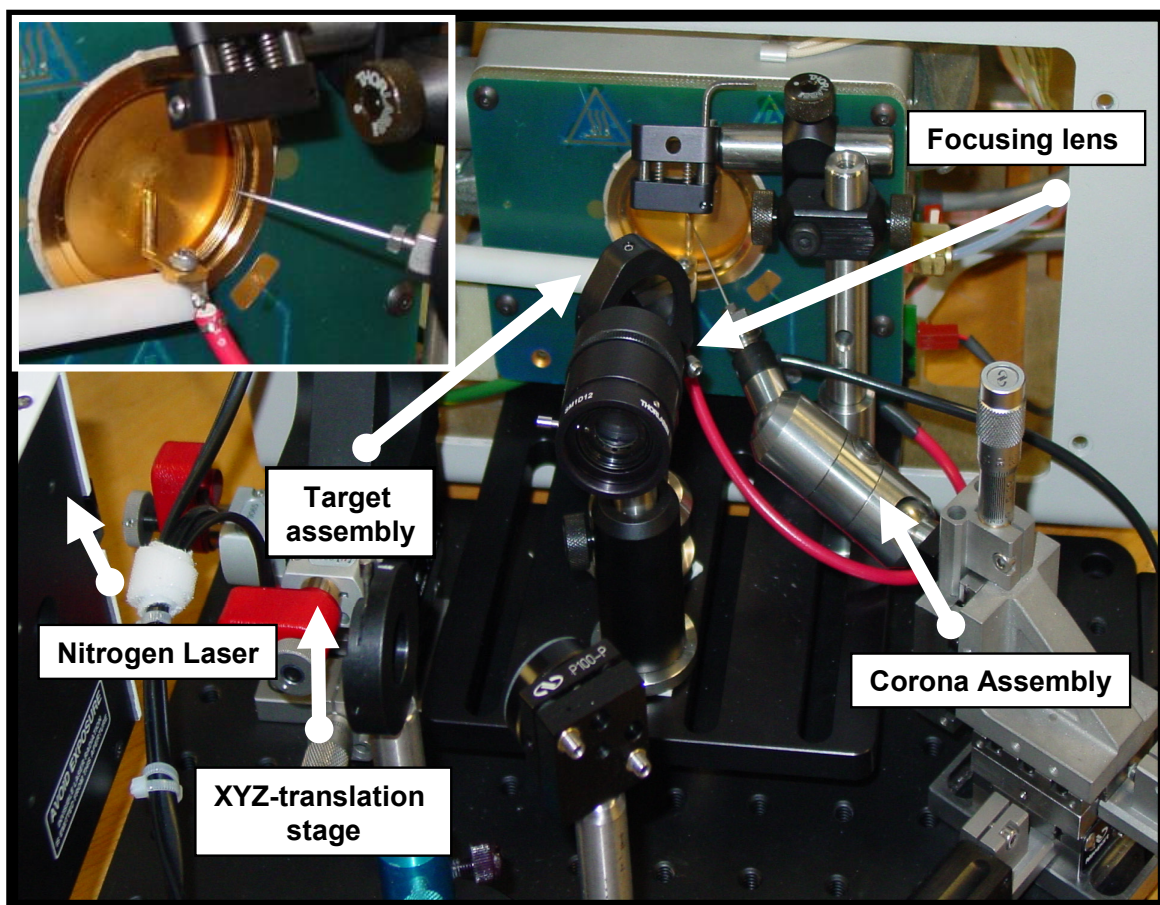


Figure 6-2. A photograph of the LD-APCI source is shown. The corona needle has been added to an atmospheric pressure matrix-assisted laser desorption/ionization source. The corona needle assembly is positioned by an *xyz* translational stage and held in place using a flexible lock mount.

### Matrix and Analytes

Liquid matrices were prepared by mixing  $\alpha$ -cyano-4-hydroxycinnamic acid (CHCA) with a liquid support. The liquid support was equal parts of 50% aqueous ethanol and diethanolamine (DEA). Chromophore concentration, CHCA, was 600 mM. To ensure homogeneity and dissolution, the matrix solution was sonicated for 10-15 minutes. Immediately before analysis the matrix was vortexed for 10 seconds. For each

analysis, 0.5  $\mu\text{L}$  analyte solution and 0.5  $\mu\text{L}$  matrix solution were deposited on target, and in the order presented.

For direct analysis, analytes were prepared in aqueous 0.1% TFA. Stock solutions of analyte were prepared at 50  $\text{pmol}\cdot\mu\text{L}^{-1}$ , and diluted as noted. All analytes (angiotensin II, bradykinin fragment 1-7, bradykinin, reserpine, and spiperone), matrix, and solvents were used unpurified (Sigma Aldrich, St. Louis, MO, USA).

## Results and Discussion

### Secondary Ionization of Desorbed Neutrals

Initial experiments demonstrated reagent ions interacting with UV laser desorbed neutral molecules, producing protonated molecular ions. The source was operated with the corona discharge powered on and off while using APMALDI desorption for neutral formation. Figure 6-3 shows the total ion chromatogram as the source is operated in three different modes: LD-APCI, corona only, and APMALDI.

In all three source modes, the target was maintained at the same position and only the corona voltage and/or the laser were turned on or off. Increased ion signal intensity is present with the corona discharge added to UV laser desorption. The reagent ions formed from the atmospheric pressure discharge allowed ionization of MALDI neutrals. In the APMALDI and LD-APCI modes, the laser power was attenuated providing minimal laser fluence. The lower fluence reduced the laser desorption ion signals allowing increases from reagent ions to be viewed. Reduced fluence was obtained by limiting the pulse energy with a neutral density filter wheel and then altering the diameter of a variable iris placed after the laser beam output. With the iris diameter at  $\sim 3$  mm, pulse energy was reduced to  $\sim 8$   $\mu\text{J}$ .

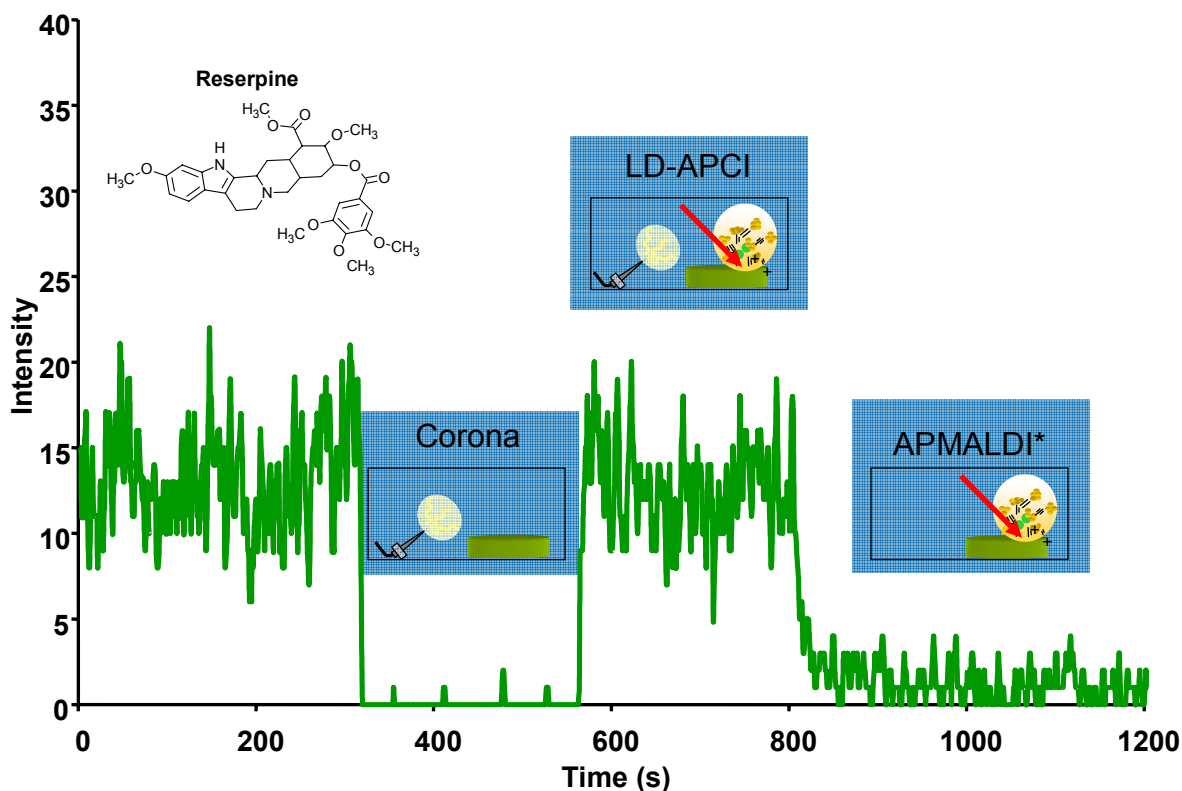


Figure 6-3. The total ion chromatogram for three modes of source operation is shown. Total ion counts were monitored for LD-APCI, corona only, and low fluence APMALDI modes.

The laser spot size was altered to  $\sim 200 \mu\text{m}$  yielding a fluence of  $\sim 250 \text{ J}\cdot\text{m}^{-2}$ . Therefore, with the corona needle off, the source should be considered attenuated APMALDI. A comparison of the optimal APMALDI conditions versus LD-APCI shows much larger analyte ion intensity for APMALDI. Mass spectra demonstrating the APMALDI and LD-APCI modes are shown in Figures 6-4A and 6-4B, respectively.

A weak APMALDI ion signal, due to the attenuated laser flux, could be enhanced when the corona discharge was operated. While numerous differences were present for UV LD-APCI versus IR LD-APCI, results show that ion molecule reactions still occur.

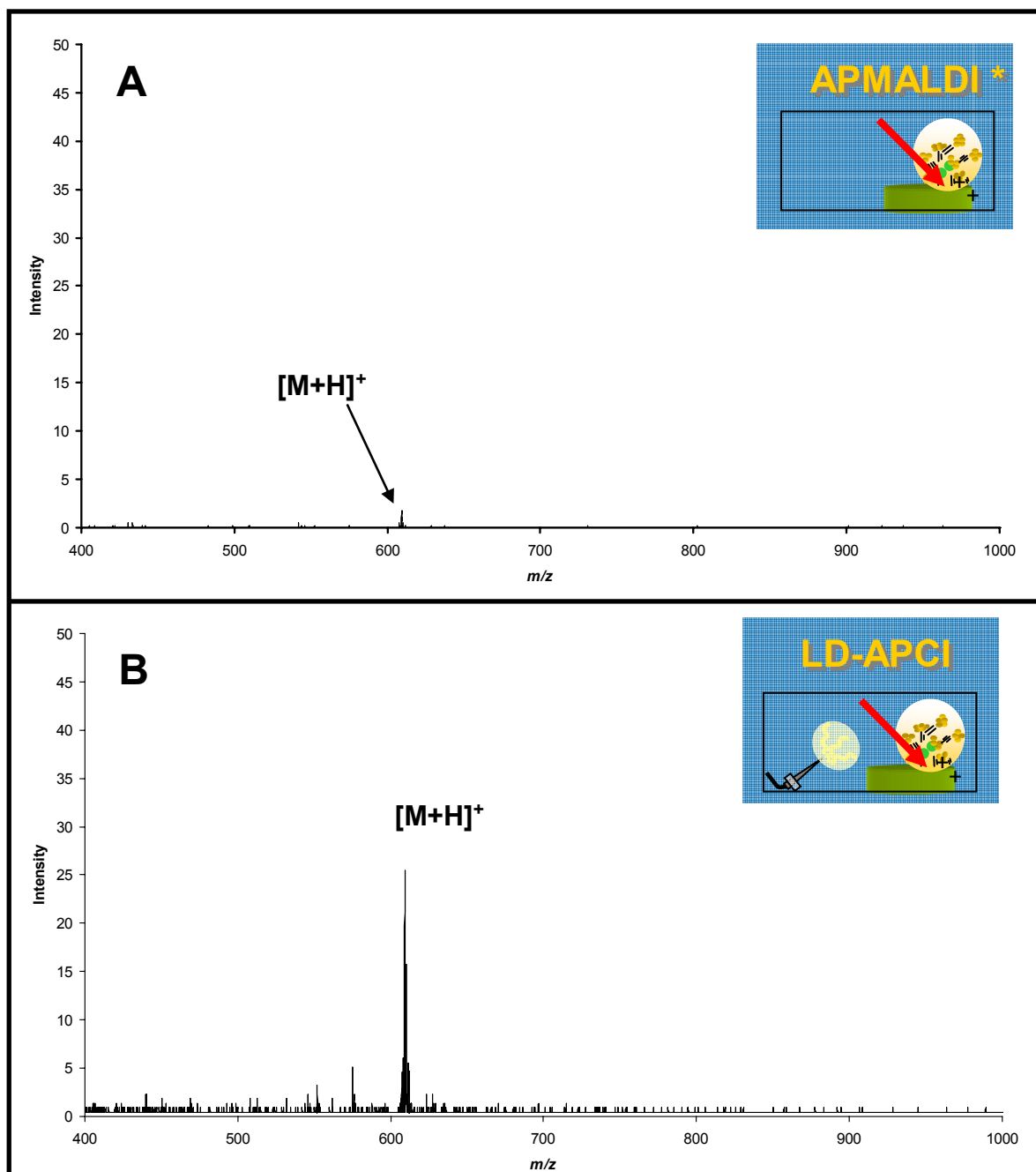


Figure 6-4. Mass spectra for reserpine using a CHCA liquid matrix in A) APMALDI and B) LDAPCI source modes are shown. Each spectrum was a 1 minute summation. The mass spectra correspond to the ion chromatogram in Figure 6-3.

## Corona Discharge

The two-step approach used in LD-APCI (laser desorption and then chemical ionization) affords additional analytical utility, but requires individual optimization. Both the laser desorption and the corona discharge processes must be characterized to evaluate the technique.

For the corona discharge, the needle voltage plays a vital role. Evaluating needle potentials has shown that the discharge can transition from a corona discharge to glow discharge as voltage is increased. Additionally, during the process, ion signal intensities drop.

## Discharge mode

The discharge mode affects LD-APCI signal intensities. The corona discharge mode allows ion signal increases; however, when the discharge moves to the glow mode, degradation of ion signals occurs. Townsend's semi-empirical relationship for a corona discharge provides a means to distinguish discharge transitions.<sup>204-205</sup> Equation 6-1 presents the Townsend semi-empirical relationship:

$$I = kU(U - U_0) \quad (6-1)$$

where  $I$  is corona current,  $U$  is potential difference across electrodes,  $U_0$  is the onset voltage of the corona discharge (a function of corona needle geometry), and  $k$  is a factor that is inversely proportional to the gas density and interelectrode distance.

A linear relationship holds for a corona discharge, but not for a glow discharge. As the relationship turns to exponential increase, the system moves from a corona to a glow. By plotting  $I/U$  versus  $U$  the transition to a glow discharge can be determined.

Figure 6-5 shows the transition from a corona to glow discharge occurring at 9 kV with 16  $\mu\text{A}$  of current.

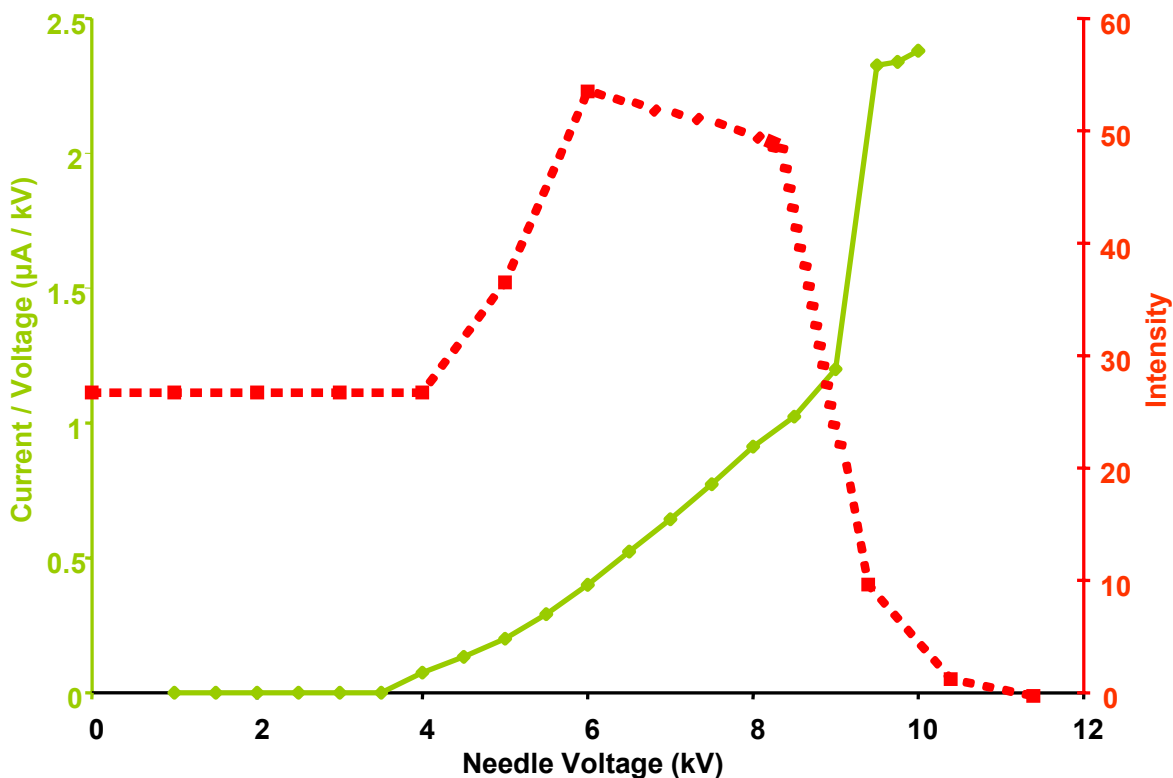


Figure 6-5. The figure shows the transition from a corona to glow discharge. The intensity for the angiotensin II molecular ion was tracked during this transition. The molecular ion reaches a maximum before the transitions occurs.

Needle distance from the orifice is  $\sim 8$  mm. The intensity for the angiotensin II molecular ion was tracked during this transition. The molecular ion reaches a maximum before the transition occurs.

### Water clusters

The reagent ions created from the corona discharge at atmospheric pressure have been studied numerous times.<sup>206-208</sup> Reagent ion populations for atmospheric pressure

chemical ionization are primarily solvated protons.<sup>12</sup> The steps for positive reagent ion formation are:



followed by water clustering. The dominant positive reactive ions are  $H^+(H_2O)_n$ , the value of  $n$  depending on the partial pressure of water in the air. Providing the proton affinity for the analyte is greater than that of the reagent ion, a proton transfer reaction will occur. The proton affinity for monosolvated water is  $166.5 \text{ kcal mol}^{-1}$ ; therefore, analytes with a higher proton affinity will be protonated. Most nitrogen containing species exhibit proton affinities that range from 205 to  $240 \text{ kcal mol}^{-1}$ . Thus, peptides and small molecule pharmaceuticals present an avenue for a proton transfer reactions.

When the desorption target was removed and the heated counter-current gas flow turned off (reducing cluster prevention), reagent ions produced from the corona discharge could be sampled. Figure 6-6 shows a mass spectrum collected with the corona needle placed  $\sim 10 \text{ mm}$  from the inlet orifice. The voltage was set at 6 kV with the current near  $13.5 \mu\text{A}$ . The peaks detected between  $m/z$  50 - 200 represent a series of water clusters. This data verifies that reagent ions are being formed when the corona discharge is activated at ambient conditions.

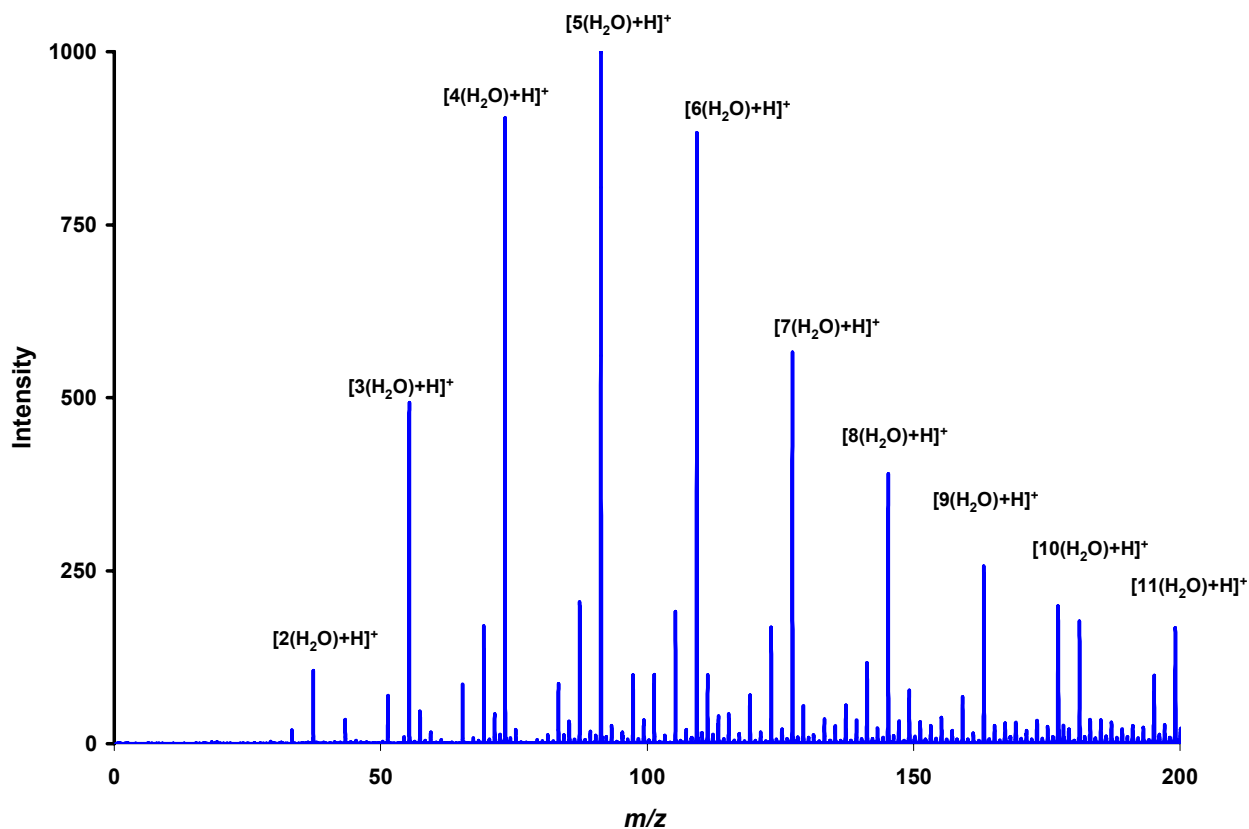


Figure 6-6. A mass spectrum of the water clusters produced from the corona discharge in air is shown. The corona needle had a  $\sim 50 \mu\text{m}$  radius at the tip, and was in a point-to-plane configuration with the inlet orifice. The distance from tip to inlet was 10 mm. Applied voltage was 6 kV.

### Neutral Molecule Fluence Threshold

Reducing the laser fluence below the ion threshold fluence for APMALDI yields no ions during the laser desorption step. For LD-APCI, ion detection resulted from ion-molecule reactions with the neutral population. Probing the neutrals created at atmospheric pressure was possible by using the reagent ions formed from the discharge. Figure 6-7 shows the voltage dependence of an analyte ion signal, bradykinin 1-7, when using a corona discharge with low fluence laser desorption ( $\sim 100 \text{ J}\cdot\text{m}^{-2}$ ).

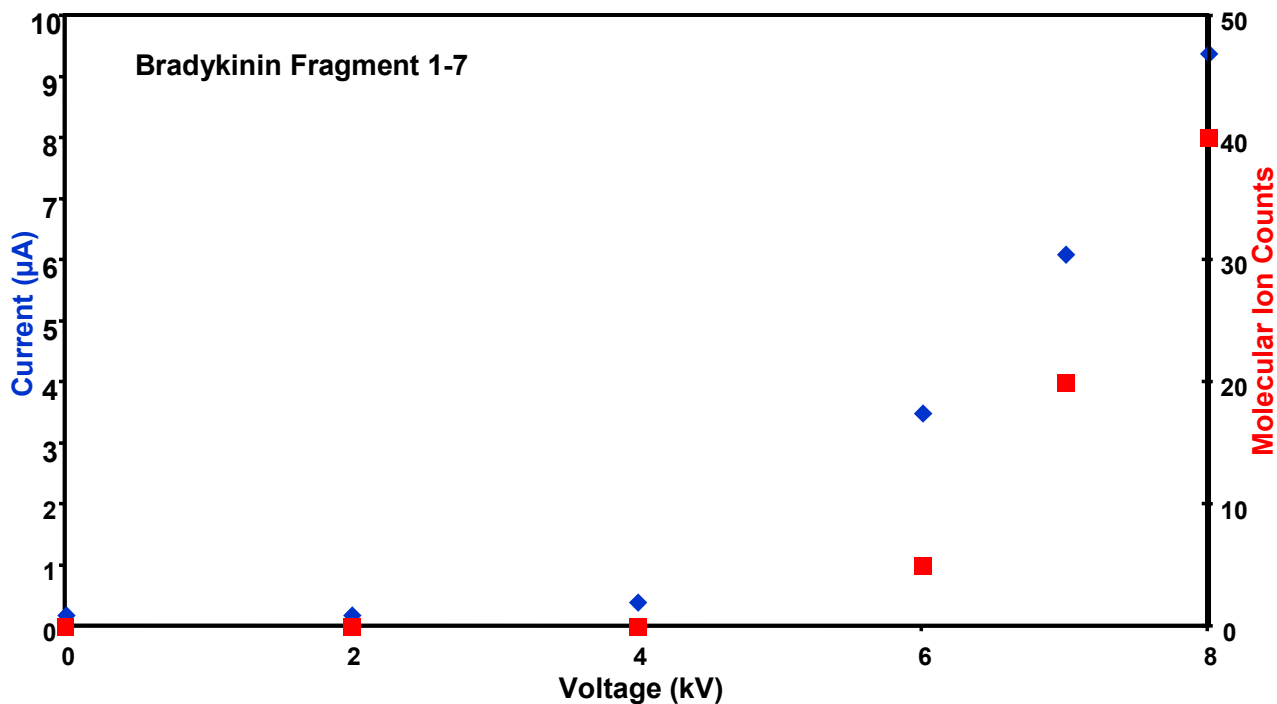


Figure 6-7. A plot of the analyte ion intensity and corona current as the needle voltage was adjusted with low fluence laser desorption. The analyte is bradykinin fragment 1-7.

The spectra confirmed that neutral molecule populations exist below ion threshold levels. As the voltage was increased, the current shows that reagent ions begin to be produced. Once the current was near 4  $\mu\text{A}$  the analyte ion signals increased through ion-molecule reactions. At a corona voltage of zero, ion production is from laser desorption only, so ions were produced. Ions are detected only with the corona on.

Figures 6-8, 6-9, and 6-10 demonstrate neutral molecule probing using the corona discharge as a secondary ionization source. Keeping the fluence just below ion threshold values allows for ion-molecule reactions from the water cluster reagent ions to produce protonated molecular ions. The fluence was maintained throughout the experiments.

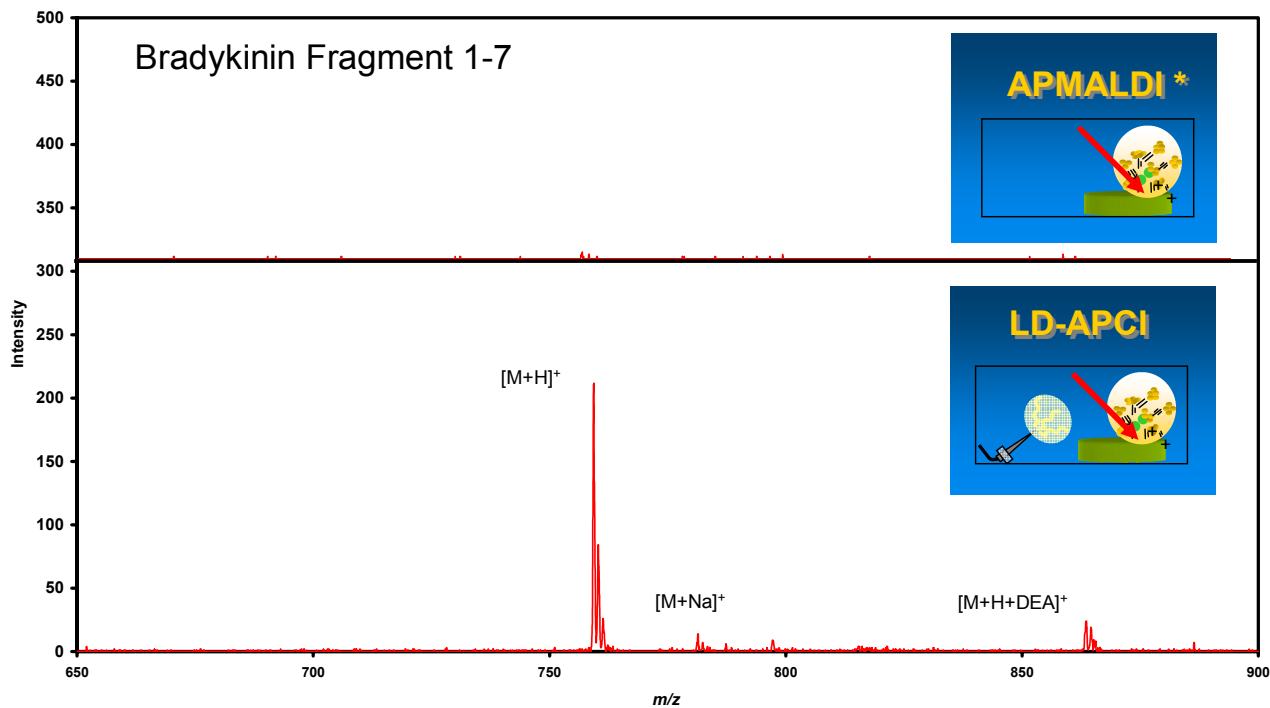


Figure 6-8. Mass spectra of bradykinin fragment 1-7 using low fluence APMALDI and LD-APCI modes are shown. The corona discharge enables protonated molecular ions to be produced for bradykinin fragment 1-7; 25 picomoles were placed on target. Each spectrum is a 5 minute sum.

The corona discharge, acting as a secondary ionization technique, did not result in enhanced UV APMALDI signals. The production of ions was only seen during lower fluence studies. Figure 6-11 shows the production of protonated molecular ions using higher fluence values ( $\sim 600 \text{ J}\cdot\text{m}^{-2}$ ); pulse energy of  $60 \mu\text{J}$  and a laser spot size of  $\sim 300 \mu\text{m}$  were used with no iris attenuation.

With the larger population of neutrals present during desorption the stagnation or reduction of ion signals with increasing corona voltage was puzzling. To further investigate the negative effects of the corona discharge, details of the ion transmission were sought.

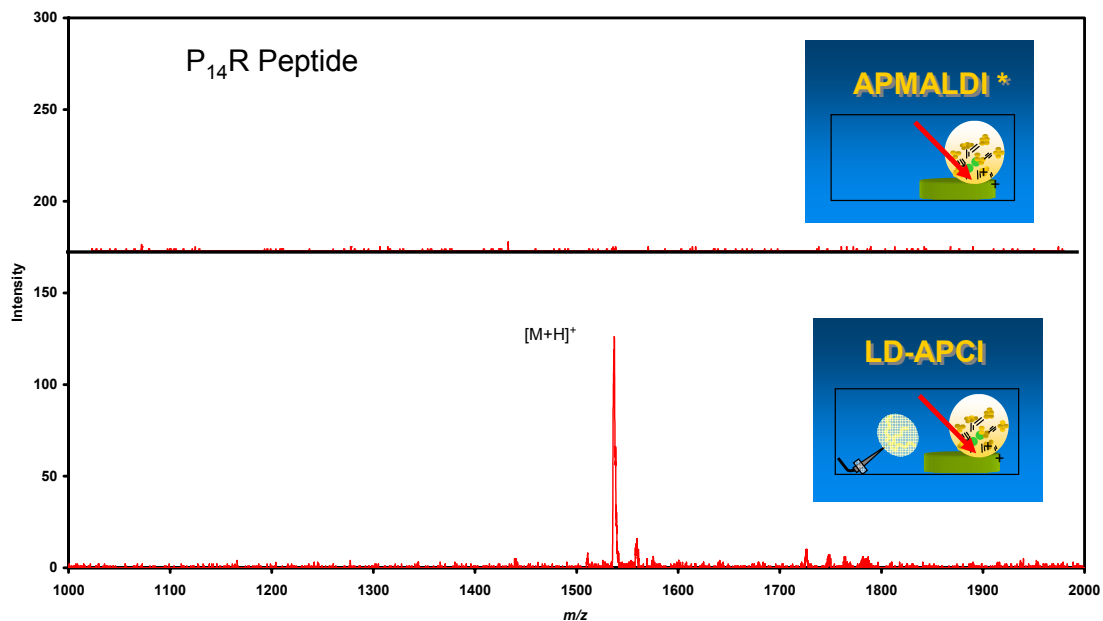


Figure 6-9. Mass spectra for P<sub>14</sub>R using low fluence APMALDI and LD-APCI modes is shown. The corona discharge enables protonated molecular ions to be produced for P<sub>14</sub>R; 25 picomoles were placed on target. Each spectrum is a 5 minute sum.

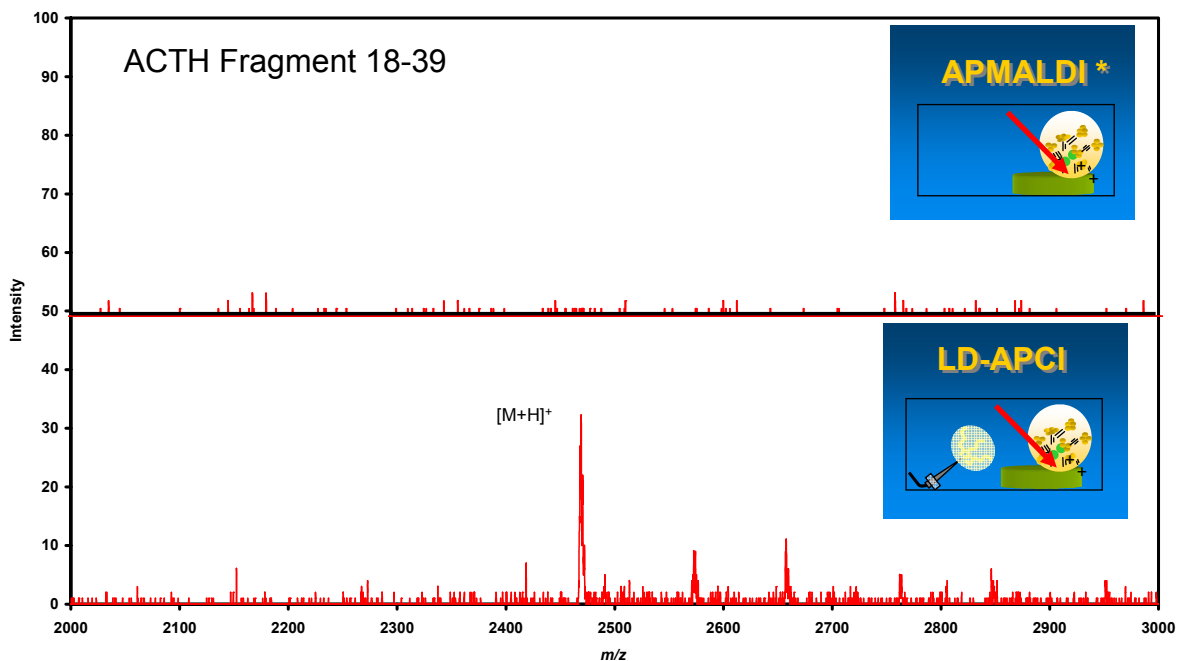


Figure 6-10. Mass spectra for ACTH fragment 18-39 using low fluence APMALDI and LD-APCI modes is shown. The corona discharge enables protonated molecular ions to be produced for ACTH fragment 18-39; 25 picomoles were placed on target. Each spectrum is a 5 minute sum.

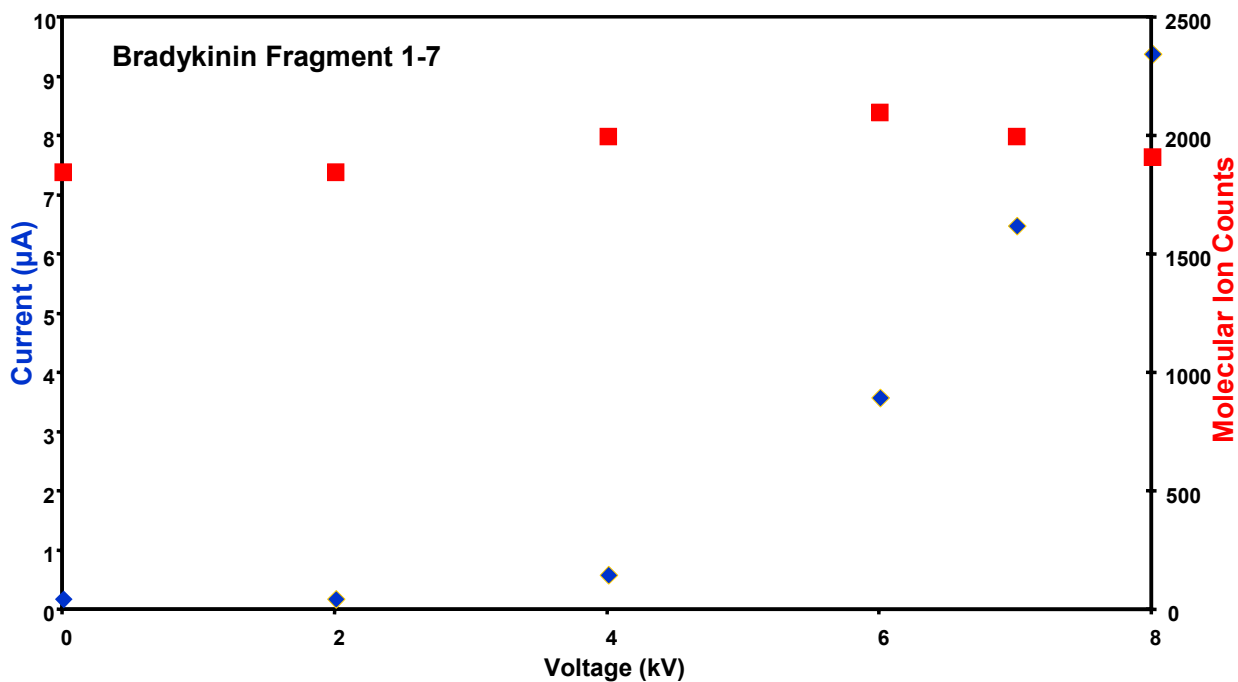


Figure 6-11. A plot of the analyte ion intensity and corona current as the needle voltage was adjusted with high fluence laser desorption. The analyte is bradykinin fragment 1-7.

### Ion Transmission

Potentials over 8 kV on the corona needle resulted in reductions in the analyte ion signals. This can be attributed to ion collection problems from the high potential fields created at the needle point. Increased voltages altered the potential fields, which are required for effectively transferring ions into the mass spectrometer. The corona acts as an intense point source. For both APMALDI and LD-APCI, potential fields for ion transport were critical. Additional evidence of the corona discharge disturbance was seen with the major deviations in signal from needle positioning. At ~2 mm above the target and 10 mm from the orifice the system operated well. Movements beyond 0.5 mm in any direction resulted in no ions detected.

Ion collection problems may also be a factor for the diminished LD-APCI signals at higher laser fluence. The ions present for APMALDI create a region of higher space charge preventing corona reagent ions from entering the orifice. Ion transmission was approximated using an ion optics computer modeling software program (SIMION 3D 7.0, Scientific Instrument Services, Ringoes, NJ, USA). Dr. Tony Appelhans, Idaho National Laboratory, compared SIMION models for both the APMALDI and LD-APCI arrangements. It was determined that at higher voltages, the potential fields needed to transport ions into the mass spectrometer orifice were disturbed. Only operating at lower voltages, or with a different source arrangement, could an enhancement of APMALDI signals occur.

### **Conclusions**

The construction of a UV LD-APCI source and its characterization was demonstrated in this chapter. Atmospheric pressure chemical ionization, an established ion production technique, allowed secondary ion-molecule reactions to probe the neutral molecules produced from UV laser desorption by attenuating the laser. The addition of secondary ionization processes may prove useful not only as an IR MALDI enhancement technique, but also as a methodology to probe atmospheric pressure UV desorbed neutral populations.

## CHAPTER 7 CONCLUDING REMARKS

Research in genomics, proteomics, and systems biology has necessitated improvements in biomolecule analysis. In particular, the technique of biological mass spectrometry has received well-deserved attention for its role in biopolymer characterization. The expansion of biological mass spectrometry can largely be attributed to the development and characterization of two complementary ionization sources, electrospray ionization (ESI) and matrix-assisted laser desorption/ionization (MALDI). Our research contributes in this area by expanding upon atmospheric pressure ionization techniques, in particular MALDI, and the unique applications available to them.

For MALDI analysis a suitable matrix for energy absorption and transfer to the analyte is required. Recent advances allow atmospheric pressure MALDI sources to be coupled to a variety of mass analyzers. The ambient conditions available extend matrix formulations from solid crystalline formats to homogeneous liquid sampling systems. Ultraviolet compatible liquid matrices have not been previously studied at AP, and allow possible variations focused on desorption and ionization. The liquid matrices we examined provided self-renewing surfaces that eliminated sampling heterogeneity, increased sample lifetime, and offered shot-to-shot reproducibility. Liquid sampling also allows measurements for laser penetration depth, solution viscosity, and chromophore concentration. Together these fundamental studies contribute to the fundamental knowledge of MALDI.

With formulation studies of the liquid matrices completed, the focus shifted to characterizing the desorption and ionization processes inherent for liquid systems. While the details of ion formation in MALDI are still heavily debated, parametric studies relating laser variables to analyte signals must be conducted for application development. The measurements made throughout this dissertation provide a basis for further atmospheric pressure liquid matrix applications.

Variations in laser parameters allowed for the characterization of the laser-liquid interface. Optimized fluence is both matrix and pressure dependent; therefore, fluence levels were adjusted while monitoring analyte ion yields. The liquid matrix at AP tolerated higher fluences while providing protonated molecular ions and minimal fragmentation. At the highest pulse energies, fragmentation and particle ejections played a role in decreasing analyte ion intensities. At higher pulse energies, nanometer sized particles were ejected in conjunction with a decay in analyte ions. Ion yields can be related directly to laser parameters, yet MALDI plume interactions also played a large role in their intensities, as demonstrated through analyte signal suppression studies.

Additionally, the examination of liquid versus solid matrices suggests the possibility of softer ionization. Liquids provide added absorption of laser energy without increased analyte fragmentation. A softer ionization process and reproducible long-lasting ion signals may allow the liquid matrix to be used in high-throughput automation analyses. The liquid matrix offers advantages that complement current MALDI methods.

Liquid sampling reduces sample preparation, compared to solid matrices; however, during biological analysis separations are often the rate determining step. We have explored further reductions in preparation time for biomolecules with the use of

nanoparticles as a rapid analyte extraction technique. Using known material types and functionalization chemistry, C18 and aptamer functionalized nanoparticles can act as scavenging agents for peptide molecules. Placing the particles directly into the liquid matrix allows a rapid analysis procedure that limits analyte loss and provides an improved preconcentration of the analyte. The C18 functionalized silica particles allows extraction of a variety of peptides simultaneously while mass spectrometry analysis can be done directly in the liquid matrix. Functionalized nanoparticles provided specific extraction, retention, and concentration of simple biopolymers. The aptamer nanoparticles allowed the selective extraction of reduced D-vasopressin even in the presence of a structural analog. This approach introduces nanoparticles as an extraction and concentration mechanism for low abundance analytes in complex systems. These methods provide an avenue for advancement in liquid APMALDI sample preparation procedures. More importantly, with an increasing number of available aptamers and the growing interest in their applications, an array of particles for specific mass spectrometry analyses could result. While the mechanistic aspects of the MALDI process are still unknown, applications involving the technique are thriving.

While still extensively debated, the MALDI process involves some combination of desorption and ionization. During these processes, a large population of neutral molecules is created in the MALDI plume. Studies to date have revealed that in MALDI, for every  $10^4$  molecules desorbed perhaps only 1 ion is produced. Supplemental ionization techniques can offer a clear view of the majority species (*i.e.*, neutral molecules) produced during MALDI. At atmospheric pressure conditions, experimentation on the available neutrals can be accomplished. Using reagent ions from

an atmospheric pressure corona discharge we are able to probe the MALDI plume. We conducted experiments with a UV laser to study the details of the ion-neutral interactions. Important in the addition of a secondary ionization is the population of reagent ions and the ion transfer parameters. Preliminary results have shown that UV laser desorbed neutrals do interact with atmospheric pressure reagent ions; however, the individual optimization of each process is needed. We expect this technique to offer insight into several pressing questions in the MALDI mechanisms. The neutral molecules provide an avenue for enhancing limits of detection, ionizing non-ionized analytes, and probing ion-molecule chemistry.

The construction of an APMALDI ionization source and its characterization using UV liquid matrices is shown. Ambient conditions present at AP allow new opportunities for matrix development. The addition of secondary ionization processes may prove useful not only as an enhancement technique, but also as a methodology to probe neutral populations at low laser fluence levels in APMALDI. Liquid matrices and other interesting applications are possible with a simple atmospheric pressure source. The exploitation of AP interfaces with atmospheric pressure laser desorption techniques can provide needed advances in biological analysis.

Further research into the use of liquid matrices and their inherent applications may also demonstrate added analytical utility. Studies should embrace additional chromophores and other analyte classes. While the liquid matrix provides immediate benefits for APMALDI analysis with its ease of use, liquid matrix possibilities include an on-line liquid UV APMALDI ion source for chromatography and reaction monitoring.

Nanoparticle use with liquid APMALDI also presents interesting applications for bioanalytical analysis. Studies focusing on analyte-nanoparticle incubation ratios, functional group selectivity, and complex mixture extraction will provide further evidence for nanoparticle usage in biological mass spectrometry. Optimizing the nanoparticle synthesis and washing procedures will be useful for further experimentation. An evaluation of the particle capacity and extraction efficiency will also prove helpful for the possibility of quantitative studies.

During the optimization of the APMALDI source, the focus was on increasing reproducibility and analytical utility; however, there are possibilities for signal-to-noise enhancement. The MALDI source uses a laser pulse not synchronized to the TOF repeller pulse. At a laser repetition rate of  $\sim 20$  Hz a semi-continuous ion stream is produced. Since the liquid matrix offers continuous sampling without laser repositioning, the use of a high repetition rate solid-state UV laser could provide signal increases. Higher laser frequencies yield more overlap for individual ion packets producing a denser ion beam.

Alternatively, decreasing the laser frequency may reduce chemical noise. By gating the acquisition for each laser pulse, background ions can be discriminated against. Preliminary results have shown individual ion packets present regions of maximum analyte signal and minimum chemical background. The evaluation of temporal properties present for APMALDI could allow the optimization of the source as well as provide benefits for secondary ionization additions.

There are many aspects of the UV LD-APCI source that still must be considered. For the immediate future, a redesign of the source interface should assist in optimizing

the potential fields for ion collection and transmission. Our initial studies have shown that as the discharge transitions from a corona discharge to a glow discharge, ion signal intensity drops. At this time, it is not clear whether the reagent ions produced in each discharge mode directly affect ionization efficiency or if field disturbances are the sole factor. Source parameters should be empirically and theoretically studied using prototype sources and SIMION modeling. The inclusion of fluid dynamics calculations may assist in evaluating ion collection at atmospheric pressure. The development of the LD-APCI source also suggests the use of reagent gas studies. A detailed understanding of reagent ion populations and interactions may allow selective ion-molecule interactions in the APCI environment.

## APPENDIX MALDI MATRICES AND PREPARATION

### **MALDI Matrices**

A variety of matrix-assisted laser desorption/ionization (MALDI) matrices are used on a regular basis. While not all matrices are routine, each seems to have its own unique properties: enhanced ionization for a chemical class, reduced background for a sample matrix, or eases preparation protocol for convenient use. Listed in Table A-1 are the more common MALDI matrices.

### **Preparation Protocols**

MALDI preparation protocols are often as daunting to choose as the MALDI chromophore itself. Additional preparation protocols are being introduced — even this dissertation seems to suggest an advanced approach. While each preparation protocol provides benefits, there are some standard solid matrix preparations that seems to work well for general analyses. However, the author is biased towards atmospheric pressure liquid preparations.

#### **Dried-Droplet**

This is the original sample preparation procedure introduced in 1988 by Hillenkamp and Karas.<sup>3,36-37</sup> While modifications in the process exist, the basic procedure is relatively simple. A portion of matrix solution is mixed with an analyte solution left to dry. The result is a solid deposit of analyte-doped matrix crystal. One benefit of this protocol method is that the analyte/matrix crystals may be washed to

remove non-volatile components (*i.e.*, interfering salts).<sup>42</sup> This method tolerates some salts in mM concentrations and is a good choice for mixtures of proteins or peptides.

### **Vacuum-Drying**

A slight variation on the dried-droplet method is the addition of vacuum drying for crystallization. In this method, the final analyte/matrix drop applied to the target is dried in a vacuum chamber. Vacuum-drying can reduce the size of the analyte/matrix crystals, which may assist with crystal homogeneity.<sup>9-10</sup>

### **Fast-Evaporation**

The fast-evaporation method was introduced with the main goal of improving the resolution and mass accuracy of MALDI measurements.<sup>42</sup> Matrix and sample are handled separately. First, the matrix solution is deposited onto the target and allowed to evaporate. Next, on top of the matrix, the analyte solution is deposited and allowed to dry. The process delivers stable and long lived matrix films that can be used to precoat MALDI targets.<sup>10</sup>

Table A-1. Common MALDI matrices. The typical laser wavelength and chemical classes used are also listed; however, these are only guidelines not requirements.

Matrix	Mass (Da)	Laser $\lambda$ (nm)	Analyte Class
3-Amino-4-hydroxybenzoic acid	153	337	Oligosaccharides
2,5-Dihydroxybenzoic acid (DHB)	154	266,337,355	Oligosaccharides, peptides, nucleotides, oligonucleotides
5-Hydroxy-2-methoxybenzoic acid	168	337	Lipids
2[4-hydroxyphenylazo]benzoic acid (HABA)	242	266,337	Proteins, lipids

Table A-1. Continued.

Cinnamic acid	148	337	General?
$\alpha$ -Cyano-4-hydroxycinnamic acid (CHCA)	189	337,355	Peptides, lipids, nucleotides
4-Methoxycinnamic acid	178	266,337,355	Proteins
Sinapinic acid	224	266,337,355	Lipids, peptides, proteins
Ferulic acid	194	266,337,355	Proteins
6,7-Dihydroxycoumarin (esculetin)	178	337	Lipids, peptides
3-Hydroxypicolinic acid (HPA)	139	337,355	Oligosaccharides
Picolinic acid (PA)	123	266	Oligosaccharides
3-Aminopicolinic acid	138	266,337,355	Oligosaccharides
6-Aza-2-thiothymine (ATT)	143	266,337,355	Oligosaccharides, lipids
2,6-Dihydroxyacetophenone	152	337,355	Proteins, oligonucleotides
2,4,6-Trihydroxyacetophenone	168	337,355	Oligonucleotides
Nicotinic acid	123	266,337,355	Proteins, oligonucleotides
1,5-Diaminonaphthalene	158	337	Lipids
Succinic acid	118	2940	Oligosaccharides
Urea	46	2940	Oligosaccharides
Caffeic acid	180	337	Peptides, proteins
Glycerol	92	2940, 10600	Peptides, proteins
4-Nitroaniline	138	337	Peptides, proteins

## LIST OF REFERENCES

1. Nier, A. O. *Science* **1955**, *121*, 740.
2. *Measuring Mass: From Positive Rays to Proteins*; Grayson, M. A., Ed.; Chemical Heritage Press: Philadelphia, **2002**.
3. Thompson, J. J. *Carriers of Negative Electricity*, Nobel Lecture, Aula Magna, Stockholm University, December 11, **1906**.
4. McLafferty, F. W. *Science* **1966**, *151*, 641-649.
5. Dempster, A. J. *Physics Reviews* **1918**, *11*, 316-325.
6. Neir, A. O. *International Journal of Mass Spectrometry and Ion Processes* **1990**, *100*, 1-13.
7. Bleakney, W. *Physics Reviews* **1929**, *34*, 157.
8. Nier, A. O. *Review of Scientific Instruments* **1947**, *18*, 415.
9. *Mass Spectrometry: A textbook*, Gross, J. H., Springer: New York, **2004**.
10. *Mass Spectrometry: Principles and Applications*, 2<sup>nd</sup> ed., Hoffmann, E.; Stroobant, V., John Wiley and Sons: New York, **2003**.
11. *Interpretation of Mass Spectra* 4<sup>th</sup> ed., McLafferty, F. W.; Tureček, F., University Science Books: Mill Valley, **1993**.
12. *Chemical Ionization Mass Spectrometry* 2<sup>nd</sup> ed., Harrison, A. G., CRC Press: Boca Raton, **1992**.
13. Tanaka, K. *Angewandte Chemie International Edition* **2003**, *42*, 3861-3870.
14. Beuhler, R. J.; Flanigan, E.; Green, J.; Friedman, L. *Journal of the American Chemical Society* **1974**, *96*, 3990-3999.
15. Macfarlane, R. D.; Torgerson, D. F. *International Journal of Mass Spectrometry and Ion Physics* **1976**, *21*, 81-92.
16. Macfarlane, R. D.; Torgerson, D. F. *Science* **1976**, *191*, 920-925.

17. Cotter, R. *Analytical Chemistry* **1988**, *50*, 781A.
18. Sundqvist, B.; Macfarlane, R. D. *Mass Spectrometry Reviews* **1985**, *4*, 421-460.
19. Barber, M.; Bardoli, R. S.; Sedgwick, R. D. *Journal Chemical Society Chemical Communications* **1981**, 325.
20. Barber, M.; Bordoli, R. S.; Sedgwick, R. D.; Tyler, A.N. *Nature* **1981**, *293*, 270-275.
21. Honig, R. E. *International Journal of Mass Spectrometry and Ion Processes* **1995**, *143*, 1-10.
22. Barber, M.; Bordoli, R. S.; Elliott, G. J.; Sedgwick, R. D.; Tyler, A.N. *Analytical Chemistry* **1982**, *54*, 645A-657A.
23. Meili, J.; Seibl, J. *International Journal of Mass Spectrometry and Ion Physics* **1983**, *46*, 367-370.
24. De Pauw, E.; Agnello, A.; Derwa, F. *Mass Spectrometry Reviews* **1991**, *10*, 283-301.
25. Todd, P.J. *Organic Mass Spectrometry* **1988**, *23*, 419-424.
26. Miller, J. M.; Balasanmugam, K. *Analytical Chemistry* **1989**, *61*, 1293-1295.
27. van Breemen, R. B.; Snow, M., Cotter, R. J. *International Journal of Mass spectrometry and Ion Physics* **1983**, *49*, 35-50.
28. Shiea, J.; Sunner, J. *Organic Mass Spectrometry* **1991**, *26*, 38-44.
29. Sundqvist, B.U.R. *International Journal of Mass Spectrometry and Ion Processes* **1992**, *118/119*, 265-287.
30. Vastola, R. *Organic Mass Spectrometry* **1970**, *3*, 101.
31. *Time-of-Flight Mass Spectrometry: Instrumentation and Applications in Biological Research*, Cotter, R. J., American Chemical Society: Washington, DC, **1997**.
32. Wilkins, C. L.; Weil, D. A.; Yang, C.L.C.; Ijames, C.F. *Analytical Chemistry* **1985**, *57*, 520-524.
33. Posthumus, M. A.; Kistemaker, P. G.; Meuzelaar, L. C.; Ten Noever de Brauw, M. C. *Analytical Chemistry* **1978**, *50*, 985-991.
34. Tanaka, K.; Waki, H.; Ido, Y.; Akita, S.; Yoshida, Y.; Yhoshida, T. *Rapid Communications in Mass Spectrometry* **1988**, *2*, 151-153.
35. Karas, M.; Bachmann, D.; Hillenkamp, F. *Analytical Chemistry* **1985**, *57*, 2935.

36. Karas, M.; Bachmann, D.; Bahr, U.; Hillenkamp, F. *International Journal of Mass Spectrometry and Ion Processes* **1987**, *78*, 53-68.
37. Karas, M.; Hillenkamp, F. *Analytical Chemistry* **1988**, *60*, 2299-2301.
38. Tanaka, K.; Ido, Y.; Akita, S., Proceedings of the Second Japan-China Joint Symposium on Mass Spectrometry; Matsuda H.; Linag X.-T., Eds.; Bando Press: Osaka, **1987**.
39. Hillenkamp, F.; Karas, M. *International Journal of Mass Spectrometry* **2000**, *200*, 71-77.
40. Dreisewerd, K.; Berkenkamp, S. Leisner, A. Rohlfing, A. Menzel, C. *International Journal of Mass Spectrometry* **2003**, *226*, 189-209.
41. Hillenkamp, F. International Mass Spectrometry Conference, Bordeaux, France, August, **1988**.
42. *The Expanding Role of Mass Spectrometry in Biotechnology*, Siuzdak, G., MCC Press: San Diego, **2003**.
43. Zenobi, R.; Knochenmuss, R. *Mass Spectrometry Reviews* **1998**, *17*, 337-366.
44. Menzel, C. Dreisewerd, K. Berkenkamp, S. Hillenkamp, F. *International Journal of Mass Spectrometry* **2001**, *207*, 73-96.
45. Dreisewerd, K. *Chemical Reviews* **2003**, *103*, 395-425.
46. Karas, M. Krüger, R. *Chemical Reviews* **2003**, *103*, 427-439.
47. Niu, S. Zhang, W. Chait, B. T. *Journal of American Society of Mass Spectrometry* **1998**, *9*, 1.
48. Berkenkamp, S.; Menzel, C.; Karas, M.; Hillenkamp, F. *Rapid Communications in Mass Spectrometry* **1997**, *11*, 1399.
49. Ehring, H.; Karas, M.; Hillenkamp, F. *Organic Mass Spectrometry* **1992**, *27*, 427.
50. Heise, T. W.; Yeung, E. S. *Analytica Chimica Acta* **1995**, *199*, 377.
51. Karbach, V. Knochenmus, R. *Rapid Communications in Mass Spectrometry* **1998**, *12*, 968.
52. Preston-Scaffer, L. M., Kinsel, G. R.; Russell, D. H. *Journal of American Society of Mass Spectrometry* **1994**, *5*, 800.
53. Ehring, H.; Sundqvist, B. U. R. *Applied Surface Science* **1996**, *96-98*, 577.
54. Karas, M. *Organic Mass Spectrometry* **1993**, *28*, 1476.

55. Johnson, R. E. *International Journal of Mass Spectrometry and Ion Processes* **1994**, 139, 25.
56. Chevrier, M. R.; Cotter, R. J. *Rapid Communications in Mass Spectrometry* **1991**, 5, 611.
57. Dreisewerrd, K. Schürenberg, M., Karas, M., Hillenkamp, F. *International Journal of Mass Spectrometry and Ion Processes* **1995**, 141, 127.
58. Beavis, R. C. *Organic Mass Spectrometry* **1992**, 27, 864.
59. Breuker, K.; Knochenmuss, R.; Zenobi, R. *International Journal of Mass Spectrometry and Ion Processes* **1998**, 176, 149-159.
60. Lehmann, E.; Knochenmuss, R.; Zenobi, R. *Journal of American Society of Mass Spectrometry* **1997**, 11, 1483.
61. Liao, P.-C.; Allison, J. *Journal of Mass Spectrometry* **1995**, 30, 408.
62. Zhu, Y.; Lee, K. L.; Tang, K.; Allman, S. L.; Taranencko, N. I.; Chen, C. H. *Rapid Communications in Mass Spectrometry* **1995**, 9, 1315.
63. Cotter, R. J. *Analytica Chimica Acta* **1987**, 195, 45.
64. Cramer, R.; Haglund, Jr. R. F.; Hillenkamp, F. *International Journal of Mass Spectrometry and Ion Processes* **1997**, 169/170, 51.
65. Chen, X.; Carroll, J. A.; Beavis, R. C. *Journal of American Society of Mass Spectrometry* **1998**, 9, 885.
66. Zhigilei, L. V.; Yingling, Y. G.; Itina, T. E.; Schoolcraft, T. A.; Garrison, B. J. *International Journal of Mass Spectrometry* **2003**, 226, 85-106.
67. Vertes, A.; Irinyi, G.; Gijbels, R. *Analytical Chemistry* **1993**, 65, 2389.
68. Puretzky, A. A.; Geohegan, D. B. *Chemical Physics Letters* **1997**, 286, 425.
69. Sunner, J. *Organic Mass Spectrometry* **1993**, 28, 805.
70. Harrison, A. G. *Mass Spectrometry Reviews* **1997**, 16, 201-217.
71. Jørgensen, T. J.D.; Bojesen, G.; Rahbek-Nielsen, H. *European Journal of Mass Spectrometry* **1998**, 4, 39.
72. Tang, X.; Sadeghi, M.; Olumee, Z.; Vertes, A. *Rapid Communications in Mass Spectrometry* **1997**, 8, 281.
73. Wang, B. H.; Dreisewerd, K.; Bahr, U.; Karas, M.; Hillenkamp, F. *Journal of American Society of Mass Spectrometry* **1993**, 4, 393.

74. Belov, M. E.; Myatt, C. P.; Derrick, P. J. *Chemical Physics Letters* **1998**, 284, 412.
75. Dogruel, D.; Nelson, R. W.; Williams, P. *Rapid Communications in Mass Spectrometry* **1996**, 10, 801.
76. Beavis, R. C.; Chait, B. T. *Rapid Communications in Mass Spectrometry* **1989**, 3,233.
77. Stephens *Physics Review* **1946**, 69, 691.
78. Stephens, W. E. Mass Spectrometer. U.S. Patent 2,612,607, September 30, **1952**.
79. *Mass Spec Desk Reference*, Sparkman, O. D., Global View Publishing: Pittsburgh, **2000**.
80. *Introduction to Mass Spectrometry 3<sup>rd</sup> Ed.*, Watson, J. T., Lippincott-Raven: Philadelphia, **1997**.
81. Wiley, W. C. Mass Spectrometry. US Patent 2,685,035, July 27, **1954**.
82. Lobo, A. V.; Ackloo, S.; Chernushevich, I. V. *Rapid Communications in Mass Spectrometry* **2003**, 17, 2508-2516.
83. Chernushevich I. V.; Ens, W.; Standing, K. G. *Analytical Chemistry* **1999**, 71, 452A-461A.
84. Vestal, M. L.; Juhasz, P.; Martin, S. A. *Rapid Communication in Mass Spectrometry* **1995**, 9, 1044-1050.
85. Guilhaus, M. *Journal of Mass Spectrometry* **1995**, 30, 1519-1532.
86. *Mass Spectrometry 2<sup>nd</sup> Ed.*, Barker, J., John Wiley and Sons: New York, **1999**.
87. Kovtoun, S. English, R. D., Cotter, R. J. *Journal of American Society of Mass Spectrometry* **2001**, 13, 135.
88. Guilhaus, M.; Selby, D.; Mlynski, V. *Mass Spectrometry Reviews* **2000**, 19, 65-107.
89. Standing, K. G. *International Journal of Mass Spectrometry* **2000**, 200, 597-610.
90. O'Halloran, G. J.; Fluegge, R. A.; Betts, J. F.; Everett, W. L.; Technical Report No. ASD-TDR 62-644; Bendix Co.: **1964**.
91. Krutchinsky, A. N.; Loboda, A. V.; Spicer, V. L.; Dworschak, R.; Ens, W.; Standing, K. G. *Rapid Communication in Mass Spectrometry* **1998**, 12, 508-518.
92. Chernushevich I. V.; Ens, W.; Standing, K. G. *Analytical Chemistry* **1999**, 71, 452A-461A.

93. Mirgorodskaya, O. A.; Shevchenko, A. A.; Chernushevich, I. V.; Dodonov, A. F.; Miroshnikov, A. I. *Analytical Chemistry* **1994**, *66*, 99.
94. Dodonov, A.; Kozlovski, V.; Loboda, A.; Raznikov, V.; Sulimenkov, I.; Tolmachev, A.; Kraft, A.; Wollnik, H. *Rapid Communications in Mass Spectrometry* **1997**, *11*, 1649.
95. *Electrospray Ionization Mass Spectrometry*, Cole, R. B., ed., Wiley: New York, **1997**.
96. Fenn, J. B.; Mann, C. K.; Wong, S. F.; Whitehouse, C. M. *Science* **1989**, *246*, 64.
97. Chen, Y.H.; Gonin, M.; Fuhrer, K.; Dodonov, A.; Su, C.S.; Wollnik, H. *International Journal of Mass Spectrometry* **1999**, *185-187*, 221-226.
98. Lobo, A. V.; Ackloo, S.; Chernushevich, I. V. *Rapid Communications in Mass Spectrometry* **2003**, *17*, 2508-2516.
99. Vestal, M. L.; Juhasz, P.; Martin, S. A. *Rapid Communication in Mass Spectrometry* **1995**, *9*, 1044-1050.
100. Kantrowitz, A.; Grey, J. *Review of Scientific Instrumentation* **1951**, *22*, 328.
101. Fenn, J. B. *International Journal of Mass Spectrometry* **2000**, *200*, 459-478.
102. Chernushevich, I. V.; Thomson, B. A. *Analytical Chemistry* **2004**, *76*, 1754-1760.
103. Laiko, V. V.; Baldwin, M. A.; Burlingame, A. L. *Analytical Chemistry* **2000**, *7*, 652-657.
104. Laiko, V. V.; Burlingame, A. L. Atmospheric Pressure Matrix-Assisted Laser Desorption. U. S. Patent 5,965,884, October 12, **1999**.
105. Laiko, V. V.; Moyer, S. C.; Cotter, R. J. *Analytical Chemistry* **2000**, *72*, 5239-5243.
106. Callahan, J. H.; Galicia, M.; Vertes, A. In Proceedings of the 48<sup>th</sup> ASMS Conference on Mass Spectrometry and Allied Topics; Long Beach, CA, **2000**.
107. Galicia, M.C.; Vertes, A.; Callahan, J. H. *Analytical Chemistry* **2002**, *74*, 1891-1895.
108. Doroshenko, V. M.; Laiko, V. V.; Taranenko, N. I.; Berkout, V. D.; Sang Lee, H. *International Journal of Mass Spectrometry* **2002**, *221*, 39-58.
109. Süßmuth, R. D.; Jung, G. *Journal of Chromatography B* **1999**, *725*, 49-65.
110. Hillenkamp, F.; Karas, M. *International Journal of Mass Spectrometry* **2000**, *200*, 71-77.

111. Rockwood, A. L., Davis, L. J., Jones, J. L., Lee, E. D. Printed Circuit Boards as Insulated Components for a Time-of-Flight Mass Spectrometer. U.S. Patent 6,316,768, November 13, **2001**.
112. Rockwood, A. L., Davis, L. J. Multi-anode Time to Digital Converter. U.S. Patent 5,777,326, July 7, **1998**.
113. Dale, M.J.; Knochenmuss, R.; Zenobi, R. *Rapid Communications in Mass Spectrometry* **1997**, *11*, 136-142.
114. Moyer, S.; Cotter, R. *Analytical Chemistry* **2002**, 469A-476A.
115. Miller, C.; Yi, D.; Perkins, P. *Rapid Communications in Mass Spectrometry* **2003**, *17*, 860-868.
116. Cech, N. B.; Enke, C. G. *Mass Spectrometry Reviews* **2001**, *20*, 362-387.
117. *Physical Chemistry 6<sup>th</sup> Ed.*, Atkins, P. W., Freeman: New York, **1998**.
118. Hang, W.; Lewis, C.; Majidi, V. *Analyst* **2003**, *128*, 273-280.
119. Douglas, D. J.; French, J. B. *Journal of the American Society of Mass Spectrometry* **1992**, *3*, 398.
120. Xu, H. J.; Wada, M.; Tanaka, J.; Kawakami, H.; Katayama, I.; Ohtani, S. *Nuclear Instruments and Methods in Physics Research Section A* **1993**, 333, 274.
121. Garden, R.; Sweedler, J. *Analytical Chemistry* **2000**, *72*, 30-36.
122. Hanton, S.; Cornelio Clark, P. A.; Owens, K. G. *Journal of the American Society of Mass Spectrometry* **1999**, *10*, 104-111.
123. Axelsson, J.; Hoberg, A.; Waterson, C.; Myatt, P.; Shield, G. L.; Varney, J.; Haddleton, D. M.; Derrick, P. J. *Rapid Communications in Mass Spectrometry* **1997**, *11*, 209-213.
124. Hensel, R. R.; King, R. C.; Owens, K. G. *Rapid Communications in Mass Spectrometry* **1997**, *11*, 1785-1793.
125. Li, L.; Doucette, A.; Zhang, N. *Analytical Chemistry* **2001**, *73*, 2968-2975.
126. Fitzgerald, M. C.; Wang, M. Z. *Analytical Chemistry* **2001**, *73*, 625-631.
127. Owens, K. G.; Cornelio Clark, P. A.; Hanton, S. *Journal of the American Society of Mass Spectrometry* **1999**, *10*, 104-111.
128. Barber, M.; Bordoli, R. S.; Elliott, G. J.; Sedgwick, R. D.; Tyler, A. N. *Analytical Chemistry* **1982**, *54*, 645A-57A.

129. De Pauw, E.; Agnello, A.; Derwa, F. *Mass Spectrometry Reviews* **1991**, *10*, 283-301.
130. Hercules, D. M.; Gusev, A. I.; Williams, J. B. *Macromolecules* **1996**, *29*, 8144-8150.
131. Li, L.; Wang, A. P. I.; Coulson, L. D. *Analytical Chemistry* **1999**, *65*, 493-495.
132. Ring, S.; Rudich, Y. *Rapid Communications in Mass Spectrometry* **2000**, *14*, 511-519.
133. Zhao, S.; Somayajula, K. V.; Sharkey, A. G.; Hercules, D. M.; Ingendoh, A.; Karas, M.; Hillenkamp, F. *Analytical Chemistry* **1991**, *63*, 450-453.
134. Hillenkamp, F.; Dreisewerd, K.; Schürenberg, M. *Analytical Chemistry* **1999**, *71*, 221-229.
135. Kinumi, T.; Saisu, T.; Takayama, M.; Niwa, H. *Journal of Mass Spectrometry* **2000**, *35*, 417-422.
136. Sunner, J.; Dratz, E.; Chen, Y. *Analytical Chemistry* **1995**, *67*, 4335-4342.
137. Zenobi, R.; Knochenmuss, R.; Dale, M. J. *Analytical Chemistry* **1996**, *68*, 3321-3329.
138. Zöllner, P.; Stübiger, G.; Schmid, E.; Pittenauer, E.; Allmaier, G. *International Journal of Mass Spectrometry and Ion Processes* **1997**, *169/170*, 99-109.
139. Wang, G.; Chan, T-W. D.; Sze, E. T. P. *Journal of the American Society of Mass Spectrometry* **1998**, *9*, 166-174.
140. Amster, J.; Duncan, M. A.; Cornett, D. S. *Analytical Chemistry* **1993**, *65*, 2608-2613.
141. Beavis, R. C.; Chaudhary, T.; Chait, B. T. *Organic Mass Spectrometry* **1992**, *27*, 156-158.
142. Menzel, C.; Berkenkamp, S.; Hillenkamp, F. *Rapid Communications in Mass Spectrometry* **1999**, *13*, 26-32.
143. Cotter, R.; Moyer, S.; Von Seggern, C. E. *Analytical Chemistry* **2003**, *75*, 3212-3218.
144. Chernushevich, I.; Loboda, A.; Thomson, B. *Journal of Mass Spectrometry* **2001**, *36*, 849-865.
145. Berkenkamp, S.; Menzel, C.; Hillenkamp, F.; Dreisewerd, K. *Journal of the American Society of Mass Spectrometry*. **2002**, *13*, 209-220.

146. *Spectrochemical Analysis*, Ingle, J. D. Jr.; Crouch, S. R., Prentice Hall: Upper Saddle River, **1988**.
147. Luo, G.; Marginean, I.; Vertes, A. In Proceedings of the 50<sup>th</sup> ASMS Conference on Mass Spectrometry and Allied Topics; Orlando, FL, **2002**.
148. Krutchinsky, A.; Chait, B. T. *Journal of American Society of Mass Spectrometry* **2002**, *12*, 129-134.
149. *Principles and Practice of Biological Mass Spectrometry*, Dass, C., John Wiley and Sons, Inc.: New York, **2001**.
150. Brown, R. S.; Carr, B. L.; Lennon, J. J. *Journal of the American Society of Mass Spectrometry* **1996**, *7*, 225-232.
151. Cohen, S. L.; Chait, B. T. *Analytical Chemistry* **1996**, *68*, 31-37.
152. Westmacott, G.; Ens, W.; Hillenkamp, F.; Dreisewerd, K.; Schürenberg, M. *International Journal of Mass Spectrometry* **2002**, *221*, 67-81.
153. Dreisewerd, K.; Schürenberg, M.; Karas, M.; Hillenkamp, F. *International Journal of Mass Spectrometry and Ion Processes* **1995**, *141*, 127-148.
154. Alves, S.; Kalberer, M.; Zenobi, R. *Rapid Communications in Mass Spectrometry* **2003**, *17*, 2034-2038.
155. Horneffer, V.; Dreisewerd, K.; Luedemann, H.C.; Hillenkamp, F.; Laege, M.; Strupat, K. *International Journal of Mass Spectrometry* **1999**, *185/186/187*, 859.
156. Berkenkamp, S.; Menzel, C.; Hillenkamp, F.; Dreisewerd, K. *Journal of American Society of Mass Spectrometry* **2002**, *13*, 203-220.
157. Zhigilei, L. V.; Garrison, B. J. *Journal of Applied Physics* **2000**, *88*, 1281.
158. Berkenkamp, S.; Menzel, C.; Hillenkamp, F.; Dreisewerd, K. *Journal of American Society of Mass Spectrometry* **2002**, *13*, 209-220.
159. McLean, J. A.; Russell, W. K.; Russell, D. H. *Analytical Chemistry* **2003**, *75*, 648-654.
160. Quist, A. P.; Huth-Fehre, T.; Sunqvist, B. U. R. *Rapid Communications in Mass Spectrometry* **1994**, *8*, 149.
161. Pingitore, F.; Polce, M. J.; Wang, P.; Wesdemiotis, C.; Paizs, B. *Journal of the American Society of Mass Spectrometry* **2004**, *15*, 1025-1038.
162. Jackson, S. N.; Mishra, S.; Murray, K. K. Proceedings of the 51<sup>st</sup> ASMS Conference on Mass Spectrometry and Allied Topics, Montreal, Quebec, Canada, June 8-12, **2003**.

163. Knockenmuss, R.; Zenobi, R. *Chemical Reviews* **2003**, *103*, 441-452.
164. Baumgart; Lindner; Kuhne; Oberemm; Wenschuh; Krause *Rapid Communications in Mass Spectrometry* **2004**, *18*: 863-868.
165. Tanaka, K. *The Origin of Macromolecular Ionization by Laser Irradiation*, Nobel Lecture, Aula Magna, Stockholm University, December, 8, **2002**.
166. Laiko, V. V.; Taranenko, N. I.; Berkout, V.; Yakshin, M. A.; Prasad, C. R.; Sang Lee, H.; Doroshenko, V. M. *Journal of the American Society of Mass Spectrometry* **2002**, *13*, 354-361.
167. Cotter, R.; Moyer, S.; Von Seggern, C. E. *Analytical Chemistry* **2003**, *75*, 3212-3218.
168. Turney, K.; Harrison, W. *Rapid Communications in Mass Spectrometry* **2004**, *18*, 629-635.
169. Lim, H.; Eng, J.; Yates, J.R. III; Tollaksen, S.; Giometti, C.; Holden, J.; Adams, M.; Reich, C.; Olsen, G.; Hays, L. *Journal of the American Society of Mass Spectrometry* **2003**, 957-970.
170. Tanq, N.; Tornatore, P.; Weinberger, S. R. *Mass Spectrometry Reviews* **2004**, *23*, 34-44.
171. Petricoin, E.; Liotta L. *Current Opinion in Biotechnology* **2004**, *15*, 24-30.
172. Gevaert, K.; Demol, H.; Sklyarova, T.; Houthaeye, T. *Electrophoresis* **1998**, *19*, 909-917.
173. Gevaert, K.; Demol, H.; Puype, M.; Broekaert, D.; De Boeck, S.; Houthaeye, T.; Veenstra, T. *Electrophoresis* **1997**, *18*, 2950-2960.
174. Villanueva, J.; Philip, J.; Entenberg, D.; Chaparr, C.; Tanwar, M.; Holland, E.; Tempst, P. *Analytical Chemistry* **2004**, *76*, 1560-1570.
175. Yaneva, M.; Tempst, P. *Analytical Chemistry* **2003**, *75*, 6437-6448.
176. Zhao, X. J.; Tapeç, R.; Wang, K. M.; Tan, W. H. *Analytical Chemistry* **2003**, *75*, 3476-3483.
177. Zhao, X.; Tapeç-Dytioco, R.; Tan, W. *Journal of the American Chemical Society* **2003**, *125*, 11474-11475.
178. Brody, E. N.; Gold, L. *Reviews in Molecular Biotechnology* **2000**, *74*, 5-13.
179. Fang, X.; Mi, Y.; Li, J. J.; Beck, T.; Schuster, S.; Tan, W. *Cell Biochemistry and Biophysics* **2002**, *37*, 71-81.

180. Rajendran, M.; Ellington, A. D. *Optical Biosensors* **2002**, 369-396.
181. Neubert, H.; Jacoby, E. S.; Bansal, S. S.; Iies, R. K.; Cowan, D. A.; Kicman, A. T. *Analytical Chemistry* **2002**, *74*, 3677-3683.
182. Jayasena, S. D. *Clinical Chemistry* **1999**, *45*, 1628-1650.
183. Ellington, A.; Szostak, J. W. *Nature* **1990**, *346*, 818-822.
184. Robertson, D. L.; Joyce, G. F. *Nature* **1990**, *344*, 467.
185. Tuerk, C.; Gold, L. *Science* **1990**, *249*, 4968.
186. Luzi, E.; Minunni, M.; Tombelli, S.; Mascini, M. *Trends in Analytical Chemistry* **2003**, *22*, 810-818.
187. Michaud, M.; Jourdan, E.; Villet, A.; Ravel, A.; Grosset, C.; Peyrin, E. *Journal of the American Chemical Society* **2003**, *125*, 8672-8679.
188. Williams, K. P.; Liu, X. H.; Schumacher, T. N.; Lin, H. Y.; Ausiello, D. A.; Kim, P. S.; Bartel, D. P. *Proceedings of the National Academy of Sciences of the United States of America* **1997**, *94*, 11285-11290.
189. Qhobosheane, M.; Santra, S.; Zhang, P.; Tan, W. H. *Analyst* **2001**, *126*, 1274-1278.
190. Schroedter, A.; Weller, H. *Angewandte Chemie International Edition* **2002**, *41*, 3218-3221.
191. Stober, W.; Fink, A.; Bohn, E. *Journal of Colloid Interface Science* **1968**, *26*, 62-69.
192. Massart, R. Magnetic Fluids and Process for Obtaining Them. U.S. Patent 4,329,241, May 11, **1982**.
193. Kleinjung, F.; Klussmann, S.; Erdmann, V. A.; Scheller, F. W.; Fuerste, J. P.; Bier, F. F. *Analytical Chemistry* **1998**, *70*, 328-331.
194. Girault, S.; Chassaing, G.; Blais, J. C.; Brunot, A.; Bolbach, G. *Analytical Chemistry* **1996**, *68*, 2122-2126.
195. Barford, R. A.; Sliwinski, B. J.; Breyer, A. C.; Rothbart, H. L. *Journal of Chromatography* **1982**, *235*, 281-288.
196. Wehr, C. T.; Correia, L.; Abbott, S. R. *Journal of Chromatography Science* **1982**, *20*, 114-119.
197. Issaq, H.; Veenstra, T.; Conrads, T.; Felschow, D. *Biochemical and Biophysical Research Communications* **2002**, *292*, 587-592.

198. Cotter, R. J. *Analytical Chemistry* **1980**, 52, 1767-1770.
199. *Lasers and Mass Spectrometry*, Lubman, D. M., Ed., Oxford University Press: New York, **1990**.
200. Mowry, C. D.; Johnston, M. V. *Rapid Communications in Mass Spectrometry* **1993**, 7, 569.
201. Mowry, C. D.; Johnston, M. V. *Journal of Physical Chemistry* **1994**, 98, 1904.
202. Coon, J. J.; McHale, K. J.; Harrison, W. W. *Rapid Communications in Mass Spectrometry* **2002**, 16, 681.
203. Coon, J. J.; Harrison, W. W. *Analytical Chemistry* **2002**, 74, 5600-5605.
204. Benocci, R.; Galassi, A.; Mauri, L.; Piselli, M.; Sciascia, M. *The European Physical Journal D* **2003**, 25, 157-160.
205. Carreno, F.; Bernabeu, E. *Journal of Physics D: Applied Physics* **1994**, 27, 2136-2144.
206. Bruins, A. P. *Trends in Analytical Chemistry* **1994**, 13, 37-43.
207. Bruins, A. P. *Trends in Analytical Chemistry* **1994**, 13, 81-90.
208. Carroll, D. I.; Dzidic, I.; Horning, E. C.; Stillwell, R. N. *Applied Spectroscopy Reviews* **1981**, 17, 337-406.

## BIOGRAPHICAL SKETCH

Kevin Paul Turney was born in Lakenheath, England. He attended Eastern Washington University in Cheney, Washington, graduating *summa cum laude* with a Bachelor of Science degree in chemistry and a minor in physics. In the fall of 2000, he enrolled in the Analytical Division of the Chemistry Department at the University of Florida. Under the direction of Professor W. W. Harrison, he completed his graduate studies with a Doctor of Philosophy in December 2004.